UNIVERSITY OF SOUTHAMPTON

Multi-beam pulsed laser deposition for engineered crystal films

by

Katherine Alice Sloyan

A thesis submitted for the
degree of Doctor of Philosophy

in the
Faculty of Physical and Applied Sciences
Optoelectronics Research Centre

May 2012

UNIVERSITY OF SOUTHAMPTON

ABSTRACT

FACULTY OF PHYSICAL AND APPLIED SCIENCES
OPTOELECTRONICS RESEARCH CENTRE

Doctor of Philosophy

by Katherine Alice Sloyan

Pulsed laser deposition (PLD) is a quick, versatile technique for crystal film growth. Multi-beam PLD extends the basic PLD setup to include multiple lasers and targets, and has shown immense promise for the engineering of custom crystal films and structures. The full potential of the technique has not, however, yet been fully explored. The experiments in this thesis have been designed to investigate, extend and improve multi-beam PLD, to provide new avenues for fabrication of sophisticated designer films and to find applications that truly exploit the technique's potential.

The effect of relative delay between plasma plumes on crystal properties was investigated and was found to influence lattice constant for delay values of $\leq$400 µs due to higher energy ion bombardment of the growing film. The shutter technique for multi-beam crystal engineering was developed and demonstrated via the automated growth of garnet mixed films, superlattices and chirped structures. The method was used to grow crystalline garnet Bragg reflectors with a range of designs, including π-phase shifted and quarter-wave stacks with up to 145 layers and 99% peak reflectivity. A Gaussian profile, grating-strength apodised Bragg stack was grown, with the resulting reduction in side band reflections observed as expected. This represents the first known example of such sophisticated crystal engineering by PLD. Routes to using single- and multi-beam PLD for rapid prototyping of laser crystals were also explored. Double-clad crystalline channel waveguides were fabricated via physical micromachining of PLD-grown garnet multilayer films and subsequent overgrowth. Millimetre-sized crystalline features were grown via single-beam PLD through shadow masks and funnels, culminating in fabrication of a hybrid garnet crystal by a combination of multi-beam PLD and plume funnelling.

The results in this thesis represent steps towards the true exploitation of PLD, but much is still to be done. Many routes for future improvement have been suggested, building on the novel techniques developed for this thesis, including the growth of sesquioxides as component layers of functional Bragg stacks capable of withstanding high powers and temperatures.

Contents

List of Figures

List of Tables

Declaration of Authorship

I, Katherine Alice Sloyan, declare that this thesis titled, “Multi-beam pulsed laser deposition for engineered crystal films” and the work presented in it are both my own, and have been generated by me as the result of my own original research. I confirm that:

- This work was done wholly or mainly while in candidature for a research degree at this University.
- Where any part of this thesis has previously been submitted for a degree or any other qualification at this University or any other institution, this has been clearly stated.
- Where I have consulted the published work of others, this is always clearly attributed.
- Where I have quoted from the work of others, the source is always given. With the exception of such quotations, this thesis is entirely my own work.
- I have acknowledged all main sources of help.
- Where the thesis is based on work done by myself jointly with others, I have made clear exactly what was done by others and what I have contributed myself.
- Parts of this work have been published before submission, with a list of such publications given in section 1.4.

Signed: ________________________________

Date: ________________________________

Acknowledgements

The work presented in this thesis has been primarily funded by EPSRC grant number EP/F019300/1. I am also grateful for the support of an EPSRC studentship.

Various people have made direct contributions to many of the results described in this thesis. Although they have also been acknowledged in the appropriate chapters, I would like to particularly highlight the help of Amol Choudary, Michalis Zervas and Lewis Carpenter (ORC, University of Southampton), James Lunney (Trinity College Dublin), David Walker and Steven Huband (University of Warwick) and Sebastian Heinrich (University of Hamburg).

I would like to thank Rob and Tim for all their advice and support, and for generally being excellent supervisors even in the face of many other competing priorities. Thanks also to my friends and colleagues in the ORC, ECS and beyond, whether for helping with experiments, making the shed bearable or generally showing their support for tea and other extracurricular activities. Some credit for this thesis should also go to Anne Fox, Gi Sierant, Alan Dryer, Thornton Naylor and Roger Conibear. I would not have got to this point without them.

My thanks go especially to my family, particularly my parents, for always supporting and encouraging me in whatever I've chosen to do, and finally to Ali for helping me to stay within the realms of sanity.

“You know, I have one simple request. And that is to have sharks with frickin’ laser beams attached to their heads! - Dr. Evil

Chapter 1

Introduction

1.1 Engineering with pulsed laser deposition

Pulsed laser deposition (PLD) is a quick, versatile method of depositing thin films of a wide range of materials. Laser pulses, usually in the UV, are focussed onto a target containing the atomic constituents of the material to be deposited. The irradiated spot is ablated, leading to ejection of material that is heated further by the laser and forms a plume of partially-ionised material. This plume expands away from the target and deposits components of the target material onto a substrate. This process is repeated over many pulses to form a film, with possible thicknesses ranging from a single unit cell (∼1 nm) to tens or even hundreds of microns. If the substrate is crystalline and heated then epitaxial crystal films can be obtained, provided that the many interconnected deposition conditions (background gas pressure, substrate temperature, laser fluence etc.) are tuned correctly.

Although not without drawbacks (chiefly particulate production), in many applications PLD compares favourably with other thin film deposition techniques. It is suitable for depositing multi-component materials with complex stoichiometries. The apparatus is relatively simple and does not require harmful precursor chemicals. Growth rates can be high at upwards of several µm per hour, and costs are relatively low. Most importantly, the high number of controllable growth parameters makes PLD an extremely versatile deposition method.

The interactions between a target and a laser beam were investigated within a few years of the invention of the laser, with the first rudimentary deposition of thin films reported in 1965. The 1970s saw a leap forward with the invention of Q-switching and second harmonic generation, which made nanosecond pulses with high peak power density at short wavelengths readily available. Growth of high-quality high temperature superconducting (HTS) perovskite films in the 1980s presented an even greater breakthrough, which, combined with the wider availability of affordable laser systems, led to an explosion in the popularity of PLD in the following years.

With the growth of HTS films, PLD was proven to be an effective tool for growth of complex oxide crystals, and was soon extended to growth of multi-component optical materials. The first example of garnet growth by PLD was reported in 1991 [1], with planar waveguide lasing first achieved in 1996 [2]. Since then growth has been demonstrated in a variety of materials for a wide range of applications, including photonics (see chapter 2): milestones include growth of lasing garnet films with loss values as low as <0.1 dB per cm [3], multilayer cladded waveguide growth [4] and fabrication of magneto-optic multilayers and superlattices [5, 6, 7]. However, while PLD is now well-established and one-off device growth via PLD has been successful, the technique has not yet managed to make the leap out of the lab and prove itself as a viable industrial fabrication tool.

Multi-beam PLD is one major route for improvement of the technique, increasing speed and versatility whilst helping to solve problems such as particulates. This approach extends the basic PLD setup to include multiple lasers and targets, allowing the growth of mixed and graded films in custom proportions as well as easy multilayer fabrication [8]. Originally developed as a method of particulate reduction, over recent years the technique has shown immense promise for the engineering of custom crystal films and structures. Successes have already been demonstrated: stoichiometry in complex oxides has been corrected by addition of otherwise lost elements [9], mixed layers of custom refractive index grown [10] and tools for the control of film strain developed [11].

The true potential of pulsed laser deposition in general and multi-beam PLD in particular, however, has not yet been fully explored. The experiments in this thesis have been designed to investigate, extend and improve multi-beam PLD, to provide new avenues for fabrication of sophisticated custom films and to find applications that truly exploit the potential of this quick and versatile technique.

1.2 Structure of this thesis

To provide some understanding of the motivation and theory for the results reported in this thesis, some background information (chapter 2) and theory (chapter 3) concerning PLD and the devices of interest has been presented. Alternative deposition and waveguide fabrication methods have been introduced and compared, highlighting the significant drawbacks and advantages of PLD growth. The relevant experimental methods have been described in chapter 4 and mitigation of drawbacks discussed (e.g. tools for particulate reduction), along with details of the analytical techniques used. Chapters 5-8 contain the results of experiments developing and using multi-beam PLD, including growth of Bragg stacks, rapid prototyping of thick crystal channel waveguides and growth of hybrid crystals for thin disc laser applications. Chapter 9 summarises the results in this thesis and discusses possible steps for future improvement. Three appendices are also included, providing further derivation of waveguide and Bragg stack theory (appendices A and B respectively) as well as details of preliminary sesquioxide growth (appendix C).

1.3 Summary of achievements

The following is a summary of the main achievements of this thesis:

- The effect of laser plume synchronicity on the structure and composition of crystal films was investigated, and was found to significantly influence the lattice constant for delay values of $\leq$400 µs.
- A technique for automated mixed, graded and multilayer crystal growth based around computer-controlled mechanical shutters was designed and implemented. In order to prove the technique's efficacy, simple and chirped crystalline superlattices were grown along with mixed and thicker multilayer stacks.
- Using the shutter technique, growth of Bragg reflectors by multi-beam, multi-target PLD was demonstrated for the first time. Stacks were crystalline and grown from alternating layers of single-phase YAG and GGG. Designs included π phase-shifted and quarter-wave stacks with up to 145 layers and >99% peak reflection.
- An approximately Gaussian profile, grating strength-apodised Bragg stack was grown, with side band reflections reduced as expected. This represents the first known example of such a design in stack geometry.
- Double-clad crystalline channel waveguides were fabricated via physical micromachining of multilayer PLD-grown garnet films and subsequent overgrowth. This is believed to represent the first example of both crystal waveguide fabrication by micromachining and growth of double-clad crystalline channel waveguides.
- Millimetre-sized crystalline features were grown via single-beam PLD through shadow masks and funnels.
- A hybrid garnet crystal was grown by combining multi-beam PLD and plume funnelling. YAG growth was confined to the centre, with GGG grown around the outside and a smooth graded layer in between. This is believed to be the first example of controlled horizontal grading by multi-beam PLD.

1.4 List of publications

The following publications describe results arising directly from experiments detailed in this thesis:

Journal articles

- **K.A. Sloyan**, T.C. May-Smith, R.W. Eason *Hybrid garnet crystal growth for thin disc lasing applications by multi-beam Pulsed Laser Deposition* Applied Physics A 2011 (in review)
- **K.A. Sloyan**, T.C.May-Smith, M.N.Zervas, R.W.Eason, S.Huband, D.Walker, P.A.Thomas *Growth of crystalline garnet mixed films superlattices and multilayers for optical applications via shuttered Combinatorial Pulsed Laser Deposition* Optics Express 2010 **18**(24) pp.24679-24687
- **K.A. Sloyan**, T.C. May-Smith, R.W. Eason, J.G. Lunney *The effect of relative plasma plume delay on the properties of complex oxide films grown by multi-laser multi-target combinatorial pulsed laser deposition* Applied Surface Science 2009 **255**(22) pp.9066-9070

Conference papers

- **K.A. Sloyan**, T.C. May-Smith, M.N. Zervas, R.W. Eason *Fabrication of crystalline Bragg reflectors for high power and integrated optical applications by multi-beam pulsed laser deposition* Conference on Lasers and Electro-Optics (CLEO) 2012 San Jose May 2012 (accepted)
- **K.A. Sloyan**, T.C. May-Smith, R.W. Eason *Horizontally structured garnet growth via pulsed laser deposition for hybrid crystal thin disc applications* 11th International Conference on Laser Ablation (COLA-11) Playa del Carmen, Mexico Nov 2011
- **K.A. Sloyan**, T.C. May-Smith, R.W. Eason *Optical and structural micro-engineering of planar waveguiding films using multi-beam pulsed laser deposition* COLA-11 Playa del Carmen Nov 2011
- **K.A. Sloyan**, L.G. Carpenter, T.C. May-Smith, C. Holmes, J.C. Gates, P.G.R. Smith, R.W. Eason *Fabrication of multilayer crystalline rib waveguides by a combined multi-step Pulsed Laser Deposition/precision machining technique* CLEO Europe 2011 Munich May 2011
- **K.A. Sloyan**, T.C. May-Smith, A. Sposito, R.W. Eason *Pulsed Laser Deposition: Growing crystals with lasers* International OSA Network of Students (IONS)-9 Salamanca April 2011

- **K.A. Sloyan**, T.C. May-Smith, R.W. Eason *Combinatorial Pulsed Laser Deposition: Making lasers with lasers* IONS-8 Moscow June 2010
- **K.A. Sloyan**, T.C. May-Smith, R.W. Eason *Growth of garnet mixed layers and superlattices by dual-beam pulsed laser deposition* European Materials Research Society (EMRS) Spring Meeting 2010 Strasbourg June 2010
- **K.A. Sloyan**, T.C. May-Smith, R.W. Eason *The effect of laser pulse synchronicity on thin garnet films fabricated by dual-beam combinatorial pulsed laser deposition* EMRS Spring Meeting 2009 Strasbourg June 2009

Invited talks (presenter)

- **K.A. Sloyan**, T.C. May-Smith, A. Sposito, R.W. Eason *Multi-beam pulsed laser deposition: Advanced structures and future directions* Physics with new coherent radiation sources (seminar series) University of Hamburg 15 Feb 2011 (Invited)

Book chapters

- R.W. Eason, T.C. May-Smith, **K.A. Sloyan**, R. Gazia, M. Darby, A. Sposito *Emerging pulsed laser deposition techniques* in "Laser growth and processing of photonic devices" edited by N. Vainos, Publisher: Woodhead UK Jul 2012

The following publications contain work carried out during my time as a PhD student, but are not described in detail in this thesis:

- T.C. May-Smith, **K.A. Sloyan**, R. Gazia, R.W. Eason *Stress engineering and optimization of thick garnet crystal films grown by pulsed laser deposition* Crystal Growth & Design 2011 **11**(4) pp.1098-1108
- C.L. Sones, K.S. Kaur, M. Feinäugle, J.Y. Ou, **K.A. Sloyan**, T.C. May-Smith, R.W. Eason, F. Di Pietrantonio, E. Verona *Printing of amorphous and crystalline materials pre-machined using focussed ion beam patterning* CLEO Europe 2011 Munich May 2011
- T.C. May-Smith, **K.A. Sloyan**, R. Gazia, R.W. Eason *A possible route to minimisation of strain in thick garnet films grown by pulsed laser deposition for optical waveguide applications* EMRS Spring Meeting 2009 Strasbourg June 2009

Chapter 2

Background

2.1 Introduction

This chapter introduces some of the materials and structures of interest to this thesis, and aims to provide some context and motivation for the techniques and experiments described in later chapters. Examples of previous growth of similar films and devices are given, as well as discussion of various competing film and waveguide fabrication methods. Emphasis has been placed on optical materials, particularly garnets, and on growth and engineering utilising multi-target PLD.

2.2 Film growth via PLD

2.2.1 Materials of interest

Garnets are cubic materials of the generic formula $A_3B_2C_3O_{12}$ (B and C are often the same). They have a number of physical properties particularly suited to optical applications, including high mechanical strength and hardness, high thermal conductivity, optical isotropy and optical transparency over a wide range of pump and emission wavelengths. The garnet family has many members that have varying refractive indices (indices of common garnets include $n_{YAG} = 1.82$ and $n_{YIG} = 2.2$ at 1060 nm [12]) but the same crystal structure, making them ideal candidates for mixed- and multilayer film fabrication. Iron-based garnets such as YIG also have unusual magnetic properties, and are hence of great interest as magneto-optic devices such as Faraday rotators. PLD is capable of depositing layers of multi-component crystal, and as such is particularly suitable for the growth of complex oxides such as garnets.

Garnet growth by PLD was first achieved in 1991 [1] and since then a wide range of garnets have been successfully deposited, a selection of which has been listed in table 2.1.

Material	Fomula	Application	Reference
Undoped GGG	$Gd_3Ga_5O_{12}$	Materials characterisation (optical)	[14]
Nd:GGG	Nd:$Gd_3Ga_5O_{12}$	Waveguide laser	[3, 15, 2]
Nd,Cr:GGG	Nd,Cr:$Gd_3Ga_5O_{12}$	Waveguide (for Q-switch laser)	[16]
Pr:GGG	Pr:$Gd_3Ga_5O_{12}$	Waveguide (for laser)	[17]
Yb:YAG	Yb:$Y_3Al_5O_{12}$	Waveguide (for planar and thin disc laser)	[18]
Nd:YAG	Nd:$Y_3Al_5O_{12}$	Waveguide (for laser)	[19, 20, 21]
YbAG	$Yb_3Al_5O_{12}$	Waveguide/thin disc laser	[18, 22, 23]
YGG	$Y_3Ga_5O_{12}$	Multilayer waveguide	[22, 4]
Nd,Cr:GSGG	Nd,Cr: $Gd_3Sc_2Ga_3O_{12}$	Waveguide (for Q-switch laser)	[22]
Hybrid GGG:YSGG	$Gd_3Ga_5O_{12}$: $Y_3Sc_2Ga_3O_{12}$	Multilayer waveguide	[10]
Nd,Cr:YSAG	$Y_3Sc_2Al_3O_{12}$	Materials characterisation	[22]
Cr:GSAG	$Gd_3Sc_2Al_3O_{12}$	Materials characterisation (optical)	[22]
LGG	$La_3Ga_5O_{12}$	Multilayer magneto-optic devices	[24]
Undoped YIG	$Y_3Fe_5O_{12}$	Materials characterisation (magnetic) Magnetooptic devices	[25, 26]
Bi:YIG	Bi:$Y_3Fe_5O_{12}$	Materials characterisation (magnetic)	[1]
Ce:YIG	Ce:$Y_3Fe_5O_{12}$	Magneto-optic devices	[26]
LBIG	$Bi_aLu_bFe_cGa_dO_{12}$ (proportions vary)	Magneto-optic devices	[27]
BIG	$Bi_3Fe_5O_{12}$	Magneto-optic devices	[28, 29, 30]
SmIG	$Sm_3Fe_5O_{12}$	Materials characterisation (magnetic)	[31]

TABLE 2.1: Examples of garnets grown by PLD

Stoichiometry does not always precisely match that of bulk, with films often found to exhibit deficiencies of light or volatile elements (e.g. Ga in GGG, Al in YAG). However, routes to solve this problem have been suggested, including use of element-compensated targets [13] or simultaneous ablation of a second target to "add in" elements otherwise lost [9].

Of particular interest for purely optical applications has been GGG, first grown by PLD in 1995 [14]. As well as being relatively easy to grow, GGG presents a close lattice match ($\sim$3% difference) but large refractive index contrast (Δn $\simeq$0.14) to the most readily available crystal substrate, YAG. As such, many examples of GGG for waveguiding and lasing have been reported with a variety of dopants including neodymium [3, 15, 2], chromium [16] and praseodymium [17].

Material	**Substrate**	**Reference**
Nd(Gd,Lu)$_2$O$_3$	Y_2O_3	[34, 33]
Er:Sc$_2$O$_3$	Sc_2O_3	[35]
Y_2O_3, L_2O_3 and S_2O_3	Al_2O_3	[36]
(Eu,Nd):Y_2O_3	Al_2O_3	[37]
Yb:(Gd,Lu)$_2$O$_3$ (lasing)	Y_2O_3	[32]
Eu:Gd$_2$O$_3$	Al_2O_3	[38]

Table 2.2: Examples of cubic sesquioxides grown by PLD

Cubic sesquioxides are also of great interest for lasing applications. Materials of the form X_2O_3, where X includes elements such as yttrium, lutetium and scandium, they have very high thermal conductivities and very good mechanical properties, even compared to garnets. They are easily doped with a variety of rare earth ions, and being cubic materials are optically isotropic (no scattering at grain interfaces if the film is not single-crystal).

A summary of reported material growth is shown in table 2.2. Although fluorescence has been demonstrated in various samples, only two reports of lasing have been found [32, 33]. High temperatures ($\geq$850 °C) appear to be required for crystalline growth, limiting the number of systems capable of sesquioxide deposition. The high growth rates required for growth of thin disc laser crystals have not yet been achieved, with reported film thicknesses limited to $\sim$2 µm.

Although not isotropic, Ti:sapphire (α-Al_2O_3) is of particular interest as a lasing material due to its widely tunable output and for applications in mode-locked waveguide lasing [39]. Substrate temperatures of >950 °C are required to achieve the correct phase of alumina [40]; examples of single-phase growth are hence limited. However, growth by PLD with film thicknesses as high as $\sim$12 µm has been reported on a number of occasions [41, 19, 42, 43]. Particulates have proven a problem in many cases, with particulate densities and hence waveguide losses potentially very high (8.7 dBcm^{-1} planar waveguide loss reported by Uetsuhara et al [43], for example). Lasing has been reported on two occasions, in planar and channel waveguide geometry [44, 42] with losses of 1.8 and 1.7 dBcm^{-1} respectively. Rare earth ion doping of sapphire has also been achieved, something not achievable in bulk crystal form [45]. Undoped sapphire growth has proven particularly challenging due to the poor absorption of sapphire at wavelengths above $\sim$200 nm [46]. A capping layer [42] and multi-phase growth with 248 nm at 850 °C with post-annealing [47] are two reported examples.

PLD has also been successfully used to grow a variety of other materials for optical applications, including semiconductors, ferroelectrics and glasses [40], but these have not been investigated in detail in this thesis.

2.2.2 Epitaxy and post-annealing

Post-annealing can be used to obtain crystalline films that cannot be grown epitaxially, or to improve the crystal order and quality in films already exhibiting some crystallinity [48]. This may be done by heating in a furnace for some hours, or by exposure to an excimer laser at a fluence below the ablation threshold [49]. Both these methods have the effect of giving an amorphous or poorly crystalline film enough additional energy for the atoms to be redistributed via diffusion into a more favourable or ordered crystal lattice site, without exceeding the material melting point. Annealing has also been used to change the valence state of ytterbium atoms in a YbAG film from 2^+ to the 3^+ state required for lasing [50].

2.2.3 Multi-target growth

2.2.3.1 Single-beam

Single-beam, multi-target PLD can be used to deposit multilayered structures as well as mixed materials. Most examples utilise a rotating target carousel, although it is possible to place one small target on top of a larger one, as in the growth of $NiAl_2O_4$ films by ablation of both a ceramic Al_2O_3 target and a strip of nickel foil placed on top reported by Shin et al [51].

Heterostructures have been grown with a variety of materials. These include multilayers containing perovskites such as $SrTiO_3$, $LaAlO_3$, $LaNiO_3$ and $BaTiO_3$ [52, 53, 54], of interest for superconducting or multiferroic applications, as well as MoS_2/Sb_2O_3 structures for solid lubrication [55]. Garnet multilayers based on GGG and magneto-optic YIG and BIG have also been demonstrated [5, 56, 7].

Mixed materials can also be fabricated with a single beam system by depositing layers of sub-unit cell thickness from each target in turn. This can be done to create doped materials, such as the C-doped CdS semiconductor example by Orlianges et al [57], or mixtures of two or three materials. By tilting each target to direct the plume to a different place on a large substrate (see figure 2.1), areas of film mixed in different component ratios are obtained, which may be analysed to build up a material library [58]. An extension to this idea, described by Fukumura et al [59], combines this sub-layer deposition mixing with a moving mask, to create layers that are graded horizontally over the entire substrate. This approach has also been taken to create a library of mixed perovskites $SrTiO_3$ and $LaAlO_3$ [53].

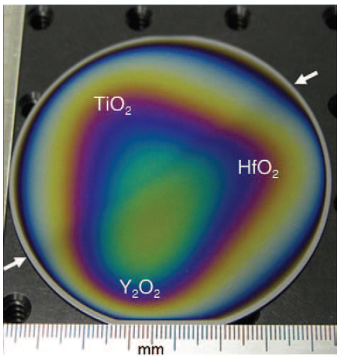

FIGURE 2.1: Plumes are directed to different points on the substrate to obtain a library of mixed materials in different ratios [58].

2.2.3.2 Multi-beam

Multi-beam, multi-target PLD was suggested first by Gaponov in 1982 as a method of particulate reduction [60] (see figure 2.2), and developed further by Gorbunov as "cross-beam PLD" with the introduction of an angled diaphragm [61]. The substrate is placed away from the direct line of sight of the plumes. The interaction of high-density parts of the plume causes lighter species to be redirected, in the latter case through the diaphragm. The front (fastest) and rear (slowest) parts of the plume, which respectively include the most energetic ions and heavier species such as particulates, are not deflected and hence do not reach the substrate. The technique therefore has a bearing both on particulates and the stress of the resulting layer, as the growing film is not subjected to bombardment from the high-energy ions in the plume. Cross-beam PLD traditionally requires both targets to be the same; however, it is possible to combine cross-beam PLD with the target carousel approach mentioned previously, ablating targets alternately to create multilayered structures [62]. The cross-beam approach results in films with drastically reduced particulate densities; however, it does so at the expense of growth rate.

If higher growth rates are required, multi-beam PLD is also possible in a simpler arrangement, with both plumes directed towards the substrate. "Multi-beam" can refer to multiple lasers [10] or a split beam from a single laser [63]; the former provides greater control and versatility, although the latter requires less investment. As with single-beam multi-target PLD, both multilayer and mixed films can be grown, although the use of multiple beams allows a much greater degree of control over mixing to be achieved. Targets are usually held separately, although a carousel may be used or targets may be placed on top of one another, as in the case of Ag-doped $La_{2/3}Sr_{1/3}MnO_3$ reported by Li et al [64].

Plumes can be combined in custom proportions to obtain mixed amophous, crystalline

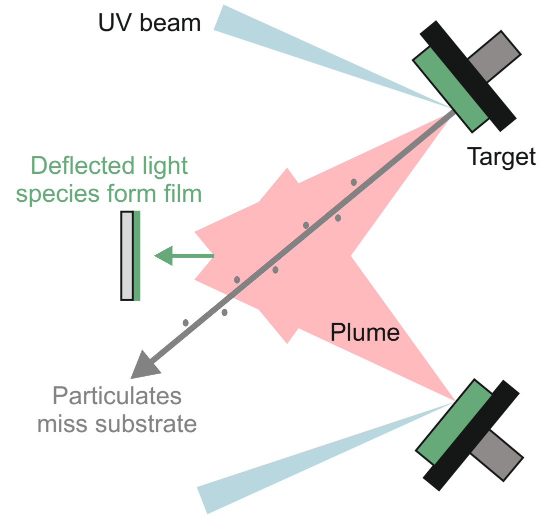

FIGURE 2.2: Illustration of dual-beam approach for particulate reduction pioneered by Gaponov et al [60].

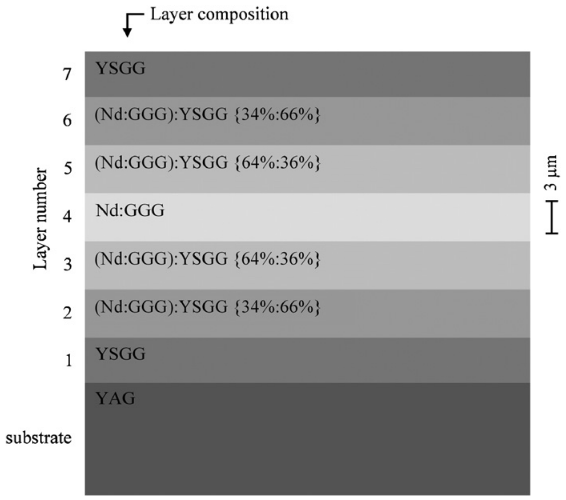

FIGURE 2.3: Schematic of mixed-garnet multilayer waveguide grown by Gazia et al [10].

and metallic layers [65, 66, 67]. Dopants can be introduced, such as in the case of Al-doped ZnO growth for transparent conducting layers [68], and stochiometry of complex oxides can be adjusted by the addition of elements from a second target [9]. Gold and silver nanoparticles have been embedded in oxides for high temperature superconductor [64] and photocatalytic applications [69] respectively. Growth of a mixed, multilayer garnet waveguide was achieved by Gazia et al (see figure 2.3) using a multi-beam setup very similar to the one used for most of the results in this thesis [10].

Different ways have been suggested for controlling the ratio of components in mixed materials, including changing spot size and/or fluence to vary deposition rate [63] and using a beam chopper to vary relative laser repetition rate [70]. It is also possible to block beam paths manually, although this is cumbersome.

2.3 Structures of interest

2.3.1 Planar waveguides

A planar or slab waveguide consists of a layer of material of high refractive index sandwiched between layers of lower refractive index (whether grown or simply the substrate and surrounding air). These layers have a width much greater than their thickness, and light is hence confined in one dimension via total internal reflection. If the core is an active medium, the structure may act as an amplifier or laser. Heat is dissipated perpendicularly to the direction of emission and there is a large surface area to volume ratio, thus reducing thermal lensing. Compared to bulk lasers, such structures are compact, allow greater overlap between pump and lasing beams (resulting in higher efficiencies), can be easily pumped by laser diode arrays and have the potential to be used in integrated optical circuits.

A single-mode, single-layer waveguide laser may be difficult to pump efficiently, particularly with high-power laser diode bars or stacks. The minimum pump beam diameter may be much larger than the core thickness, and hence only a small fraction of diode output may be guided in the core. Layer thickness can be increased to allow efficient diode pumping; this, however, can result in multimode operation and hence a reduction in the quality of the output beam. Instead, multiple cladding and capping layers can be used, whereby pump light is guided by the cladding but absorbed only by the core, an approach somewhat analagous to large mode area optical fibre lasers. As shown by Bhutta et al [71], it is not the absolute core thickness but rather the ratio of core to undoped cladding thickness that determines single mode output (single mode output possible in cases where the core is $\leq$3 times the thickness of each cladding layer). This assumes that the index contrast between the core and cladding is much smaller than the contrast between cladding and cap/substrate, as is the case for a YAG/GGG/Nd:GGG multilayer.

Planar waveguides and lasers can be fabricated using a wide range of methods, many of which are described in section 2.5. Single- and multilayer waveguides with high numerical apertures (NAs) and bulk crystal quality may be created by bonding layers of crystal [72], although the process is time consuming. Refractive index modification methods may be used to fabricate single layers. This can involve indiffusing or exchanging ions on the substrate surface with ions from a layer placed on that surface (e.g. indiffusion of Ti into sapphire from a Ti:metal strip sputtered on the surface) or with ions contained in a bath surrounding the sample. Bombardment with high energy light ions (ion implanatation)

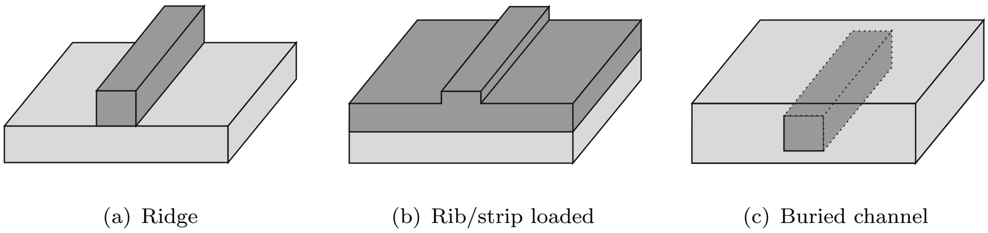
(a) Ridge (b) Rib/strip loaded (c) Buried channel

FIGURE 2.4: Illustration of common channel waveguide structures.

can induce a change in material refractive index to create a waveguide. While these methods can be very slow and resulting waveguide thickness limited, they can be very effective and have been used to fabricate waveguides in various crystalline and amorphous materials [73, 74, 75].

Waveguides may also be fabricated by depositing layers of high-index material onto planar substrates. Such techniques include amorphous or polymer thin film deposition methods such as sputtering, flame hydrolysis deposition and sol gel, as well as high quality but slow epitaxial crystal growth methods such as molecular beam epitaxy. Some are capable of depositing at high growth rates (>10 µm per hour) whilst maintaining crystallinity, such as liquid phase epitaxy. However, each has limitations in terms of growth rate, film quality, materials available or flexibility, particularly for multilayer deposition.

The lasing of a planar waveguide manufactured via PLD was first demonstrated in 1996 with Nd:GGG on YAG [2], and since then the range of PLD-grown waveguide materials has expanded to include $YbVO_4$ [76], Ti:sapphire [41, 44], $YAlO_3$ [77] and SiO_2 [78]. Reported thicknesses range from ∼200 nm to tens of microns, although thickness of layers with different thermal expansion coefficients to the substrate can be limited due to strain (see section 3.2.4). Losses are often high, usually due to the presence of particulates, although losses of less than 0.1 dB/cm have been demonstrated [3]. Waveguiding multilayer structures have been demonstrated [10, 4]; however, their overall structure thickness is limited due to strain-induced delamination and cracking.

2.3.2 Channel and rib waveguides

A channel waveguide confines light in two dimensions. It consists of a thin stripe structure with width similar to thickness, which may be overlaid on a substrate (ridge or rib, figures 2.4(a) and 2.4(b)), or embedded within it (buried channel, figure 2.4(c)). Advantages over bulk are similar to those of planar waveguides, with the additional advantage of confinement in two axes rather than one (of particular interest for integrated optical applications). Propagation losses can, however, be higher than in the planar geometry if the channel surfaces/interfaces are rough.

Material	**Max output (mW)**	**Slope efficiency (%)**	**Losses (dBcm^{-1})**	**Reference**
Nd:GGG	1.35	0.2	-	[91]
Yb:(Gd,Lu)$_2$O$_3$	12	6.7	7	[32]
Ti:Al$_2$O$_3$	27	5.3	1.7	[42]
Yb:YAG	800	68	1.3	[83]
Nd:GGG	27	48	0.25	[89]

Table 2.3: Resulting parameters of examples of lasing channels. All cases except [83] and [89] were fabricated by processing of PLD-grown films.

Various approaches to crystalline channel waveguide fabrication have been demonstrated, more details of which are given in section 2.5. Channels may be fabricated in bulk materials or films by refractive index modification, via proton or ion beam implantation [79, 80, 81], indiffusion [73], ion exchange [74] or laser writing. The latter can be used to write waveguides directly [82] or to create areas of stress-induced refractive index change between two laser-induced damage tracks within a bulk crystal, something which has been demonstrated in doped YAG [83] and vanadates Nd:YVO$_4$ and Nd:GVO$_4$ [84, 85]. In such cases, induced refractive index changes (and hence NAs) are usually small, typically $\Delta n \sim 10^{-3}$.

Methods of physical structuring include femtosecond laser machining and ion beam etching or milling, often machined directly into deposited films [86, 87, 88, 89]. Ridge waveguides have been fabricated by machining of a number of crystalline materials grown via PLD, including Nd:GGG [90, 91], Yb:(Gd,Lu)$_2$O$_3$ [32], BSTO/STO[92, 93] and Ti:sapphire [42].

Lasing has been achieved for some of the PLD-grown examples described (see table 2.3 for results). The contribution to the total loss from coupling, poor film quality (e.g. particulates) and scattering due to poorly defined channels varied in each case, with the non-perpendicular polishing of ridge end presents a potential issue in the case of the Ti:sapphire laser. The lasing performance of PLD films has generally been poor compared to that of some non-PLD examples, such as the Yb:YAG laser demonstrated by Siebermorgen et al [83]. PLD, however, has the advantage of being a quick, simple deposition method useful (in conjunction with further processing) for fabricating structures with a high NA.

2.3.3 Superlattices and Bragg reflectors

Superlattices, periodic multilayer structures with layers no more than a few tens of nanometers thick, are of interest both in their own right and as a test bed for growth of thicker layers, such as those required for Bragg reflectors. Thus far, particular emphasis has been placed on growth of semiconductor superlattices for quantum well applications such as diode lasers. CVD is generally the favoured manufacturing method for such structures [94, 95, 96, 97], although MBE [98, 99] and sputtering [100, 101] have also been investigated. Growth of epitaxial oxide superlattices by PLD has also been reported. An area of particular interest has been the growth of ferroelectric and multiferroic materials; heterostructures of such materials often show very different properties to single layers, and PLD is an ideal method for depositing such multi-component crystals. Example materials include $LiNbO_3/LiTaO_3$ [102], $PbTiO_3/BaTiO_3$ [103], $Pr_{0.7}Ca_{0.3}MnO_3/SrRuO_3$ [104] and $PbZr_{0.53}Ti_{0.47}O_3/CoFe_2O_4$ [105]. Growth of garnet superlattices by PLD has been reported, with emphasis on magneto-optic YIG and BIG [5, 6].

Magneto-optic garnets have also been grown with thicker layers beyond the superlattice regime. Simple PLD-grown YIG/BIG heterostructures with varying numbers of layers were reported by Simion et al [56]. More complex structures include magneto-photonic crystals (MPCs), thick magnetic single layers or multiple magnetic layers sandwiched between reflective Bragg stacks. These devices, which are designed to enhance the optical or magnetic effects (such as Faraday rotation), may consist of a crystalline layer between amorphous reflective stacks (e.g. sputtered SiO_2/TiO_2) [106] or be fully crystalline [7, 107]. Examples of non-magnetic reflective Bragg stacks grown via PLD include ZnO/MgO [108] and multi-phase/amorphous ZrO/Al_2O_3 [109], with ZnO-based microresonators for lasing applications also reported [110, 111]. The examples described above have been undertaken using conventional single-beam, single-target PLD and limited growth rates. It is expected that multi-beam PLD under one set of conditions (as detailed in chapter 6) will allow much quicker growth of many more layers.

Garnet crystals are able to withstand temperatures of >1500 °C and can have higher thermal conductivities and higher damage thresholds than amorphous materials. Crystalline Bragg reflectors are hence potentially of interest for high temperature sensing and rapid prototyping of high-damage threshold optical components, as well as backing mirrors for integrated thin disc laser crystals. As yet, however, reports have not focussed on such applications. Polycrystalline stacks of mixed Al_2O_3-MgO and Al_2O_3 have been deposited via physical vapour deposition (PVD) onto sapphire fibre tips, in preparation for high temperature sensing. Layer definition, however, is lost at temperatures higher than 1000 °C [112].

Apart from the magneto-optic structures mentioned above, sophisticated Bragg geometries have not been investigated in depth. Examples of chirped polymer gratings fabricated by spin casting have been reported [113], as have tunable Bragg reflectors and microcavities fabricated using transparent polymer rubbers [114]. However, although the deposition process is quick and simple and a variety of materials are available, the stacks cannot withstand high powers or temperatures >150 °C. Modelling of apodised stacks has been carried out [115], but such structures have not yet been realised experimentally.

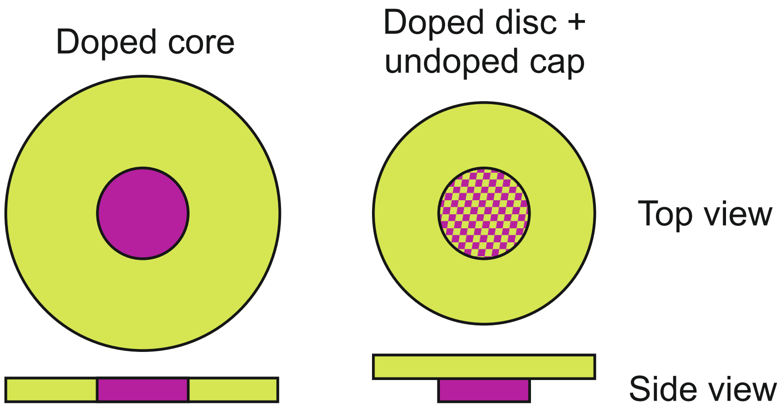

FIGURE 2.5: Diagram of two approaches to composite thin discs. Purple areas represent doping.

2.3.4 Thin disc lasers

A thin disc laser consists of a layer of material typically 100-300 µm thick and 3-5 mm in diameter, highly reflective on its back side and bonded to a heat-sinking substrate. The chief advantage of such systems over bulk lasers is that heat dissipation is efficient due to the large surface-to-volume ratio. This allows large pump power densities to be achieved, whilst thermal effects (such as lensing) remain much reduced compared to bulk. This results in a laser that is efficient and high power (up to 6.5 kW reported for end-pumped single disc [116], 300 W for side pumped [117]) but with excellent beam quality [118]. Systems with powers of up to 16 kW are commercially available, based around the combination of beams from multiple discs.

Such discs have traditionally been quasi-end pumped: the pump beam enters the crystal at an oblique angle and single-pass absorption efficiency is low. A parabolic mirror arrangement is then used to direct the beam back into the crystal for multiple passes. This is, however, very complicated to set up, and hence a move has been made towards the simpler side pumping configuration [117, 118, 119, 120, 121].

Composite crystals and/or ceramics may be preferred over single crystal samples, both to simplify the laser setup by guiding side-pumped light to the core and to reduce the effect of amplified spontaneous emission by allowing it to escape the gain area. Such structures can consist of a doped core surrounded by an undoped region of similar material [117, 120] or a small active disc topped with an undoped cap [119, 122, 116] (see figure 2.5). While the latter may be simpler to manufacture, the former allows all pump light to be absorbed and does not require bonding of two crystals of different sizes, which may render the sample more vulnerable to fracture upon heating.

Ytterbium is an attractive dopant for such systems, as it has a simple electronic structure, and hence is not subject to effects such as excited state absorption or upconversion, and can easily be accommodated into the YAG lattice with up to 100% doping (YbAG).

However, excessive heating can be problematic: as temperature increases, the lower laser transition level becomes more populated, making population inversion more difficult to achieve and increasing the likelihood of laser reabsorption. This has a major effect on threshold pump power, and hence highlights the need for effective heatsinking. Because of this, concentrations are generally restricted to a value between around 5 and 15%, with 20% viewed as "heavily doped"[123].

Thin disc laser host materials are not limited to YAG, although it is the most common. GGG has recently been investigated as a potential ytterbium host for thin disc lasers [124], with initial reports suggesting that thermal conductivity is higher than that of similarly doped Yb:YAG for doping concentrations greater than 4%. By contrast, Yb:LuAG has very similar thermal properties to Yb:YAG, but a larger emission peak cross section and higher quantum efficiency (high absorption at 968 nm rather than 940, emission at 1030 nm) [125]. Sesquioxides such as Y_2O_3 (yttria), Lu_2O_3 (lutetia) and Sc_2O_3 (scandia) [126] are also of interest due to their high thermal conductivities and absorption cross sections compared to YAG, although with their high melting points they can be difficult to grow as bulk crystals.

Generally thin discs have consisted of slices cut and polished from bulk crystals, limiting thicknesses to greater than ∼100 µm (it is mechanically difficult to fabricate thinner samples). Polycrystalline ceramics have been investigated in thin film geometry [127] as they are harder and more resistant to damage, particularly from thermal shock. They also have the potential to be heavily doped and made into composite structures [121, 123]. However, like single crystal examples, the thicknesses are often limited due to the fabrication methods.

This situation is not ideal: to reduce thermal effects and damage during operation, disc thickness should ideally be smaller than 100 µm. Liquid phase epitaxy has been employed to grow Yb:$KLu(WO_4)_2$ layers [128]. As the dopant concentration could be increased relative to bulk without difficultly, lasing was attained using a 50 µm thick layer.[1] PLD growth of thick films has generally been limited (see section 3.2.4), and no examples of thin disc lasing of PLD-grown films have been found. With the experimental setup detailed in this thesis, however, growth rates for applicable materials (garnets, sesquioxides etc.) of 5-10 µm/hr are regularly observed. We also have the potential to quickly and easily create hybrid crystals with our multi-beam setup.

---

[1] LPE has also been used to grow Yb:YAG layers, although these were 200 µm thick [129].

2.4 Alternative thin film deposition techniques

2.4.1 Sputtering

Ions (usually Ar^+) are accelerated by an electric field onto the surface of a target, ejecting material that is deposited onto a substrate. Deposition can occur with a background gas (reactive and/or as a buffer) or under vacuum. Epitaxy may be achieved by heating the substrate, although post-annealing of an amorphous film is usually preferred for simplicity. The plume is generally widely distributed, leading to chamber contamination and low growth rates but allowing large areas to be deposited at one time. It is a method suited to deposition of various materials, particularly simpler materials such as metals, semiconductors and simple oxides, for applications including antireflection coatings and photovoltaic cells [130].

Multi-target sputtering has been used to grow YIG [131] and YAG [132, 133]; however, plume spreading again led to wide stoichiometry variations across the film, and the post-annealing approach has resulted in polycrystalline films.

2.4.2 Flame hydrolysis deposition (FHD)

An oxygen-hydrogen flame is directed towards the substrate. Precursors of the desired materials (e.g. silicon halides) are fed into the flame, reacting to form particles that are deposited onto the substrate. The wafers are subsequently annealed to form layers of glass. Areas of $\sim$100 cm^2 can be covered by translation of the flame across the substrate, and growth rates (excluding annealing) can be high at $\sim$10 µm per hour. Dopants can be incorporated to change refractive index, melting point and photosensitivity of the layers, of importance for subsequent use in integrated optical device fabrication. Additional dopants that cannot be deposited by FHD (e.g. lasing ions) can also be incorporated into the structures by solution doping prior to annealing. The method is commonly used for silica-on-silicon waveguide fabrication [134]; however, while low loss layers can be deposited ($\sim$0.1 dBcm^{-1}), the materials available (even with solution doping) are restricted by the chemistry involved.

2.4.3 Thermal vapour deposition (TVD)

The substrate is positioned above a crucible of material to be deposited. The material is heated, forming a vapour that is deposited onto the substrate. As with sputtering, TVD can be used to deposit over large areas. However, use is limited to simple materials with low melting points and high vapour pressures, and as the vapour is difficult to control, growth rates are low and chamber contamination is high. Stoichiometry of multi-component materials can also be difficult to maintain, as the different constituents have different vapour pressures.

2.4.4 Cathodic arc physical vapour deposition (arc-PVD)

An electric arc is formed on the surface of a cathode target. The high local temperature ($\sim 1.5 \times 10^4$ °C) vaporises the cathode, forming a jet of material that is deposited onto a nearby substrate. The method is prone to droplet formation, target damage can be high (particularly for materials with lower melting points) and ion velocities very high, potentially leading to stresses in the film. However, arc-PVD is a useful method for growing extremely hard materials with high melting points, such as diamond-like carbon (DLC), that may be difficult to deposit via other methods[2].

2.4.5 Chemical vapour deposition (CVD)

A mixture of precursor chemicals containing components of the material to be deposited is passed across the substrate surface, where the precursors react to form a layer of material. There are a number of different forms of CVD, including laser assisted (LACVD) and plasma enhanced (PECVD), which extend the basic CVD setup to control or enhance reaction dynamics, growth rates and/or available materials. Growth rates vary from 0.1 to 100 µm per hour depending on the material and the variant of CVD being used. The quality of deposited films is usually high, such as the YAG samples grown by Bai et al using metalorganic CVD (MOCVD) [135]. However, both precursors and reaction by-products are often harmful, and deposition is limited by available material-precursor mixes.

2.4.6 Molecular beam epitaxy (MBE)

Film constituents are held in separate cells and heated to produce molecular beams of material. These beams are directed onto a substrate where they combine to form an atomically thin layer. Control over the thickness and stoichiometry of these layers is extremely precise, allowing high-quality crystals and intricate structures to be fabricated. The technique is hence widely used for growth of semiconductor devices, including semiconductor lasers [98]. Growth rates are very low, however (typically <0.5 µm per hour), and cost is high.

---

[2] Deposition of DLC is possible with PLD also. [40]

2.4.7 Liquid phase epitaxy (LPE)

The material to be deposited is dissolved in a liquid melt. A substrate is dipped into this solution and is cooled, whereupon the material condenses and is deposited as a thin film. Although initial experiments to determine optimum conditions can be time-consuming (as with PLD), growth rates can be relatively high with high crystal quality (YIG growth rate typically 6-60 µm per hour, for example [136]). Multilayer growth is possible by re-dipping the substrate in another melt, assuming that the melting point of the second solution is below that of the original film. The technique is, however, limited to those materials for which a suitable solvent can be found, and multilayer growth can be problematic.

2.4.8 Sol-gel

A substrate is dipped into a continuous suspension, or gel, formed by partial drying of liquid particles or polymers suspended in a liquid, known as a sol. A thin solid film of that material is formed after further drying. High temperatures are not required, which is of interest particularly when depositing polymers[3] or biomolecules [137], and the method is quick and inexpensive. However, epitaxy is very difficult to achieve, and materials are limited to those for which an appropriate solvent can be found.

2.5 Alternative waveguide fabrication techniques

2.5.1 Direct bonding

In general, intermolecular forces (e.g. van der Waals) are not strong enough to bind together two rigid layers of material, due to surface roughness/imperfections. However, if surfaces are polished optically flat (to within ∼10 Å) and kept clean of dust and grease the contact area can be great enough to allow the layers to bond. Further annealing encourages the formation of stronger covalent bonds, preventing delamination of the structure. In this case, it is important to select materials with similar thermal expansion coefficients, to prevent cracking upon cooling. Unlike epitaxial growth methods, however, direct bonding is not limited to materials with similar lattice constants.

Bonding of thin layers can be difficult, as they may be prone to cracking. It is hence preferable to bond thicker crystals and polish back, although this can be time consuming in the context of fabricating multilayer structures. However, direct bonding of thicker layers has proven to be very effective for the fabrication of planar waveguide lasers [138].

---

[3] Polymers layers are more commonly deposited by spin coating.

2.5.2 Indiffusion

A layer of metal or metal oxide, typically some hundreds of nanometres thick, is deposited onto a substrate. The sample is left in a furnace typically at >1000 °C for some hours/days until the metal has diffused into the substrate. This may serve to increase the refractive index only, forming a waveguide, or may also allow dopants to be incorporated (e.g. Ti indiffusion of sapphire). By depositing strips of material only, for example by photolithography, channel waveguides may be formed [73]. Materials are limited to those which may be diffused into the particular substrate, and the time taken to create waveguides more than a few microns in depth can be very long.

2.5.3 Ion exchange

Ion exchange is similar to indiffusion and shares many of its limitations. Substrates are placed in a bath of heated (molten) salt. Ions in the salt are exchanged with ions in the substrate to create an area of increased refractive index. By applying a mask before placing the sample in the bath, channel waveguides may be formed, and the technique can be applied to both crystal [74] and glass substrates [139].

2.5.4 Ion implantation

Ions accelerated to high energies (∼MeV) are fired at a sample to modify the material (changing density, structure or stoichiometry [75]) and hence induce a change in refractive index (usually small, $\sim 10^{-3}$). Ions are typically light, such as H^+ (protons) or He^+, and penetration depth can be controlled by changing the ion energy. The index change can be positive or negative, depending on the material and damage mechanism involved, and hence waveguides can be formed directly (positive Δn) or by inducing low-index tracks/layers, between which light can be guided. The whole surface of a sample can be flooded with ions or the beam can be directed, to create planar and channel waveguides respectively. The technique can be applied to a wide variety of materials, including doped YAG [79, 80, 81].

2.5.5 Focussed ion beam machining (FIB)

A film may be physically machined via ion beam machining to create waveguiding structures. Ions (e.g. gallium) are accelerated to energies of some tens of keV and focussed onto a sample, causing elements to be sputtered from the surface. Very precise control can be achieved over feature size and position (smallest features ∼10-100 nm), allowing devices such as waveguides and Bragg gratings to be fabricated [140]. However, due to the very low material removal rate (∼ µm^3 per second) larger structures can be prohibitively slow to machine.

2.5.6 Photolithography

Arrays of raised structures such as ridge waveguides may be fabricated by a combination of photolithography and chemical or ion beam etching. A layer of photosensitive polymer (“photoresist”) is applied to the sample by spin coating. This layer is exposed to UV light shone through a photomask. The light “cures” exposed areas of the surface, rendering them soluble or insoluble (positive or negative photoresists respectively) in a solution known as developer. After developing and baking to solidify the remaining photoresist, the surface is left patterned with areas that are resistant to subsequent etching. Chemical etching is suitable for some materials, such as glasses; in this case the substrate is left in a chemical bath for some minutes/hours. Alternatively, the substrate is exposed to an ion beam and material is etched similarly to FIB. Any remaining photoresist is removed after etching, for example chemically using “resist stripper” liquid.

The process has many steps and involves the use of hazardous chemicals in the case of chemical etching. Etching rates may be low etching, limiting the size of features that can be fabricated, and control over vertical feature profiles (e.g. sloping sides) can be difficult to achieve. However, very precise surface patterning can be achieved and large substrate areas can be processed simultaneously, making the technique cost-effective for batch production. Lasing has been achieved in a number of ion beam etched samples, including Nd:GGG [89], sesquioxides [32] and Ti:sapphire [42].

2.5.7 Direct writing

This term covers two distinct techniques, both of which use laser light to modify a material to create a channel waveguide. The first of these uses a CW UV laser to modify photosensitive materials such as doped glasses [134] or lithium niobate [82], increasing the refractive index either continuously, to create a waveguide, or variably, to form a Bragg grating. This technique has been used to fabricate a variety of devices, including sensors, and is of particular interest for integrated optical applications.

The second technique involves using femtosecond pulsed lasers to physically machine bulk or thin film crystals via multi-photon ionisation-induced damage. A thin film may be machined/ablated to form tracks either side of a strip or ridge waveguide [90, 91], although such tracks are typically very rough and hence waveguide losses can be high. Alternatively, by focussing inside the material, a pair of damage tracks may be machined below the surface of a bulk sample [83, 84, 85]. The resulting strain induces a change in refractive index of ∼10^{-3} in the area between the tracks, creating a waveguide with low loss (∼1 dBcm^{-1} [84]) but small numerical aperture.

2.6 Conclusions

A wide range of techniques, both thin film-based and others, are available to fabricate optical devices from a wide range of materials. PLD, in both single- and multi-target form, has proven highly effective at depositing a range of optical crystals, with multi-component oxides such as garnets being of particular interest. While it has strong competitors (particularly LPE), PLD displays advantages over other techniques in terms of speed, ease and/or flexibility in a number of applications, particularly multilayer growth. However, much is still to be done to harness these positive aspects of PLD. The multi-beam, multi-target variant is an area particularly rich for exploitation to grow functioning optical devices.

Chapter 3

Theory

3.1 Introduction

This chapter introduces some of the theoretical concepts underlying the techniques and devices described in this thesis. Explanations are mostly qualitative, with some equations included where helpful. The processes involved in PLD are discussed first, highlighting some of the most important factors to consider when using and extending the technique. Some theory underpinning the key applications and devices in this thesis is subsequently given, calling attention to the notable design features.

3.2 PLD theory

Pulsed laser deposition is a highly complex process with many interdependent variables and mechanisms. Although models have been reported for separate parts of the process, modelling of the complete process has proven prohibitively difficult. This section gives an overview of the mechanisms involved in PLD and discussion on the impact they have on the potential for growth of thick, high quality films.

3.2.1 Laser ablation

A basic overview of the laser ablation process is shown in figure 3.1. A number of mechanisms have been suggested to explain how a laser pulse incident upon a target can induce the expulsion of material from the target surface, many of which can be categorised as follows [141]:

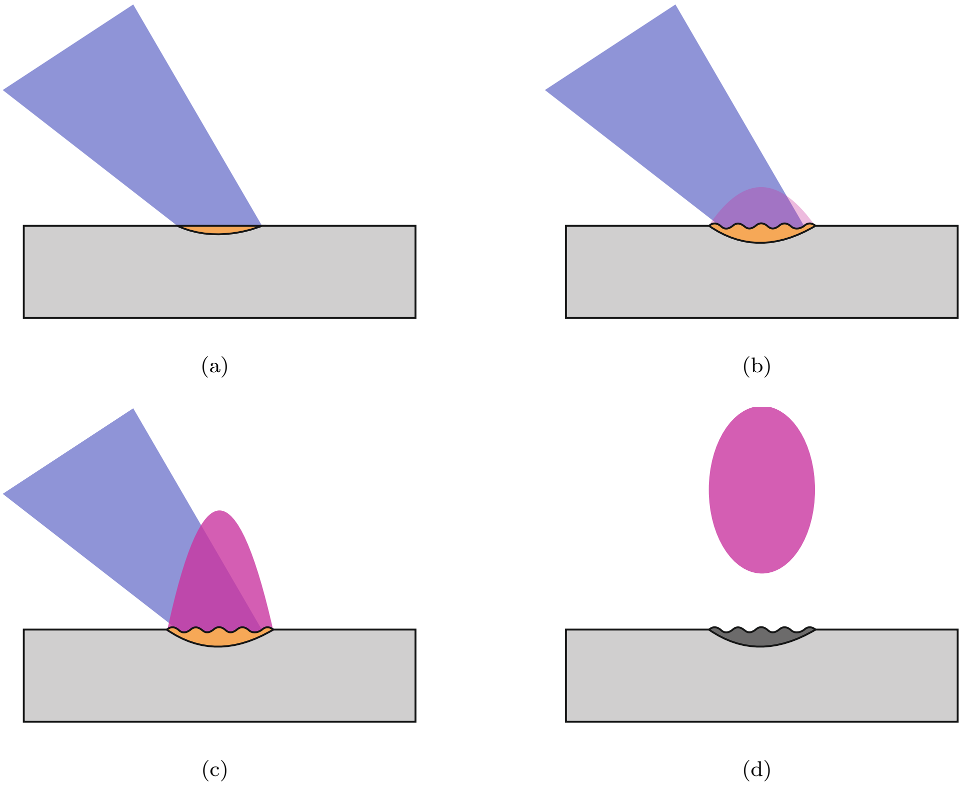

FIGURE 3.1: Illustration of the nanosecond ablation process. (a) Laser pulse is absorbed by the target, leading to heating. (b) Target melts, then evaporates releasing a plume of material. (c) Plume becomes dense enough to absorb laser directly, becomes partially ionised and expands away from the target. (d) The laser pulse ends and plume expands away from the target; target resolidifies having been modified.

- **Thermal** The ablated area melts and vaporises to form a plume of ejected material. The effects of this mechanism can be observed in the formation of wave-like structures or reposited droplets on the target surface post-ablation (solidified and/or splashed molten areas, see section 3.2.5). For this mechanism to be realised, heat should not be transported away more quickly than it can be absorbed i.e. absorption length L_a must be greater than thermal diffusion length L_d. These quantities are given by equations 3.1 and 3.2 respectively [23]:

$$L_d = 2\sqrt{(D \cdot \tau)} \tag{3.1}$$

$$L_a = \frac{1}{\alpha} \tag{3.2}$$

  where D and α are thermal diffusivity and absorption coefficient respectively and τ is pulse duration. Assuming $L_d < L_a$, the depth of material removed by ablation d is given by equation 3.3:

$$d = \frac{1}{\alpha} \ln |\frac{F}{F_t}| \tag{3.3}$$

  where F and F_t are laser pulse fluence and ablation threshold fluence respectively.

A number of ideal laser properties hence become apparent. Short pulse durations minimise the time a target has to react to a pulse, reducing heat diffusion, and shorter wavelengths have shorter absorption depths in most materials. Nanosecond-pulse ultraviolet lasers are therefore often appropriate;

- **Electronic** A broad category which includes *multi-photon absorption*, the dominant effect at very short pulse lengths i.e. femtosecond PLD [142], where atoms are ionised directly by the simultaneous absorption of two or more photons. A free electron created via multi-photon ionisation can be accelerated by interaction with a bound electron. The subsequent increase in kinetic energy allows this free electron to ionise a second bound electron, leading to an exponential increase in ionisation. This process is known as *avalanche ionisation* [143]. Material may be ejected by a *Coulomb explosion*, an effect also limited to short timescales (∼100 fs [144]). As electrons escape, positive charge can build up on the surface as electrons escape, resulting in an explosive release of energetic ions, a consequence of Coulomb repulsion;

- **Collisional** Some fraction of ions ejected from the target may be accelerated back towards the surface by collisions within the plume, leading to sputtering of an area of the target surface larger than the ablated spot [145];

- **Hydrodynamic** Extended features form on a molten surface (see above) that are expelled as droplets (i.e. particulates). Such features may reach the film surface or be redeposited on the target surface and exfoliated at a later time (see section 3.2.6) [146].

- **Exfoliation** Chunks/flakes detach from the target surface due to thermal shock. This effect is particularly problematic for brittle target materials, such as the garnets used predominantly in this thesis [141].

For the nanosecond ablation described in this thesis, electronic processes are significant in the first ∼picoseconds of the pulse [143], after which thermal sputtering becomes the dominant mechanism [145]. Free electrons, generated for example by multi-photon absorption, are accelerated by the continuing laser pulse. This results in heating of the surrounding target material by electron-phonon interactions [147], leading to melting and vaporisation of the material as described above. However, very high temperatures are required for significant ionisation fractions to be achieved (see section 3.2.2), which may not be reasonable via thermal mechanisms only. Other processes (laser hotspots, multi-photon ionisation, impurities etc. [148] must hence also be taken into account: these result in the production of local areas of high ionisation fraction and hence temperature.

3.2.2 Plume formation and propagation

The ratio of singly charged ions to neutrals in a gas in local thermal equilibrium (which the evaporated plume can be assumed to be) can be predicted using the Saha equation [149]:

$$\frac{n_i}{n_n} = 2.4\times10^{15}\frac{T^{3/2}}{n_i}e^{-U_i/kT} \tag{3.4}$$

where n_i and n_n are the ion and neutral densities respectively (number per cm^3), k is Boltzmann's constant, T is the temperature and U_i is the first ionization potential in eV. The fraction of ions in the plume $n_i/(n_i+n_n)$ hence remains small compared to neutrals until the temperature increases to the point where U_i is only a few times larger than kT. At this point, the fraction of ions increases dramatically and a plasma plume is formed. The temperature will increase as the nascent plume absorbs laser energy directly via inverse Bremsstrahlung absorption [148]; heating of the target decreases as the laser energy is absorbed directly and it resolidifies. Typical values of U_i are of the order of 10 eV; temperatures of ~6000 K or ion densities of $>10^{18}$ are hence required before significant ionisation (ionisation fraction > 0.1) will occur, which may be unreasonable for typical fluences [149]. However, nonuniformities in the electron density may locally increase n_i, seeding ionisation of the whole nascent plume [148].

Once the plume is sufficiently ionised such that plasma frequency $\nu_{plasma} \geq$ laser radiation frequency ν, the laser light will be reflected, preventing further heating [150]. The plasma frequency is is related to the electron density n_e by equation 3.5.

$$\nu_{plasma} = 8.97\times10^3\sqrt{n_e} \tag{3.5}$$

The plume expands away from the substrate into areas of lower pressure, with the greatest rate of expansion along the axis with the greatest pressure/density differential. The shape of the plume will depend on spot size: a large spot size results in a plume that travels mostly perpendicular to the substrate, while a smaller spot size leads to a more divergent plume (and hence a lower growth rate), an effect known as 'flip-over' [23] (see figure 3.2). Many PLD setups do not use circular spots (e.g. rectangular excimer beams) and hence plume cross sections are often elliptical.

The angular distribution of the plume has been fitted in many cases to a $\cos^n\theta$ function, where n can range from 2 to 20, depending on the particular system (fluence, pressure etc.) [148]. Different elements in a multicomponent target may have different angular distributions, with lighter elements being scattered preferentially and hence being found at the edges of the plume. This effect has particular relevance for the garnet deposition described in this thesis; a GGG film may be gallium deficient, for example, due to the

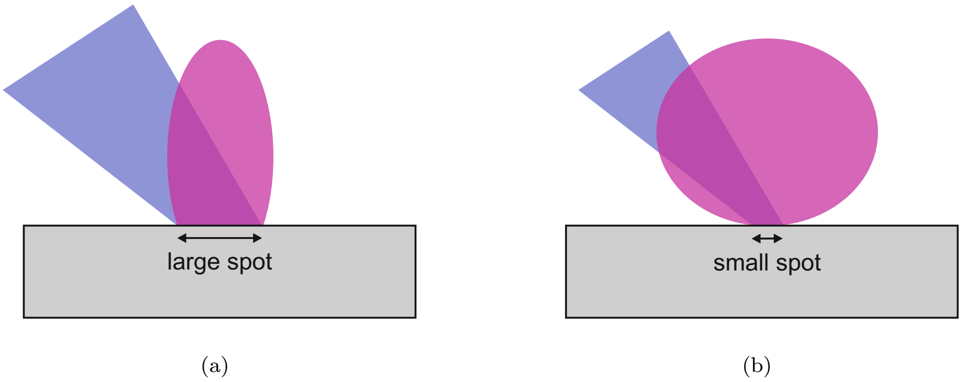

FIGURE 3.2: Diagram of flip-over effect. The expansion of the plume is faster in the initially smaller axis [23], hence a large spot results in a confined plume while a small spot results in a widely distributed plume (and consequently lower deposition rate).

increased scattering of gallium compared to the heavier gadolinium[1]. A plume in general will be much more widely distributed under lower pressure than higher pressure; as a result, deposition at low pressure (typically $<10^{-2}$ mbar) leads to coating of the inner faces of vacuum chamber windows. Increasing the background pressure will in general result in slowing of the plume and hence greater spatial confinement, placing an upper limit on the practical gas pressures and target-substrate distances that can be used.

It is possible that some components of a plume will undergo no collisions with a background gas and hence will travel with a much higher velocity than components that do undergo collisions. This can result in a time-of-flight (TOF) spectrum with a split peak at the substrate, as opposed to the single peak observed in vacuum (examples in chapter 5) [152].

If a reactive gas is chosen, the background gas can also serve to alter the composition or stoichiometry of the resulting film. Depositions described in this thesis have taken place in an oxygen atmosphere, providing a source of oxygen atoms that can be incorporated into a growing film to replace oxygen otherwise scattered from the plume.

A typical plume contains neutrals and particulates as well as ions, electrons and clusters. Neutrals may arise as the plume expands due to ion-electron recombination; particulate generation is described in detail in section 3.2.6. In general, ions (particularly light ions) have high velocities, travelling at the front of the plume and reaching the substrate before neutrals and particulates, which travel more slowly [148]. Techniques making use of this effect can hence be used to reduce the number of particulates in the resulting film (see section 3.2.6). Electrons tend to attain the highest velocities but do not escape the plasma due to the strong space-charge field generated by their collective movement away from the ions within the plume.

---

[1] Gallium reaching the substrate may also be lost from the growing film due to its high volatility compared to gadolinium.

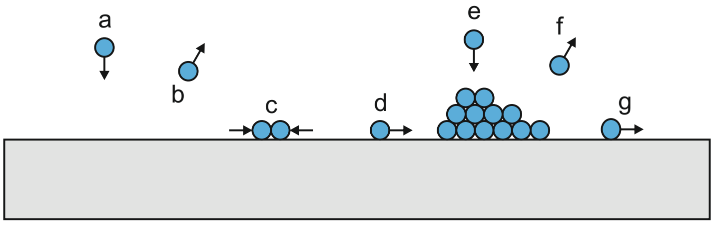

FIGURE 3.3: Diagram of various nucleation processes on substrate: (a) Atom deposited on substrate, (b) atom desorbed from substrate, (c) cluster nucleation, (d) atom diffuses to cluster, (e) atom deposited on cluster, (f) atom desorbed from cluster, (g) atom dissociated from cluster

3.2.3 Crystal growth

3.2.3.1 Growth mechanisms

The properties of the plume as it arrives at the substrate, as well as those of the substrate itself, will affect the stoichiometry, deposition rate, stress, crystallinity and particulate size/density of the resulting film. Because these variables are interdependent, it may be necessary to compromise to achieve practical film growth: for example, non-bulk stoichiometry may have to be accepted in order to obtain a high enough growth rate.

For deposition within a background gas, plume constituent energies at the substrate may not be high enough to allow adatoms (atoms on the surface) to migrate to the appropriate lattice sites. Substrates are hence usually heated to obtain films of the desired crystalline phase. Heating can, however, increase the rate of desorption of volatile elements, leading to stoichiometric deficiencies [9]. Ion energies can be high enough to cause sputtering of the film surface (again changing stoichiometry) and/or induce compressive stresses within the film [153]. The latter in particular can be used as a tool to control overall film stress via changing pressure and fluence [11].

Figure 3.3 shows a diagram of the various nucleation processes occurring at the substrate surface. Crystals may initially form in one of three modes [154]:

- As clusters or islands (Volmer-Weber growth), if film components are more strongly bound to each other than to the substrate;
- As 2D monolayers (Frank-van der Merwe growth), if film components are more strongly bound to the substrate than to each other ;
- Initially as monolayers, followed by island growth (Stranski-Krastinov growth); free energy states in the growing film change with changing strain e.g. relaxing lattice mismatch.

3.2.3.2 Crystal defects

PLD-grown crystals are likely to contain defects, which fall into one of three classes [155]:

- **Point defects** Atoms missing or in incorrect lattice sites e.g. vacancies, interstitials (atoms where none would normally be found), substitutions etc.;
- **Line defects** Groups of atoms in incorrect positions e.g. edge dislocations formed by relaxing lattice mismatch;
- **Planar defects** Interfaces between regions of material e.g. grain boundaries.

Such defects can influence various film properties including strain and refractive index. Vacancies and substitutions may also lead to the creation of colour centres.

Crystal defects of some kind are likely to be the cause of an effect observed for YAG film growth: while growth of YAG on bulk YAG substrates results in a water-clear layer, YAG films grown on GGG layers (for capping or Bragg structures) are brown and opaque until subsequent overgrowth or annealing. The exact mechanism for this is not yet known. Reports exist of F- or colour-centre formation in bulk YAG when the crystal is Al deficient, a mechanism that leads to brown colouration [156]. It may be the case that Al or O atoms from the film diffuse into the GGG layer below, leading to vacancies and hence colouration in the YAG film that persist until another GGG layer is deposited, filling those vacancies again by diffusion. The effect has not, however, been examined in detail.

3.2.3.3 Lattice mismatch

Deposited material will grow epitaxially where possible. Lattice constants differing by up to 9% can be accommodated via strain and/or edge dislocations in the growing film [23]; below a threshold thickness it is energetically favourable for the lattice to strain, while above this threshold, dislocations will be introduced. Mismatches larger than 9% will generally lead to polycrystalline or amorphous growth. Films with lattice constant that is an integer multiple of that of the substrate may also be successfully grown (harmonic mismatched growth) (see figure 3.4). The threshold thickness after which lattice mismatch fully relaxes has been shown experimentally in the case of GGG on YAG to be ~4 µm [11].

3.2.3.4 Thermal expansion mismatch

Heteroepitaxial crystal films may grow in an unstrained state while heated but may become highly strained on cooling to room temperature as a result of a mismatch in

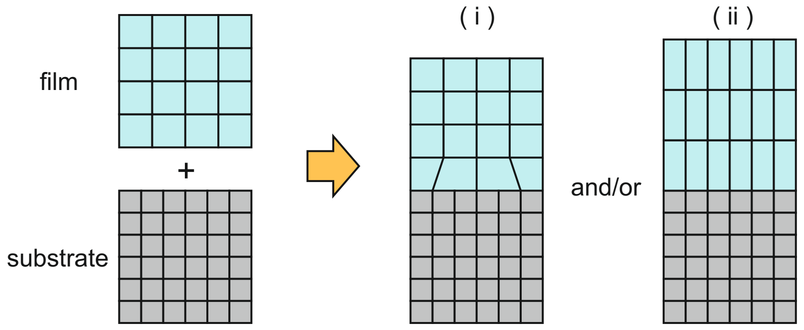

(a) If substrate and film are not lattice-matched then dislocations (i) and/or strain (ii) will be introduced to the film

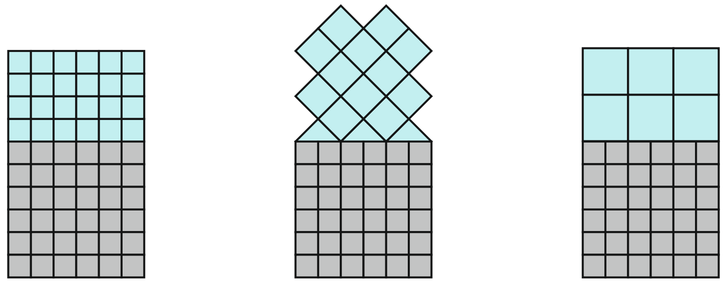

(b) Match (c) Match (d) Harmonic mismatch

FIGURE 3.4: Diagrams of possible lattice states. Films in cases (b), (c) and (d) will not be strained due to lattice mismatch

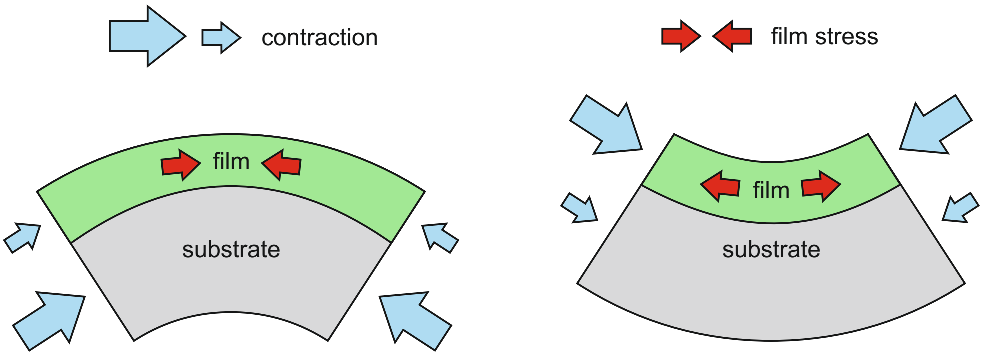

(a) $\alpha_{film} < \alpha_{substrate}$, compressive strain in film (b) $\alpha_{film} > \alpha_{substrate}$, tensile strain in film

FIGURE 3.5: Effect on film and curvature of thermal expansion coefficient α mismatch.

thermal expansion coefficient α. Substrate and film will contract by different amounts, causing either compressive strain in the film when $\alpha_{film} < \alpha_{substrate}$ or tensile strain when $\alpha_{film} > \alpha_{substrate}$ (see figure 3.5). Once thickness increases beyond a certain point, the film may not be able to flex and instead will crack on cooling or polishing. For GGG films grown on YAG substrates at ~650 °C this threshold thickness has been found to be ~40 µm [23].

3.2.4 Thick film growth

Two main factors appear to place an upper limit on practically achievable film thicknesses: growth rate, which may be limited by the conditions required for high-quality film growth, and thermal expansion mismatch, as described in the previous section. The former can be combated in multi-beam chambers by the introduction of a second plume and target.

A route to solving the problem of thermal expansion mismatch has been suggested by May-Smith et al [11], using the example of GGG films on YAG. Thermal expansion mismatch resulted in tensile strain of the films. However, compressive strain could be introduced by increasing fluence and therefore the energy of ion bombardment (similar to the results in chapter 5). These two sources of strain may hence be balanced to create a film with lesser or no overall strain at room temperature, which is hence able to grow to greater thicknesses without cracking on cooling. The amount of compressive strain that can be induced is limited, however, as films can crack during deposition due to the lack of counteracting strain from thermal expansion mismatch.

3.2.5 Target modification

A target will be left modified after ablation has taken place, leaving laser-induced features such as cones and ripples. These features affect subsequent ablation (e.g. fluence is altered by changes in effective surface area) and can lead to the production of particulates. An example of a target surface after ∼6 hours of ablation can be seen in figure 3.6 (target rotated but not tilted). Cones are produced at the outer edge of the ablated ring, with ridges in the centre.

The term “cones” comprises features ranging from truly conical to irregular columns or clusters. They are thought to arise from poor ablation of points on the surface (impurities or deposited debris, for example). Material surrounding or between these points is ablated at a higher rate than the points themselves, building up a cone after many successive laser pulses [157, 158]. As a result of this process, cones will grow in length as the number of shots increases, always pointing in the direction of the incoming laser beam. As the effective surface area is increased, the presence of such structures can change the effective fluence and hence change the ablation characteristics of the surface. Cones can also be exfoliated from the surface and be deposited as particulates.

An example of cone growth can be seen in figure 3.6(a). These cones have formed around the edge of an ablated ring, suggesting that cone formation may primarily be caused by deposited debris or splashing. In the centre of the ring are large scale wave-like features. With a separation of ∼20 μm, these ripples are similar in shape and scale to surface features observed by Ang et al [159]. The suggested mechanism for their production

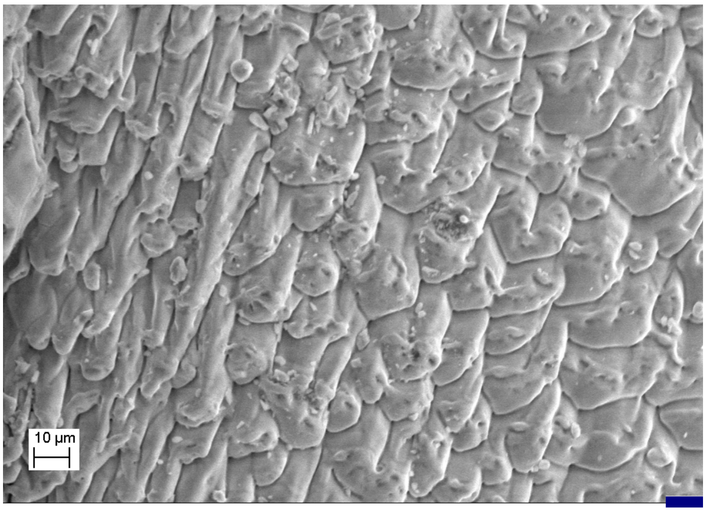

(a) Cones form at the edge of the ablated ring

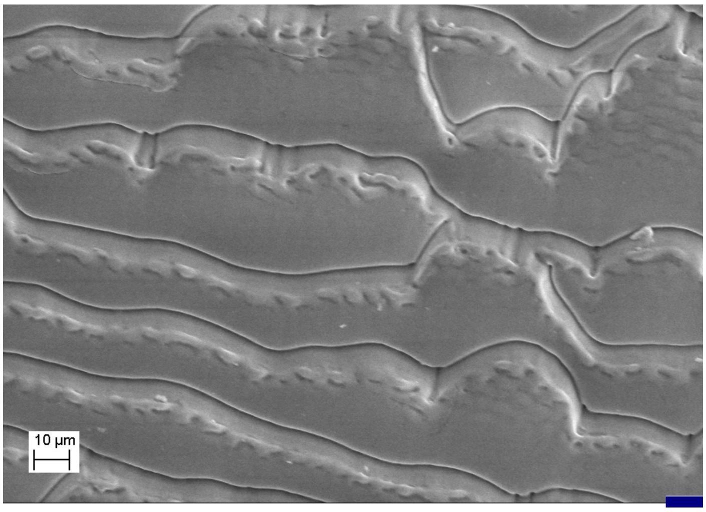

(b) Large scale wave-like structures form in the centre of the ablated ring

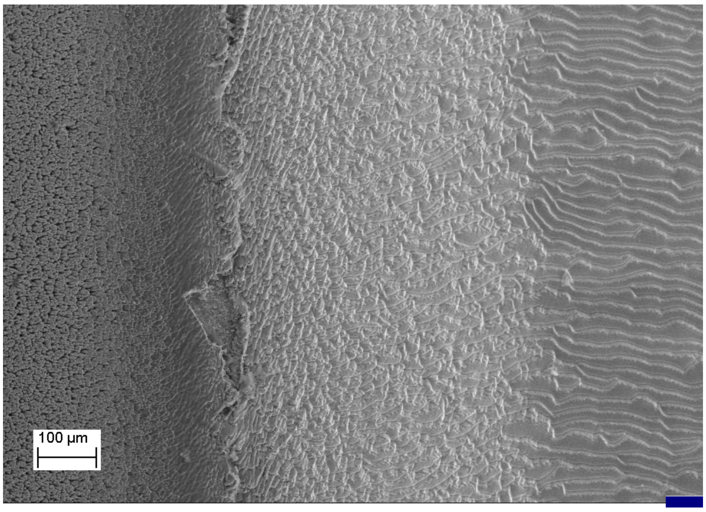

(c) The transition from lapped surface (left) to cones (middle) to large scale ridges (right) can be observed

FIGURE 3.6: Different surface features produced in different parts of an ablated ring.

was a Kelvin-Helmholtz instability (a result of a velocity difference between two fluids). This can be thought of as analogous to waves that are produced when wind blows across a water surface, with molten parts of the target serving as water and the expansion of the plasma plume as wind.

Ripples on a wavelength scale may also be observed for fluences below the ablation threshold (i.e. not in the case described above). Such features are known as laser-induced periodic surface structures (LIPSS) and have been demonstrated in metals, semiconductors and dielectrics at a range of pulse durations and wavelengths, though the mechanisms for formation are not yet well understood [160].

Consequences of target modification, whether direct or as a result of surface feature formation, include:

- **Structure and composition** More volatile elements may be lost or reactive elements may react with the background gas. Stratified layers may be formed as target components with higher melting points freeze while others remain molten (surface segregation). Elements in the target may be redistributed by diffusion, or crystallinity altered or lost as the target cools.
- **Deposition rate** Deposition rate can diminish as cones are formed, eventually reaching a constant value [157]. As mentioned previously, surface structuring can influence the effective fluence, which will in turn affect the deposition rate. Absorption characteristics or threshold fluence may also change as a result of modified stoichiometry or crystallinity of the target surface, which will directly affect deposition rate.
- **Film stress** Differences in fluence will impact the energy of the plume components, while changes in target stoichiometry will affect the species present in the plume, both of which will affect the resulting stress state of the film.
- **Particulates** Surface structuring greatly increases the production of particulates. The processes involved and some approaches to reduce particulates are described in section 3.2.6.

3.2.6 Particulate formation

Particulate formation is a significant drawback of PLD compared to many other deposition techniques. Several mechanisms of particulate formation have been proposed, depending on the material and conditions used. These include:

- Exfoliation of laser-induced surface features or redeposited debris by laser-induced thermal or mechanical shock (submicron to micron sizes particles).

- Splashing i.e. expulsion of liquid droplets from the surface, caused by sub-surface boiling at high fluence and/or the shockwave from the plume (submicron to micron).
- Condensation of vapour species in the plume (submicron).

The latter two in particular can be minimised by optimisation of deposition parameters such as gas pressure, laser fluence[2] and wavelength and target-substrate distance. Further particulate reduction can be achieved using more sophisticated methods such as velocity filtering, pulsed gas jet, off-axis deposition and the dual-beam cross plume approach pioneered by Gaponov et al [157] (see section 2.2.3.2). All of these have significant disadvantages, however, whether in the form of a more complex deposition setup or a much reduced growth rate.

A relatively simple way to reduce particulates caused by exfoliation is to periodically lap or polish a target to remove laser-induced surface structures and debris. In order to increase the time between reconditioning and utilise a single target more effectively, many groups employ some technique to increase the surface area ablated over the course of a deposition. Such methods include raster scanning the ablating beam across the surface, rotating the target with an offset cam so that the ablating laser follows an approximately epitrochoidal path, and tilting targets during ablation. The latter two methods have been employed in the experiments detailed in this thesis (see section 4.2).

As well as allowing more efficient use of the target surface, target tilting can also be used to control film curvature. To utilise this level of control, however, it may be necessary to dwell at certain target tilt angles rather than tilt continuously. This dwelling results in a build up of cones/splashed areas at the edges of the ablated track which are likely to be exfoliated when the target moves to its next tilt position. A larger number of particulates may hence have to be tolerated in order to reduce film curvature. Figure 3.7 shows the average particulate count per cm^2 for three GGG films grown without tilt, with continuous tilt and with a tilt program designed for flat film growth (varying dwell times). The order of magnitude difference that the tilt program can make to particulate density is easily observed.

It was possible to achieve virtually particulate-free growth of YAG by ablation of the fresh surface of a sintered target with no tilt (see figure 3.8), but as sintered targets can be difficult to recondition (see section 4.2.5) target use is limited.

---

[2] A compromise must be found between high and low fluence, which can result in droplet formation due to subsurface superheating/exfoliation and poor ablation/condensation respectively.

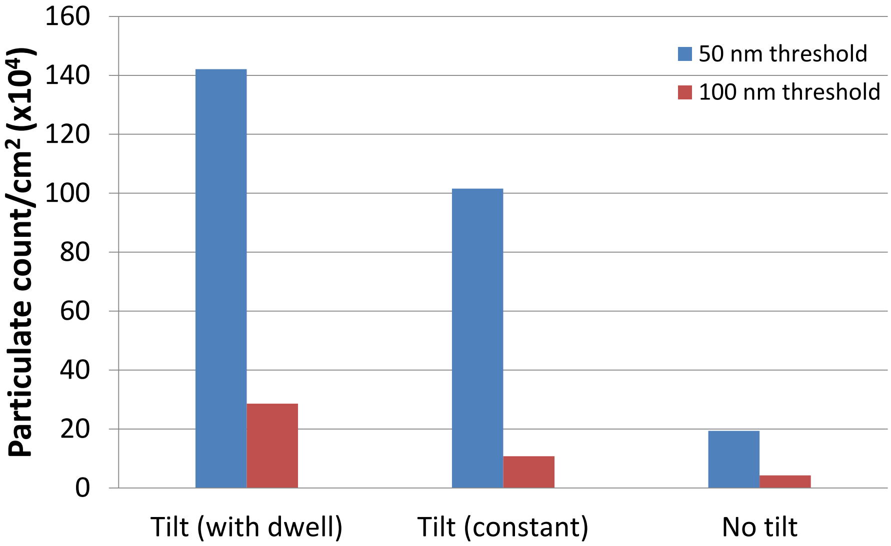

Figure 3.7: Graph comparing average particulate counts of GGG films of ∼12 µm thickness with different target tilting programmes. Average total particulate counts for heights >50 and >100 nm are shown.

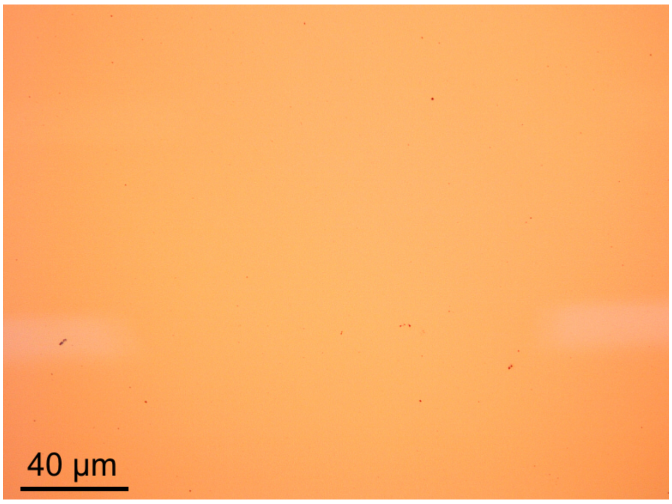

Figure 3.8: Optical microscope image of a ∼5 µm thick YAG film grown by ablating sintered YAG target without tilting. The number of particulates observed is very low (<500 per cm^2 with height >40 nm).

3.3 Waveguide theory

An optical waveguide is a structure that confines the spatial region in which light can propagate, consisting of a region of high refractive index (the core) surrounded by lower index cladding. The work in this thesis has involved the fabrication of waveguides confining light in one and two dimensions, known as planar and channel waveguides respectively; diagrams of these geometries are shown in figure 3.9. Some of the theory highlighting design features of such structures has been described in this section, with more detailed derivations given in appendix A.

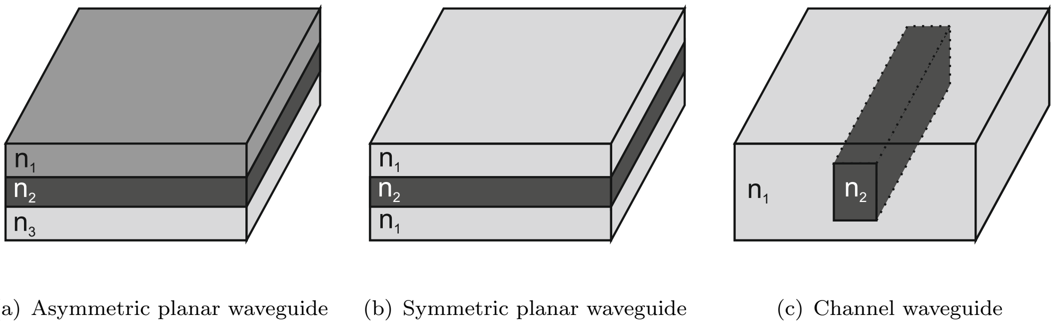

(a) Asymmetric planar waveguide (b) Symmetric planar waveguide (c) Channel waveguide

FIGURE 3.9: Different waveguide geometries. In each case the index of the core $n_2 > n_1, n_3$.

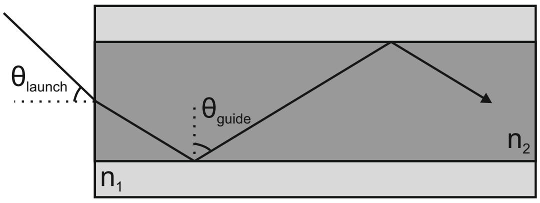

FIGURE 3.10: Diagram of waveguiding via total internal reflection; $n_2 > n_1$.

Guidance of light can occur in the core due to total internal reflection (TIR), assuming the index of the core is higher than that of the cladding (see figure 3.10). The critical angle θ_c for waveguiding is given by Snell's law:

$$\theta_{guide} \geq \theta_c = \sin^{-1}\left(\frac{n_1}{n_2}\right) \tag{3.6}$$

The maximum incident acceptance angle θ_{max}, beyond which light will not be confined within the guide, can be determined from the refractive indices of the guide and substrate/cladding by the relation:

$$n_0 \sin\theta_{max} = \sqrt{n_2^2 - n_1^2} = \mathrm{NA} \tag{3.7}$$

where NA is the numerical aperture of the guide and n_0 is the index of the medium surrounding the waveguide.

Waveguide modes are a set of electromagnetic fields which maintain their spatial distribution at they propagate, varying only by a phase factor. The modes are solutions of the wave equation (equation A.3) in each part of the guide. For a symmetric planar waveguide, a waveguide where substrate and cladding have the same refractive index (the case for most examples described in this thesis), the number of modes M above the fundamental of wavelength λ that a guide of thickness d can support is given by:

$$M = \frac{2d}{\lambda}\mathrm{NA} \tag{3.8}$$

A thicker waveguide or one with a larger refractive index contrast (higher NA) will hence support a larger number of modes. This can present a problem with high contrast, high NA waveguides such as the garnet films described in this thesis; single layers thick enough to allow for significant diode pump absorption are likely to support a large number of modes, leading to multimode laser output. This can be avoided, however, by careful selection of layer thicknesses in a multilayer clad waveguide, as described in section 3.4.2.

A rectangular channel waveguide guides light in two dimensions rather than one. It can be approximated by treating the guide as two separate three-layer planar waveguides, and the same conclusions regarding multi-mode behaviour for a given thickness and NA may be applied.

3.4 Laser theory

3.4.1 Lasers of interest

Laser materials of primary relevance to this thesis are Nd^{3+}-doped garnets, with Yb^{3+}-doped garnets also potentially of interest (although not yet grown) for use with the novel techniques described.

Growth of neodymium-doped GGG waveguides has been described in this thesis, while Nd:YAG lasers have been used for ablation in some cases. Nd^{3+}-doped gain media may be thought of as a classic four-level laser system (although energy levels are Stark split, the sub-levels usually do not play different roles in the scheme). The pump wavelength typically used is 808 nm, with emission typically at 1064 nm ($^4F_{3/2}$ to $^4I_{11/2}$ transition, see figure 3.11(a)). Other laser transitions are possible, although steps must be taken to suppress emission of 1064 nm radiation, for example by selecting mirrors that do not reflect at this wavelength. Nd^{3+} systems can also be operated as three-level lasers emitting at 946 nm, with the ground state $^4I_{9/2}$ acting as the lower laser level.

Nd^{3+} ions replace Gd^{3+} in the GGG lattice and Y^{3+} in the YAG lattice. The atomic radius of Nd^{3+} is larger than that of Gd^{3+}/Y^{3+}. Doping concentrations are hence limited to a few percent due to the increased crystal strain.

Yb^{3+} has a simpler electronic structure than Nd^{3+} (see figure 3.11(b)). It has a small quantum defect which makes Yb^{3+}-doped materials ideal for high power applications (efficiency is high and thermal effects relatively low), and excited-state absorption cannot occur due to the simple structure. Yb^{3+}-doped lasers are quasi-three-level systems,

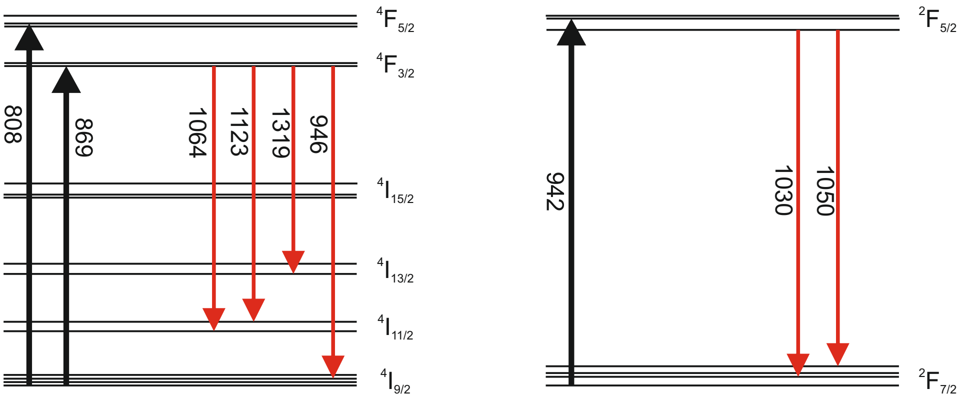

(a) Nd^{3+}:YAG

(b) Yb^{3+}:YAG

FIGURE 3.11: Energy structures for Nd:YAG and Yb:YAG, with possible transitions shown and corresponding wavelengths (in nm) labelled.

however. As such they suffer from a number of problems not applicable to four-level systems, which can include high pump powers requirements, high lasing thresholds and/or the stimulated emission of electrons from the upper laser level to the ground state. Lasing at 1030 and 1050 nm can be achieved with a pump wavelength of 942 nm. Yb^{3+} and Y^{3+} atoms have very similar ionic radii, allowing Yb^{3+} to be substituted into crystals such as YAG and Y_2O_3 at doping levels of up to 100%.

3.4.2 Lasing waveguides

Waveguide lasers have a number of potential advantages over their bulk crystal counterparts. These include [161, 162, 72]:

- **Lower lasing thresholds**, with the advantage increasing with increasing waveguide length and pump/lasing confinement. The effect is more pronounced in channel waveguides than in planar, due to the greater beam confinement. However, the advantage can be negated if round trip loss in the waveguide is significantly higher than bulk (more likely in channel waveguides than planar).
- **Comparable/higher slope efficiencies** due to the greater overlap between pump and laser beams in a waveguide geometry. Again, however, this assumes that losses are relatively low.
- **Heat removal** can be efficient compared to bulk crystals due to the large surface area to volume ratio, allowing much higher pump powers to be applied before thermal stress becomes damaging. In the planar case, heat flow is effectively one-dimensional, and for a practical slab of some tens of microns thick the maximum

power density allowed is hence many orders of magnitude higher than the power densities required [162].

- **Potential for integration** as part of an on-chip optical circuit, particularly in the case of channel waveguides. Compact laser systems can also be based around waveguide lasers, due to the compatibility with diode pumping (only relatively simple optics required).

- **High power single mode output** can be achieved with diode-pumped clad waveguides (i.e. planar multilayers) by careful choice of layer thickness, as described in section 2.3.1, assuming such structures can be fabricated in practice.

As can be seen above, many of the advantages of a waveguide laser geometry require losses to be low compared to bulk. PLD-grown waveguides are particularly vulnerable to scattering loss due to particulate formation; particulate production should hence be avoided as much as possible.

3.5 Bragg reflector theory

In a planar geometry, a Bragg reflector or Bragg mirror consists of stacked alternating layers of two or more materials[3]. Each interface in the stack contributes a reflection due to the change in refractive index. At certain wavelengths (which depend on the stack design) these reflections will interfere constructively and a peak in reflection will be observed, corresponding to a trough in the transmission spectrum.

This section describes some of the basic principles of Bragg reflection, along with discussion of more advanced geometries. More detailed derivations of some equations have been given in appendix B. Equations have been derived assuming that any absorption is negligible, which is believed to be the case for examples of PLD-grown Bragg reflectors described later in this thesis.

A program to model the reflection/transmission response of quarter-wave and π shifted Bragg stacks has been created by Michalis Zervas of the ORC, University of Southampton. A flowchart of the operation of this program has also been included in appendix B.

3.5.1 Quarter-wave

One of the simplest Bragg reflectors geometries is the quarter-wave stack, an example reflection spectrum of which is shown in figure 3.12. This consists of a series of layers

---

[3] Channel and fibre Bragg gratings may also be created, usually by UV writing of photosensitive glass; however, these have not been discussed.

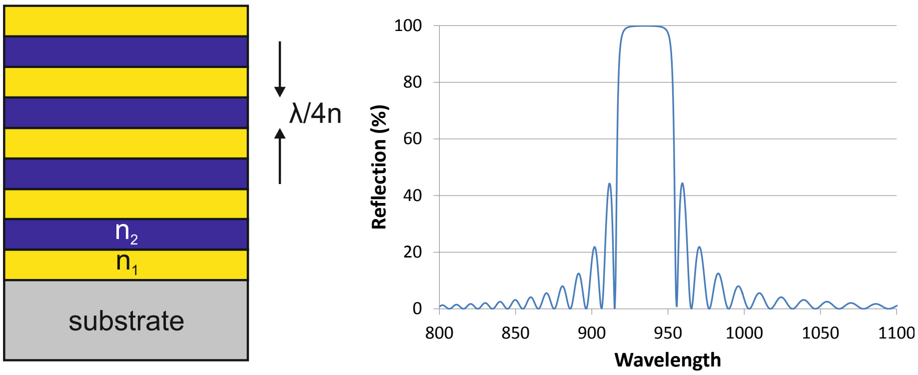

(a) (b)

FIGURE 3.12: Concept diagram (a) and example spectrum (b) of a quarter-wave Bragg stack

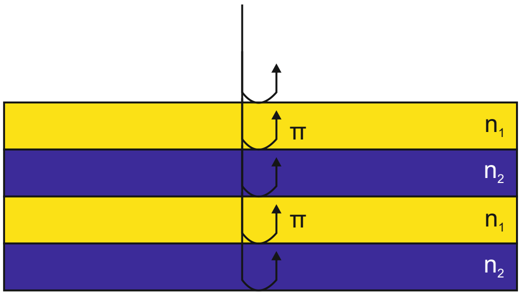

FIGURE 3.13: A fraction of the incident beam will be reflected at each interface in the stack, with an additional π phase shift when going from n_1 to n_2 (assuming $n_1 < n_2$).

of alternating refractive index n but different physical thickness d, such that each layer has an optical thickness (i.e. nd) of $\lambda/4$, where λ is the peak reflection wavelength.

The reasoning for this is illustrated in figure 3.13. Some fraction of the incident beam will be reflected at each interface in the stack (Fresnel reflections). The difference in phase of the reflected waves is given by δ where (assuming an incident angle of 0°):

$$\delta = \left(\frac{2\pi}{\lambda}\right) 2nd \tag{3.9}$$

For two reflections from adjacent interfaces to interfere constructively, δ equals a multiple of 2π. An additional π phase shift occurs when the ray is reflected from an interface where $n_1 < n_2$. As a result:

$$q2\pi = \frac{4\pi nd}{\lambda} + \pi \tag{3.10a}$$

$$nd = \frac{m\lambda}{4} \tag{3.10b}$$

where m is an odd integer. Side band peaks can also be observed, corresponding to constructive interference between reflections from non-adjacent layers (i.e. where path

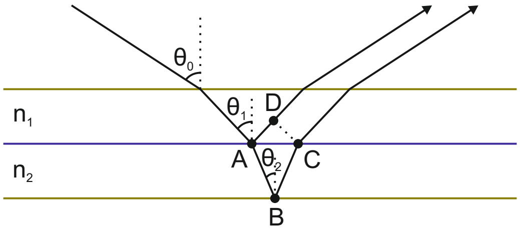

Figure 3.14: Diagram to derive the change in peak reflection wavelength with changing incident angle

difference is an integer multiple of d $\neq 2$).

The effect on the peak wavelength of changing incident angle can be understood by considering the system geometrically (see figure 3.14). The path difference for waves reflected from interfaces 1 and 2 is given by $ABC - AD$, which, as previously, should be equal to $m\lambda$ for constructive interference to occur. Considering the system geometrically and invoking Snell's Law:

$$n_1 \sin\theta_1 = n_2 \sin\theta_2 \tag{3.11}$$

we obtain the relation:

$$m\lambda = ABC - AD = \frac{2d_2 n_2}{\cos\theta_2} - 2d_2 n_2 \tan\theta_2 \sin\theta_2 \tag{3.12}$$

which with some manipulation gives:

$$m\lambda = 2d_2 n_2 \cos\theta_2 \tag{3.13}$$

It can hence be seen clearly that tilting a stack will decrease the peak reflection wavelength, with a maximum reflection wavelength being obtained when the incident light is perpendicular to the stack face.

The total reflectance R of a quarter-wave stack with an odd number of layers and high index top and bottom layers is given by:

$$R = \left(\frac{1-Y}{1+Y}\right)^2 = \left[\frac{1 - \frac{n_H^{2p+2}}{n_L^{2p} n_{sub}}}{1 + \frac{n_H^{2p+2}}{n_L^{2p} n_{sub}}}\right]^2 \tag{3.14}$$

where Y is the admittance of the structure, n_H, n_L and n_{sub} are the refractive indices of the high index layers, low index layers and substrate respectively and $2p+1$ is the

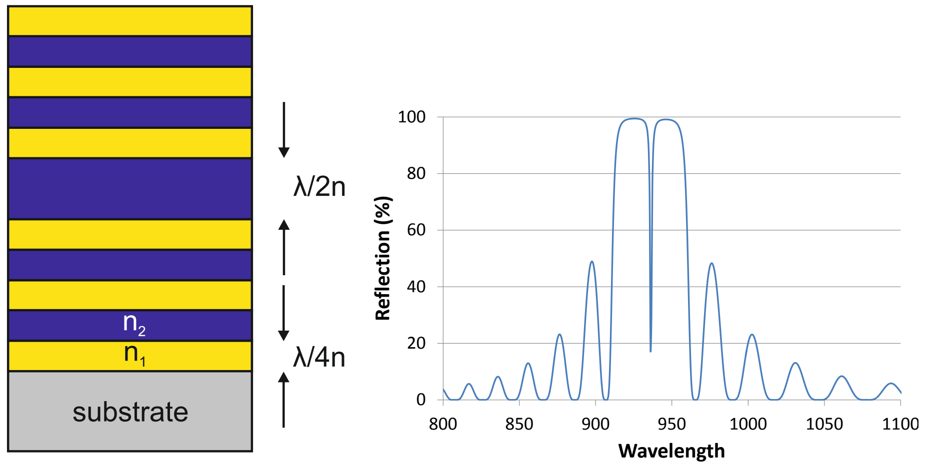

(a) (b)

FIGURE 3.15: Concept diagram (a) and example spectrum (b) of a π shifted Bragg stack

number of layers (derivation in appendix B). Assuming $n_H > n_L$ and $2p+1$ is large then the transmission $T = 1 - R$ can be approximated as:

$$T = 4\left(\frac{n_L}{n_H}\right)^{2p}\left(\frac{n_{sub}}{n_H^2}\right) \tag{3.15}$$

i.e. the peak transmission can be reduced (and hence the reflectance increased) by increasing the number of layers and/or the refractive index contrast between the layers. The width of the high reflection zone can also be increased by increasing the index contrast. This is also described in greater detail in appendix B.

3.5.2 π shifted

A π shifted structure has the characteristic reflection spectrum shown in figure 3.15(b), i.e. a reflection peak similar to that of a quarter-wave structure but with a sharp dip in the centre. It consists of two quarter-wave stacks separated by a spacer layer of thickness $\lambda/2n$, and can be considered as a Fabry-Perot etalon.

The difference in phase δ between two waves, one of which passes straight through and the other of which is reflected twice within the cavity (spacer layer), is given by:

$$\delta = \frac{4\pi n d}{\lambda} \tag{3.16}$$

The peak transmission through the structure will occur where waves interfere constructively, i.e. where $\delta/2 = m\pi$ (hence "π shifted") and:

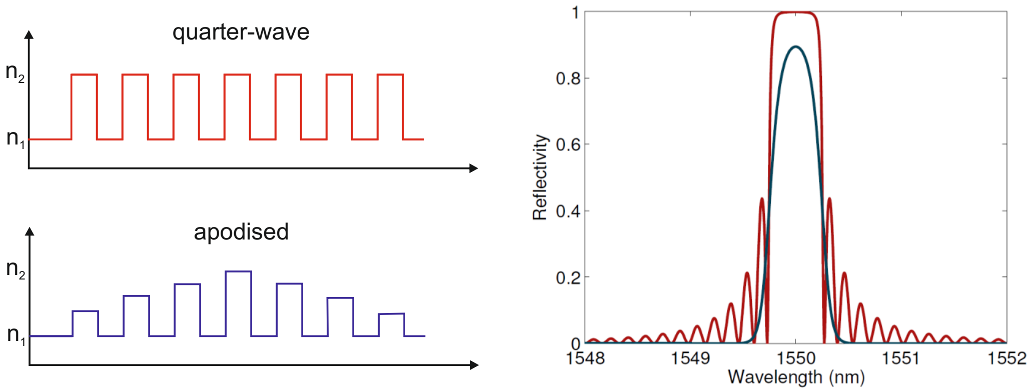

(a) Comparison of grating strength profiles

(b) Example spectra comparing quarter-wave (red) and apodised (blue) Bragg stacks [163]

FIGURE 3.16: Grating strength profile and example spectrum of a Gaussian apodised grating

$$nd = m\frac{\lambda}{2} \tag{3.17}$$

where m is an integer.

3.5.3 Apodisation

As can be seen in figure 3.12, as well as the main reflection peak a quarter-wave Bragg grating spectrum exhibits a number of side lobes or bands. To remove these side bands and allow the grating to reflect only within a desired reflection band (e.g. for sensing, filtering), gratings can be apodised i.e. the optical thickness of the layers can be varied as a function of position in the grating. Gratings may be chirped-apodised (physical layer thickness variation), grating strength-apodised (refractive index profile variation, see figure 3.16(a)) or a combination of the two. The Gaussian-apodised grating profile (i.e. of the form e^{x^2/c^2}) is one common example, and is the form used to generate the spectrum illustrated in figure 3.16(b) [163].

A good approximation of the shape of a grating's response can be gained by taking the Fourier transform of the grating's structure [134]. A quarter-wave stack has a top hat form and the transform is a sinc function (i.e. central peak with side lobes); if the grating has a Gaussian apodised structure, however, the response will also be a Gaussian (i.e. no side lobes). For a deeper understanding of stack behaviour as a result of apodisation, the characteristic matrix of the stack should be evaluated by computer (see appendix B).

3.6 Conclusions

An overview of PLD theory has been presented. Emphasis has been placed on the interconnectedness of variables and the subsequent need for experimental verification of conditions, rather than modelling from first principles. Some of the potential barriers to achieving high quality crystal growth have been discussed, including particulate production and limitations to thick film growth. Aspects of waveguide, laser and Bragg reflector theory have been considered, with details of operation and design requirements of such devices described. Knowledge of basic PLD concepts, as well as the devices the technique can be used to fabricate, is invaluable in going forward to choose and design the experimental and analytical methods detailed in chapter 4.

Chapter 4

Experimental and analytical methods

4.1 Introduction

This chapter describes the equipment and techniques employed to fabricate and analyse the samples presented in this thesis. Overviews of single- and multi-beam PLD are presented, as well as other experimental techniques including the shutter technique used to grow sophisticated multilayers. Methods of material and structure analysis are also discussed, along with the ion probe setup used to directly analyse ablation plumes.

4.2 Pulsed Laser Deposition

4.2.1 Single-beam PLD

Apparatus used for conventional PLD is illustrated in figure 4.1. It is designated *Chamber 1* for the purposes of this thesis. Features of the set-up are listed below:

- A single pulsed UV laser is incident upon a rotating target;
- Target rotation is driven via an offset cam assembly, providing an epitrochoidal ("spirograph") ablation path and hence efficient use of the target surface;
- A background gas, typically O_2, is used to modify plume dynamics and/or control film stoichiometry;
- Substrates are heated via a CO_2 laser. The beam is incident upon a ZnSe tetraprism (see section 4.2.4) to generate a homogenised, square profile;

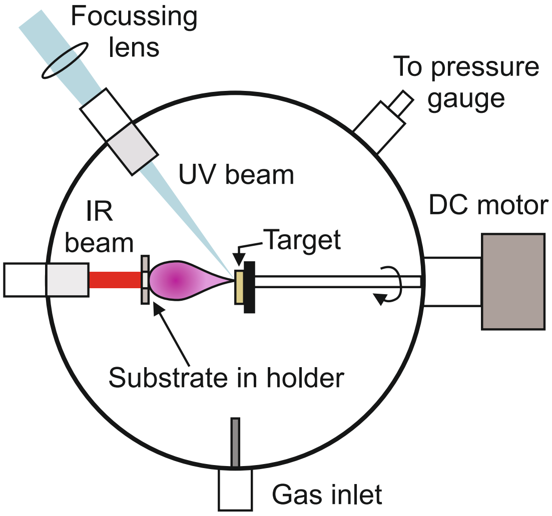

Figure 4.1: Diagram of single beam conventional PLD set-up.

- Laser spot size (and hence fluence and plume divergence) is varied by moving the position of the focussing lens and/or changing the lens used (different focal lengths result in different values of magnification);
- Substrates are held inside a metal holder at opposite corners using two notched cylindrical ceramic posts;
- Target-substrate distance may be varied;
- Targets are preferably single-crystal. Dense sintered targets may also be used if affordable single-crystals cannot be obtained; however, target reconditioning can be problematic (see section 4.2.5);
- A two stage vacuum system is used (turbo pump backed by roughing pump);
- The substrate can be shielded using a metal blocker.

4.2.2 Multi-beam PLD

Apparatus used for combinatorial PLD is illustrated in figure 4.2, designated *Chamber 2*. Many features are shared with the single-beam PLD setup described above. However, there are a number of fundamental differences:

- This set-up has the capacity to ablate up to three targets with up to four lasers simultaneously, although for all experiments detailed in this thesis only two targets and lasers were used (as illustrated);
- The substrate may be rotated while simultaneously heated;

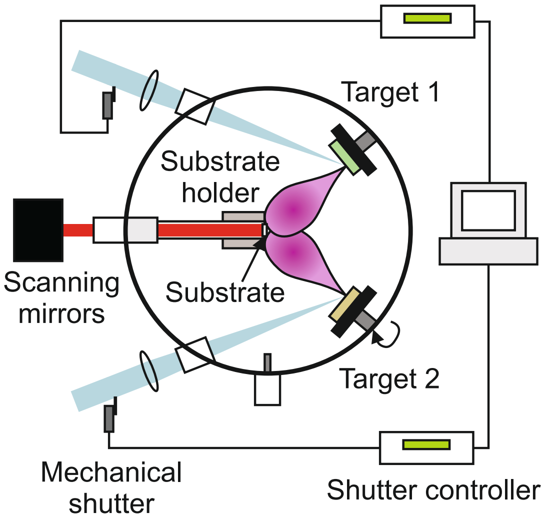

Figure 4.2: Diagram of multi-beam combinatorial PLD set-up, including mechanical blockers (see section 4.3.1).

- Laser-target angle of incidence may be varied over a range of 8° (for the target configuration used for experiments in this thesis). This angle may be kept constant, or alternatively targets can be tilted continuously to scan the plume across the substrate. While this can result in an increase in the number of particulates (a consequence of ablating ridges or splashed areas, as detailed in section 4.2.5, tilting allows control over film thickness profile (e.g. to obtain flat film growth) and more efficient use of the target surface;
- CO_2 laser heating is achieved by raster scanning the beam across the back of the substrate, allowing a number of shapes and sizes of substrate to be heated (see section 4.2.4);
- Control of all components apart from substrate heating and roughing pump is controlled via a computer rig. Parameters can nominally be programmed, although in practice only continuous target tilting was achieved automatically.

4.2.3 Lasers

Two UV ablating laser systems have been employed in the experiments detailed in this thesis: frequency-quadrupled Nd:YAG and excimer.

The Nd^{3+}:YAG-based laser systems used throughout experiments detailed in this report (Continuum Surelite II) are flashlamp-pumped, operating with a repetition rate of 10 Hz with pulse durations of 5 ns and typical energies of up to ∼100 mJ per pulse. Fundamental emission occurs at 1064 nm, but this is frequency quadrupled via non-linear crystals to generate emission at 266 nm.

Nd:YAG systems do not require the use of toxic halogen gases, and are cheaper than excimer lasers[1]. There are, however, three main drawbacks when compared to excimer systems:

1. While many materials absorb well at 266 nm, some do not, including yttrium-based garnets such as YAG. Fluence must therefore be increased to reduce droplet formation, which, as a smaller spot size results in a larger angular distribution of the plume, leads to low growth rates (<1µm per hour).
2. Beam output should be as uniform as possible. Nd:YAG crystals can, however, suffer from thermal effects and defects that affect output quality. These lead to hotspots of much higher fluence, particularly after two harmonic generation steps. As such, plumes resulting from Nd:YAG laser ablation may include higher kinetic energy components compared to top-hat excimer beams, potentially resulting in greater changes in stoichiometry relative to bulk, increased particulate production and target damage.
3. UV emission requires precise tuning of non-linear crystals. This tuning can drift over time due to changes in temperature or humidity, leading to a drop in performance and small changes in beam profile.

Excimer lasers are generally accepted as the preferred system for standard PLD [40]. These emit directly in the UV, have a nearly uniform rectangular output and are capable of achieving pulse energies of 400 mJ or more even at repetition rates of 10 Hz or higher. The system used for experiments detailed in this thesis is a Coherent COMPexPro 102. It is capable of operation at 193 nm and 248 nm, utilising ArF and KrF gas mixtures respectively, although only 248 nm radiation has been used for experiments described here. The maximum repetition rate available is 20 Hz and the maximum energy per pulse is ∼480 mJ (maximum voltage, new gas refill). It is not advised to operate the laser continuously at maximum voltage; generally, pulsed energies used are between 300 and 380 mJ. Pulse energy obtained for a given voltage reduces over time as halogen concentration decreases due to the reactive halogen forming stable compounds, necessitating a gas change every few weeks.

4.2.4 Substrate heating

Various approaches may be taken to heat a substrate. These may utilise conduction, via metal plates, foils or filaments bonded directly to the substrate, or radiation, via sources including quartz lamps [164]. These methods can, however, have significant disadvantages:

---

[1] Considering base cost only: excimer lasers generally have a higher “energy per pound” ratio

- Temperature uniformity can be difficult to achieve;
- Methods such as filament heating may not be suitable for high temperatures (>600 °C), due to oxidising and burn out;
- Radiative methods in particular may not be highly directional, leading to inefficient performance and heating of the chamber walls;
- Outgassing, either of heating elements or chamber walls, can lead to film contamination.

To combat these problems, a 30W Synrad CO_2 laser of wavelength 10.6 µm was used for substrate heating in all cases described in this thesis. This method is very directional and allows high substrate temperatures to be achieved without significant heating of the chamber. Temperature uniformity is not an intrinsic feature of this method due to the laser's Gaussian beam profile; however, two approaches have been taken to remedy this, which are described below.

4.2.4.1 Tetra-prism

A relatively flat-top beam profile may be obtained using the concept of beam folding. A CO_2 beam is passed through a ZnSe pyramidal prism (tetra-prism) [165], dividing the beam into sections and subsequently overlapping them to transform the profile from circular Gaussian to approximately square top hat (see figure 4.3). Although the overlap of beam sections leads to interference, the presence of fringes does not significantly affect the performance of the tetra-prism. The diffusing nature of the substrate allows slight heat variations on the back surface, caused by intensity modulations, to be smoothed out on the front.

The angles of the prism facets are determined by experimental parameters such as working distance and substrate size, and hence the system is not easily adapted to other configurations. However, the tetra-prism is relatively inexpensive, and gives a minimum theoretical standard deviation over the surface of 2.2 K, comparing favourably with minimum values obtained for an untransformed Gaussian beam and square-tapered beam pipe (43 K and 7.2 K respectively [143]).

4.2.4.2 Raster scanning

A more complex but more versatile system utilises a computer-controlled, two-axis mirror scanner to raster scan the beam across the back surface of the substrate. Precise control over dwell time at each point allows compensation for any differences in temperature over the substrate area, and because hardware design is not configuration-specific, the system is adaptable for different substrates and working distances.

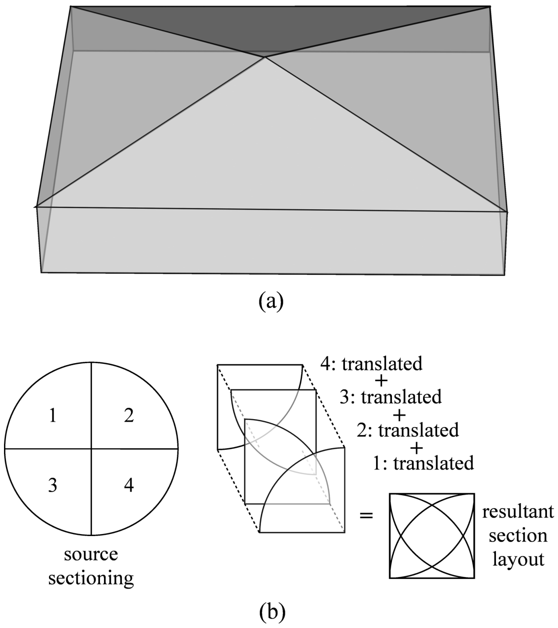

(a)

(b)

Figure 4.3: Diagrams of (a) tetraprism and (b) transformation of beam profile from Gaussian to approximate square top hat [165].

4.2.4.3 Temperature calibration

One may expect the temperature of the substrate to follow that of a grey body, allowing the temperature to be determined from the emitted power by the Stefan-Boltzmann law:

$$P_E = A\epsilon\sigma T^4 \tag{4.1}$$

where P_E is power emitted (which in a steady state is equal to the power absorbed), A is surface area, ϵ is emissivity and σ is the Stefan-Boltzmann constant. This relation is complicated, however, by the fact that the emissivity of both the substrate and the film are dependent on wavelength, temperature and surface topography. Temperature cannot therefore be assumed to be directly proportional to $P_E^{\frac{1}{4}}$ over the whole temperature range.

Accurate measurement of substrate temperature is, however, somewhat difficult. Direct contact methods are not appropriate due to heat sinking through the measurement probe, and indirect methods (e.g. pyrometry) are inaccurate due to the unknown wavelength-dependent emissivity of both the substrate and the growing film. Given that temperature values can be estimated only, a cheap and simple method of converting CO_2 laser power to estimated growth temperature was used:

1. Metal foils of known melting points were balanced on a YAG substrate. Laser power was increased until the metals melted, giving an indication of substrate temperature. These temperature estimates were then plotted against power absorbed by the substrate[2].

---

[2] This investigation was carried out by Tim May-Smith

2. The variation in laser power absorbed by the substrate with nominal CO_2 output (% on dial) was found by measuring transmitted laser power with and without a YAG substrate for different laser power percentage points.

The temperature of a substrate may therefore be estimated by calculating the power absorbed for the nominal CO_2 value (via the first plot) and converting this into temperature (via the second plot). The advantage of this two step method is that it allows substrate temperature estimates to be obtained regardless of the specific heating method employed and without assuming emissivity values. It does provide only rough surface temperature estimates. By comparison with growth conditions as reported by other groups, temperatures are assumed to be correct to within ~50 °C. In the context of the experiments in this thesis, however, absolute temperature measurements are not required as long as temperature values are repeatable.

4.2.5 Particulate minimisation

As described in section 3.2.6, careful choice of deposition parameters, particularly fluence and ambient gas pressure, can go some way to minimising particulates. In addition, single-crystal target surfaces can be reconditioned (lapped) after some hours of ablation (time depends on the target and the conditions used) to remove any surface structuring. After thorough cleaning, targets are subjected to some minutes ablation before the deposition begins, with the substrate covered. This removes the rough lapped surface, ablation of which would result in a film with many particulates, leaving a relatively smooth surface for subsequent ablation.

While lapping is an effective tool for reconditioning single-crystal targets, reconditioning of sintered targets has proven more problematic. While surface features can be easily removed, lapping powder abrasive particles can become stuck in target voids. Such particles cannot be removed by ultrasonic cleaning, but are released when the target is ablated, leading to an extremely large number of particulates. As yet, a solution to this problem has not been found, and hence sintered targets have not been reused.

4.3 Other experimental techniques

4.3.1 Beam shutters

Mechanical beam shutters are used to physically block the ablating beams, reducing the effective repetition rates of one or more lasers. The specific shutters used in the context of this thesis are Laser 2000 SH-10 Laser Safety Shutters (illustrated in figure 4.4), which consist of a 0.25 mm thick anodised aluminium flag mounted on a rotary solenoid. The

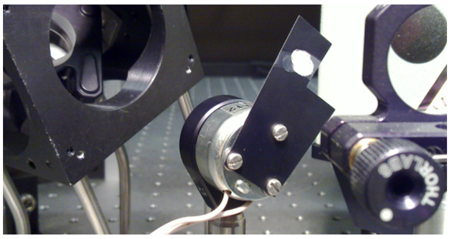

FIGURE 4.4: In situ photograph of Laser 2000 SH-10 Laser Safety Shutter. Damage to the flag from repeated irradiation by an Nd:YAG laser can be observed.

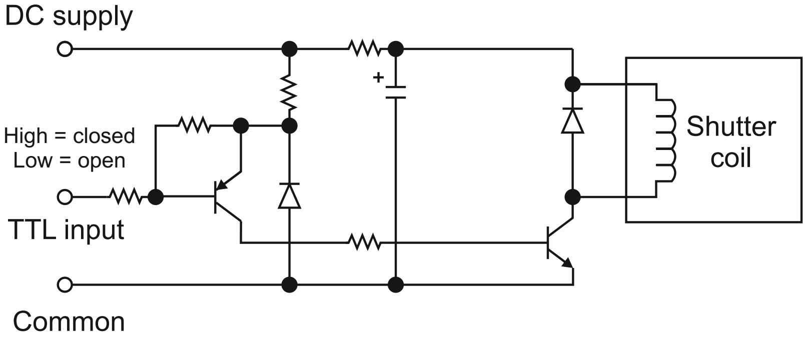

FIGURE 4.5: Drive circuit for Laser 2000 SH-10 Laser Safety Shutter, 12V AC supply.

blade can be removed or replaced if damaged or if a larger flag is required. The shutter body is held inside a 25 mm diameter lens mount, allowing for ease of access and setup changes whilst requiring no additional components. With lengthy use at high repetition rates, shutters with larger flags (e.g. for excimer laser) can become slightly loose due to the vigorous movement of the flag. In such cases it is hence important to tighten the mount when required, to ensure that the flag will still block the beam.

When the shutter is powered, the flag moves to the "open" position and is held there until the power is removed. Each shutter is connected to the circuit illustrated in figure 4.5 to allow control of the shutter position via a TTL input signal, in this case provided by a Thorlabs SC10 shutter controller. The shutter controllers have a number of available settings (defined number of repetitions, a single open-close movement, manual control etc.) and may be triggered internally or externally via a separate TTL signal source. Open and closed timings are set separately to millisecond precision, although the mechanical response of the shutters limits the practically available repetition rate. Minimum response times (open or closed) were 0.2 and 0.3 seconds for Nd:YAG and excimer-line shutters respectively. Modes may be set and times adjusted manually by the controller unit front panel, or automatically by PC via an RS-232 serial port connection.

Sophisticated control is given via a set of *LabVIEW* Virtual Instruments (subroutines). By incorporating these into a *LabVIEW* program, it is in theory possible to create a program to grow any arbitrary grading profile or lattice structure, assuming it lies within the shutters' mechanical capabilities. A simple program to create alternating distinct multilayers by following a set of spreadsheet instructions was used to create the majority of multilayer stacks described in chapters 5 and 6. A number of programs have also been written to achieve linear or polynomial grading in depth; however, samples have not yet been grown using such programs.

4.3.2 Cleaning

As cleanliness of as-supplied substrates cannot be guaranteed, substrates should be cleaned before deposition to remove any contaminants. Similarly, care should be taken to remove grease from films subjected to XRD before any deposition of subsequent layers. Substrates/samples are initially placed in a beaker of acetone in an ultrasonic bath (40 °C) for twenty minutes, then rinsed with isopropanol and de-ionised water. Finally, substrates/samples are dried with a nitrogen gas jet.

Films and targets that have been lapped or polished are subjected to additional cleaning steps. Objects are soaked in non-solvent cleaning fluid (Ecoclear) overnight then placed in an ultrasonic bath (40 °C) for twenty minutes. Other solvent cleaning steps follow as described above.

4.3.3 End polishing

End faces of films designed for waveguiding and lasing (e.g. channels described in chapter 7) must be polished to an optical finish before investigation of optical parameters can occur. Samples are attached with wax to a metal block which is then mounted on a jig. The jig is held face down on a rotating circular plate, onto which polishing fluid or grit mixed with DI water (for lapping) is fed. Multiple samples can be stacked together and polished at the same time. Packing pieces (usually blank substrates) are placed at either side of each stack or sample to prevent damage to film corners.

Samples are initially lapped with 600 grit silicon carbide (average particle diameter ∼16 µm) to achieve approximately the same flatness for all samples and packing pieces. This grit is also used to recondition target surfaces. Further lapping takes place in stages with 9 µm, 3 µm and finally 1 µm diameter aluminium oxide powder, to remove any scratches from the previous stage. A high-quality, optical grade finish is achieved by polishing with SF1 alkaline colloidal silica polishing fluid. As opposed to the lapping stages, which are purely mechanical, polishing is both an abrasive and chemical process.

End faces must be polished parallel in order to achieve lasing. Once one face is polished, the mounting block is rotated (samples remain attached) to allow the polished face to be used as a reference mirror in an autocollimator (see figure 4.6).

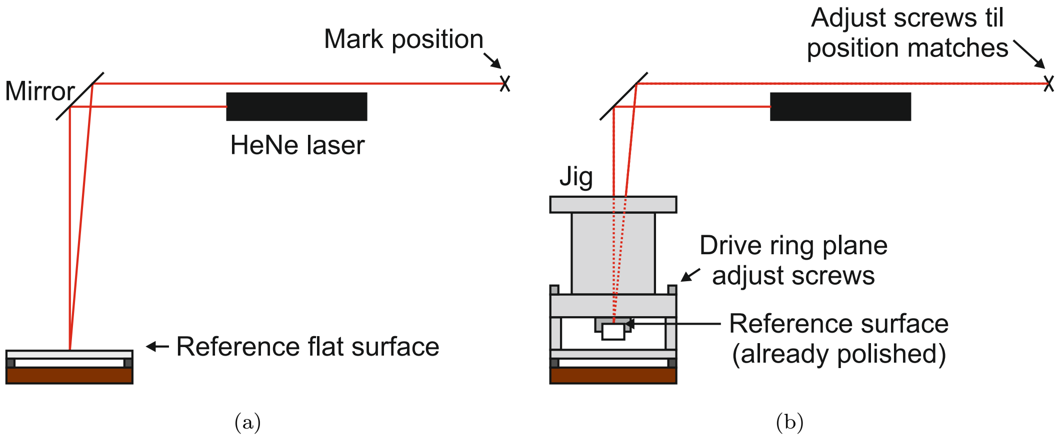

FIGURE 4.6: Diagram of autocollimator operation as used to ensure parallelism of polished end faces: (a) mark laser position with a reference flat (b) use the already-polished sample surface as a reference and adjust drive ring plane screws until laser position matches the position measured in step (a).

4.4 Surface analysis

4.4.1 Microscopy

Films that have non-bulk stoichiometry, large numbers of particulates or have been grown at non-optimal temperatures may appear frosted, opaque or even cracked on visual inspection. Optical microscopy can be used to further analyse the extent of cracking or flaking, as well as provide some information about the extent and size of particulates (although pores and particulates can be difficult to distinguish).

Scanning electron microscopy (SEM) allows a closer examination of film surfaces. A beam of electrons is incident upon the sample. Interactions between these electrons and the sample lead to the emission of secondary electrons via inelastic scattering. The strength of detected signal depends on the number of electrons collected, which is determined by the angle of incidence of the beam onto the sample. The variation in signal with position will hence depend on the surface topography, and so when the beam is raster scanned across the area of interest, an image of that surface is produced. Electrons produced via elastic scattering (“back scatter”) are also of interest: the signal strength is strongly dependent upon the atomic number of the interacting element, and hence may be used to identify areas of different composition.

Conventional SEM can be slightly destructive, as it requires the sample to be coated with a conductor (usually gold) to prevent the accumulation of charge on the sample surface. The environmental SEM removes this requirement. Instead, a relatively high pressure is maintained around the sample which, due to ionisation of the gas by the incident electron beam, allows charge to be transported away from the sample surface. A differential pumping system is used to maintain a vacuum around the cathode gun itself. Environmental SEM was used for all the examples of SEM described in this thesis and the instrument was a Zeiss EVO-50.

4.4.2 Surface profiling

A surface profiler is used to determine surface curvature and quality. Bare areas exist in the two opposite corners where the substrate has been shielded by the holder posts. Film thickness and curvature values can hence be estimated by scanning across the sample from corner to corner, although film curvature can be difficult to resolve if substrate curvature is high. More accurate values will be obtained if substrate curvature has been measured before deposition as a reference measurement. Two surface profiling approaches have been used in this thesis: stylus and optical profiling.

4.4.2.1 Stylus profiler

This profiler consists of a stylus on the end of a cantilever, the point of which rests on the sample. The sample is moved and the vertical movement of the stylus measured. The cantilever is extremely sensitive, allowing changes in profile of the order of Angstroms to be measured. There is, however, a limitation in the horizontal resolution, due to the sloping sides of the stylus. The instrument used for all stylus profile measurements described in this thesis is a KLA Tencor P-6.

4.4.2.2 Optical profiler

The optical profiler is an interference microscope consisting of three white light interferometers (5x, 10x and 50x resolution) in two geometries (see figure 4.7). The profiler measures the intensity of fringes while head height is scanned vertically, and sophisticated signal processing algorithms are applied to create a 3D image of surface morphology. The system is theoretically capable of sub-nanometre resolution, although vibration and air currents reduce resolution to a few nanometres in the practical system. Because a 3D image is measured, information about particulates and pores can be obtained. Automatic particulate counting was achieved using the Image Metrology *Scanning Probe Image Processor* (SPIP) software package, and the instrument used for all measurements described in this thesis was a Zemetrics ZeScope.

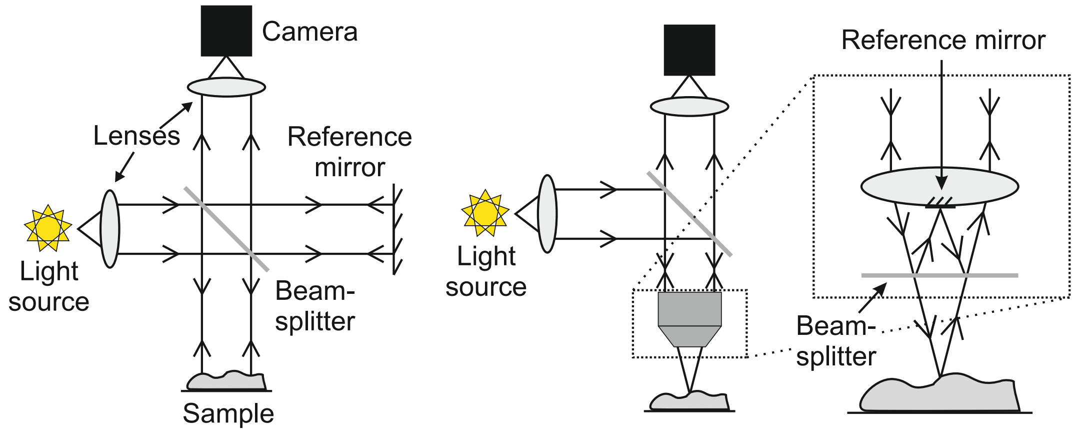

(a) 5x magnification (Michelson interferometer)

(b) 10x and 50x magnification (Mirau interferometer)

Figure 4.7: Diagrams of the white light interferometers used for optical surface profiling (Zescope).

4.5 Crystallinity, structure and composition analysis

4.5.1 X-ray diffraction

X-ray diffraction (XRD) is a non-destructive, rapid method of determining crystal structure. The X-ray diffractometer consists of an X-ray source and detector which rotate about a stationary holder, resulting in a spectrum of X-ray counts against twice the incident angle 2θ. This spectrum may be compared against database values to give information about crystal structure and orientation. Unless otherwise indicated, a Siemens D5000 powder X-ray diffractometer was used to obtain results described in this thesis.

Defects in the crystal result in slightly varied values of plane separation d (see below), and hence will result in broadening and/or shifting of the 2θ peaks. A peak shift relative to the textbook value indicates a uniform change in lattice spacing, and hence may be evidence of non-standard stoichiometry. Instrument factors, crystallite size and non-uniform strain all contribute to peak broadening. It can be difficult to separate the contribution of each effect; however, some qualitative understanding can be gained by comparing the peak FWHM of a film with that of the underlying substrate (assumed to be “perfect” crystal).

4.5.1.1 Stacked planes model

An intuitive understanding of how XRD peaks arise can be gained by viewing a crystal as a series of radiation scatterers (such as atoms) arranged in planes. If these planes are separated by a distance d, scattered X-rays will constructively interfere only when the

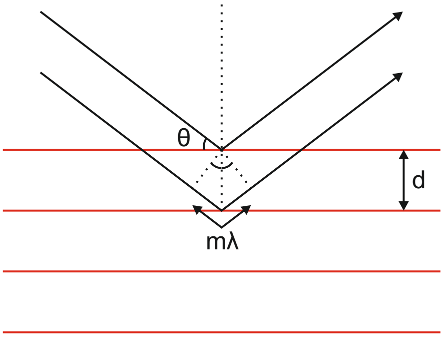

FIGURE 4.8: A basic understanding of XRD can be obtained by considering a crystal as a series of planes (see Equation 4.2.

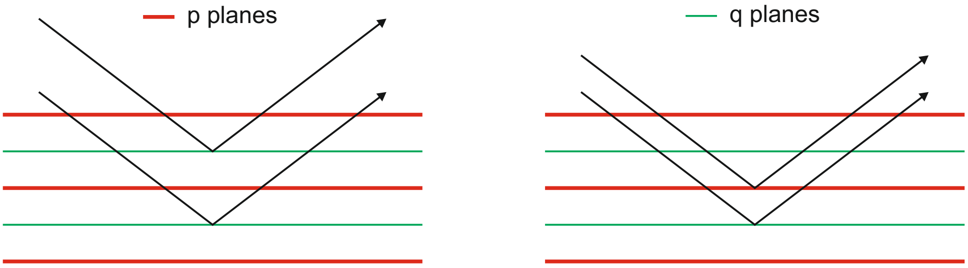

(a)

(b)

FIGURE 4.9: Diagrams of (a) (400) (between p-planes and/or q-planes) and (b) (800) diffraction (between p- and q-planes) diffraction

Bragg condition (Equation 4.2) is met:

$$2d \sin \theta = m\lambda \tag{4.2}$$

where d is the spacing between planes, θ is the incident angle, m is an integer (the order of the diffraction peak) and λ is the wavelength of the incident X-rays (see figure 4.8).

A unit cell of garnet crystal (general formula $A_3B_2C_3O_{12}$) can be considered as consisting of eight crystal planes, two types alternating. The first type (p-plane) has four A lattice sites, four B lattice sites and four C lattice sites per unit cell, whereas the second type (q-plane) has only two A sites and two C sites. (400) diffraction is defined by the spacing between similar planes (p-planes with p-planes, q-planes with q-planes), although the contribution of the denser p-planes is likely to dominate. By contrast (800) diffraction is defined by spacing between p- and q-planes, and hence is more sensitive to any changes in stoichiometry. Is it therefore expected that the (800) diffraction peak will be shorter and broader than in (400) cases. (400) and (800) diffraction is illustrated in figures 4.9(a) and 4.9(b) respectively.

4.5.1.2 Superlattice characterisation

While it is possible to understand some aspects of X-ray diffraction by considering a crystal as a series of planes, a fuller understanding requires consideration of scattering from each atom in a crystal. This is of particular relevance when dealing with multilayer structures exhibiting both short- and long-range periodicities: superlattices.

Two approaches may be taken, both of which consider the sum of the scattering contributions from each atom in the crystal. Dynamical theory provides the most complete picture by taking into account such effects as secondary reflections and interaction between X-rays. These are ignored in kinematical theory; however, even this approximation can provide a good description of peak positions and intensities, and given its relative simplicity is generally the approach used when fitting models to data.

To model scattering from a crystal, one must have knowledge of the position vector of each atom within each unit cell, as well as the level of scattering (the scattering factor) from a single atom of that type. This does not present an insurmountable challenge for simple materials, e.g. metallic lattices [166]. However, modelling the scattering from a complex oxide system where the level of diffusion, stresses, dislocations and stoichiometry are not known is much more complex and time consuming. As such, modelling from first principles has not been attempted in this thesis.

Rather than predicting results directly from theory, the approach usually taken is one of fitting a model to data obtained to gain system parameters. A web-based dynamical X-ray simulation program GID_sl [167], for example, was used to fit a model to XRD data in section 5.3 to obtain information about layer thickness and strain. Ishibashi et al [99] provide an example of the influence of different crystal and structure parameters and fitting approaches on the accuracy of the fit.

Some basic parameters can be obtained relatively simply by taking values directly from XRD spectra:

- **Superlattice period** Difference in 2θ position of satellite peaks gives superlattice period P by modified Bragg law [94]:

$$P = \frac{\lambda}{2(\sin\theta_{n+1} - \sin\theta_n)} \tag{4.3}$$

- **Flatness of surfaces** *Pendellösung fringes* are a result of interference between front and back surfaces, and hence their presence gives an indication of the angle of the top surface of the crystal layers relative to the back/substrate.
- **Layer quality** As usual with XRD, peak broadening is an indication of crystal quality. A higher number of visible satellite peaks also suggests sharper boundaries/less diffusion between layers and hence a higher quality superlattice. The

widths of satellite peaks may also be compared to that of the central diffraction peak to give an indication of the thickness variation.

4.5.1.3 Growth rate measurements

It is possible to use superlattice period as a measure of growth rates. Equation 4.3 gives the period of a superlattice, and hence the average layer thickness for a given number of shots of growth. It is hence possible, by taking values from two superlattices of the same materials, to obtain growth rate values much more accurate than those found by surface profiling (where curvature of the substrate can be a significant problem).

4.5.2 X-ray reflectometry

X-ray reflectometry (XRR) was used to gain layer thickness and roughness values for superlattice samples (see section 5.3). Unlike XRD, XRR does not give information about material crystallinity and can hence be used to analyse amorphous and liquid samples as well as crystal, providing films are limited to some hundreds of nanometres.

X-rays irradiate a sample at grazing incidence (between 0 and 5°) and the reflected intensity is measured. At incident angles less than a critical angle θ_c (below 0.3° for most materials [168]) the beam is totally reflected. θ_c is dependent upon the material's refractive index and hence density, and therefore can, if known, be used to determine the material density. At angles larger than θ_c, reflections are obtained from the top and bottom of the film (or each interface within a multilayer structure) that interfere to form peaks. Surface or interface roughness gives rise to greater scattering, reducing the intensity of the reflected beam. Fitting of reflectometry data, particularly peak positions and intensity drop-off, can hence provide information about layer thickness and roughness, often to within a few angstroms.

For all samples detailed in this thesis, measurements and analysis were carried out by Steven Huband and David Walker at the University of Warwick, with data fitted using the *Panalytical* reflectivity software.

4.5.3 Energy dispersive X-ray analysis

Energy dispersive X-ray analysis (EDX) is used to determine elemental composition of a small, tear-drop shaped interaction volume below a sample surface. A high energy electron incident upon a sample may excite an electron in an atom's inner shell, ejecting it from that shell and creating a hole. An upper level electron will then fall down to fill the hole, emitting an X-ray whose energy will be equal to the gap between the upper and lower levels. The levels from which electrons are ejected and fall will vary between interactions, and hence a number of different energy values may be measured. Because the energy gaps between shells are defined by the particular structure of an atom, the pattern of energies of the collected X-rays indicates the elements present in a sample. The intensity of the peaks gives an indication of the relative abundance of each element.

Various factors will affect the accuracy of EDX:

- Broad peaks can be formed by the overlap of energy peaks from different elements, making individual peaks difficult to discern;
- Lower energy X-rays can be absorbed by the detector window (this will particularly affect lighter elements with fewer shells and hence fewer and lower-energy peaks);
- Analysis is limited to a depth of up to ∼2 µm below the surface, and hence may not be representative of the entire sample.

These sources of error may prevent accurate abundance values of light (e.g. oxygen) or scarce elements being obtained. As a result, oxygen is assumed to be stoichiometric in cases described in this thesis, unless stated otherwise. Unlike many other elemental analysis techniques, however, EDX is straightforward and non-destructive. Steps can be taken to assess the extent of errors, for example by statistically analysing multiple readings and calibrating to standards of known composition.

EDX is undertaken in conjunction with SEM, using the same beam of electrons. The system used for all composition measurements was an Oxford Inca PentaFet-x3 EDX analyser.

4.6 Ion probe analysis

Analysis of plasma plumes was carried out using a planar Langmuir probe (see figure 4.10). The probe consists of a copper plate (copper-faced board) connected to a simple circuit (Koopman circuit), illustrated in figure 4.11. The conducting area is surrounded by insulating epoxy and is held within a metal collar. The probe is immersed in the plume with the conducting surface normal to the direction of plasma flow, and the voltage change with time (ion time-of-flight (TOF)) is measured on an oscilloscope. The probe bias can be positive or negative, to collect electrons or ions respectively, and capacitors are included to prevent charge saturation. The measured voltage drop across the load resistor is used to compute to the collected current I, which is itself proportional to the ion density and velocity of the plasma by the relation:

$$I = evAn \tag{4.4}$$

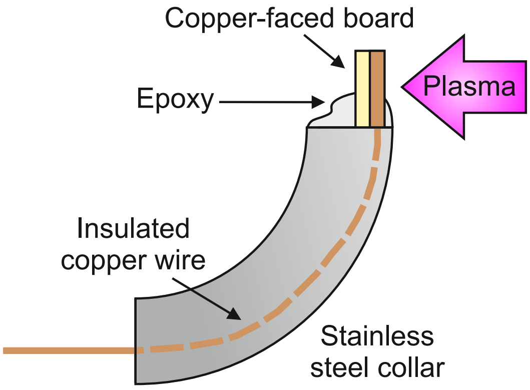

FIGURE 4.10: Schematic of planar Langmuir probe.

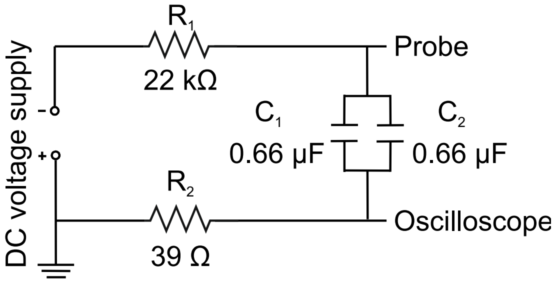

FIGURE 4.11: A typical Koopman circuit, showing component values used in ion probe experiments detailed in section 5.2.

where e is the charge on the electron, v is the plasma flow velocity, A is the probe area and n is the ion density. It should be noted that this holds for singly charged ions only, and only in cases where the bias voltage is negative enough to prevent electrons in the plasma from reaching the probe.

Due to the high plasma densities in a PLD plume, charged components of the plume are shielded from the probe potential until a certain distance from the conducting area, given by the Debye length λ_d [149]:

$$\lambda_d = \left(\frac{kT}{4\pi n_e e^2} \right)^{\frac{1}{2}} \tag{4.5}$$

which for typical values of a plume close to a substrate $\simeq 10\mu\text{m}$. Ions in the plume will hence not be influenced by the probe potential until they are within some tens of microns from the probe, and so should not significantly influence the data measured.

4.7 Conclusions

The experimental setups for conventional and multi-beam PLD have both been introduced, along with other experimental techniques used to fabricate the structures and materials detailed in this thesis. The shutter technique, developed to allow easy and automated mixed and multilayer growth, has been presented in detail. A number of analytical methods have been described, used to describe both the structures and materials grown and the plasma plumes themselves. All of the techniques, experimental and analytical, have been used to obtain the results presented in the subsequent chapters of this thesis.

Chapter 5

Development of multi-beam PLD tools for crystal engineering

5.1 Introduction

Multi-beam PLD has been established as a particulate reduction technique for some time (see chapter 2); however, the approach has huge potential for crystal and structure engineering that has not yet been exploited. This chapter describes the investigation and development of two tools for growth of crystals with designer structures and properties. The first of these uses relative plume delay to influence strain in the film, while the second, the shutter technique, uses computer-controlled mechanical blockers to allow mixed, graded and automated multilayer growth.

The main contributions detailed in this chapter are as follows:

- Determination of the effect of laser plume synchronicity on the structure and composition of a crystal film;
- Design and implementation of the shutter technique for automated mixed, graded and multilayer crystal growth;
- Growth of simple and chirped crystalline superlattices.

5.2 Plume synchronicity

Whilst combinatorial PLD shows great potential, many new parameters must be tuned before this potential can be fully exploited. One such parameter is the relative delay between the laser pulses (the “synchronicity”), and, by extension, the relative delay between plasma plumes. Results of experiments detailed in this chapter suggest that these parameters are indeed significant, influencing primarily the stress states of the crystal and hence lattice constant for certain delay values. While initially investigated purely to determine the effect, the results of these experiments suggest that relative plume delay may have the potential to be used as a tool to control lattice constant and hence also refractive index, as well as illuminating the role of pressure and synchronicity on film stress.

5.2.1 Experimental setup

5.2.1.1 Depositions

Depositions were carried out in Chamber 2. Two frequency-quadrupled Nd:YAG lasers of wavelength 266 nm ablated targets of single-crystal GGG and (Nd,Cr):GSGG. Films were deposited with an ambient oxygen pressure of 4×10^{-2} mbar, and targets were tilted from 20° to 28° in order to obtain an approximately flat thickness profile. Laser fluence was approximately $\sim$1 Jcm^{-2} for both plumes, and target-substrate distance was maintained at $\sim$50 mm for both targets.

Material from the two plumes was deposited onto single-crystal (100) orientated YAG substrates of size $10\times10\times1$ mm^3, producing epitaxially-orientated films of mixed GGG and GSGG. Films of pure GGG and GSGG were also grown on YAG substrates for comparison, using conventional single laser, single target deposition (in Chamber 2). A substrate temperature of $\sim$650 °C was maintained, and the substrate was rotated to aid uniform temperature film growth and film thickness.

A Stanford DG535 digital delay generator was used to introduce a discrete delay between the two laser pulses ranging from 3.2 µs to 50 ms for each of the 22 films investigated excluding pure GGG and GSGG (i.e. one delay value per film). The laser flash lamps were triggered by the output signal from the DG535, with subsequent Q-switching and laser pulse output occurring around 180 µs later, according to each lasers' optimised internal settings.

A difference in the optimised Q-switching time of the two lasers was measured using a photodiode and oscilloscope and was found to be 3.55 µs ± 0.05 µs. This difference was not taken into account before the films were deposited, and hence in two cases "different" delays in fact fell within the same error bounds, and in one case the order that plumes arrived at the substrate (GGG plume first, GSGG following and vice versa) was the opposite of that intended. Although this meant that no films were grown at very small delays (less than $\sim$3.2 µs), the presence of multiple films at one nominal delay value allowed simple statistical analyses of XRD and EDX errors.

Lattice constant was determined from powder XRD 2θ peaks and elemental concentrations measured via EDX (see chapter 4). Three EDX measurements were taken for each film at points around the centre of the sample surface separated by ~1 mm, and the averages taken.

Films were also grown with synchronised plumes, equivalent to a delay of 100 ms due to the laser repetition rate of 10 Hz. For this case, a single pulse was split from the DG535 and used to simultaneously trigger the flash lamps of both lasers. A second pulse was similarly used to trigger the Q-switch of each laser, synchronously to ±1 ns. The difference in path length (from laser to target surface) was measured as ~30 cm, corresponding to an additional relative delay of 1 ns. It should be noted that cable lengths, in both the synchronous and asynchronous cases, were equal, and hence should not account for any unintentional further error in delay measurements. It was also assumed for both lasers that error in laser response time (i.e. Q-switch to firing time) was negligible.

5.2.1.2 Ion probe

Further analysis of the plasma plumes themselves was carried out using a Langmuir probe biased at -30 V. Experiments were conducted at the same deposition ambient oxygen pressure (4.2×10^{-2}mbar), and a constant plume-substrate angle of incidence of 23° was maintained. After around 2 minutes, the probe became coated with deposited non-conducting oxide material that progressively and substantially reduced the measured signal strength. Measurements were therefore obtained in groups, each group taking no more than ~60 seconds, after which the probe was taken out of the chamber, the oxide layer removed with sandpaper and the probe replaced. Ion probe experiments were carried out in collaboration with James Lunney (Trinity College Dublin), who also carried out ion flux and infill time calculations.

5.2.2 Results and discussion

Figure 5.1 shows the variation in film lattice constant normal to the film plane (as determined via XRD) with increasing plasma plume delay. Delay values here take into account the difference in Q-switching times between the two lasers. Two distinct regions of lattice constant (A and B) are observed, with a transition region (C) between ~150 µs and ~1 ms. Although the exact position of this transition region appears to vary slightly depending on plume order, the same overall trend is observed both in the case of the GGG plume arriving at the substrate first (followed by the GSGG plume) and vice versa. It should be noted that the lattice constant obtained using a delay of 100 ms (i.e. completely synchronous plumes) shows the same behaviour (within experimental error) as the lattice constant for a delay of 50 ms (i.e. completely asynchronous).

Figure 5.2 shows the variation in composition with increasing delay, irrespective of plume order. Oxygen content was assumed to be stoichiometric for this analysis. Additional

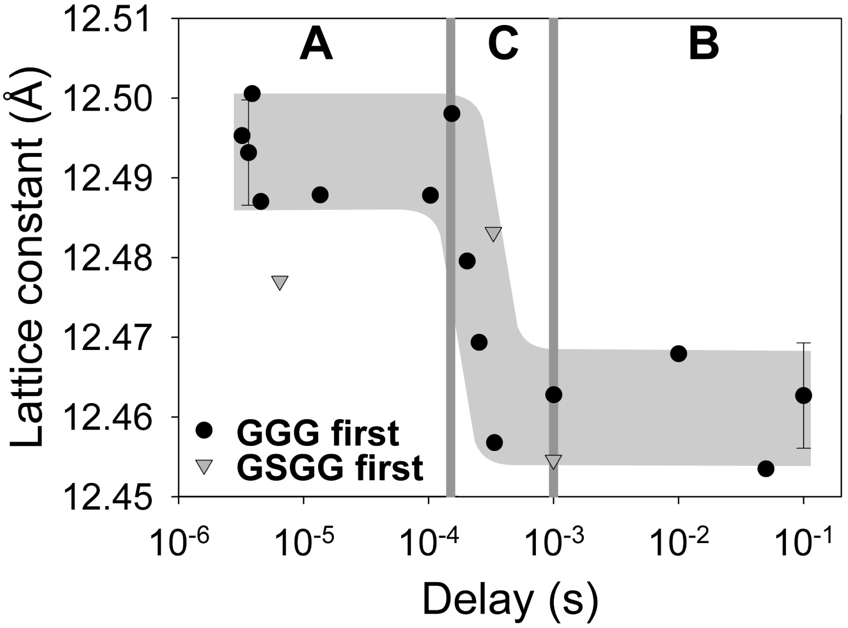

Figure 5.1: Graph of film lattice constant for different plume delay values.

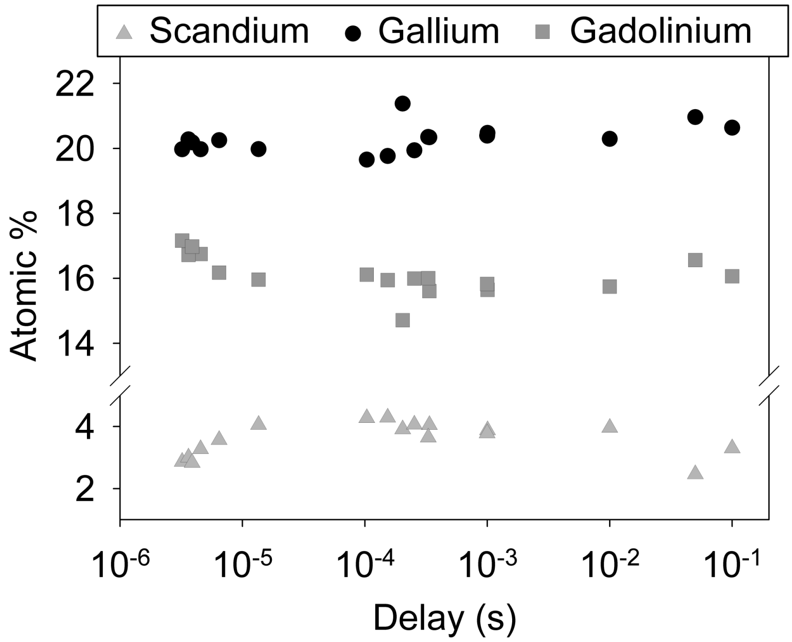

Figure 5.2: Graph of film elemental composition for different plume delay values, including data from both plume arrival orders (GGG plume first, GSGG plume first).

dopant concentrations were neglected, as the concentrations were too low to be detected via EDX. Any significant trend corresponding to the change in lattice constant is not apparent, as composition does not appear to change significantly over most of the delay range. However, a small increase in Gd concentration, corresponding to a decreasing Sc concentration, is observed for delays below approximately 13 µs.

Random small fluctuations in O_2 pressure and laser power, as well as small variations in temperature due to differences in heat sinking, can be expected to lead to variation in crystal quality and lattice constant between different films at the same plume delay. The effects on lattice constant and composition of both these fluctuations and instrument errors were estimated using the standard error over multiple experiments, i.e. two films grown with the same delay. This analysis was carried out for delays of 3.63 µs and 100 ms (i.e. synchronous), and the results for lattice constant are illustrated in figure 5.1.

Small variations in elemental composition were also observed across the surface of each film, due to the radial distribution of elements within the plumes. Composition values stated represent the average of three readings per film obtained at points around the centre of the sample. Error bounds were computed from the error values given by the EDX software (based on the element, peak height and definition etc.), although the resulting error bars were too small to be seen in figure 5.2. These did not, however, take into account any sample surface roughness, the effect of which could not be quantified.

Ion probe experiments were carried out with the GGG plume following the GSGG plume, the opposite plume order to the majority of the data presented in figure 5.1. Total ion flux (proportional to the integrated voltage-TOF curves i.e. figure 5.3) was found to be only 1% of the deposited cations as estimated from the growth rate. Ion signals are hence not fully representative of the overall deposition flux; however, overall trends could be observed and compared with lattice and composition data.

Figure 5.3 shows ion probe signals for both the GSGG and GGG plumes at background pressures of 4.2×10^{-2} mbar (a) and (b), and 1.2×10^{-5} mbar (i.e. "vacuum") (c) and (d). In case (b), the signal shown represents the GGG plume only (i.e. no GSGG plume in the chamber), to prevent the signal being disrupted by a previous plume. A sharp spike may be observed before the main pulse, labelled 'S' on figures 5.3(a) and 5.3(b). This serves as a zero time marker for measuring ion time-of-flight (TOF), and is due to electron emission from the probe caused by extreme ultraviolet emission of the ablation plasma during laser irradiation. In vacuum, each signal shows a single peak, rising to a maximum at a TOF of 4.4 µs after the ablation plasma front reaches the probe. In gas, the ion signal has two peaks: an attenuated peak around the same TOF as in vacuum and a second peak around 10 µs. This 'plume splitting' is a well-known feature of propagation of laser ablation plumes in a low pressure gas [152]: some plume ions arrive at the probe without collision with the gas, while the remainder collide and propagate within a blast wave which arrives at a later time.

Of primary interest is the change in propagation of the second plume as a function of delay between first and second laser plumes. Figure 5.4(a) shows the ion signal for both plumes for a time delay of 16 µs and figures 5.4(b-e) show signals for the second plume only at time delays of 40, 200, 400 and 1600 µs respectively. For a 16 µs delay, the two

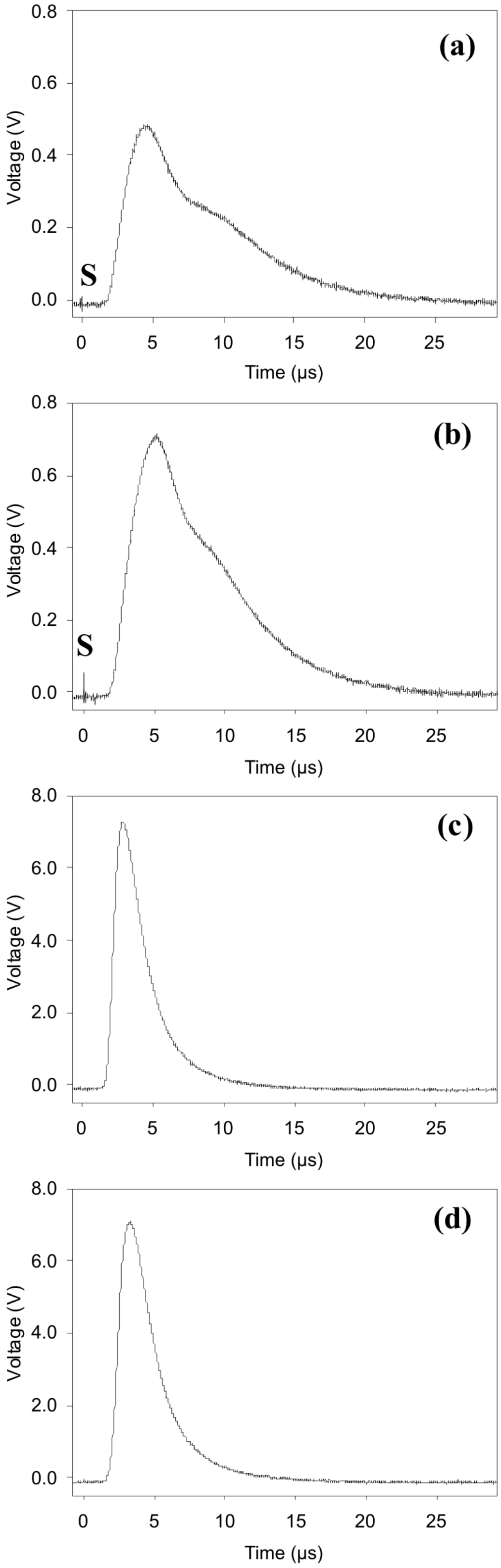

FIGURE 5.3: Ion probe signals for plumes 1 and 2: (a) GSGG plume signal, (b) GGG plume signal, both at background pressure of 4.2×10^{-2} mbar (c) GSGG plume signal, (d) GGG plume signal, both in 'vacuum' (background pressure = 1.2×10^{-5} mbar).

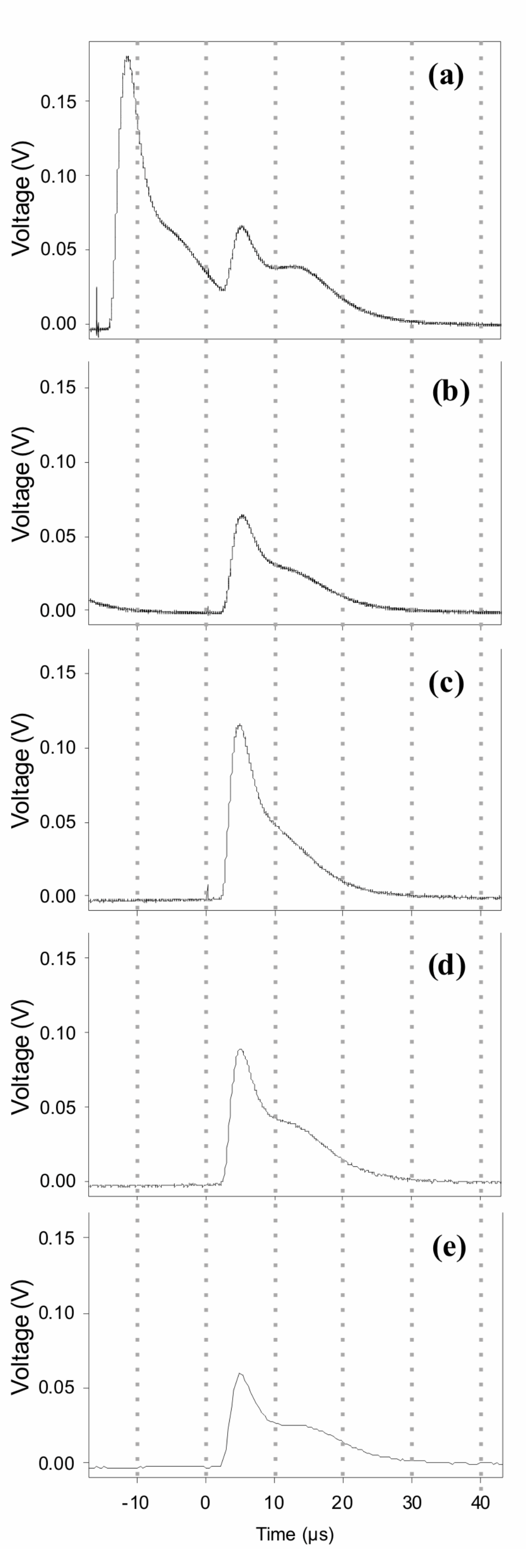

FIGURE 5.4: Examples of plume 2 ion probe signals for various delays: (a) 16, (b) 40, (c) 200, (d) 400, and (e) 1600 μs.

ion signals are partially overlapped and are similar to the addition of the signals from single plumes in gas. At 40 µs delay (figure 5.4(b)), the signal for the second plume is similar, but is now separate from the first plume signal. At a 200 µs delay, however, the signal for the second plume has changed: the first peak is less attenuated and the second peak is relatively weaker, appearing as though, in this delay regime, the second plume is propagating in a lower gas pressure. This effect, i.e. partial vacuum generation by the first plume sweeping away gas in front of the target-probe region, has been observed at higher gas pressure [169]. For delays beyond ∼400 µs, the signal of the second plume is again similar to that of the plume on its own in gas. It would appear, therefore, that for long delays the partial vacuum created by the first plume is refilled by gas flow before the second plume arrives.

The small decrease in lattice constant for delays beyond ∼200 µs coincides with the change of plume 2 ion signal from more vacuum-like to more gas-like. Ion bombardment of the growing film can cause in-plane compressive stress [153] by introducing interstitial defects (i.e. implantation of high energy ions into the lattice, see section 3.2.3), an effect also known as “atomic peening” [170]. The compressive stress manifests as a higher value of lattice constant normal to the film plane than would otherwise be expected. The higher value of lattice constant for delays between around 40 and 200 µs may therefore be due to higher energy ion bombardment of the growing film. For greater delays, the partial vacuum created by the first plume will be refilled and collisions with oxygen will slow down a significant fraction of the ions in the second plume.

At delays of ∼40 µs and below, the plumes appear more gas-like, and hence the same effect is unlikely to be causing the observed changes in lattice constant. However, the effect in play at this delay is not yet understood. While the charged parts of the plumes (detected by ion probe experiments) do not interact at this delay time, it is likely that some plume overlap is present when slower neutrals and particulates at the tail-end of plume 1 are considered. However, it is not known how such interaction would induce an increase in lattice constant, particularly given that a completely mixed film does not exhibit the same behaviour. EDX analysis has shown that composition does not change significantly for delays between ∼10 and ∼40 µs; another mechanism must be acting to increase the lattice constant of the film in this delay region.

For delays less than ∼10 µs, the arrival of the two ablation plumes at the substrate is substantially overlapped in time. It is not clear why this overlap should cause the observed compositional changes (see figure 5.2), although it is clear that lighter, less well-bound species are being preferentially lost from the film. It may be that the plumes are forcing a certain amount of gas into the region near the substrate, and the lightest of the cations are being preferentially scattered sideways or the least bound species in the growing film are desorbed from the surface. Further studies and/or modelling of the interaction between plumes, crystal nucleation and the impact of plume dynamics on garnet growth may help to shed some light on the various mechanisms involved.

Although not all mechanisms are well understood, in the broader context of minimising the effect of plume delay on a growing film in multi-beam PLD geometries two conclusions can be presented:

- Delay should be sufficiently long as to avoid plume interaction near the substrate,
- Delay of a following plume should be long enough to allow refilling of any partial vacuum created by the propagation of the earlier plume.

A delay greater than ∼1 ms is, for example, appropriate for the geometry and materials used in this experiment if additional stresses are to be avoided. It may also be possible, however, to use relative plume delay as a tool to tweak stress state/lattice constant of the film.

5.3 The shutter technique

5.3.1 Introduction

While it is possible to grow simple multilayer structures by manually blocking laser pulses, an automated approach is preferred in order to easily fabricate many-layered stacks, as well as more complicated chirped and apodised structures. The shutter technique, as outlined in section 4.3.1, was developed in order to meet this demand. Before growth of practical structures could be undertaken, however, an investigation into the growth of thin layer structures was carried out, which also served as a practical test of the shutter technique.

Some degree of mixing between layers in a multilayer system is unavoidable, due to indiffusion, particulates and the potential for island crystal growth. There is hence a minimum thickness of growth required to obtain distinct layers. An understanding of the transition from mixed to distinct layers is advantageous in terms of designing both multilayer and smoothly graded systems, where discrete and mixed layers are preferred respectively. Preliminary experiments were undertaken to determine this transition thickness. Following this, chirped superlattices were grown to test the efficacy of the shutter technique. XRD analysis was undertaken in collaboration with the Department of Physics, University of Warwick, and XRD modelling was carried out by Steven Huband and David Walker of the University of Warwick.

5.3.2 Experimental setup

Depositions were carried out in Chamber 2, with the addition of mechanical shutters as detailed in section 4.3.1. UV pulses from two frequency quadrupled Nd:YAG lasers were incident upon single-crystal targets of undoped GGG and (2 at.% Nd, 0.5 at.% Cr):GSGG. Growth rates could not be measured directly, but are known to be approximately equal for similar spot sizes and fluences (see section 5.2). Targets were rotated and target-substrate distance was maintained at ∼45 mm. The angle of plume incidence (i.e. tilt angle) was equal and constant for both targets. Growth was carried out in a background O_2 pressure of 4.0×10^{-2} mbar, and substrates were heated to ∼700 °C using a raster-scanned CO_2 laser.

Shutters were operated alternately, allowing bursts of pulses to deposit GGG and GSGG sequentially on single crystal (100) orientated (YAG) substrates of size 10×10×1 mm. The opening time for each shutter, and hence the number of shots per burst (i.e. thickness of material deposited), was varied for each sample.

Ten multilayer films were grown in total, with the numbers of shots per burst ranging from 5 to 5000 across the range of samples. Total deposition time in all but two cases was 30 minutes, yielding a total film thickness of ∼400 nm; the number of layers was hence different for each sample. For the 5000 shot sample, total deposition was 1 hour (∼800 nm total thickness) and for the 3500 shot sample, total deposition was 47 minutes (∼600 nm). Single-material films of both GGG and GSGG were also grown for comparison. Deposition conditions were the same as those for the multilayer samples, with a total deposition time in each case of 15 minutes. For samples with 5 to 1000 shots per layer, a Stanford signal generator programmed by hand was used in place of the PC to trigger the control boxes; all others used custom *LabVIEW* programs.

5.3.3 Analysis and simulation

Low resolution X-ray diffraction (XRD) was carried out using a Siemens D5000 powder diffractometer using Cu $K_{\alpha 1}$ and Cu $K_{\alpha 2}$ radiation. High-resolution XRD and X-ray reflectometry (XRR) were carried out using a Panalytical X'Pert Pro Materials Research diffractometer giving pure Cu $K_{\alpha 1}$ radiation, and a solid state PiXcel detector. For high resolution XRD only, the scans were optimized to the (400) Bragg peak of the YAG substrate. In the low resolution case, peak positions were normalized relative to the position of the underlying YAG substrate peak after measurements were taken. It should be noted that the instrumental functions of the two diffractometers are different, with low-resolution XRD resulting in spectra with much broader peaks.

XRD scans for the 5 shot to 500 shot cases were simulated using a web-based dynamical X-ray simulation program GID_sl [167]. Simulations were convoluted with the instrumental function, with background and noise added after the convolution had been performed. Inputs to the program included layer thickness and layer strain with respect to the substrate, quantified as the difference between the layer and substrate lattice parameters divided by the substrate lattice parameter da/a. These quantities were varied

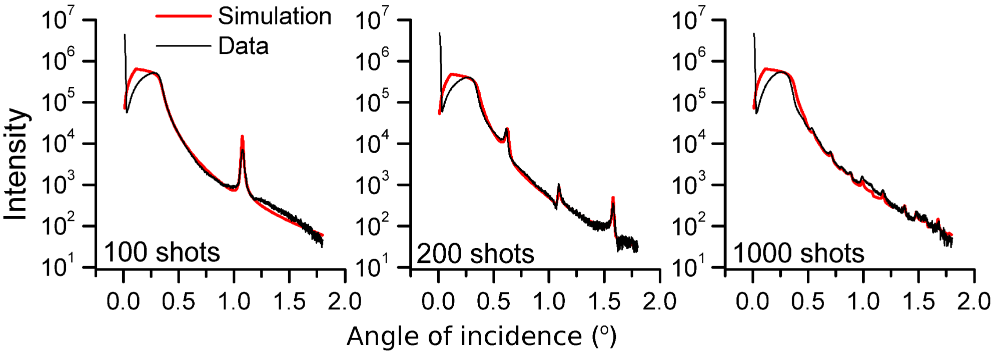

Figure 5.5: Examples of x-ray reflectivity measurements (black) and simulated fit (red)

to fit the positions and heights of the satellite peaks (by fitting overall periodicity and individual layer thicknesses respectively) and position of the 0^{th} order peak respectively. In this way, the experimental values for each compared sample were approximated. Spectra of the samples with 5 shots and 20 shots per layer consist of an average layer peak without any satellite peaks. To fit the data to these samples the GGG and GSGG layers were set to have the same lattice constants.

Reflectometry measurements were fitted using the Panalytical Reflectivity software. Crystal density, layer thickness and roughness were inputs to the program and, as above, were varied in order to achieve the best fit.

5.3.4 Results and discussion

All films grown were crystalline and optically clear. Although single-crystal growth was not explicitly verified, the presence of only those peaks exhibited by the substrate in the XRD spectra of single target films, and the good match between substrate and film peak shapes, suggest that the films grew in the epitaxial direction. Fitting of XRR data (examples illustrated in figure 5.5) suggests that GGG and GSGG layers have average roughnesses of 2.5 Å +0.8/-0.4 Å and 4 Å +2/-3 Å respectively, values that compare well to previously reported garnet multilayer PLD films [5]. The (400) 2θ peak of the underlying YAG substrate (at 29.74°) is clearly seen in all XRD data (see figure 5.6).

XRD scans show three regimes of behavior: single peak, superlattice and multilayer (see figure 5.6). The samples grown with 5 shots per burst, 500 shots per burst and 5000 shots per burst are examples of each regime respectively. There is also a superlattice-multilayer transition region, with samples of between 500 and 3500 shots per burst showing a combination of superlattice and multilayer behavior.

For the single peak cases (5 shots to 50/~0.1 to 1 nm thickness of material deposited per burst), a strong 2θ peak around 28.4° is observed. This peak position corresponds roughly to the average of the two component peaks, with the spectra consistent with those obtained for fully mixed films (such as those described in section 5.2).

For samples grown with 100 to 1000 shots per burst, satellite peaks can be observed either side of the main central peak. This is consistent with XRD spectra reported in the literature for superlattice structures (see section 2.3.3) i.e. a periodic array of discrete layers. The intensity of the central peak decreases as number of shots per burst increases from 100 to 1000. From 2500 shots per layer onwards, the central peak is not observed, satellite peaks become less significant and the pattern approaches that of the two component materials. Such a pattern, the two single peaks observed in the 5000 shots per burst case (∼100 nm per layer), approaches that exhibited by "thick" multilayers (<1 µm per layer) [10, 4].

The presence of satellite peaks in conjunction with a central peak is the result of the combination of two periodicities: that of the crystal lattice, and the "superperiodicity" of the superlattice. For layer thicknesses less than a threshold, the crystal can be thought of as a single crystal with periodic distortions [171]. Greater than this threshold, the X-rays no longer "see" the superperiodicity, and the crystal can no longer be thought of as an overall composite; this is the point at which a structure can be defined as a multilayer structure rather than a superlattice. An example of multilayer diffraction is given by Gazia et al [10]; here, distinct single peaks for each of the layers (2-3 µm thick) were observed. It would appear that for 1000 shots (i.e. around 20 nm), we begin to approach the transition period from superlattice to multilayer. The central, averaged peak is greatly reduced in intensity, and satellite peaks approaching the 2θ values of the individual components are much more pronounced (particularly the GGG, understandable as GGG growth rate is slightly higher).

The superlattice period P is given by the modified Bragg law (equation 4.3). The values obtained for the films grown are illustrated in table 5.1; average thickness of growth per shot is estimated to be ∼0.02 nm. As such, growth of one unit cell in thickness was achieved per ∼60 shots. A slight drop in growth rate was observed for the 2500 shots per layer case, likely due to target damage following extensive ablation. Single-target 2θ values were somewhat different from literature values: 28.08° for GSGG and 28.60° for GGG, corresponding to lattice parameters of 1.270 and 1.247 nm respectively. This is thought to be the result of a compositional deficiency of gallium, known to occur for PLD of Ga-containing garnets, as well as residual stress in the lattice.

The central peak positions observed do not correspond exactly to the mid point between the GGG and GSGG peak positions, due to slight differences in the growth rates of GGG and GSGG. Layer thickness values were obtained by fitting XRR peaks in the 100, 200 and 1000 shot cases (see figure 5.5), and suggest that the ratio of GSGG to GGG is approximately 1:1.2. This is not unreasonable, given that growth rates were not optimized.

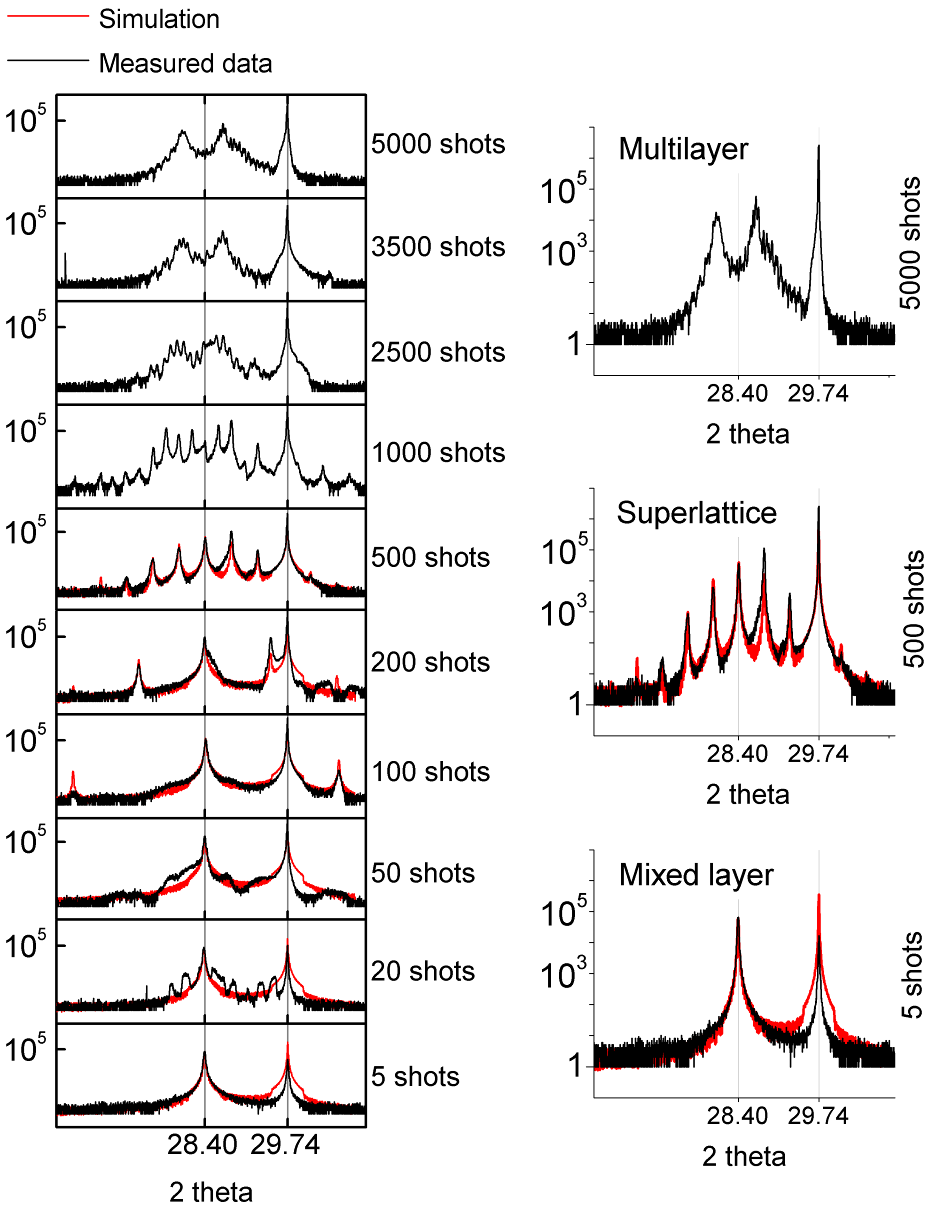

FIGURE 5.6: High resolution logarithmic X-ray diffraction data (black) and simulation (red) for structures fabricated via alternating pulse bursts per target. The number of shots per burst on each target ranges from 5 to 5000 over the range of samples.

	Measured parameters		*Simulated parameters*			
Shots/ layer	**Superlattice period (nm)**	**Growth/ shot (nm)**	**Superlattice period (nm)**	**Growth/ shot (nm)**	**GGG** *da/a*	**GSGG** *da/a*
5	-	-	0.22	0.022	0.046	0.046
20	-	-	0.98	0.025	0.047	0.047
50	-	-	2.18	0.022	0.034	0.058
100	4.2	0.021	4.24	0.021	0.034	0.058
200	8.5	0.021	8.54	0.021	0.035	0.058
500	21	0.021	21.5	0.022	0.039	0.058
1000	41	0.021	-	-	-	-
2500	84	0.017	-	-	-	-

Table 5.1: Period and layer quality of superlattices

The fitting of XRD data gives further indication of strain and growth rates (see table 5.1). Growth per shot values are in good agreement with those measured. Calculated GGG *da/a* decreases by around 15% over the 100 to 500 shots cases towards the single-material value of 0.039, suggesting that strain marginally decreases. This change, along with the effect of different sources of stress in combination has not however been examined experimentally.

An anomalous XRD 2θ peak around 30.5° can be seen in the 50 and 200 shot cases. A number of overlaying peaks are also observed in the 20 shot case, and peak broadening in the 50 shot case. The cause of these anomalies has not been determined. However, they are inconsistent with both modelling and low-resolution XRD, and are hence unlikely to be due to the overall multilayer structure.

In general, we see evidence of layering in structures where deposition thickness per pulse burst is 2 nm or more, but mixed-crystal behavior where this thickness is 1 nm or less, i.e. less than a unit cell. The fact that we see evidence of layering right down to the unit cell level suggests that the effect of interdiffusion is limited (even at substrate temperatures of ~700 °C) and any island growth may not be significant at this scale. However, some level of atomic interdiffusion is expected, as the number of shots per layer does not correspond to a complete unit cell e.g. in the 100 shots per layer case. It may be possible to encourage 2D monolayer growth of different materials, obtaining even more distinct layers, by utilising the pulsed laser interval deposition (PLID) approach[1] developed by Blank et al [172].

It may, however, be the case that layering is present even at thicknesses below one unit cell. XRD simulations of the 50 shot case (layer thickness ~1 nm) show that this single-peak pattern would be practically observed even for a layered material; similarly, XRR simulation suggests that a peak at around 2° incident angle would be expected for a

---

[1] A single complete monolayer is deposited in a precise number of shots, following which there is a delay interval in which no deposition occurs. This allows the film to organise into a single layer, rather than encouraging island growth.

layered structure, but such a peak would not be discernable from noise in the current setup. The garnet crystal structure, containing 8 planes within the unit cell, is complex enough to allow the possibility of sub-unit cell layering. Similarly, although errors are relatively large due to difficulties in curve fitting, roughness values obtained lie below half a unit cell, and hence roughness is likely not high enough to completely remove layer definition at this scale.

This potential for layering must be considered in any application where such length scales are significant, and in the context of growing "true" multilayer and graded structures, simultaneous deposition (i.e. maximum of 1 shot alternating) is recommended if a mixed layer is desired. However, for many of the applications of interest (Bragg reflectors, planar waveguides etc.) it is unlikely that variation on such a small scale will be significant. In such cases, thickness grown per pulse burst could practically be increased to a few unit cells. It should be noted that significant interdiffusion between garnets (yttrium iron garnet and GGG) has been observed previously for superlattice growth at substrate temperatures of ∼750 °C and above [5]. While the temperature above which interdiffusion is observed is likely to vary somewhat depending on the materials, high temperatures may prove a tool for smoothing layers via deliberately induced interdiffusion, assuming that such high temperature growth can still be achieved.

5.3.5 Chirped structures

Having achieved simple multilayer growth, more sophisticated structures were fabricated as an effective demonstration of the capabilities of the shutter technique.

These samples were grown using the same setup as the simple multilayers, and again consist of alternating layers of GGG and GSGG. Unlike the simple multilayers, however, the periodicity of the samples varies across the structure. Each chirped structure can be considered as a series of multilayers ("sections") grown on top of one another. Periodicity of a single section is constant (i.e. layers are of approximately equal thickness) but different from that of other sections. Two configurations were grown:

- **Structure 1: Simple chirp** Thirteen sections, each consisting of a pair of GGG and GSGG layers. The first section was grown with pulse bursts of 700 shots on each target (i.e. 700 shots per layer); the second with 650 shots per burst, the third with 600 shots per burst and so on in steps of 50, with layers in the final sections grown with 100 shots per burst.
- **Structure 2: Compensated chirp** Consisting of nine sections, the number of layers in each section was varied as illustrated in figure 5.7, so that each section was grown using ∼6000 shots in total. This means that each section has approximately equal thickness, and hence scatters an equal contribution of X-rays (ignoring attenuation).

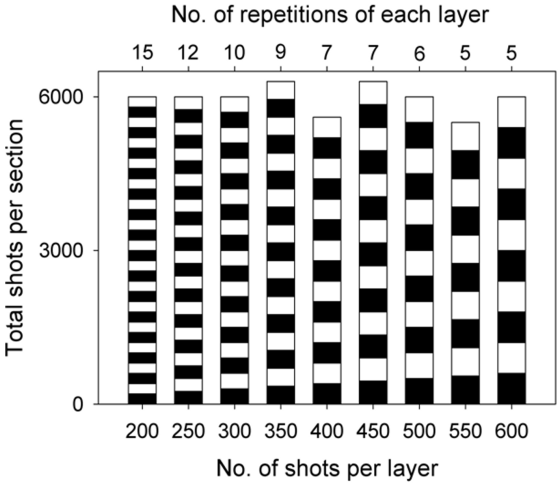

Figure 5.7: Diagram showing the number of repetitions of each layer in each component superlattice section within the compensated chirped structure. Layers of GGG and GSGG are represented by black and white areas respectively.

The thickest layers for chirped samples were grown with pulse bursts of 700 shots per layer, corresponding to ~15 nm thick layers. Superlattice XRD pattern behavior is therefore expected and indeed, is observed. Low-resolution XRD spectra for both chirped samples exhibit satellite peaks, and can be considered as a superposition of the individual spectra for each of the component superlattice sections (see figure 5.8). In both cases, structures are crystalline, with the width of central film peaks matching that of the substrate. For the compensated chirp structure (sample 2), there is a greater contribution from each of the components, due to their increased thicknesses. This was as expected, and served as further proof of the potential for control over the design and growth of more sophisticated structures.

5.4 Conclusions

The relative delay between plasma plumes in PLD was found to have an impact on the lattice constant of a film grown by multi-beam PLD. The first plume sweeps out an area of gas, leaving a partial vacuum that takes some hundreds of microseconds to infill. In the case of the materials and conditions used (GGG and GSGG), this characteristic infilling time was ~400 µs. If the second plume follows within this time it travels through an effectively lower deposition pressure, leading to greater ion bombardment of the growing film. This results in additional strain in the film which manifests as a larger lattice constant. At delays between 10 and 40 µs another mechanism not as yet understood serves to also increase lattice constant. Plume delay may hence be used as a tool to finely tune the strain/lattice constant in a growing film.

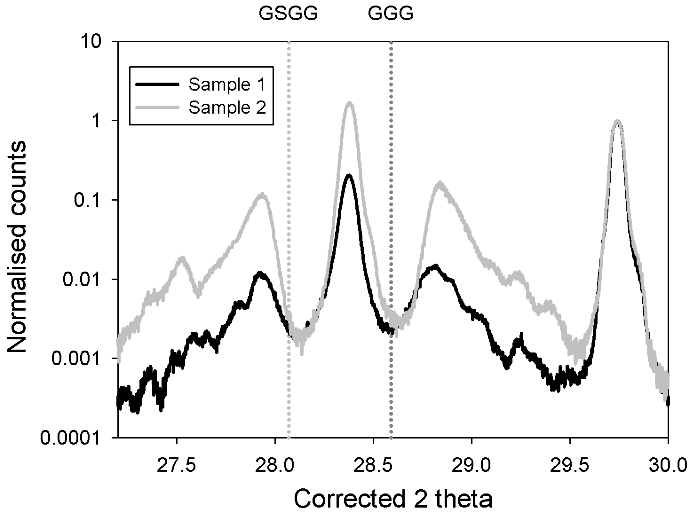

FIGURE 5.8: Low resolution XRD data for two chirped multilayer structures. Sample 1 (simple chirp) is shown in black, sample 2 (compensated chirp) is in grey.The peak at 29.74° is that of the underlying YAG substrate.

A second, more versatile tool has also been implemented in the form of the shutter technique. This comprises mechanical blockers placed in the path of each beam, the opening and closing times of which are controlled via control boxes or via *LabVIEW* programs. Mixed layers, superlattices, multilayers and chirped structures with various layer thicknesses have been grown to demonstrate the efficacy of the technique. Having developed and tested the technique for crystalline multilayer growth, the stage has been set for growth of functional devices in the form of Bragg stacks.

x

Chapter 6

Bragg reflectors

6.1 Introduction

Having proven the efficacy of the shutter technique for multilayer growth, functional devices in the form of Bragg stacks were fabricated. Crystalline Bragg structures have a range of exciting potential applications: garnet crystals have high melting points (YAG melts at >1900 °C, for example) and high thermal conductivities and damage thresholds compared to many amorphous materials. Such structures may therefore be suitable for high temperature sensing applications and custom high-power laser mirror applications, with multi-beam PLD potentially a powerful, versatile tool for their fabrication.

The main contributions detailed in this chapter are as follows:

- The first demonstration of growth of Bragg reflectors by multi-beam, multi-target PLD;
- The first known example of a PLD-grown Bragg reflector with more than 45 layers
- The first known example of grating strength apodisation of crystal Bragg stacks;
- The first demonstration of the suitability of PLD-grown crystalline Bragg reflectors for high temperature and high power laser applications.

6.2 Experimental setup

6.2.1 Depositions

A number of designs were attempted, with all samples bar the apodised example (see section 6.5) grown automatically using the custom *LabVIEW* program mentioned in

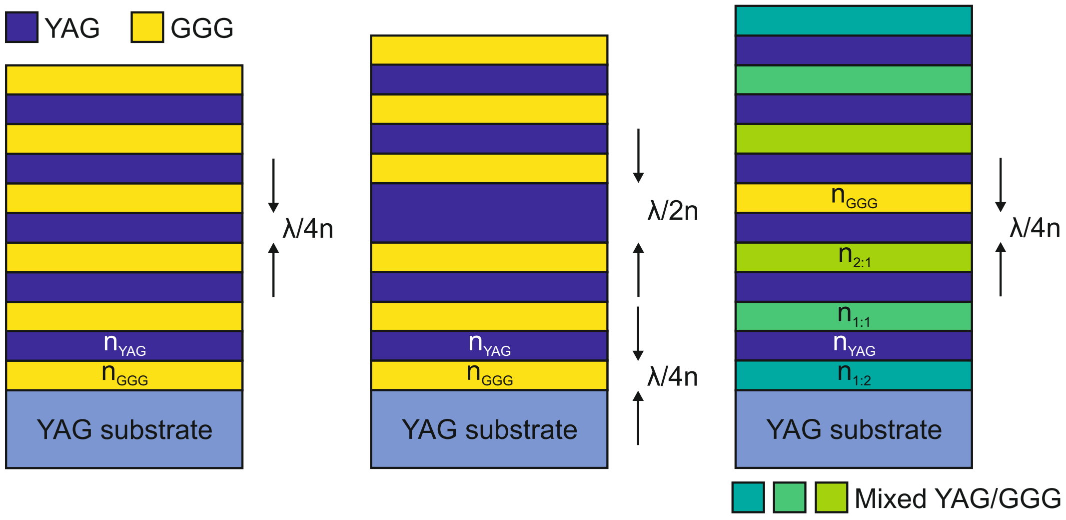

(a) Quarter-wave Bragg stack (b) π phase-shifted Bragg stack (c) Grating strength apodised Bragg stack

FIGURE 6.1: Diagrams representing various design of Bragg stack.

chapter 5. Simple quarter-wave Bragg reflectors consisted of alternating layers of thickness $\lambda/4n$, where n is the refractive index of the layer (see figure 6.1(a)). π phase-shifted structures, described in figure 6.1(b), were similar with a central layer of thickness $\lambda/2n$. A grating strength apodised sample was also grown, the concept of which is illustrated in figure 6.1(c). Plumes were combined to obtain layers of mixed YAG/GGG in varying ratios with a custom refractive index. Further details of the apodised design and growth process are detailed in section 6.5.

All samples described here were composed of YAG and GGG layers grown on single-crystal YAG substrates of size 10 × 10 × 1 mm^3, polished on both sides. Rather than grow each layer under the respective materials' optimum conditions, a compromised common set of deposition conditions was chosen for ease of fabrication and to allow mixed layer growth for grating strength apodisation. Substrates were heated via CO_2 laser to temperatures of ∼750 °C to obtain single-phase crystalline growth. Deposition took place in an O_2 background gas pressure of 1×10^{-2} mbar and target-substrate distance was ∼40 mm. An excimer laser of fluence ∼2.6 Jcm^{-2} and wavelength 248 nm ablated a single-crystal YAG target, while a frequency quadrupled Nd:YAG laser of fluence ∼2.5 Jcm^{-2} ablated a single-crystal GGG target.

As a consequence of these compromised deposition conditions, layers (particularly of GGG) exhibited stoichiometry, and hence refractive index, far from bulk values (see table 6.1). Pressure was much lower and substrate temperature slightly higher than for optimum GGG growth conditions, leading to a substantial decrease in gallium content relative to bulk: the crystal formula of a representative test film, for example, was $Gd_{5.16}Ga_{2.86}O_{12}$ compared to $Gd_3Ga_5O_{12}$ for bulk. A decrease in aluminium content relative to bulk in the case of YAG was also observed. XRD and EDX data for two

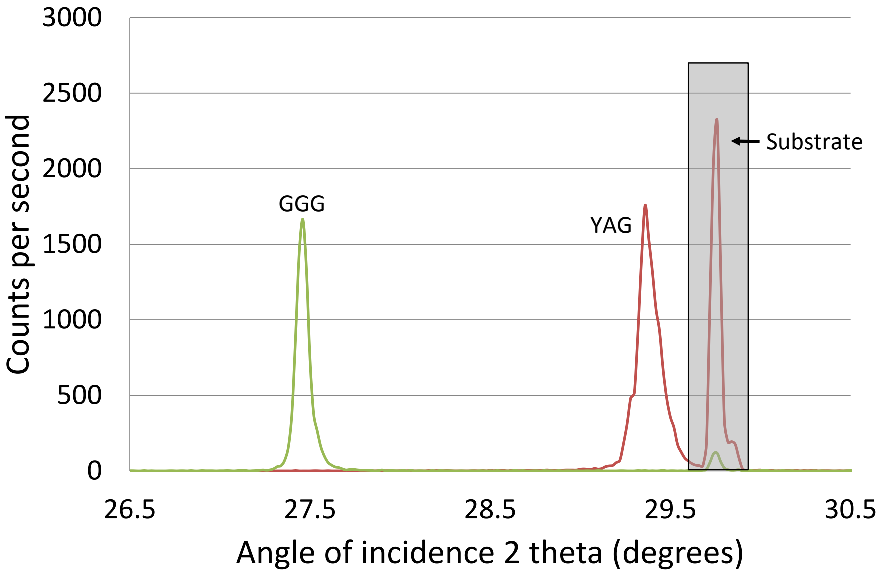

FIGURE 6.2: XRD spectra of GGG (green) and YAG (red) test films, normalised to the underlying YAG substrate peak.

example single-material test films are given in table 6.1, with values for bulk crystal given for comparison. XRD spectra are displayed in figure 6.2. While these conditions resulted in non-stoichiometric growth, growth at higher pressures was not advisable due to the higher number of particulates that are observed for YAG growth at pressures of 2×10^{-2} mbar and above. Growth at much lower pressures was also to be avoided as it can lead to coating of chamber windows, and attempts to change conditions to the optimum for each layer during deposition resulted in a prohibitively long fabrication time.

GGG and YAG were chosen for these experiments as both are garnets known to grow well as multilayers, but which have a relatively large refractive index contrast (n_{YAG} and n_{GGG} are nominally 1.82 and 1.96 respectively). Multiple single-crystal targets were also readily available. In each case, stacks consisted of an odd number of layers with GGG layers first and last. The reason for this was twofold: firstly, to obtain as large an index contrast as possible between the first layer and substrate and secondly, to remove any colour or opacity from the topmost YAG layer. As detailed in section 3.2.3, growth of YAG on a deposited GGG layer without subsequent overgrowth or annealing has been observed to result in a frosty brown film.

A model of quarter wave and π shifted Bragg structures was created in *MATLAB* by Michalis Zervas (ORC) (see appendix B for an overview of operation). This model incorporates chirp (e.g. due to a linear drop in laser ablation energy over time) and loss, in the latter case by introducing an attenuation term. This term does not discriminate between absorption and scattering loss (e.g. due to particulates), although with undoped materials and total structure thicknesses less than 20 μm thick, it is assumed that absorption is negligible.

	Bulk YAG	**Test YAG**	**Bulk GGG**	**Test GGG**
2θ (°)	29.76	29.36	28.84	27.46
Lattice constant (Å)	12.006	12.158	12.383	12.982
Crystal formula	$Y_3Al_5O_{12}$	$Y_{3.61}Al_{4.39}O_{12}$	$Gd_3Ga_5O_{12}$	$Gd_{5.16}Ga_{2.86}O_{12}$

Table 6.1: Crystal data of two test films grown under conditions used for Bragg stack deposition. 2θ and lattice constant values were obtained via XRD, crystal formulae computed from EDX data. Textbook values for bulk crystal are shown for comparison.

6.2.2 Measurement techniques

6.2.2.1 Thickness estimates

With no in situ diagnostics to measure thickness during deposition, deposition rates were inferred from analysis of test films. A very rough estimate of physical deposition rate could be gained by stylus profiling of pre-measured substrates; however, the values were not precise enough to be of great use (as in section 6.3.1). Analysis of XRD spectra of two YAG/GGG superlattices grown under the desired condition gave a more specific indication of thickness. However, given that refractive indices could not be measured directly, the approach taken for films of designed peak reflection wavelength was to estimate optical thickness as a single value via spectrophotometry of test films.

Spectrophotometry data of single-material YAG and GGG test films are shown in figure 6.3. A value for optical thickness can be obtained by comparing positions of interference peaks. Assuming no dispersion between adjacent peaks (i.e. the refractive index is the same for both peaks)[1], the optical thickness (product of physical thickness d and refractive index n) is give by Equation 6.1:

$$nd = \frac{\lambda_1 \lambda_2}{2(\lambda_1 - \lambda_2)} \tag{6.1}$$

Further analysis of spectrometry data can allow values of refractive index and physical thickness to be obtained separately [174]. However, doing so requires the peak and trough envelopes of the transmission spectrum to be well defined, something that was not the case in these experiments (as can be seen in figure 6.3). Useful separate values of index and physical thickness could hence not be determined using this method.

As the refractive index contrast between the film and substrate is so small, particularly in the case of the YAG film, the peaks are often not well defined, and obscured by noise. Test films were grown on glass substrates to obtain more defined peaks (see figure 6.4) and hence allow calculation of optical thickness values with a much smaller error than previously. Substrates were heated during deposition, and it was thought that the

---

[1] The difference in the index of bulk YAG between 900 and 1000 nm is ~0.1% [173], hence this assumption is valid.

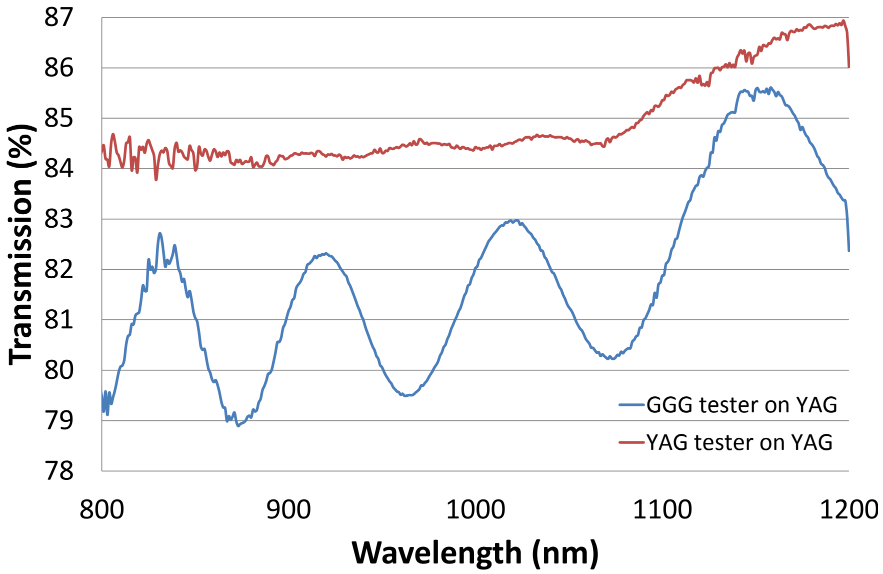

FIGURE 6.3: Transmission spectra of YAG and GGG example test films, both on YAG substrates.

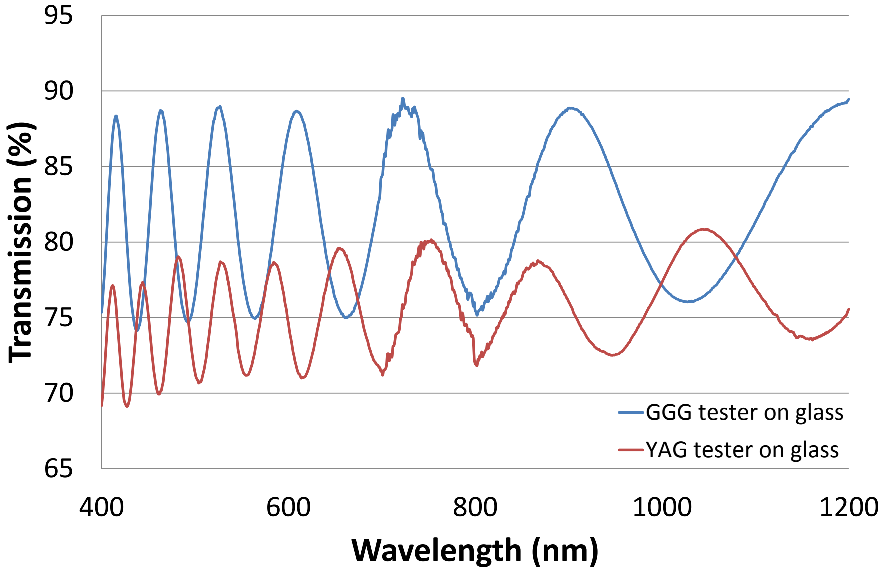

FIGURE 6.4: Transmission spectra of YAG and GGG example test films, both on glass substrates.

film might grow polycrystalline, giving a refractive index value similar to that obtained by growth on crystal. The values obtained, however, differed substantially from those obtained from both test films grown on crystal and the values inferred from test gratings grown, due to the lower density of the film, which may have been amorphous. Instead, it was necessary to take an average of the optical thickness values of a number of test gratings grown under nominally the same conditions on crystal substrates.

6.2.2.2 Transmission and reflection measurements

Three instruments were used to determine the transmission/reflection characteristics of the stacks. The most simple and readily available was a Varian Cary 500 white light spectrophotometer, used in transmission mode with a circular aperture of ~1 mm. Data from the Varian spectrophotometer was compared with that from a CRAIC 20/20 PV microscope-coupled spectrometer, used in reflection mode with a 40 µm × 40 µm square aperture. The latter measures the reflectivity of a sample relative to a reference mirror, which is itself calibrated via two other mirrors.

For reflectivity values less than 90%, data from the two spectrometers is similar around the area of interest (example data shown in figure 6.5). It is hence assumed that:

- Absorption and scattering are unlikely to be significant, and hence it can be assumed that $R = 1 - T$, where R and T are reflection and transmission intensity respectively. This is as expected, as films are only microns thick and contain no dopants.
- Any variations over a 40 µm × 40 µm square are similar to variations over a circle of 1 mm diameter.

The same consistency is not observed for reflectivity values above ~95%. This is likely due to errors in reflection measurements, however, and not a result of errors in transmission spectrometry: at values of close to 100% the error in reflectivity measurements due to noise or inaccurate calibration of the reference mirror become prohibitively large.There was also a problem with the microscope-coupled detector response in the region 650-950 nm, as can be seen in figure 6.5. As a result, transmission data has been presented in this thesis rather than reflectivity data obtained using the microscope-coupled spectrometer.

In the case of π shifted structures, where it was suspected that the short coherence length of white light might be preventing features from being observed, a transmission spectrum was also obtained using a tunable Ti:sapphire laser. These measurements were collected with the help of Amol Choudhary (ORC).

6.3 Simple Bragg stacks

6.3.1 Preliminary experiments

Preliminary growth of quarter-wave Bragg stacks was undertaken to determine whether growth of Bragg structures was viable. Transmission spectra of examples with 17, 65 and 121 layers are shown in figure 6.6. For these initial experiments, optical growth rates

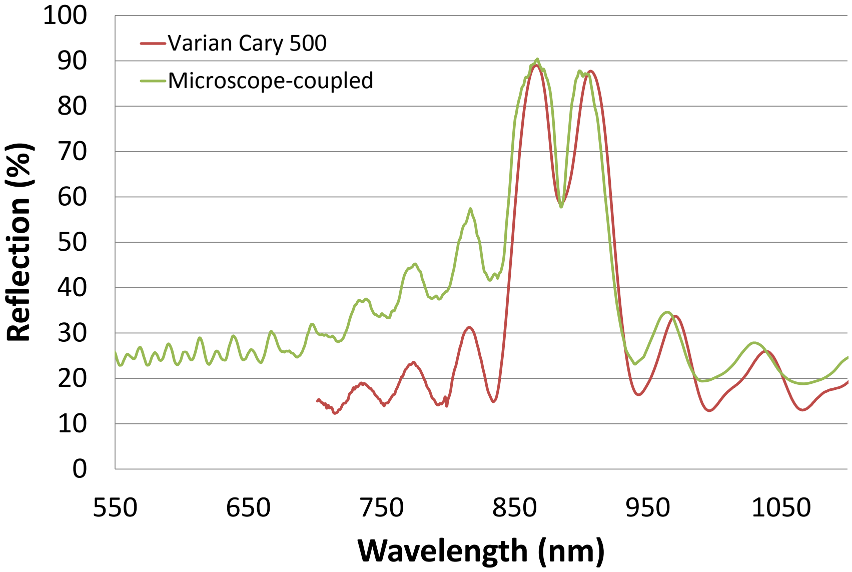

FIGURE 6.5: Reflection data for a π shifted Bragg stack (see section 6.4). In the case of the Varian Cary 500 spectrometer, reflectivity values are assumed to be 1-transmission values. Peak positions are likely slightly different due to the slightly different mounting positions (a consequence of sample curvature).

were not estimated via spectrometry of test films as described in section 6.2.2.1, rather refractive indices were assumed and physical growth rates estimated from surface profile measurements of test materials. As a result, optical growth rates for each material were not equal, as evinced by the varying side band heights. Peak reflection (i.e. 1-transmission) values were ∼41%, ∼58% and ∼97% respectively.

During the growth of such samples, some mixing of plumes (5-10 shots, variable) occurred due to the different processing times of the shutter control boxes. This was prevented by introducing a delay of 1-1.5 seconds between the closing of one shutter and the opening of another into the shutter control program. Any interaction between plumes could have led to the formation of a mixed layer with slightly different stress state or composition from the average of YAG and GGG (see chapter 5), and was hence to be avoided.

As expected, samples exhibited some curvature as a result of the deposition process. Transmission spectra peak height and definition can hence vary depending on the size of aperture used, as demonstrated in figure 6.7. It should be noted, however, that any curvature is negligible for interrogating beams of less than 1 mm, as demonstrated by the spectrometer comparison described in section 6.2.2.2. The sample curvature, though not deliberately introduced, renders the stacks tunable by position. More detail is given in section 6.6.2.

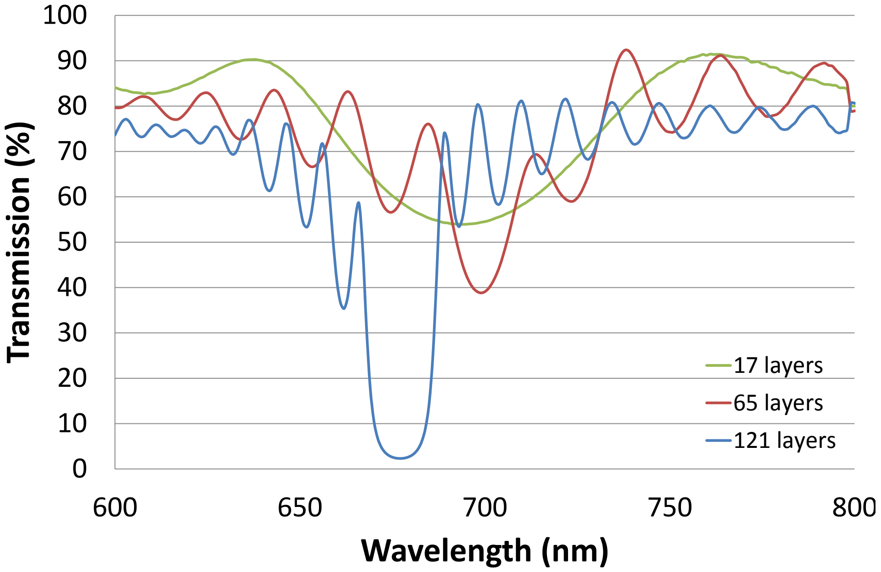

FIGURE 6.6: Transmission spectra of three prototype quarter-wave Bragg stacks with 17, 65 and 121 alternating layers of YAG and GGG.

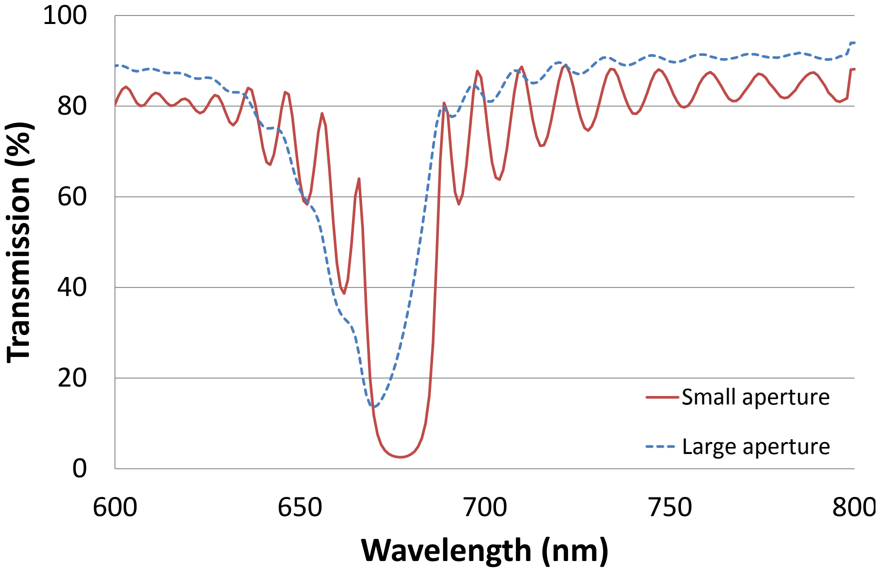

FIGURE 6.7: Transmission spectra of a 121 layer stack as obtained using small and large apertures (~1 mm and ~5 mm diameters respectively). Peak definition and height is lost as a result of the sample curvature.

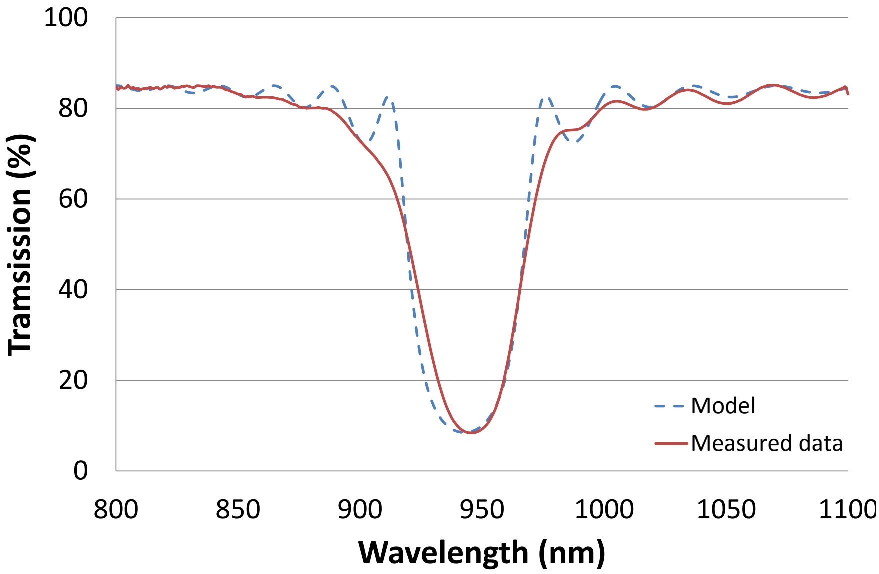

Figure 6.8: Transmission spectrum of quarter-wave Bragg stack with 67 alternating layers of GGG and YAG designed for 946 nm peak wavelength. The model (shown for comparison) suggests that while a small amount of chirping (linear index variation of <1%) may have occurred, the rates of chirp are likely different for each material.

6.3.2 Reflectors at specific design wavelengths

A number of attempts were made to grow quarter-wave (and later π shifted and apodised) stacks at specified wavelengths. Unlike the preliminary experiments described above, these samples were grown using estimates based on spectrometry of test films, as outlined in section 6.2.2.1. It was found that resultant peak reflection wavelengths generally did not exactly match the design in the centre of the sample. However, the results were close enough that, due to the tunability of the gratings (see section 6.6.2), the desired peak wavelength could be achieved (without significant loss in reflection) by changing the position of the interrogating spectrometer beam on the substrate.

The transmission spectrum of an example of a quarter-wave Bragg stack with 67 layers and a design peak wavelength of 946 nm (of interest for e.g. reflection of the quasi-3 level Nd:YAG laser transition) is shown in figure 6.8, along with an approximate model for comparison. The model assumes that there is no absorption or scattering loss, a slight linear chirp (a decrease in thickness of ~1% over the course of deposition) and refractive indices of ~1.9 and ~2.0 for YAG and GGG layers respectively. The measured peak is not completely symmetrical and hence cannot be fitted perfectly. It may be the case that chirp is not linear, for example if chirp rates of the two materials are different (plausible due to different laser energy drift rates, different target degradation rates etc.). Peak definition is also poorer, something that may be due to fluctuations in layer thickness due to corresponding fluctuations in pressure or laser energy over the deposition. These factors cannot, however, be modelled as yet.

Figure 6.9 shows the transmission spectrum of a quarter-wave Bragg stack with 145 alternating layers (red line) again designed to exhibit a peak wavelength at 946 nm. Transmission is <1%, corresponding to a peak reflection of >99%. The expected peak shape for an ideal quarter-wave stack, shown by the green dotted line, is much more square than the data observed. A much closer match is found by introducing a linear chirp term into the model (blue dashed line). This term implies that layer thicknesses decreases linearly by around 2% over the course of the ~6 hour deposition. If true, such an effect is most likely due to a downward drift in ablating laser energy such as has been observed previously for both lasers. Attempts were made once per hour during deposition to compensate for drift; any chirp is hence likely to be stepped rather than purely linear. However, whilst relatively easy to correct in the case of the excimer laser, energy drift cannot be easily corrected in the case of Nd:YAG lasers due to the difficulty in accurately retuning the harmonic crystals.

Again, modelling of the data suggests absorption or scattering loss is negligible and that the refractive indices of YAG and GGG layers are ~1.9 and ~2.0 respectively (these values will be assumed later in section 6.5). Sub-peaks such as those shown by the model cannot be observed easily in the measured data, and where small peaks can be seen (i.e. 1000-1100 nm region) the peak positions do not match those of the model. This latter may be the result of different chirping for each material or fluctuations in the growth rates, factors that the model does not take into account. It should be noted that the thickness of the sample overall (~17 μm) is greater than the coherence length of the white light, an effect that was found to be significant in the case of the π shifted structures described in section 6.4. Any effect of this loss of coherence on the spectrum, however, could not be confirmed (e.g. via Ti:sapphire laser transmission experiments) due to time constraints.

XRD spectra of the 67 and 145 layer stacks mentioned above are displayed in figure 6.10. As expected, only peaks corresponding to the (400) and (800) peaks of YAG and GGG can be observed, showing that the materials grew as epitaxially-orientated crystal.

6.4 π phase-shifted reflector

The design of the π shifted stacks grown followed that illustrated in figure 6.1(b), consisting of two 21 layer stacks of alternating YAG and GGG either side of a YAG layer of optical thickness $\lambda/2$ (i.e. physical thickness $\lambda/2n$). In an ideal structure, reflections from each stack will cancel out resulting in 0% reflection in the centre of an otherwise standard quarter-wave reflection peak (see chapter 3). If there is variation in the layer thicknesses of the stacks either side, complete cancellation will not take place and some residual reflection will still occur. If the optical thickness of the central YAG layer is not $\lambda/2$, the reflection dip will shift away from the centre of the main reflection peak.

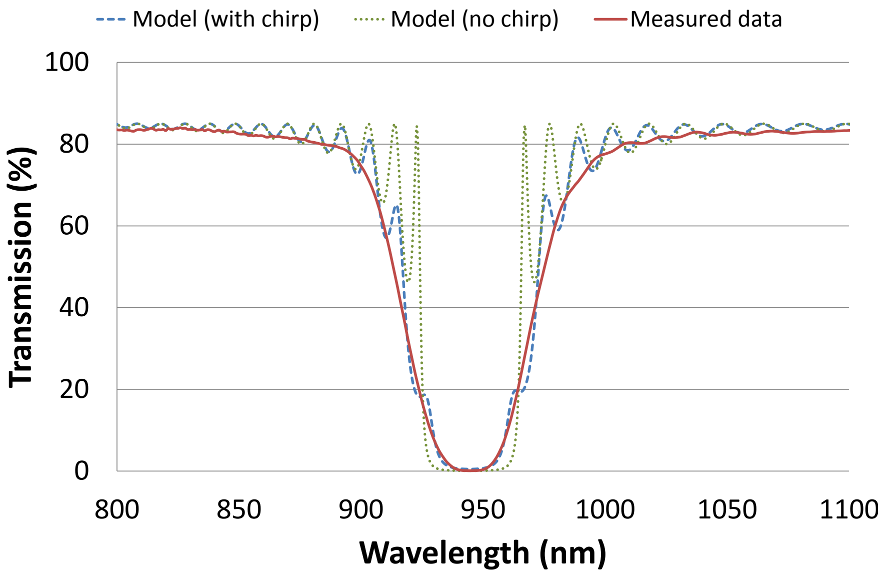

FIGURE 6.9: Transmission spectrum of quarter-wave Bragg stack with 145 alternating layers of GGG and YAG designed for 946 nm peak wavelength. Two modelled versions are shown for comparison, which suggest that some chirping may have occurred.

Two attempts at growth of a π shifted structure have been made, spectrometer data for both of which are displayed in figure 6.11. The first example (stack 1, "high loss") was deposited under the conditions described in section 6.2. A transmission increase of $\sim$20% can be observed in the main reflection peak/transmission trough, indicating that there was significant variation in the layer thicknesses of the stacks either side. The reflection dip/transmission increase can be observed in the centre of the main transmission peak, however (i.e. it hasn't been shifted), suggesting that the physical thickness of the central YAG layer was indeed $\lambda/2n$.

A "low loss" version (stack 2) was subsequently attempted. In this case, the laser-target angle of incidence was kept constant rather than varied, something that had been found previously to reduce the number of particulates in the film (see section 3.2.6). All other conditions were kept the same, and hence other fluctuations (pressure, laser energy etc.) that could not be controlled remained as a source of thickness variation. The shift in main peak position and the dramatic decrease in overall transmission suggests that one or both of the growth rates had changed, and that the optical thicknesses of the layers comprising the stacks either side of the central YAG layer of the previous sample had not both been equal to $\lambda/4n$. A $\sim$30% increase in transmission in the centre of the peak was observed, indicating that while tilt program-induced particulates influenced the layer thickness variation they were not the only significant factor. The sample's XRD spectrum, demonstrating the epitaxially-orientated crystal growth, is shown in figure 6.12.

After deposition of stack 2, it was posited that at around 8 µm thick, the path of light through the structure may have become longer than the coherence of the white light from

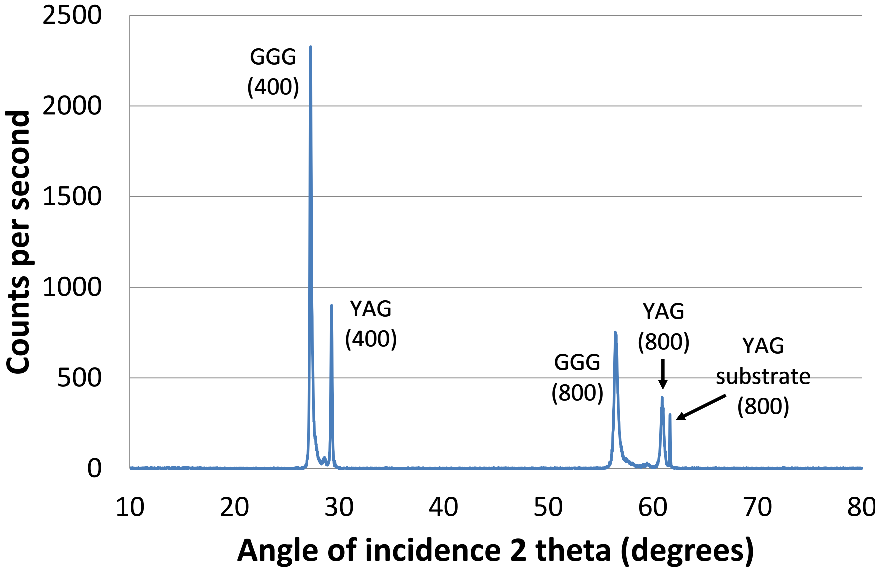

(a) 67 layer stack.

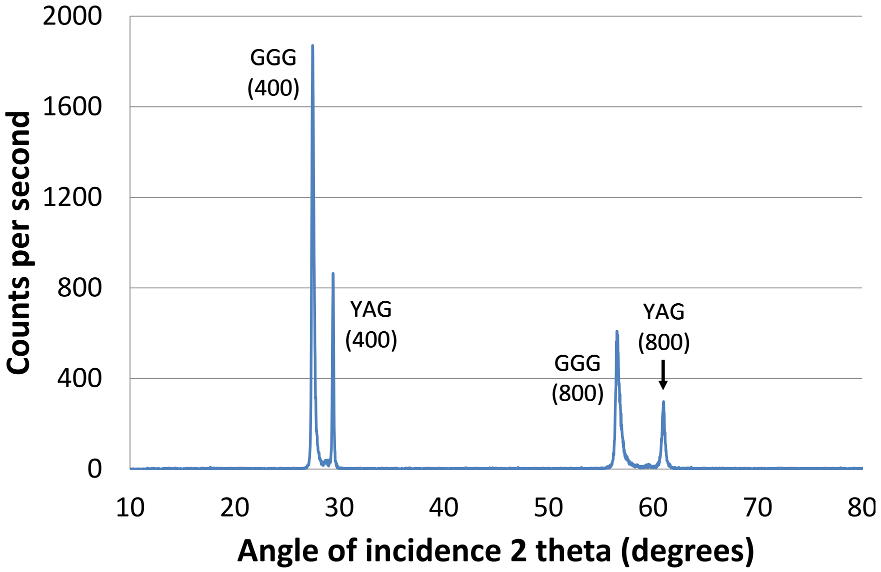

(b) 145 layer stack (data not normalised as no substrate peaks observed).

FIGURE 6.10: XRD spectrum of quarter-wave Bragg stacks. (400) and (800) peaks for GGG and YAG layers can be observed, showing that crystal growth was in the epitaxial direction.

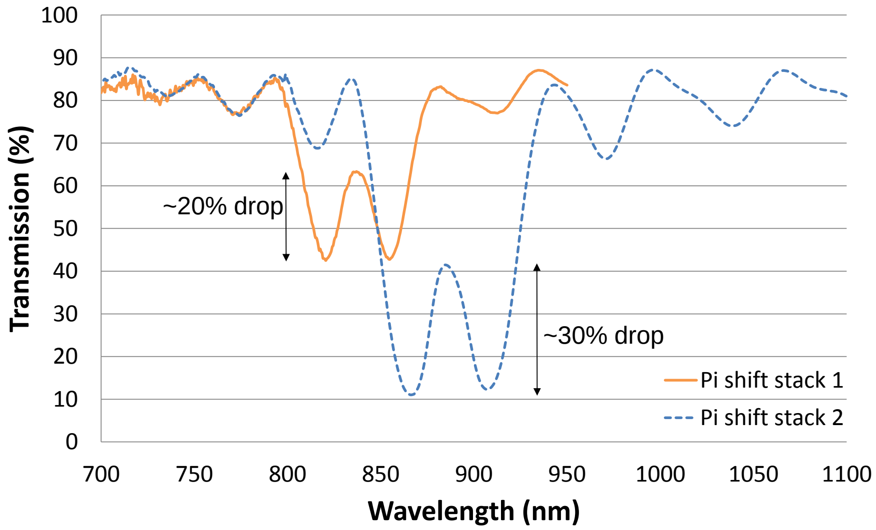

FIGURE 6.11: Transmission spectra of π shifted stacks 1 ("high loss") and 2 ("low" loss).

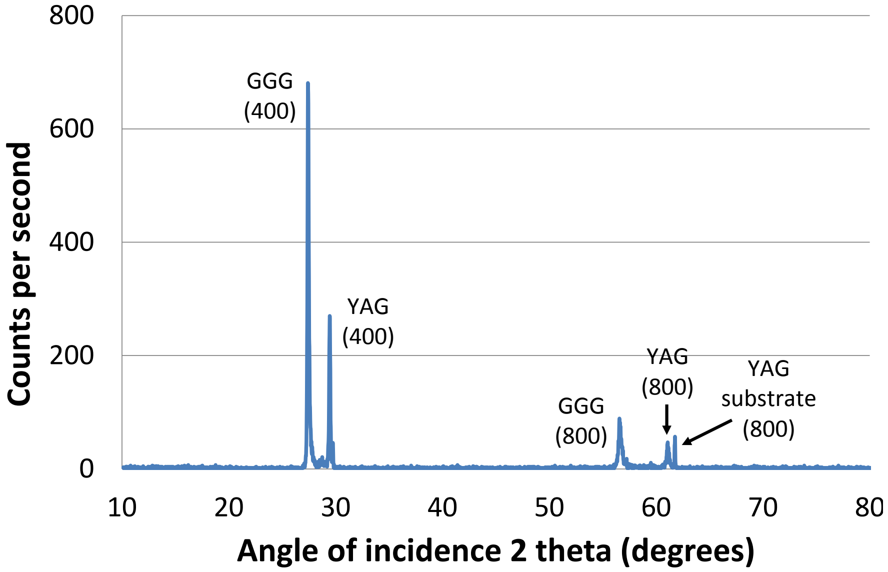

FIGURE 6.12: XRD spectrum of π shifted stack 2. (400) and (800) peaks for GGG and YAG layers can be observed, showing that crystal growth was in the epitaxial direction.

the spectrophotometer (∼1 µm). In such a situation the stack could be considered as a spacer layer with asymmetric mirrors (i.e. different reflectivity) either side, a geometry that would result in the smaller than expected increase in transmission in the centre of the main transmission trough[2]. To test this, a transmission spectrum was taken using light from a tunable Ti:sapphire laser (shown in figure 6.13). Due to time constraints and the limited wavelengths available, measurements focussed on the area of particular interest at the centre of the main transmission peak. A decrease of transmission of ∼50% can be observed, suggesting that the coherence length of the spectrometer light

---

[2] This effect was predicted via *MATLAB* modelling.

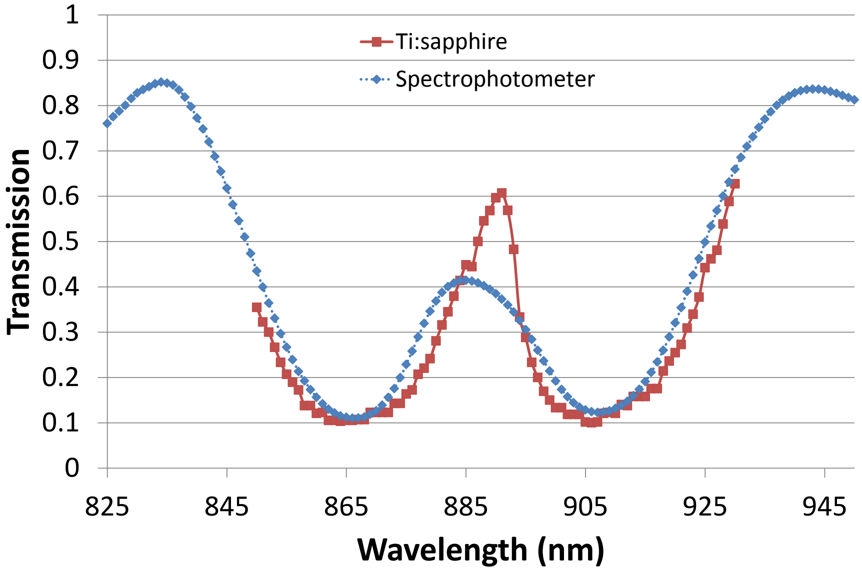

FIGURE 6.13: Transmission spectrum of π shifted stack 2 as obtained via spectrophotometer (blue) and Ti:sapphire laser (red).

did indeed play a part in limiting the observed π shift effect. However, given that the peak was limited to 60% transmission, some variation in layer thicknesses still occurs.

6.5 Apodisation

An attempt was made at grating strength apodisation i.e. varying the grating strength to produce an approximately Gaussian profile to remove side band reflections. The sample consisted of alternating layers of YAG and mixed YAG/GGG, varied in ratios of 9:1, 8:2 and so on to 0:10 and back to 9:1 to obtain an approximately Gaussian grating strength profile (see figure 6.14). The programmed optical thickness was the same for each layer (standard error of 0.02 nm, although greater variation is likely due to experimental fluctuations), resulting in a structure that was grating-strength apodised only (not chirped-apodised, where optical layer thickness also varies). As such, the physical thickness of each mixed layer was varied to compensate for the change in refractive index. This is, to our knowledge, the first example of such a structure in a stack geometry, and the first example of such sophisticated crystal engineering via PLD.

Mixing was achieved by changing the relative repetition rates of the ablating lasers using the shutters and deposition was carried out under the same compromise conditions as the Bragg stacks previously described in section 6.2. As refractive index could not be measured directly (see section 6.2.2.1), refractive indices were estimated by comparison of grown gratings with the *MATLAB* model to be 1.9 and 2.0 for YAG and GGG respectively. Due to the defined deposition rate (determined by the deposition conditions) and minimum blocker response times (0.2 s for the GGG blocker, 0.3 s for the YAG blocker

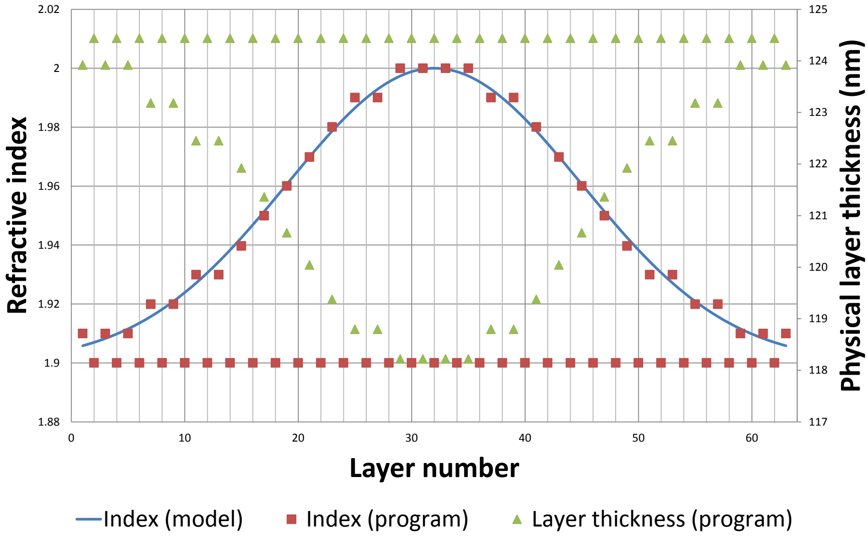

Figure 6.14: Overall approximate refractive index and physical thickness for each layer in a 63-layer grating strength-apodised stack, along with Gaussian refractive index apodisation model.

due to its larger and heavier flag), layers could not be completely mixed in all cases. However, in the majority of cases any sub-layering is on a sub-unit cell scale, and in the remainder layers thicker than 1.2 nm are interspersed with layers of less than half a unit cell in thickness, resulting in a crystal which can be practically described as “mixed”. Any layering is on a much smaller scale than the wavelength of light, and hence should not have a significant impact on the device performance.

XRD spectra of the apodised sample can be seen in figure 6.15. Only peaks corresponding to the 400 and 800 orientations of the YAG, GGG and mixed layers can be seen in the full scan (figure 6.15(a)); the sample was hence crystalline with each layer orientated in the epitaxial direction. Peaks representing diffraction from each of the eleven materials in the sample (YAG, GGG and mixtures in ratios 9:1 to 1:9) can be observed in figure 6.15(b), as can a peak corresponding to the underlying YAG substrate (to which data were normalised).

An approximate model was obtained as a guide for comparison using the GID_sl x-ray modelling program mentioned in section 5.3.3. The program was not able to accommodate mixed materials; instead the model assumed layers of GGG that were highly strained, to take into account mixed material lattice constants. Use of a different material affects peak heights but not positions, allowing comparison with the observed data. As suggested by the model, any contribution from layers in the bottom parts of the structures is lost in noise due to X-ray attenuation; peaks shown are hence likely to be reflections from the top half of the structure only. No instrument function was taken into account and roughness values used were the same as those previously determined for GGG (higher values obscure the contribution from the substrate). The model assumed that the peak around 29.43° corresponded to that of the YAG-only layers.

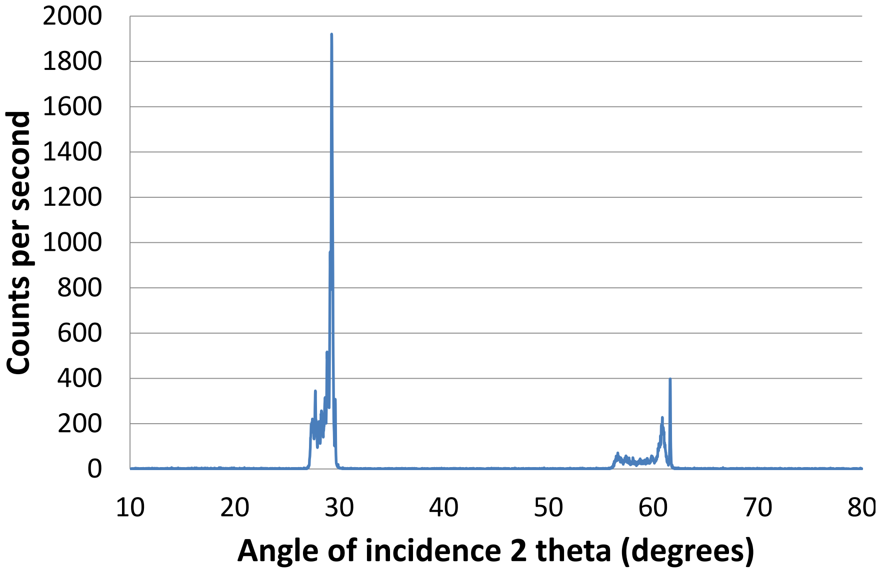

(a) Only (400) and (800) peaks can be observed, demonstrating that crystal growth was in the epitaxial direction.

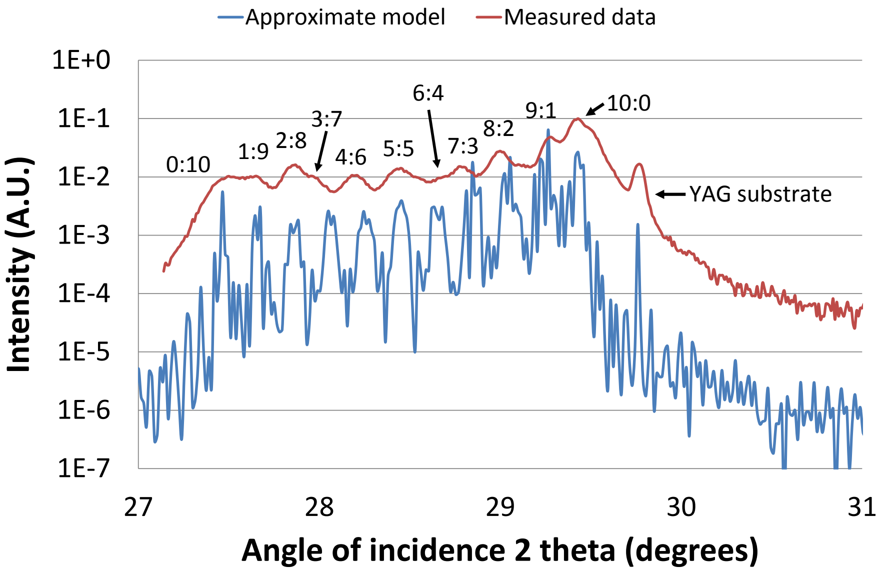

(b) Peaks corresponding to each YAG, GGG and mixed layers in ratios 9:1 to 1:9, as well as the underlying YAG substrate, can be observed. The approximate model is also shown as a comparison (blue).

FIGURE 6.15: Full (figure 6.15(a)) and zoomed-in (figure 6.15(b)) XRD spectra of apodised sample.

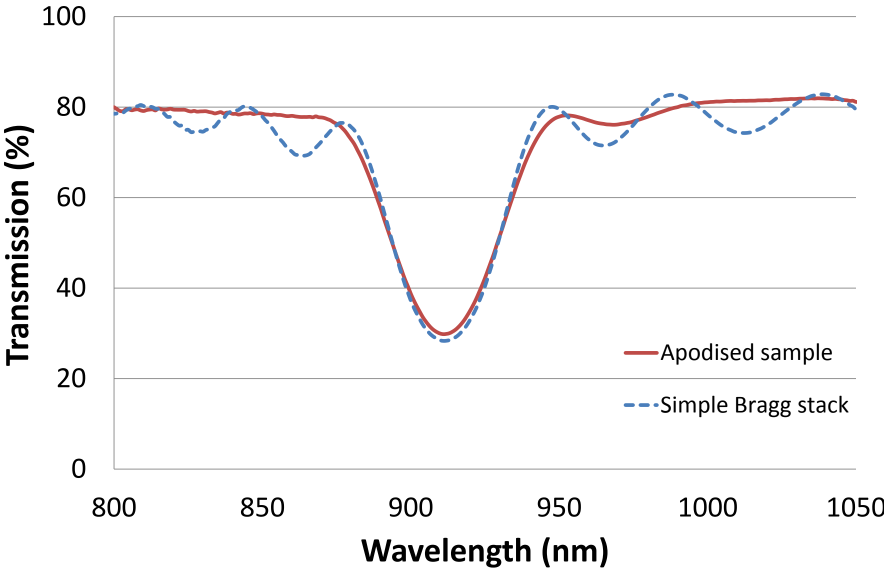

FIGURE 6.16: Transmission spectrum of an apodised sample and a simple Bragg stack of comparable peak transmission.

Peak spacing was fairly regular, although not as regular as would be expected. Four layers did not match the expected peak positions, namely those with YAG:GGG ratios of 8:2, 7:3, 3:7 and 4:6. The shifts indicate an increase in lattice constant, the cause of which has not been determined. Possible causes include an increase in relative GGG:YAG ratio (due to a change in relative growth rates), a change in the elemental content of the layers (e.g. a decrease in Al or Ga) due to changing conditions or plume interaction, or a change in strain. Relative plume delay was not taken into account in the fabrication of mixed layers, and shifts in lattice constant from expected values may hence be influenced by plume delay as described in chapter 5. Growth of layers of each ratio as separate test films, or even a repeat of the apodised growth already demonstrated, may shed some light on the mechanism for the XRD peak shifts, as well as allowing further information about true refractive indices of the mixed materials to be obtained.

Despite these flaws in implementing the design, the overall result appears to have been successful. Spectrophotometer data of the apodised sample, along with a comparable quarter-wave Bragg stack of similar peak height (deposited under nominally the same conditions but with fewer layers in order to achieve comparable peak heights), can be seen in figure 6.16. The majority of side bands are suppressed relative to the quarter-wave stack without significant increase in central peak width. It is not known whether the small peak around 970 nm, the only side band to not have been fully suppressed, is present due to growth program inaccuracies (approximations, refractive index estimation, sub-layering etc.) or due to the same material or stress factors that caused the XRD peak shifting described above. Extension of the *MATLAB* model to apply to apodised gratings may help illuminate this problem.

6.6 Applications

It is expected that crystalline Bragg stacks will be of great interest for a number of applications, particularly where amorphous materials may not be appropriate. The garnets used for grating growth in this chapter are unlikely to be ideal due to the relatively poor crystal quality obtained as a result of the compromised conditions used. However, some preliminary testing for high temperature applications has been undertaken. High power laser damage threshold testing has not yet been undertaken due to time constraints. It should be noted that, as the stacks are single-phase crystals, thick film crystal growth could be subsequently undertaken using such Bragg structures as a substrate. This may be of interest for growth of integrated mirror thin disc laser crystals, for example.

6.6.1 High temperature

A 45-layer quarter-wave grating of peak reflection wavelength of ~600 nm was grown for temperature resistance testing under standard conditions. It was subjected to CO_2 laser annealing at ~1000 °C for ~1 hour in Chamber 1, with a ramping periods of ~30 minutes. Annealing took place in an argon atmosphere at a pressure of $\sim 1 \times 10^{-2}$ mbar.

Transmission spectra before and after annealing are shown in figure 6.17. The clear difference in between the pre- and post-annealing spectra suggests that some diffusion between layers has taken place, as might be expected for garnet layers at such high temperatures (see section 5.3). The likelihood of interdiffusion and hence loss of layer definition is also greater due to the relatively poor crystal quality. However, the sample remains water-clear and is otherwise unaffected (unlike e.g. some glasses, that would begin to melt or deform at this temperature). It is expected that a different choice of materials should result in a grating capable of withstanding temperatures ≥ 1000 °C. Potential candidates are sesquioxides: these are simpler in structure than garnets and are hence less likely to suffer from changes in stoichiometry. They also are grown at higher growth temperatures (see appendix C) and so are more likely to remain intact at temperatures at and beyond 1000 °C, although interdiffusion is still a potential problem.

6.6.2 Tuning and curvature

Peak reflection wavelength can be tuned, due to film curvature. The tuning profile of an example grating of 67 layers and 5-10% peak transmission is shown in figure 6.18. While the level of curvature and hence tuning was not controllable with the setup described in this chapter, due to the restricted window of growth parameters, a different material selection (e.g. YIG and GGG, sesquioxides) with a wider overlap of ideal conditions may allow a greater variety of deposition conditions to be used, hence providing a greater

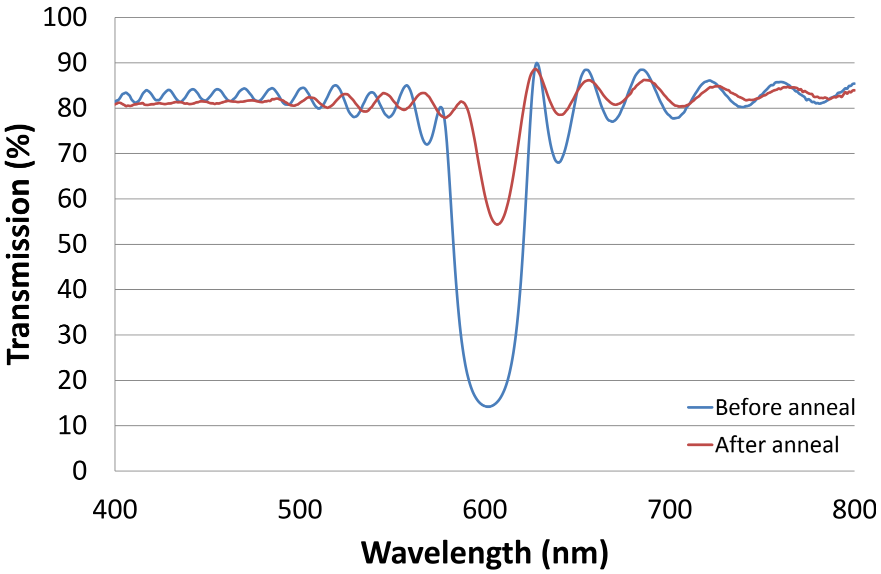

Figure 6.17: Transmission spectra of an quarter-wave grating sample before and after laser annealing at ~1000 °C.

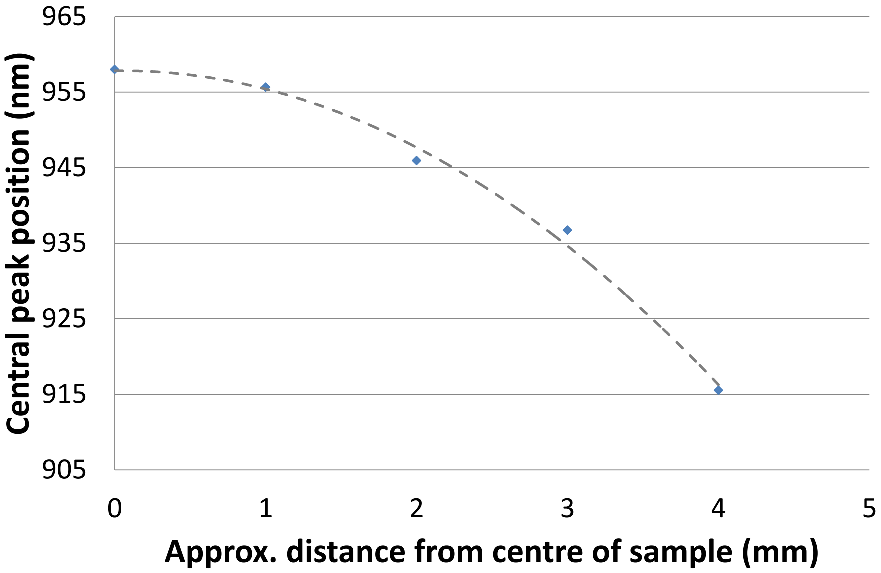

Figure 6.18: Gratings are tunable due to surface curvature. Reflection peak position can be varied from 958 to 916 nm in this 65 layer example.

level of control over curvature. This may be of interest for growth of Gaussian laser cavity mirrors, for example, as well as wavelength tuning.

6.7 Limitations and future improvements

Structures of immediate interest that have not yet been attempted include chirped and chirped-apodised structures. Unfortunately, chirped samples with 99% reflectivity but broad reflection bands (at least twice that of a standard quarter-wave stack) consist of

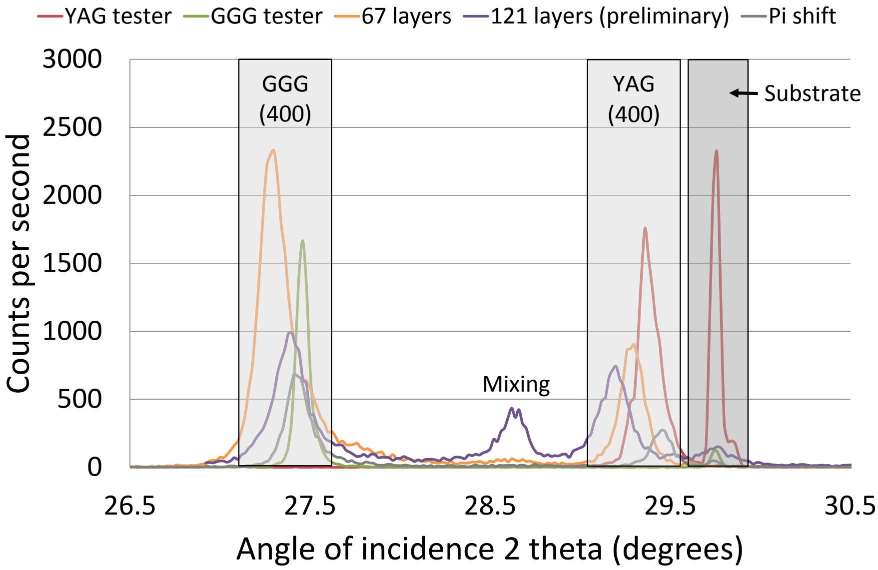

FIGURE 6.19: XRD spectra of a number of different Bragg samples showing variability in resulting lattice parameter due to fluctuations in the setup.

more than 250 layers, assuming the current materials and conditions (i.e. the current achievable Δn). While this would be achievable with the current setup, the time required was prohibitively long in the context of these experiments. Improvements to the *MATLAB* model are also required, particularly to introduce apodisation and non-linear chirp.

While the production of crystalline Bragg stacks by PLD has been successfully demonstrated, there are currently issues with repeatability in the current setup. A certain level of variation in layer thickness, refractive index and stress in unavoidable when using the technique in its present form. This variation can be easily observed in figure 6.19: lattice constants measured for a number of samples described in this chapter are different despite conditions being nominally the same. Laser energy varies from pulse to pulse, and can drift downwards over the course of a deposition, changing both the deposition rate and the stress states of the resulting film. Target damage occurs over time, something that can influence the ablation characteristics and film stoichiometry as well as particulates. Pressure can fluctuate slightly (by 1 or 2%), again changing the stress states and elemental compositions of the films. Nd:YAG laser performance was poorer than the excimer, exhibiting the larger energy fluctuations, a less flat beam profile and the periodic need to realign the harmonic crystals. Its use, however, was unavoidable in the context of these experiments.

Substrates are inserted into the holder by eye and so may exhibit slightly different levels of heatsinking in the corners, and temperature may hence vary slightly from deposition to deposition. Any such temperature variation cannot be observed using the current system. Many substrates were also found post-deposition to have been lower quality crystal than previously thought, presenting different amounts of curvature and possibly containing impurities or flaws that led to different emissivities or levels of thermal expansion coefficient (shown by cracking or discoloration at temperatures of 850-1000 °C).

Introduction of in-situ diagnostics would go some way to compensating for these fluctuations. A low power laser could be used to perform reflectivity measurements during deposition (as done by Serna and Alfonso [175]), which could be combined with the shutter controller program in *LabVIEW* to automatically stop deposition when a layer has reached the desired optical thickness. The ability to change the incident angle of this laser would allow a range of designed peak reflection wavelengths to be selected. Online temperature measurements would also be highly desirable to standardise stoichiometry and any curvature due to thermal expansion mismatch, although as discussed in section 4, such measurement can be difficult to achieve. It is important to remember when introducing additional diagnostics, however, that experimental flexibility or speed of growth and/or sample turnaround should ideally not be sacrificed: these are the real advantages of the technique over one that may otherwise allow better quality growth, such as MBE.

While simple to implement, laser reflectivity measurements were not undertaken in these experiments due to the materials used. YAG and GGG were selected for experiments for the reasons described in section 6.2; however, YAG growth on GGG layers was found to be brown and frosty until the deposition of another GGG layer on top. As such, in-situ reflectivity measurements were unlikely to have been successful. However, now that the concept has been proven, a different choice of materials may be investigated. Growth of YIG/GGG multilayers has been demonstrated previously with an emphasis on their magneto-optic characteristics (see chapter 2). Such stacks could, however, be of interest as a replacement for the YAG/GGG stacks shown here, should a common set of deposition conditions be available.

Bragg stack growth in all geometries may benefit from the use of materials other than garnets. Rare earth sesquioxides (Y_2O_3, Lu_2O_3 etc.) have high damage thresholds and thermal conductivities, even compared to garnet. They are also much simpler in terms of crystal structure, and hence less likely to be adversely affected by compromised growing conditions. Like garnets, they exhibit a range of refractive indices from 1.90 (yttria) to 1.99 (scandia) whilst having similar lattice constants and thermal expansion coefficients, and hence can be expected to grow well in a multilayer geometry. Single-layer preliminary growth has shown that single-phase yttria, lutetia and scandia can all be grown under similar conditions using the setups described in this thesis, with relatively few particulates (see appendix C). Layered sesquioxide growth may hence prove ideal for growth of Bragg reflectors for high power and/or high temperature applications.

6.8 Conclusions

Crystal Bragg reflectors have been fabricated in various geometries using the shutter technique. These include 145 layer stacks exhibiting >99% reflection as well as π shifted designs. A crystalline apodised sample with an approximately Gaussian grating-strength profile was grown by mixing plumes to obtain a custom refractive index for a particular layer. This represents the first known example of such engineering in crystal and, as expected, resulted in substantially reduced side lobe reflections. Due to the curvature of the layers, peak reflection wavelength was tunable via changing incident position.

Crystalline mirrors are of interest for high power and high temperature applications, due to the high damage threshold. YAG and GGG were used as they had the largest index contrast of the garnets available, but the compromised conditions required for automated growth resulted in layers with stoichiometry far from bulk. This choice of materials and conditions may have strongly diminished the ability of the structures to withstand high temperatures, with some layer indiffusion and hence loss of performance observed after annealing at ~1000 °C.

While the potential of the technique for practical device growth has been proven with these experiments, there is still much work to be done. Various stack geometries, including chirped and alternative apodisation profiles, have not yet been attempted due to time constraints. Issues with repeatability should be addressed by the introduction of online thickness measurements. This is likely to require a move to alternative materials, whether other members of the garnet family or new classes of materials, such as sesquioxides.

Chapter 7

Micromachined channel waveguides

7.1 Introduction

This chapter describes the first of two novel methods utilising PLD to fabricate crystalline structures for lasing applications.As described in chapter 2, channel waveguide fabrication often relies upon methods that are slow or costly (ion beam machining etc.), and as such, structures can be limited in size or number. Described in this section is a novel method of fabricating thick channel waveguides simply and easily using a combination of PLD and micromachining. Multiple cladding layers may be incorporated, and by careful choice of layer thicknesses such structures may be diode pumped (cheaper, easier optical setup) whilst maintaining single-mode output (see section 3.4.2).

This work was a collaboration between groups at the ORC: micromachining was carried out primarily by Lewis Carpenter (ORC), with input from Chris Holmes, James Gates and supervisor Peter Smith. Lasing experiments were primarily carried out by Amol Choudhary, with input from supervisor Dave Shepherd.

The main contributions detailed in this chapter are as follows:

- The first known example of garnet channel waveguide fabrication via physical micromachining;
- The first known example of a double clad crystalline channel waveguide.

7.2 Fabrication procedure

Clad channel waveguide fabrication followed a five step process, as illustrated in figure 7.1:

1. Grow a multilayer film via PLD.
2. Physically micromachine cuts to make ridges. Because the bottom of any cut is rough (see section 7.6), the cuts should be deep enough to cut into the substrate that scattering is minimised.
3. Thoroughly clean sample to remove abrasive material from the cutting process. Samples are cleaned ultrasonically in heated acetone, wiped with methanol and DI water and dried (not illustrated in figure 7.1).
4. Return clean samples to the chamber and deposit cladding layer(s).
5. Polish faces parallel.

The technique does not require the use of multiple beams and targets, although the experiments detailed here were carried out in a multi-beam chamber (Chamber 2). Physical micromachining was undertaken using a Loadpoint MicroAce 3 high precision saw.

7.3 Proof of concept: single clad

An initial sample was made to verify that machining of crystal layers was viable. Layers were deposited in Chamber 2 with a background oxygen gas pressure of 4×10^{-2} mbar and a substrate temperature of ~650 °C. Targets were loaded simultaneously so that the chamber did not need to be opened between depositions. The excimer laser fluence ablating the undoped GGG target was ~1.7 Jcm^{-2}. In the case of the doped target, spot size varied dramatically with angle of incidence, resulting in a fluence that varied from ~2.5 Jcm^{-2} to ~1.5 Jcm^{-2} as the target tilted over a range of 8°. In addition, the optimal ablating laser setup for both targets had not yet been determined, leading to formation of a large number of particulates. Each layer was ~1 µm in thickness.

A diagram of the intended design is shown in figure 7.2. Pairs of grooves of ~8 µm depth and ~60 µm width with a range of separations (hence ridge widths) were cut into the film and substrate using a precision dicing saw. Electroplated nickel bonded blades of 0.02 mm width and 5000 grit were used to dice at 15,000 rpm with a translation speed of 0.1 mm/s (dicing carried out by Lewis Carpenter, ORC). The resulting ~20 µm wide, 10 mm long multilayer ridges were subsequently overgrown via PLD with a further undoped GGG cladding layer. XRD analysis (see figure 7.3) shows that the crystal layers have

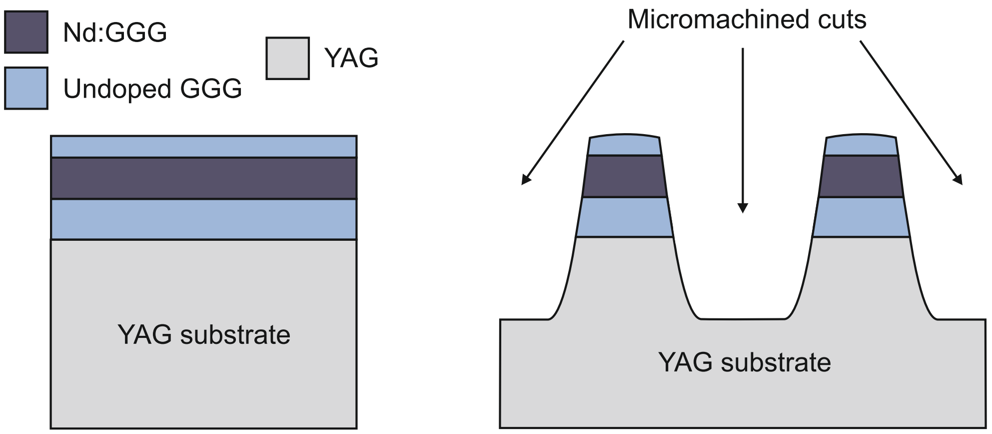

(a) 1. Deposit multilayer film

(b) 2. Physical micromachining to form ridges

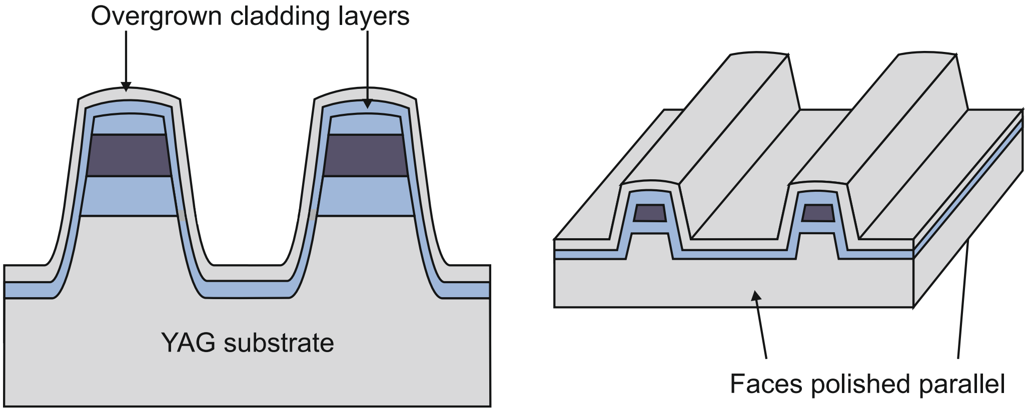

(c) 4. Overgrow cladding layers after 3. cleaning (not shown)

(d) 5. Polish end faces parallel

FIGURE 7.1: Steps involved in channel waveguide fabrication by PLD and micromachining (cleaning not shown).

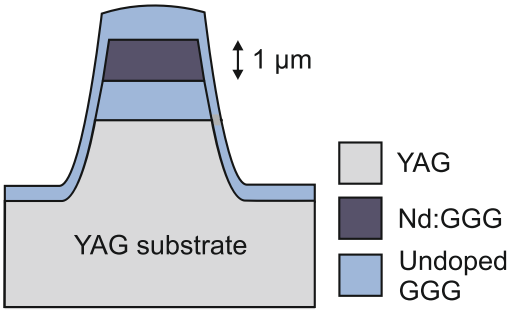

FIGURE 7.2: Diagram of design for proof-of-principle single clad channel experiments

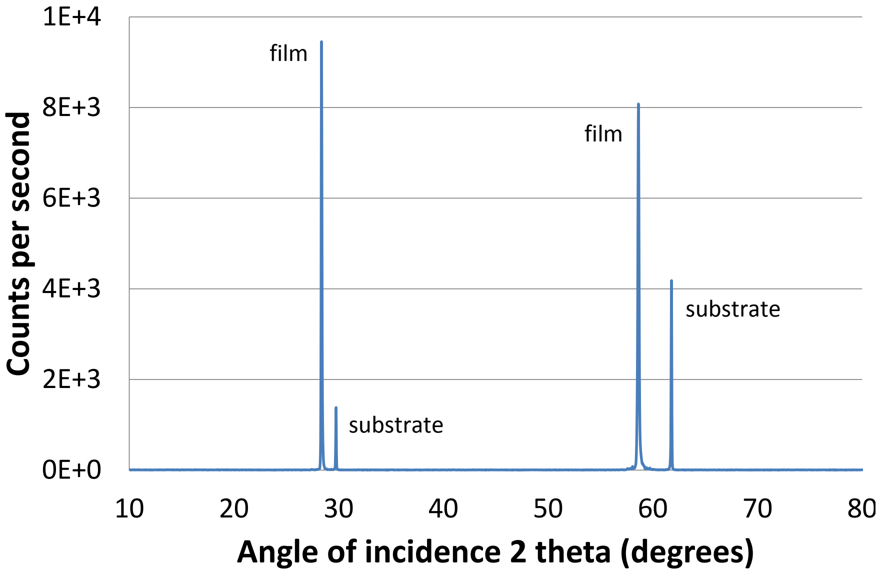

(a) Only (400) and (800) peaks can be observed, demonstrating that crystal growth was in the epitaxial direction.

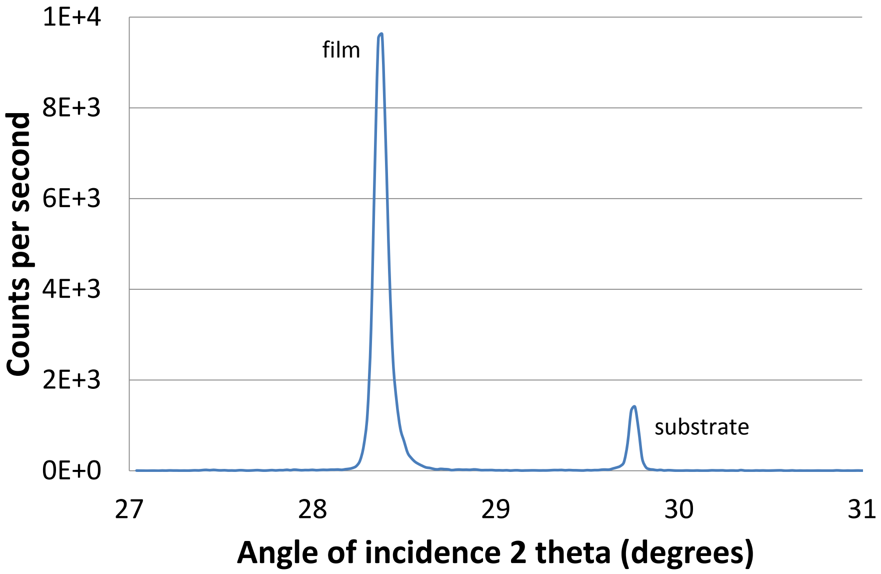

(b) Contributions from the film and substrate can be observed.

FIGURE 7.3: Full (figure 7.3(a)) and zoomed-in (figure 7.3(b)) XRD spectra of a machined single clad channel.

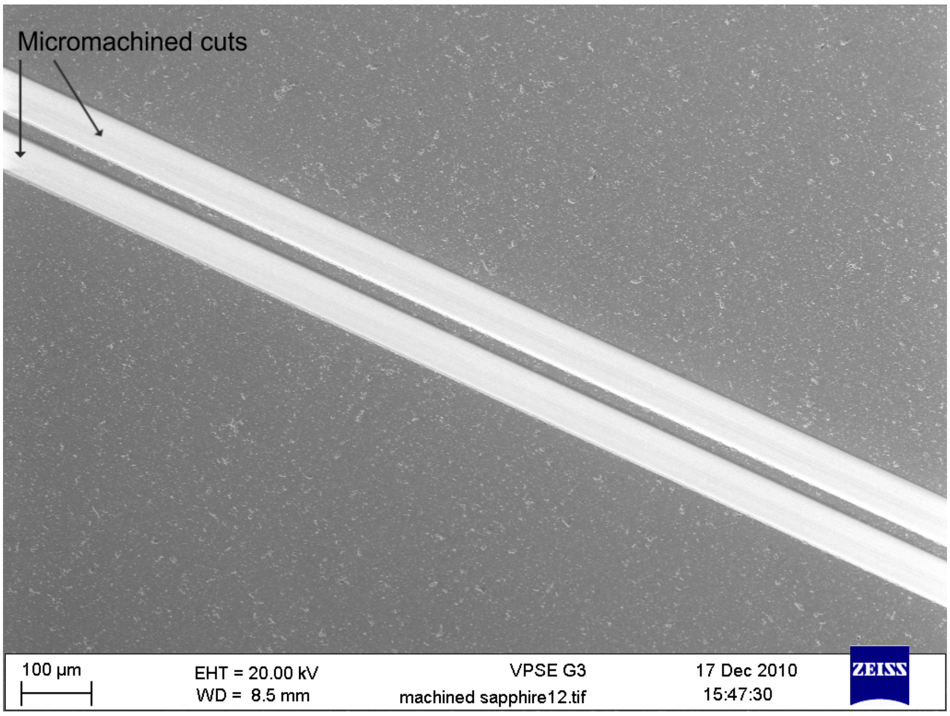

FIGURE 7.4: SEM of a section of example ridge before overgrowth. The substrate (light area) can be clearly seen, indicating that the blade has cut into the substrate. Film (dark area) quality is poor, with a large number of particulates observed.

grown in the epitaxial (100) direction and with a peak FWHM similar to that of the substrate.

An SEM image of a section of an example ridge before overgrowth can be seen in figure 7.4. The bare cut substrate and deposited GGG layers can be clearly distinguished. As expected, film quality was poor, and large numbers of particulates can be observed. Only one ridge was intact along its entire length, with others exhibiting significant chipping that, in some cases, led to sections of ridge being lost entirely (see figure 7.5(a)). Some chipping appeared to be unavoidable even when the ridge was intact (see figure 7.6). To combat the effect of such chipping, it was proposed that before machining, a layer of cladding should be grown on top of the core with one-third to one-half the full cladding thickness, rather than machining directly into the core. Any chipping would consequently be "smoothed" by the subsequent overgrowth of cladding and capping layers.

Figure 7.7 shows an SEM image of the semi-polished end face of a clad channel after overgrowth. While the core and cladding cannot easily be distinguished, the overgrown GGG layers can be observed. Chipping of the end of channels was particularly prevalent, as can be observed in figure 7.7. However, polishing of a functional device would remove enough material to also remove any chipping (something that was not done in the case illustrated due to time constraints).

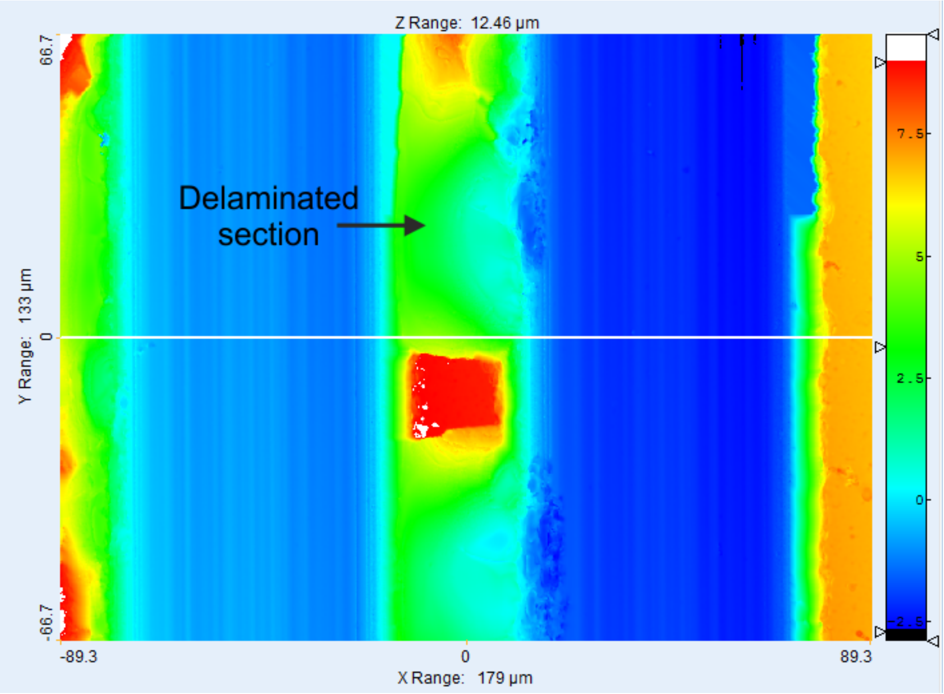

(a) 2D profile. Chipping was severe enough for sections of film to delaminate entirely.

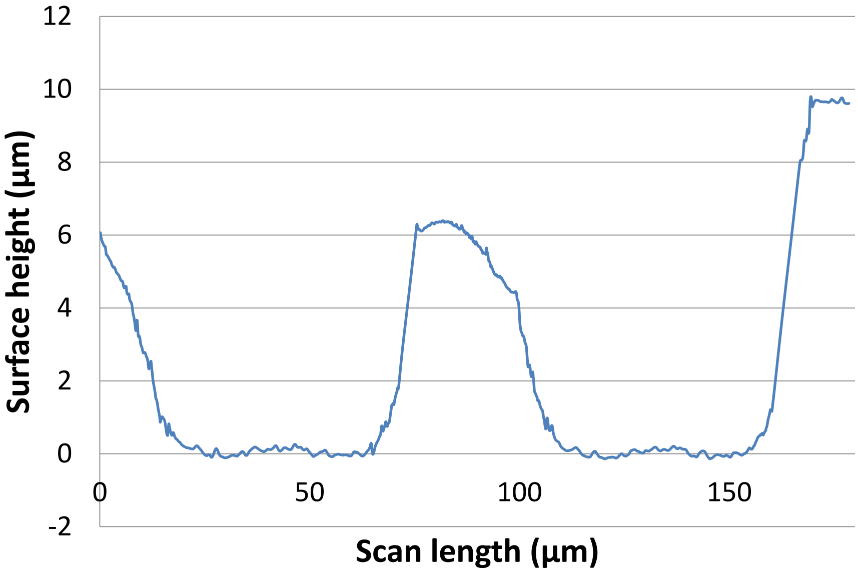

(b) 1D profile showing the roughness of the bottom of cuts.

Figure 7.5: Surface profiles of sections of ridge before overgrowth, obtained via optical profiler.

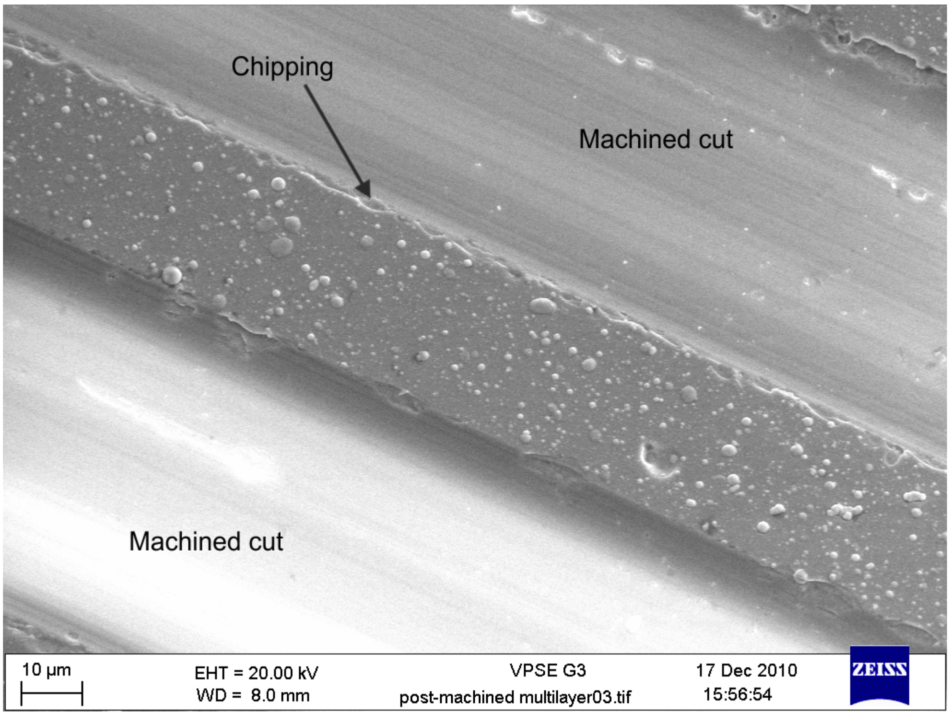

Figure 7.6: SEM image of a section of precision machined waveguide before overgrowth, showing minor levels of chipping on the top edges of the guide.

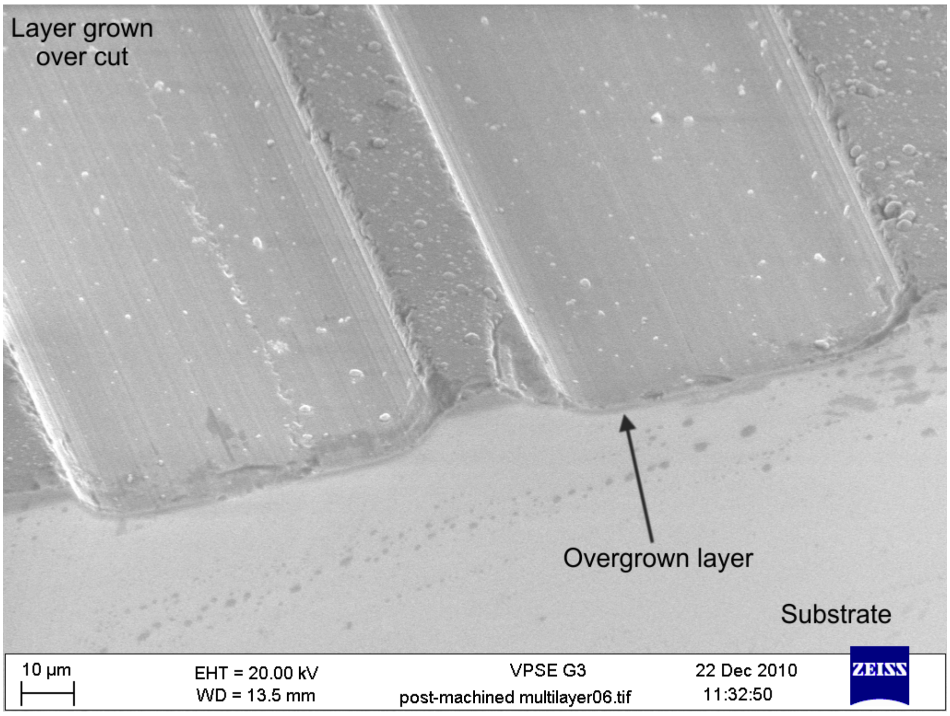

Figure 7.7: SEM image of the semi-polished end face of an overgrown channel. The overgrown GGG layer can be seen.

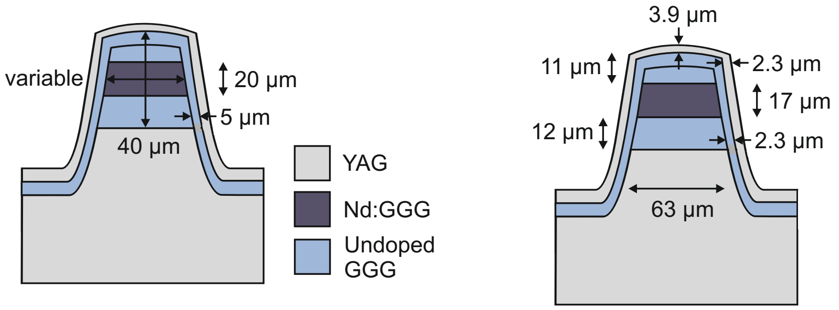

(a) (b)

FIGURE 7.8: Diagrams of double clad channels (a) as designed (width either ∼25, ∼40 or ∼60 µm) and (b) as grown.

As can be observed in figure 7.5(b), the bottom edges of a machined cut are typically rough. Care must hence be taken to ensure that the blade cuts deeply enough into the substrate to avoid these rough regions. ∼20 µm thick channels appeared to be overly vulnerable to critical damage (i.e. ridge delamination), and hence a range of larger ridge widths was tested in subsequent samples.

7.4 Double clad channels

Having created single clad channels and shown that machining of crystal layers was possible, fabrication of a double clad waveguide was attempted. Due to the levels of chipping observed, it is unlikely that crystalline channels fabricated by precision machining would be able to compete with existing examples of channel fabrication in terms of loss (see chapter 2), at least until improvements in the blades/machining process can be implemented. Instead, the advantage of the technique lies in its ability to quickly fabricate channels large enough for diode pumping, with cladding layers to allow single-mode output. A YAG cap is also advantageous when cladding pumping to reduce any scattering due to particulates or chipping. An example of the desired channel design is shown in figure 7.8(a).

Two multilayer samples were made to allow for sample attrition. All layers were deposited in Chamber 2 using an excimer laser, this time changing targets between deposition of each layer to prevent the large fluence variation observed with target tilting. In the case of doped and undoped GGG layers, the laser operated at 20 Hz with a fluence of ∼2.5 Jcm^{-2}. Background oxygen gas pressure was 4 × 10^{-2} mbar and substrates were heated to a temperature of ∼650 °C. YAG deposition took place with a laser operating at 10 Hz with a fluence of ∼2.8 Jcm^{-2}, a background gas pressure of 1 × 10^{-2} mbar and a substrate temperature of ∼750 °C. Target-substrate distance was ∼40 mm in both cases.

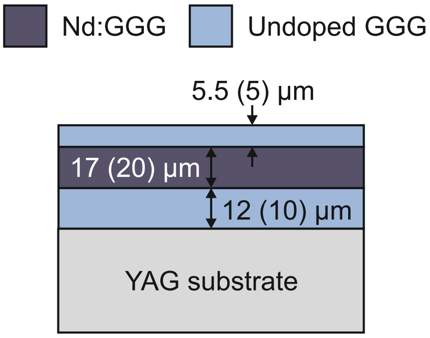

FIGURE 7.9: Diagram of multilayer film before precision machining showing film thicknesses as measured (with thickness values as designed shown in parentheses).

Before micromachining, a three layer film was grown, a schematic of which is shown in figure 7.9 (values in brackets are the approximate designed film thicknesses, while the numbers outside the brackets are those measured for the polished edge of the real film). Precise film curvature is not known as substrates were not pre-measured, but the thickness of each film is expected to be around 5-10% thicker in the centre of the film than at the edge. XRD spectra of this multilayer film before overgrowth are shown in figure 7.10.

As outlined in section 7.3, a cladding layer of half the full thickness was grown on top of the core in order to reduce the effect of chipping. As a consequence, the thickness of the GGG cladding layer in total on top of the ridges was expected to be around twice that of the thickness on the sides. The relatively small thickness of the cladding layer on the ridge sides was not, however, expected to have a particularly detrimental additional effect. Because it would not be possible to grow thicker layers on the sides than on the top due to the growth configuration, and because the width of a ridge and the thickness of a film (before machining) are limited to >20 and <40 µm in total respectively (width due to ridge delamination and film due to stress), single mode output would not be achieved in the horizontal axis.

Both films exhibited a relatively large number of particulates of diameter >100 nm compared to the best films observed previously under these conditions. However, the large thickness of the film overall (∼35 µm close to edge, ∼40 µm in centre) makes a direct comparison difficult. Particulate counts were around three times higher for sample 1 than for sample 2 (averages of $\sim 2.4\times10^{6}$ and $\sim 7.5\times15^{6}$ per cm^{2} respectively), despite conditions nominally being the same. While growth with a laser repetition rate of 20 Hz in Chamber 1 did not appear to be problematic compared to growth at 10 Hz, the effect of such growth in Chamber 2 (with its tilting targets) has not been fully investigated. It may be the case that, with a higher repetition rate and a different pattern of overlapping laser spots on the target, the formation of laser-induced surface features or the rate of exfoliation may be different. The Nd:GGG core of sample 2 was grown first, followed by the core of sample 1, and the target was not changed between depositions. Continuous

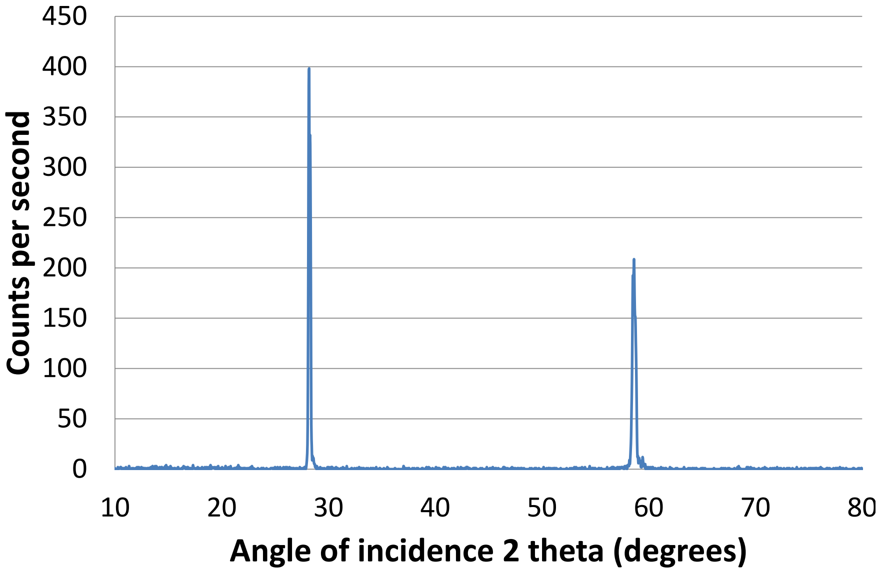

(a) Only (400) and (800) peaks can be observed, demonstrating that crystal growth was in the epitaxial direction.

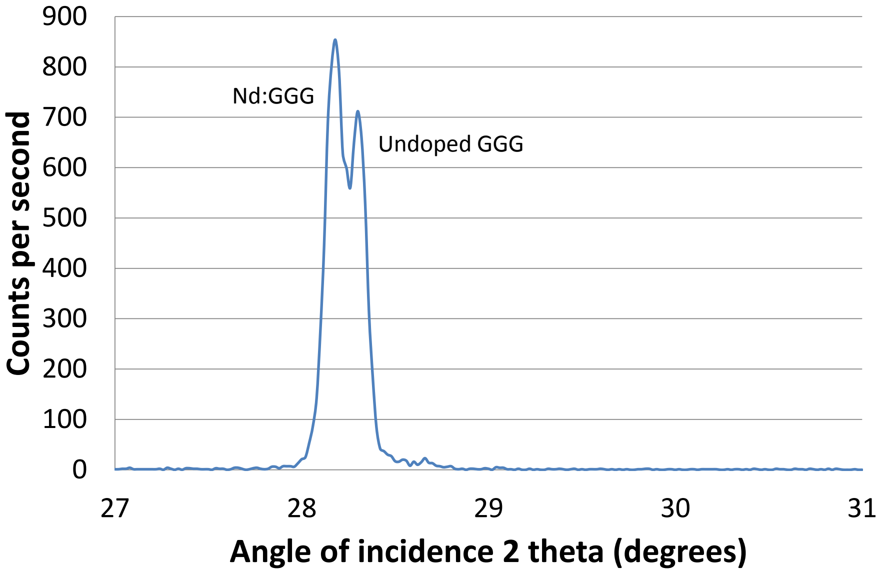

(b) Peaks corresponding to the doped and undoped GGG layers can be observed. Film is too thick for any substrate contribution to be seen.

Figure 7.10: Full (figure 7.10(a)) and zoomed-in (figure 7.10(b)) XRD spectra of multilayer film before machining.

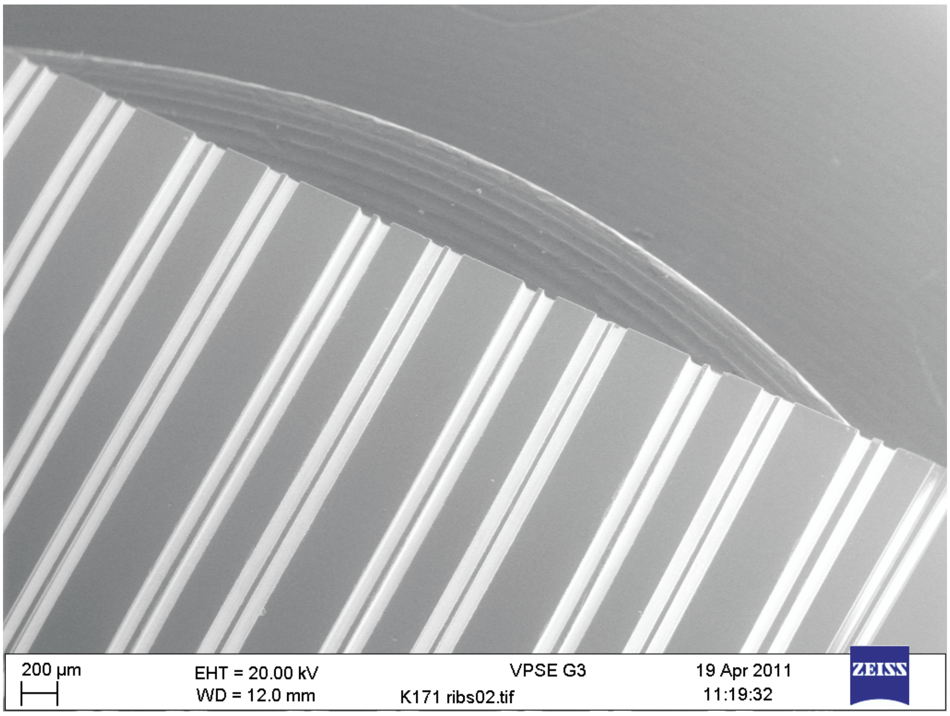

FIGURE 7.11: SEM image of an array of machined ridge waveguides before cladding layer overgrowth. Dark and light areas are the film and substrate respectively.

target usage for the five hours required to grow both cores may have been enough to pass the threshold after which particulate densities increase dramatically.

Particulate density and hence waveguide loss could be reduced by employing a number of methods, chiefly by not changing laser-target incidence angle during deposition (i.e. no target tilt) or by reducing the fluence slightly to minimise formation and exfoliation of surface features. However, compromises must be made in order to grow thick enough films to allow for diode pumping, otherwise the chief advantage of this precision machining technique is lost. As shown in [11], fluence can be used as a tool to prevent film cracking or delamination due to the thermal expansion mismatch between the film and substrate. The fluence used here, $\sim$2.5 Jcm^{-2}, was the ideal found for GGG grown under these conditions; use of a lower fluence may not allow thick film growth. Any effect on particulates resulting from either the target tilt program or use of 20 Hz laser repetition rate could be removed by depositing films in Chamber 1; this chamber was not, however, available at the time.

Arrays of seven ridges were cut into both samples; however, due to a machining error the cuts were not deep enough to cut into the substrate. Six ridges were subsequently machined in the gaps between existing ridges in one sample, of $\sim$25, $\sim$40 and $\sim$60 µm widths. An SEM image of part of the whole 13 ridge array is shown in figure 7.11. As in section 7.3, the machined trenches can clearly be seen (light area). An example ridge end is displayed in closer detail in figure 7.12. Some minor chipping on top edges can again be observed, something that was prevalent in all cases.

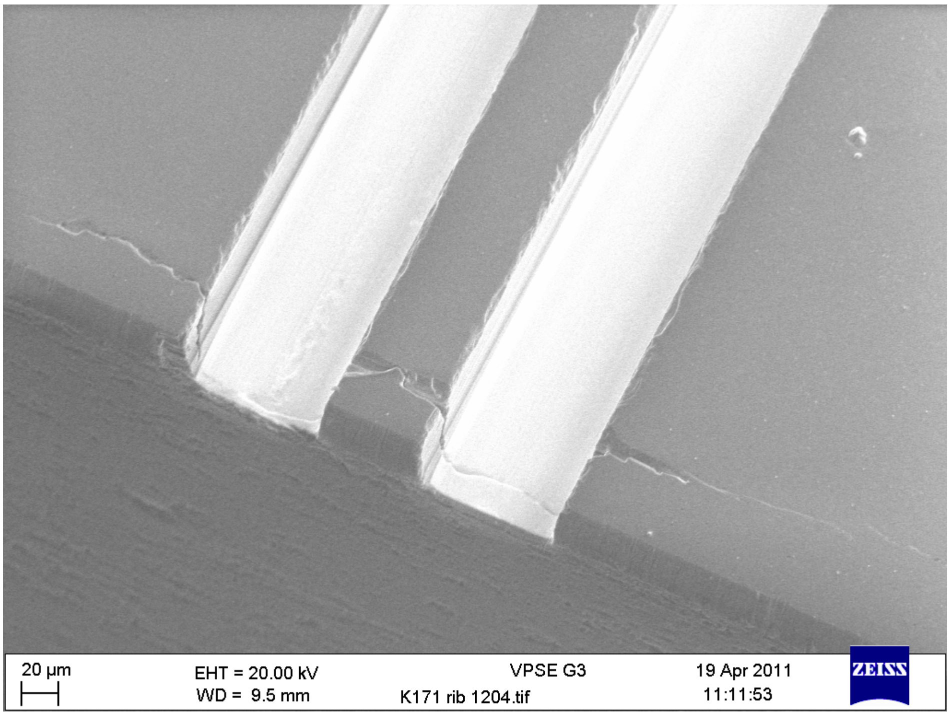

FIGURE 7.12: SEM image of a machined ridge waveguide before cladding layer overgrowth. Dark and light areas are the film and substrate respectively.

Similarly to the thin single-clad case, $\sim$25 μm thick ridges appeared to be more vulnerable to damage: neither of such ridges in this thick sample survived the machining/cleaning process (see figure 7.13). In two other cases (one $\sim$40 μm thick, one $\sim$60 μm) ridges remained intact along their length but chipping was severe enough to render the ridges unusable. Two ridges were hence available for laser experiments. Cut depth varied due to film curvature as well as linearly due to the slightly tilted mounting of the samples on the saw. In all but one case, however, the blade cut at least $\sim$15 μm into the substrate.

Overgrowth of GGG cladding layers (see figure 7.14) took place under nominally the same conditions as previous GGG growth. Growth rate on the top of ridges was much higher than growth on the sides: thickness of GGG growth on the side of the ridge was $\sim$2.3 μm compared to $\sim$5.5 μm additional growth on top of the ridge. This difference in growth rate may be significant when considering engineering for single mode output: laser output will become multimode if the core thickness is $>\sim$60% of the total core+cladding thickness (see section 2.3.1). A similar discrepancy in growth rate on sides and top was observed for the case of YAG cap overgrowth ($\sim$2.3 μm on sides, $\sim$3.9 μm on top).

YAG growth was very poor, as evinced by the large number and size of particulates shown in figure 7.15. The YAG target slipped in the holder at least once mid-deposition. As a consquence, splashed areas and previously-formed ridges were ablated, leading to exfoliation of surface features and splashed material and hence the volume of particulates

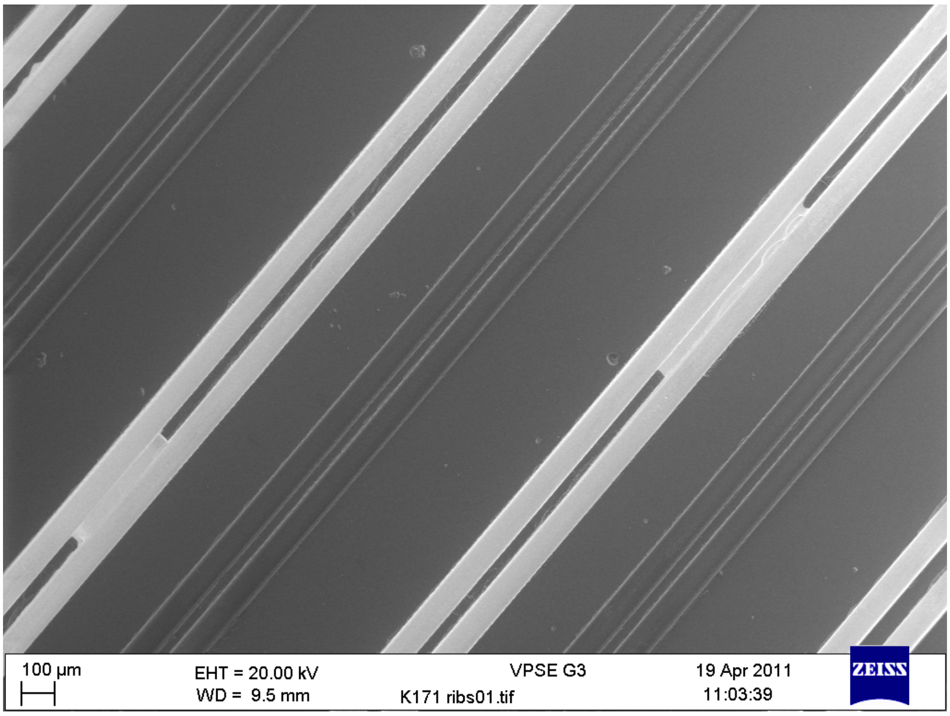

FIGURE 7.13: SEM image of machined ridge waveguides before cladding layer overgrowth showing areas where sections of ridge have delaminated.

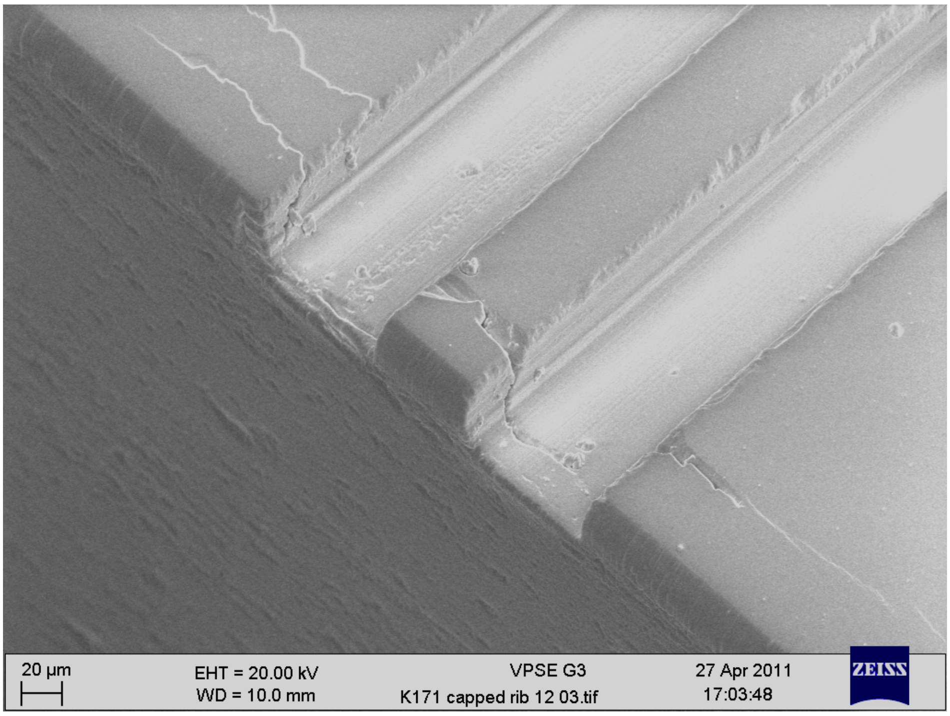

FIGURE 7.14: SEM image of an example channel waveguide after overgrowth of GGG cladding layer.

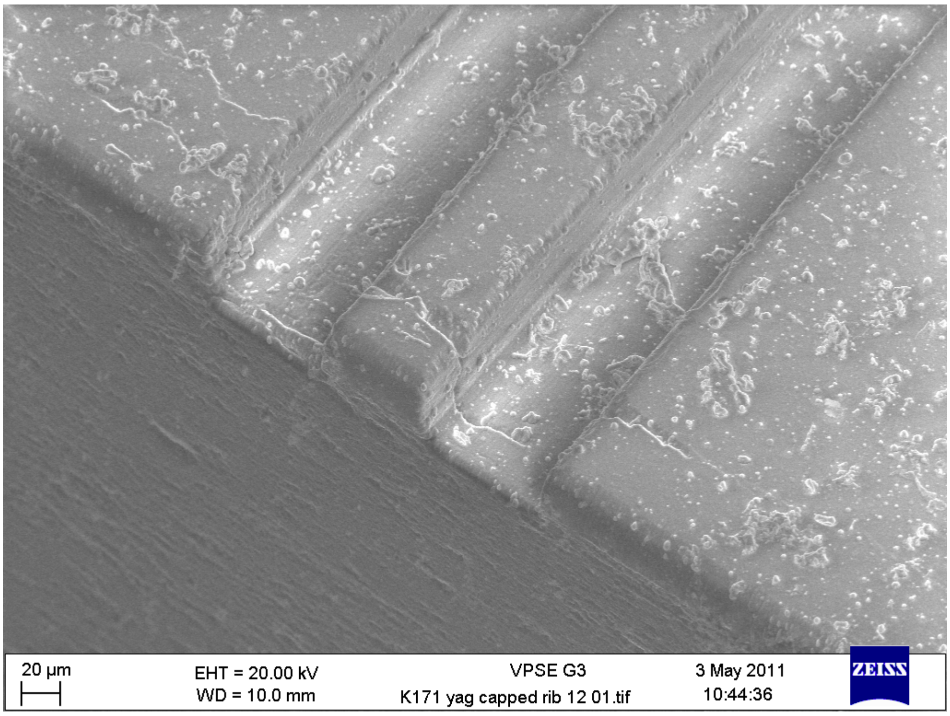

FIGURE 7.15: SEM image of an example channel waveguide after overgrowth of YAG capping layer.

shown. XRD spectra showing crystallinity of GGG and YAG cladding layers of finished channel arrays films are displayed in figure 7.16.

Figure 7.17(a) shows an SEM image of an example channel waveguide after polishing, while figure 7.17(b) shows a wider view of the array. Core and cladding layers can be distinguished, and overgrown layers observed. The layer thickness values shown in figure 7.8(b) were obtained from measurement of these polished end faces. Total length of the channels was 7.7 mm. Fabrication time of the whole array (excluding polishing and analysis) was less that 10 hours, a value that could be decreased by utilising the multi-beam setup. Assuming that material growth parameters are known, no major setup steps are required (no masks required etc.) and a very quick turnaround is possible (loading in the PLD chamber, pumping and heating can be achieved in 25 minutes, loading of the saw in 10 minutes); the method is hence potentially useful as a rapid prototyping tool.

7.5 Waveguiding and lasing experiments

Initial waveguiding and lasing experiments were carried out by Amol Choudhary using a Ti:sapphire laser as a pump source. Lasing was achieved in the planar region but not in the channels. Loss in the planar film was estimated via the Findlay-Clay technique[1]

---

[1] Threshold power is measured for different output coupler reflectivities and plotted against $-\ln(R_1 R_2)/2l$. The x-axis intercept of this plot is a good approximation of the loss coefficient.

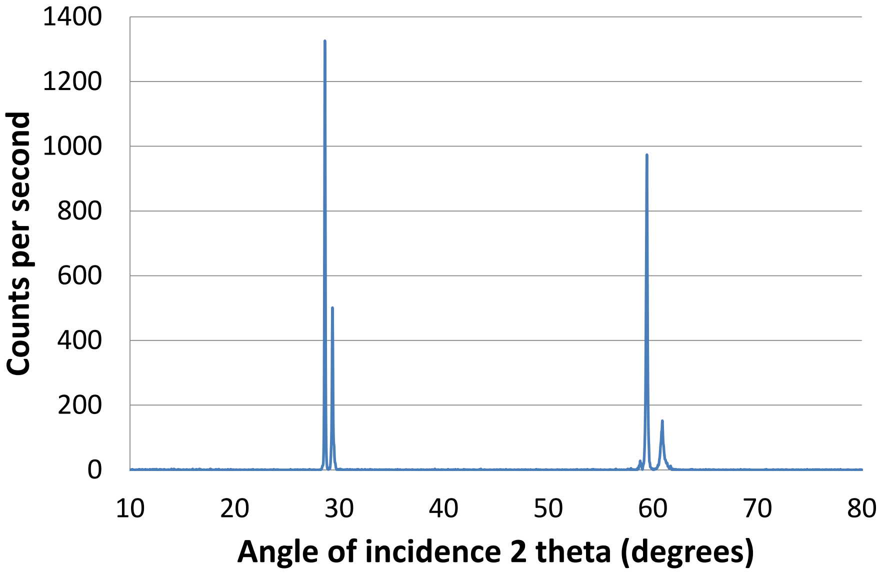

(a) Only (400) and (800) peaks can be observed, demonstrating that crystal growth was in the epitaxial direction.

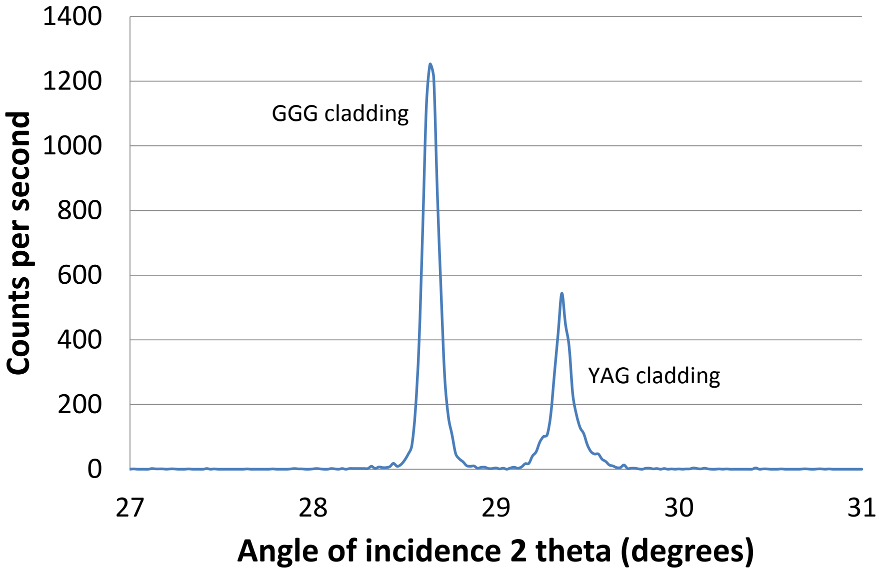

(b) Peaks corresponding to the GGG and YAG cladding layers can be observed. Film is too thick for any substrate contribution to be seen.

Figure 7.16: Full (figure 7.16(a)) and zoomed-in (figure 7.16(b)) XRD spectra of multilayer film after machining and capping.

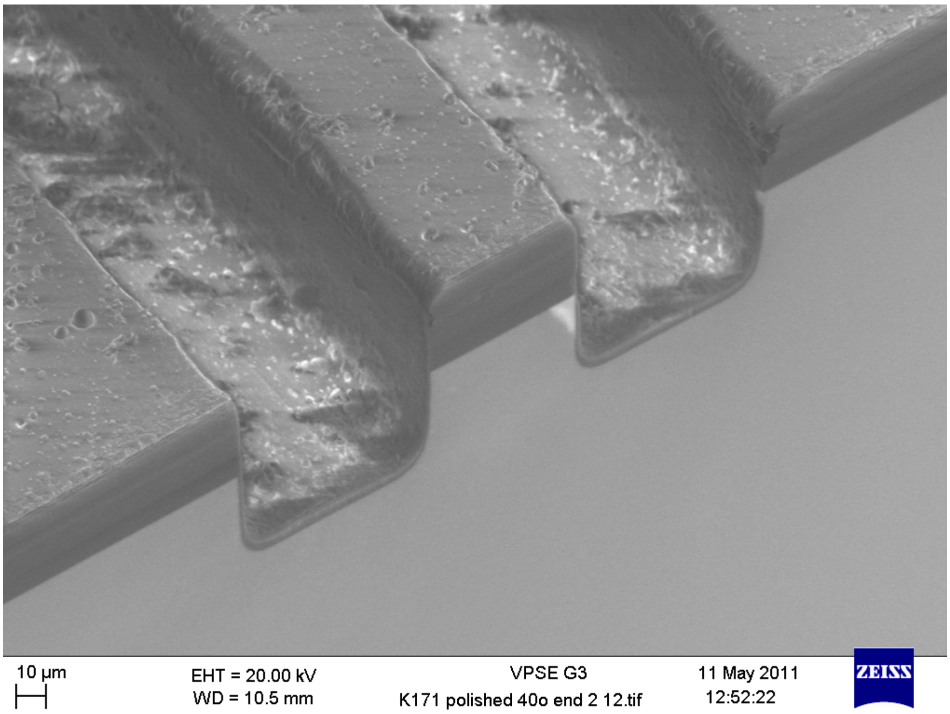

(a) SEM image of an example channel.

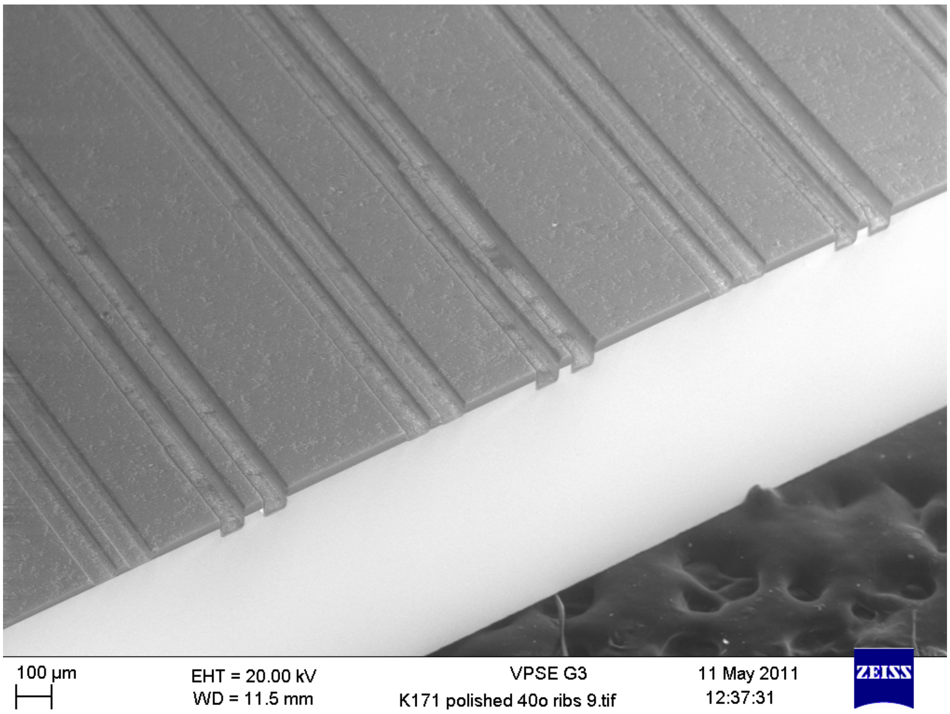

(b) SEM image of an array of channels.

FIGURE 7.17: Channel waveguides after overgrowth and polishing.

[23] to be 0.75 dBcm^{-1}; this value, however, was based on two data points only and hence may not be accurate. Losses in the planar film and channels were estimated via the transmission off-absorption as 1.39 and 5.5 dBcm^{-1} respectively. These values, however, assume 100% launch efficiency; if launch efficiency is lower then calculated losses decrease; for example, if the Findlay-Clay estimate for the planar region is correct and launch efficiency was in fact 93%, losses in the channels may be closer to 5 dBcm^{-1}. The fact that lasing was not achieved in the channels suggests that the losses are indeed very high compared to the surrounding film, but it is not known what contribution is due to chipping or side wall roughness and what is due to non-perpendicular polishing of channels.

7.6 Conclusions and future steps

While the combination of PLD and precision machining has been shown to be effective as a quick and simple technique for fabrication of waveguide arrays suitable for efficient, high power diode pumping, the apparently high losses show that a number of problems remain. Lasing may be possible by diode pumping rather than the sub-optimal Ti:sapphire systems used in the waveguiding experiments previously described, and should allow a proper analysis of channel waveguide loss by the Findlay-Clay technique. Other potential (partial) solutions include:

- Further optimisation of layer growth to reduce particulates. Side wall cladding layer thickness should also be increased if possible to allow single mode output in the horizontal axis.
- Improvements to the micromachining process, such as the use of specialist sapphire-cutting blades.
- Dicing via precision machining to ensure perpendicularity of ribs. Even if further polishing is required, it may be possible to use the diced facet as a reference surface for the autocollimator (see chapter 4).

Chapter 8

Horizontally structured growth

8.1 Introduction

This chapter describes the second of two novel methods utilising PLD to fabricate crystalline structures for lasing applications, exploiting multi-beam PLD in conjunction with a metal cone to create composite crystals with a graded interface between the two components. Preliminary shadow masking experiments are also detailed.

As described in chapter 2, a side-pumped thin disc laser crystal will ideally contain dopant in the centre only. In preparation for the growth of such crystals, two approaches have been developed to confine materials to defined areas of a substrate: physical masking and cone or funnel growth. The latter was found to be superior in the context of thin disc laser crystals; however, physical masking may still be of interest for applications that do not require side pumping.

The main contributions detailed in this chapter are as follows:

- The first known examples of growth of millimetre-sized crystalline features via shadow masked PLD;
- The first demonstration of controlled horizontal grading in crystal via PLD.

8.2 Physical masking

Two approaches to physical masking can be adopted:

- A mask or stencil is applied to the substrate and material deposited under appropriate conditions. This mask is then removed, leaving the required structure. This method is simple but requires a masking material that can be both accurately

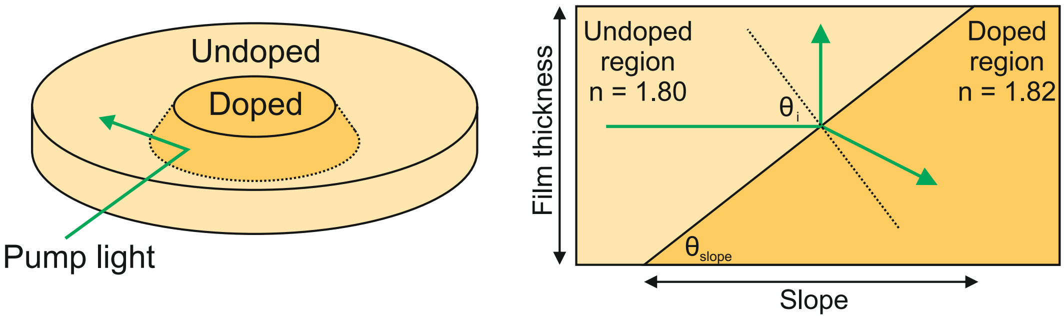

(a) Schematic of crystal (b) Diagram

Figure 8.1: Diagram of model used to approximate levels of Fresnel reflection of side-pumped light due to the interface between areas of higher and lower refractive index (doped, grown through mask and undoped, overgrown respectively). From the Fresnel Equations, if θ_{slope} is small, the percentage of light reflected from the boundary will be high.

machined and applied to the substrate without melting or indiffusing at high temperatures. The method of securing the mask to the substrate is also crucial (see below).

- Material is grown through a mask at low temperature to create a negative mask of amorphous material. The material of interest is then overgrown at high temperature. Growth is crystalline where deposited on bare substrate and amorphous where deposited on the mask. All amorphous material is then removed to leave the structure. In this case, masking material and method are not required to withstand high temperatures, widening the pool of available materials. Removal of the amorphous layer may be difficult: amorphous material can be removed by acid etching, however, relative rates of etching for crystalline garnet and amorphous material of the same composition may be similar.

For side-launching applications such as a side-pumped thin disc laser, any sloping interface between doped and undoped material will result in Fresnel reflections of the pump beam (see figure 8.1) due to the difference in refractive index (varies with doping). As soon as the plasma plume passes the mask it will begin to spread out, so close contact between mask and substrate is crucial to increase the value of θ_{slope}. This has implications both in terms of applying the mask to the substrate and the mask material itself.

Preliminary experiments were carried out using metal foils, in order to test the viability of the concept. These were moderately successful, resulting in the growth of crystalline structures on YAG, although the foils were found to be inappropriate masking materials. Machined silicon masks were then tested, along with various methods of applying the mask to the substrate.

8.2.1 Foil masking

Preliminary experiments were carried out using YAG, a potential material for thin disc lasers. A number of YAG films were deposited in Chamber 1 through masks onto single-crystal (100) orientated YAG substrates. Substrate temperature was ∼800 °C, ambient oxygen gas pressure was 1.0×10^{-2} mbar, fluence was ∼1 J/cm^2 and target-substrate distance was ∼3.5 cm. Depositions were carried out over one hour, resulting in films ∼0.14 µm in thickness. This low growth rate was expected, and was due to the use of poorly-absorbed 266 nm laser light for ablation.

Two masking materials were initially investigated: gold leaf (∼0.1 µm thick) and aluminium foil (∼25 µm thick, ∼99% pure). The edges of aluminium foil masks were hooked over the edges of the substrate, while the gold leaf was thin enough to cling to the substrate surface. Adhesives were not required in either case, a distinct advantage of using such materials.

While gold leaf adhered well to the substrate, it was prone to tearing and deforming easily due to the small thickness and the tendency to cling to both itself and cutting implements. As well as making the foil difficult to work with, sharply defined edges could not be achieved (see figure 8.2). Once covered in amorphous material, the leaf was difficult to remove from the sample even via ultrasonic cleaning. It may be possible to etch away the gold; however, it is unlikely that etchants would successfully reach the metal at all due to the creep of deposited material over the edges of the mask and substrate, and the potential for damaging the crystal is high. This approach was hence not pursued.

Two masking examples were then attempted using a mask of aluminium foil, one with a circular aperture created using a hole punch and one a straight foil strip. Successful crystalline growth was observed in the desired shapes, without the misshapen edge obtained with the gold mask. Foil was much easier to work with than leaf, although it had a tendency to deform/crease. The mask is held in place by hooking over the edges of substrates, hence contact was likely not close, as evinced by the non-melting of the aluminium foil. Figure 8.3 is a composite image of the resultant crystalline YAG circle, diameter approximately 5 mm.

Figures 8.4 and 8.5 show stylus profile scans of the circle and strip masks respectively. Slope, pump incidence angle θ_i and theoretical reflection levels of parallel and perpendicularly polarised light are shown in table 8.1. These calculations, based on the Fresnel

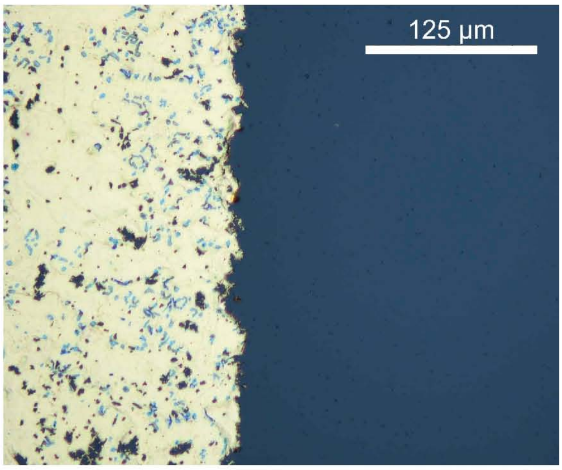

Figure 8.2: Optical microscope image (100x) of the edge of an area of substrate masked with gold leaf

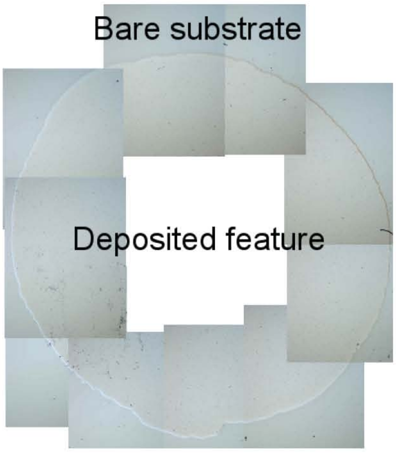

Figure 8.3: Composite image of crystalline YAG circle grown through an aluminium foil mask. Diameter is approximately 5 mm.

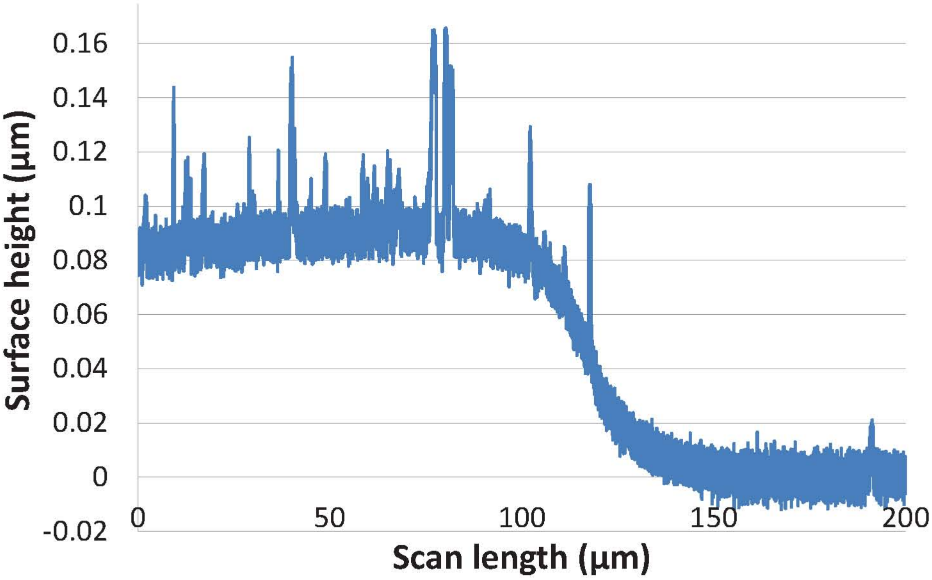

Figure 8.4: Stylus profile of transition from substrate to feature grown through circular mask of Al foil.

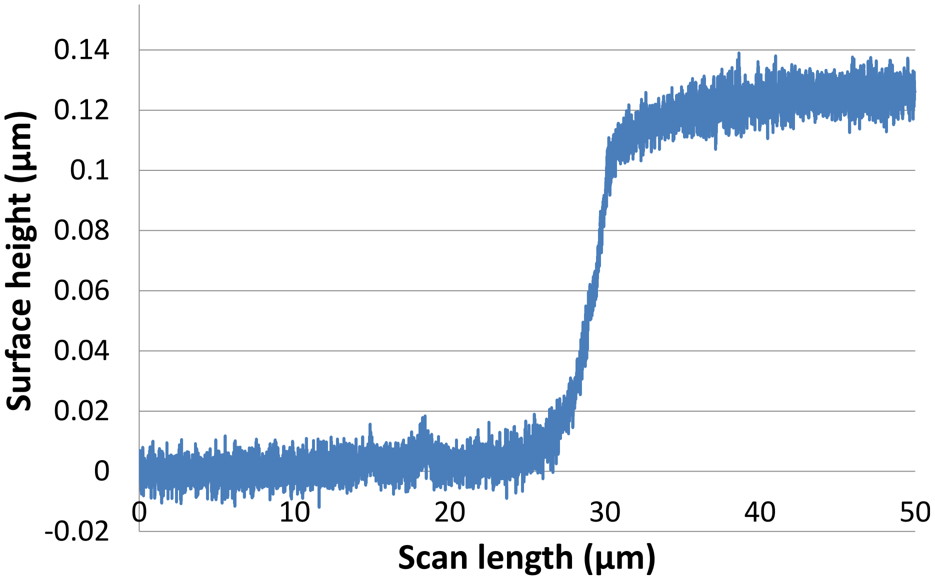

Figure 8.5: Stylus profile of transition from substrate to feature grown through straight strip mask of Al foil.

Sample	**Slope (µm) (see Fig. 8.1)**	θ_i **(degrees)**	$\mathbf{R}_{\parallel}$ **(%)**	$\mathbf{R}_{\perp}$ **(%)**
Circular mask	~60	89.91	95.7	95.8
Strip mask	~6	88.9	58.8	59.4

Table 8.1: Two examples of masked growth using aluminium foil as a masking material, with theoretical incident pump light reflection levels assuming a linear slope.

Equations [176], assume a change in refractive index Δn of 0.02 (50% Yb:YAG surrounded by undoped YAG) and a linear transition from the substrate to the top of the structure.

It should be noted that the growth rate of YAG with 266 nm light is low, and hence films are very thin. This exaggerates the slope, and leads to much higher theoretical reflection levels than would likely be seen with a thicker film (transition distance is unlikely to increase at the same rate as thickness, given the same masking contact). For example, reflections from a 20 µm doped area with a slope of 60 µm would be around only 0.2%. It also may be the case that horizontal resolution is limited by the width of the stylus.

Despite this however, the difference between samples suggests serious issues with repeatability, likely due to the unsophisticated nature of feature machining, lack of flatness and variable contact. Aluminium foil hooked over the substrate may not, therefore, be the most appropriate material or method to use.

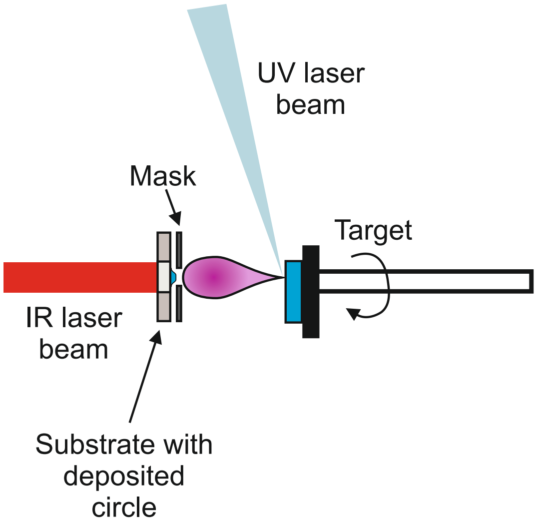

Figure 8.6: Schematic illustrating single-plume masked growth setup

8.2.2 Silicon masking

Silicon has desirable thermal properties for masking, having a low thermal conductivity (desirable to prevent heat sinking) and a high melting point, around 1400 °C. Wafers thin and flat enough to form a close mask, whilst strong enough to withstand high precision machining, are readily available.

Trial films were grown with GGG targets in Chamber 2 using the same deposition conditions as section 5.2, in order to achieve higher growth rates than achieved for the foil-masked films described previously. The setup is illustrated in figure 8.6. Wafers were laser machined into 10×11 mm rectangles, with central holes of diameter 3, 4 or 5 mm. Optical microscope images of the front and back masking surfaces are shown in figure 8.7. Edges of machined features were tapered, hence care was taken to apply the mask with the wider hole face down, to prevent mask or grown feature from being damaged when the mask is removed post-deposition.

Three mask application methods were considered:

1. **Colloidal silver** Paste was applied quickly and simply using a pen. Mask contact was poor, however, due to the thick layer of silver between mask and substrate. The mask could only be removed by bathing it and the substrate in acetone, which resulted in the continued presence of silver particles even after ultrasonic cleaning. It was expected that the silver would oxidise at deposition temperatures, limiting the method's use to low temperature experiments, although this was not observed in initial experiments.

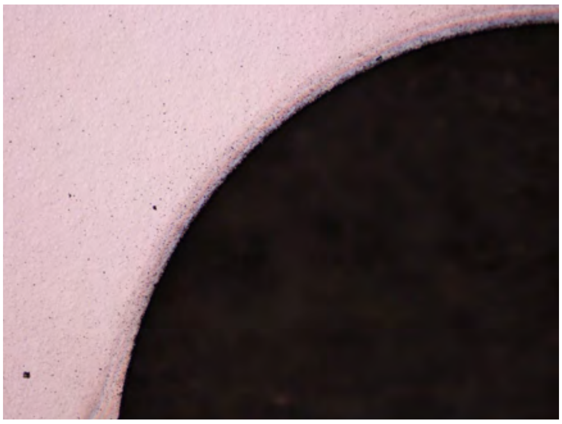

(a) Side in contact with substrate (top of taper, wider hole)

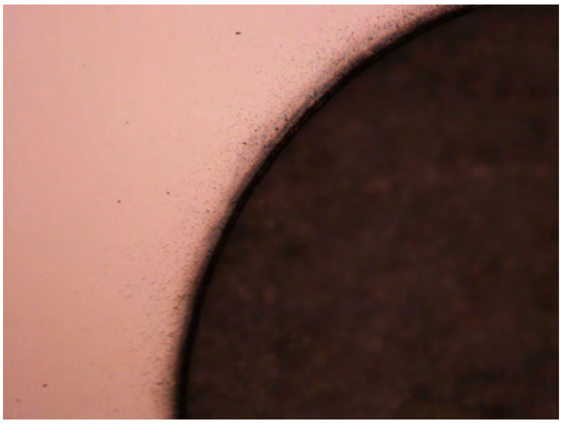

(b) Side not in contact with substrate

FIGURE 8.7: Images of the machined edge of silicon mask

2. **Gallium-indium alloy** This alloy is liquid at room temperature but hardens on heating, and hence could prove a useful high-temperature adhesive. Initial experiments showed, however, that the alloy was very difficult to apply to a confined area due to its very high viscosity. As with colloidal silver, resulting mask-substrate contact was poor and the metal was difficult to remove completely.

3. **Methanol bonding** [177] The substrate was cleaned ultrasonically, dried then placed in a dish and covered in methanol. The mask was applied and the dish left on a hotplate at 50 °C until the methanol had evaporated (around 2-3 days). Any residue remaining on the substrate was unlikely to survive being heated to deposition temperatures. Although the method overall took time to implement, preparation was not excessively time-consuming. The mask was easily removed post-deposition by applying a solvent, and mask-substrate contact was expected to be close due to the presence of no other adhesives.

As it was likely to give the best mask-substrate contact and resulted in the least substrate contamination, methanol bonding was the approach pursued. Both approaches outlined

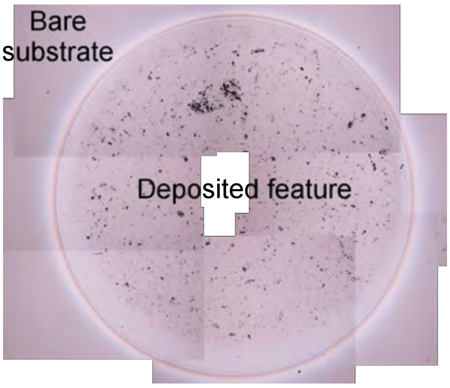

FIGURE 8.8: Composite microscope image of a crystalline circular feature grown via silicon shadow masking. Diameter is approximately 3 mm.

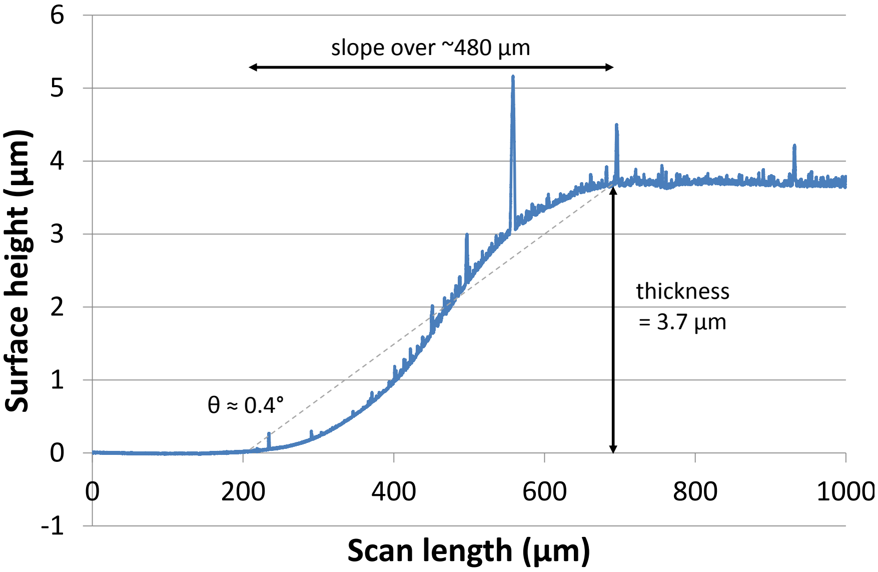

FIGURE 8.9: Stylus profile of the edge of a crystalline GGG circle grown via a machined silicon mask showing a slope angle of ∼0.4 °.

above were investigated i.e. growth of crystalline features directly through a mask, and amorphous growth through the silicon mask to form an amorphous inverse mask, followed by crystalline overgrowth and subsequent etching.

Single-phase crystalline growth of a GGG circle ∼3 mm was achieved, a composite image of which is shown in figure 8.8. Surface profiling (figure 8.9), however, shows that the slope would lead to ∼80% of pump light being reflected, implying that mask contact was very poor.

Direct crystalline growth was found to be much more effective than inverse amorphous mask growth. In the latter case, removal of the material deposited on top of the amorphous mask (assumed to also be amorphous) was attempted via ultrasonic bathing for 90 minutes at 50 °C in acetone, followed by one hour's etching in HF. However, this

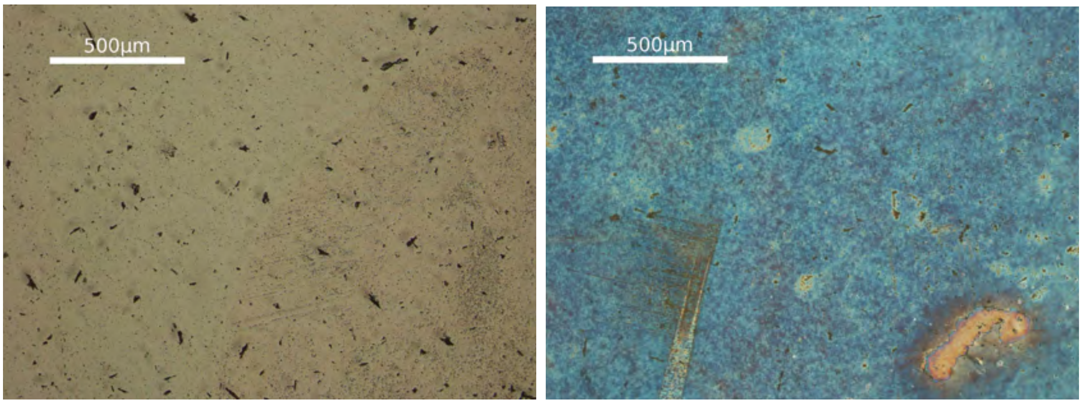

(a) Before HF etching (b) After HF etching

Figure 8.10: Optical microscope images of GGG amorphous inverse mask overgrown with crystalline GGG before and after HF etching. Amorphous material etch rate appeared to be similar to that of crystal.

resulted in damage to the crystalline film (deposited on bare substrate) with very little additional removal of the amorphous material (see figure 8.10).

Bonding was not as strong as was required, and masks appeared to come away from or fall off the substrate when in the deposition position. This is likely due to surface roughness of the mask leading to poor mask-substrate contact. Mask attrition rates were high due to the brittle nature of the silicon: even with careful handling, masks frequently cracked and/or snapped. Some force had to be applied to the masks during the bonding process, achieved using a custom setup of nuts, springs and washers. This, however, was again difficult to achieve without cracking the mask. As can be seen in figure 8.7, the surface roughness of the side in contact with the substrate appears to be greater than that of the opposite side; better adhesion may have been achieved if the wafers were machined on the opposite side. However, the issues with the wafers' mechanical properties suggested that silicon masking would not be successful even then.

8.3 Cone growth

Masking is fraught with problems, particularly in terms of achieving adequate mask-substrate contact. The issue of pump reflections is also a serious one, severely limiting the technique's usefulness for applications requiring side pumping[1]. Instead, it may be preferable to grow a structure such as that illustrated in figure 8.11. The dopant is confined to the centre of the sample; however, unlike the masked examples, dopant is graded smoothly from the centre to the outside. There is no distinct sloping boundary between areas of different refractive index and hence significant pump reflection should be eliminated.

---

[1] Although it may be of interest for end-pumping applications, where the side angles of features may be less crucial.

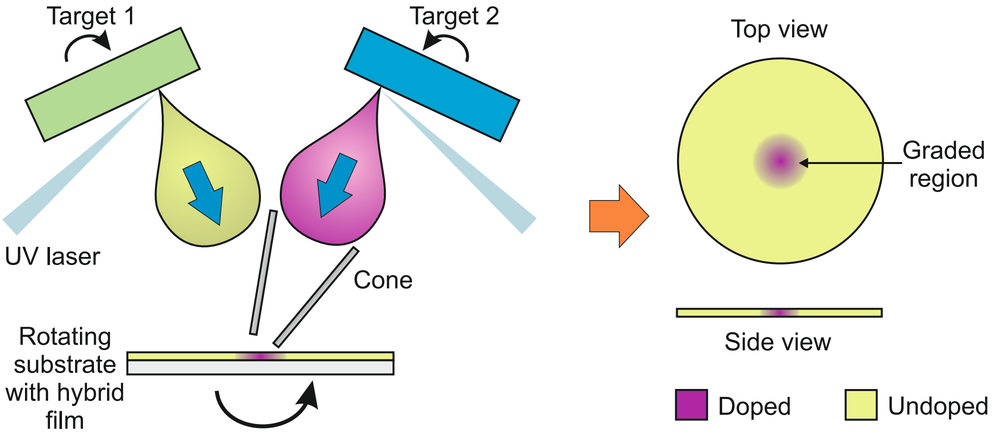

Figure 8.11: Schematic illustrating cone growth concept (left) and resulting hybrid structure (right)

This grading is achieved simply using a cone. Figure 8.11 shows a schematic of the concept. A cone is placed in front of a target of material (e.g. doped) and directed to the centre of a crystal substrate. When the target is ablated the plume is funnelled through the cone and deposition is confined to the centre of the substrate. If a second target is ablated simultaneously and the substrate is rotated, a hybrid crystal will be formed consisting of one material in the centre, a second material around the outside and a graded interface in between.

Stainless steel cake decorating cones were used for the proof of principle experiments detailed in this section. They are cheap, easy to obtain and available with apertures of a number of sizes and shapes. Single-plume experiments were carried out initially in Chamber 1 to assess the validity of the cone growth concept, followed by dual-plume experiments in Chamber 2. In both cases, a cone of 2.3 mm aperture (internal diameter) was fastened in a holder of 0.2 mm thick aluminium foil and copper wire, which was itself fastened to the respective chamber's substrate blocker arm. The cone and experimental setups are illustrated in figure 8.12.

8.3.1 Single-plume cone growth

Chamber 1 was chosen for a preliminary test of single-plume cone growth due to the relative ease of introducing a cone. The focus of the experiment was to discover whether plume confinement was at all possible, and hence high-quality crystal growth was not a priority. Ti:sapphire was already loaded into the chamber as part of separate experiments and so was used for convenience. An excimer laser of fluence ~3 Jcm^{-2} ablated a single-crystal Ti:sapphire target and the resulting plume was funnelled through the cone and deposited on a miscut sapphire substrate heated to ~950 °C. Target-substrate distance was ~50 mm and the cone was held perpendicular to the substrate with a <1 mm gap (see figure 8.12(a)). Ambient background argon gas pressure was 2×10^{-2} mbar.

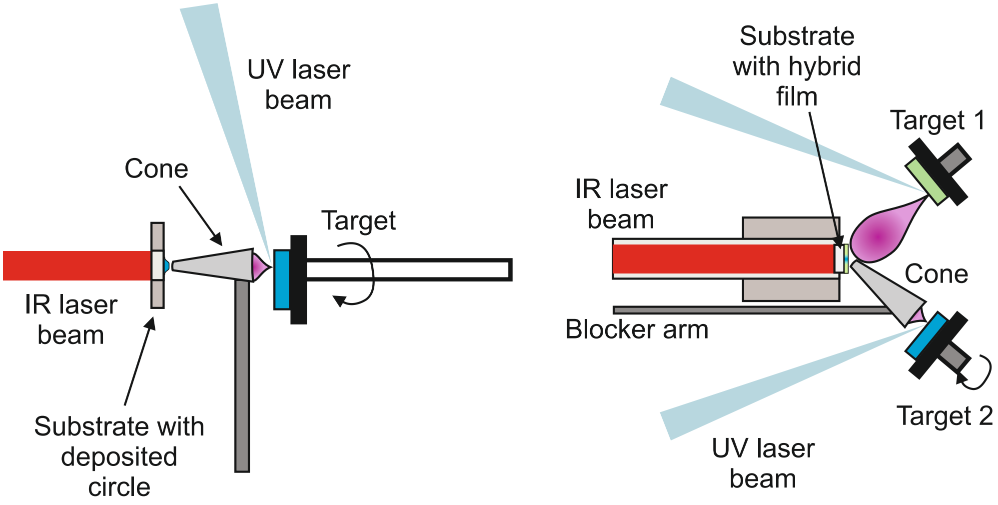

(a) Single-plume cone growth in Chamber 1 (b) Multi-plume growth in Chamber 2

Figure 8.12: Schematics of cone growth setups in Chambers 1 and 2.

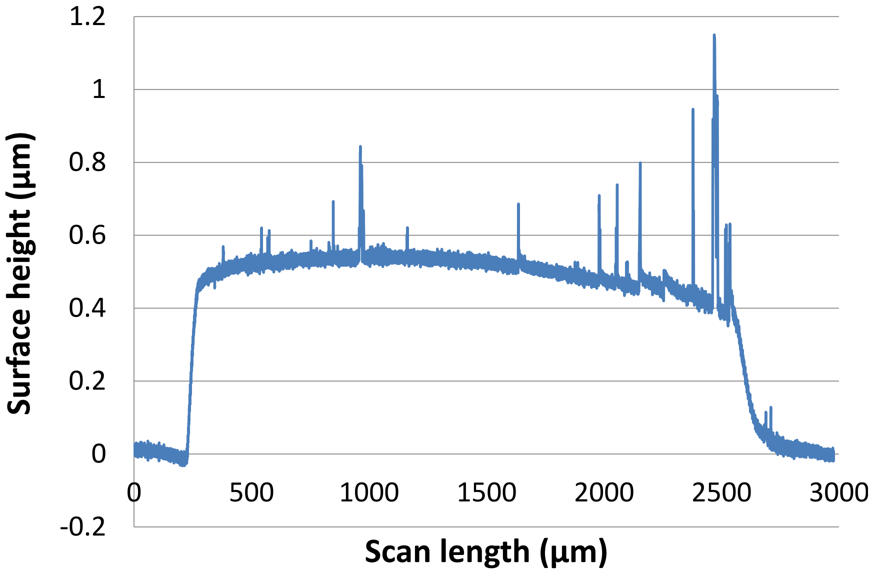

Figure 8.13: Stylus profile of an alumina circular feature grown through a stainless steel cone.

A photograph and surface profile scan of the resulting circle of material can be seen in figures 8.14 and 8.13 respectively. The circle was well defined, despite no substrate rotation, and no deposition was detected around the outside of the cone, proving that plume confinement through a cone is possible. The circle had a ∼2.4 mm diameter, slightly larger than the cone aperture (2.3 mm). This and the edge slope over ∼150 µm indicate that, as with masking, the plume expanded after exiting the cone. Growth rate was much lower than expected (∼1 µm/hr compared to ∼5 µm/hr for similar non-cone conditions) and significant coating of the inside of the cone was observed. As expected, the film was not crystalline but amorphous.

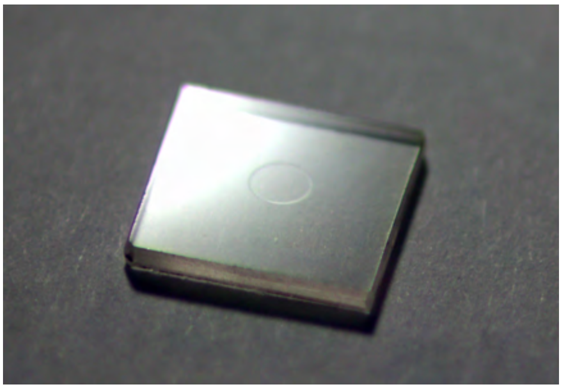

FIGURE 8.14: Photograph of alumina circle on alumina substrate via single-plume cone growth

8.3.2 Dual-plume cone growth

Having proven the possibility of horizontal structuring using a cone, dual-plume test films were grown in Chamber 2. An excimer laser was used to ablate a YAG target, with the resulting plume being funnelled through the cone, while a Nd:YAG laser simultaneously ablated an undoped GGG target. Fluences in both cases were $\sim$2.5 Jcm^{-2} and the ambient background gas pressure was 1×10^{-2} mbar. Targets were rotated but kept at a constant angle of 24°; the cone was held perpendicular to the target and hence was not perpendicular to the substrate, as indicated in figure 8.12(b). In order to include the cone without blocking either ablating beam, the minimum target-substrate distance was found to be 49 mm. YAG and GGG were chosen for the experiment as they were known to grow well as separate and mixed garnets but were dissimilar enough for relative concentrations to be distinguished via EDX analysis.

Two attempts at dual-plume cone growth were made. Due to poor cone-substrate alignment, the first of these resulted in a hybrid film with a ring of YAG surrounded by GGG, rather than the desired circle. Target-substrate distance was 49 mm and the angled tip of the cone was in contact with the substrate. This likely led to some heat sinking, resulting in rough, frosty growth as can be seen in figure 8.15.

Cone-substrate alignment was corrected by eye and target-substrate distance was increased to 50 mm for the second attempt, to introduce a 1 mm gap between the substrate and cone. The resulting structure matched well the desired design, consisting of a GGG outer region, mixed GGG/YAG centre and graded interface. The GGG plume was directed towards the centre of the substrate, hence mixing in the centre was unavoidable. Given the plume spreading, some mixing would be unavoidable even if the outer plume was directed away from the centre. However, in the context of a doped/undoped hybrid crystal, such mixing would not present a problem; target doping levels would merely need to be increased to compensate.

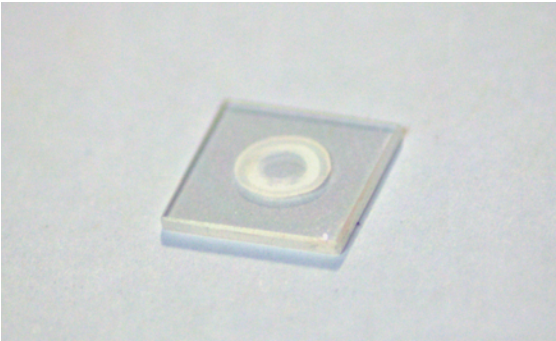

Figure 8.15: Photograph of failed dual plume cone growth attempt, consisting of YAG ring surrounded by GGG on a YAG substrate. Cone-substrate contact led to heat sinking and frosty growth, and poor cone alignment led to the formation of a ring rather than a circle.

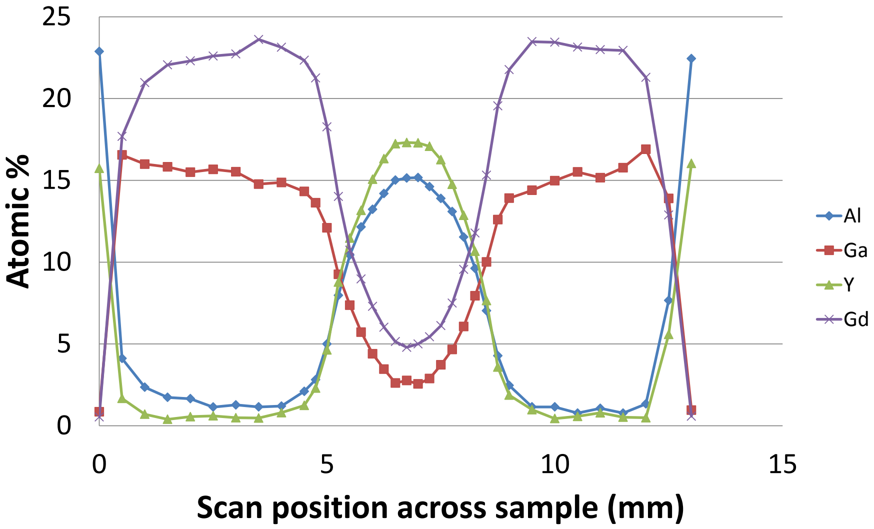

Figure 8.16: EDX scan across dual-plume cone grown sample. The grading from GGG to mixed YAG/GGG in the centre can be clearly observed.

The smooth grading from GGG into mixed YAG/GGG can be seen in figure 8.16. Gadolinium and gallium atomic percentages drop from ∼23 and ∼15% to ∼5 and ∼3% respectively, while yttrium and aluminium atomic concentrations increase correspondingly. GGG growth is far from stoichiometric, a consequence of the compromised growing conditions required to grow GGG and YAG simultaneously. The grading can also be observed via XRD, as shown in figure 8.17: a contribution from the graded and central areas can be observed between 27.8 and 28.7 °, as can a sharper peak corresponding to the GGG-only outer region at ∼27.6 °.

The total diameter of the mixed area including the graded region is ∼5 mm, demonstrating the wide spread of the funnelled plume after exciting the cone. It should be noted that a small amount of yttrium and aluminium can be detected even outside the central region; while there may be some spreading of the plume beyond the circular area, it is also likely that the substrate is being detected, due to the small film thickness

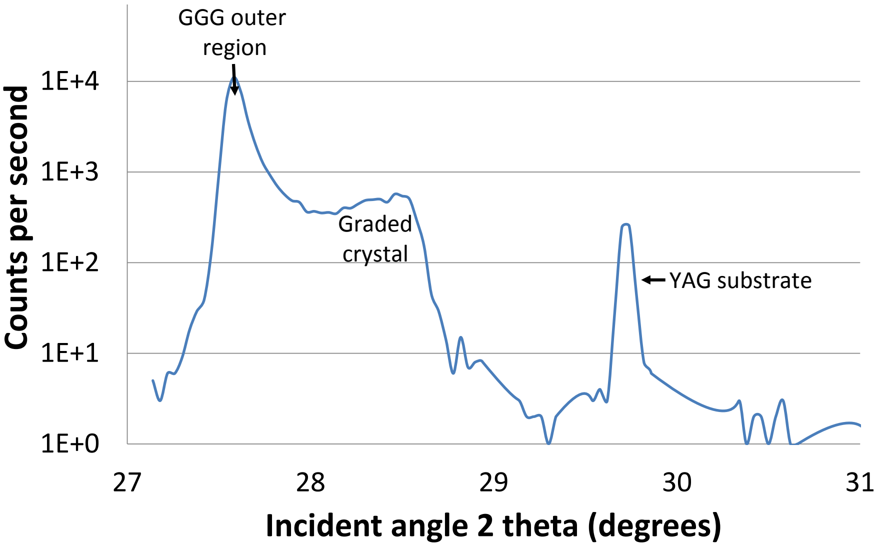

Figure 8.17: XRD spectrum of cone grown hybrid crystal. A peak corresponding to the non-stoichiometric GGG outer region can be observed around 27.6 ° next to a wide region up to ~28.7 °, a contribution from the central and graded parts of the crystal. A small peak corresponding to the underlying YAG substrate can also be observed, to which data were normalised.

(~3.5 µm) and relatively large volume interrogated by the EDX beam (some µm^3). If thickness were increased to >5 µm then traces of the substrate should not be detected.

The mixing of plumes in the centre resulted in a circular raised feature with an approximately trapezoidal diameter cross section. The size and shape of such raised areas could be controlled to some extent by choice of cone size, shape and tip angle, as well as by changing relative growth rates using blockers and condition tuning, but complete elimination of such features may prove extremely difficult. This does not present an immediate problem, as such features could be removed by polishing. They do, however, present an intriguing possibility in the field of micro- and integrated optics. If good control over feature size and shape could be achieved, crystalline microlenses could be fabricated relatively simply, similar to amorphous microlenses demonstrated previously by CW laser effusion [178].

8.4 Conclusions and future steps

Horizontal confinement of garnet crystal by PLD has been demonstrated in both single- and multi-plume geometries. In the latter case, controlled horizontal grading between the central and outer sections of the hybrid crystal has been achieved. The surface profile of the hybrid crystal was not flat but exhibited a raised central feature; control over such features may in future allow growth of crystalline microlenses.

Having proven the efficacy of the simple cone growth technique, a superior way of holding the cone is desirable. While the current arrangement of metal foils has the advantage of speed and versatility, a more rigid setup would ensure repeatability and increase efficiency in further experiments. Growth with practical materials is the obvious next step. While, Yb:YAG is a popular material for thin disc lasing, simultaneous growth from multiple YAG targets is not possible with the current ablating lasers due to the poor absorption of 266 nm light by YAG. Instead, Yb:GGG is likely to prove a more appropriate material, doped and undoped GGG having been grown successfully with both excimer and Nd:YAG lasers for many years. It is not anticipated that Yb:GGG will exhibit different growth characteristics from undoped or Nd:GGG; however, the likely necessity of using a ceramic target may present problems with particulates and/or target lifetime.

The move to GGG will in itself require a full investigation of optimum growth parameters in the cone geometry. Ambient pressure can be increased for GGG-only growth, which is expected to result in stoichiometry closer to that of bulk, as well as the higher growth rates required for practical growth of laser crystals. Outer region growth rates could also be improved by introduction of a third target and laser to deposit additional undoped GGG. The effect of the various stress states in the crystal (due to the hybrid nature of the crystal, the uneven profile, the growth conditions required and any differences in stoichiometry compared to bulk), and whether these place any restrictions on film thickness or growth rate, must also be investigated.

Chapter 9

Conclusions and future work

9.1 Conclusions summary

9.1.1 Summary of introductory chapters

Chapters 1 and 2 set the scene for the experiments described in this thesis. Previous landmarks in the field of single- and multi-beam PLD were described, with particular emphasis on materials and devices for optical applications. The relative merits of alternative deposition and waveguide fabrication techniques were discussed in comparison with PLD. It was concluded that, though film quality is not always as high (e.g. due to particulate formation), PLD in general and multi-beam, multi-target PLD in particular show great potential in terms of speed, ease and versatility compared with many other fabrication methods.

Chapter 3 introduced the theoretical concepts underpinning the experimental techniques described in chapter 4, as well as the devices introduced in chapter 2. Attention was drawn to some of the potential performance-limiting factors, such as particulate production and limits to thick film growth. Both the single- and multi-beam PLD setups relevant to this thesis were described in detail in chapter 4, and the shutter technique for automated mixed/multilayer growth was introduced. Surface, crystal structure and deposition plasma analysis methods were also described in this chapter.

9.1.2 Summary of results chapters

The relative delay between plasma plumes in multi-beam, multi-target PLD was investigated to discover any effect on the resulting film. Composition was found not to be significantly affected; however, for plumes of GGG and GSGG, lattice constant was shown to increase from the expected value when delay was $\leq$400 µs, a consequence of higher energy ion bombardment of the growing film by the second plume. The first plume sweeps out an area of gas, leaving a partial vacuum that takes some hundreds of microseconds to infill. If the second plume follows within this time it is effectively deposited at a lower background gas pressure, leading to the higher ion energies observed and resulting in increased strain in the lattice, which manifests as a larger lattice constant. A second, unknown effect was also in play for delays between ∼10 and ∼40 µs, serving to also increase the lattice constant. Plume delay may hence prove useful as a tool for fine control of strain/lattice constant in a multi-plume film.

A second tool was developed and investigated: the shutter technique. Computer-controlled mechanical blockers were placed in the path of each beam, allowing automated control of the relative repetition rates of the lasers. The technique was demonstrated initially by the growth of mixed layers, superlattices and multilayers of various layer thicknesses, and extended by growth of chirped superlattices in different configurations. Evidence of distinct layering was observed via XRD and XRR down to the unit cell level, with layering potentially occurring at the sub-unit cell level although this could not be confirmed by the analysis methods used. Layers should hence in future be deposited on a $\leq$1 nm scale in order to achieve complete mixing or grading.

Having developed and tested the technique for crystalline multilayer growth, functional devices were grown in the form of YAG/GGG Bragg stacks. Garnet crystal has a much higher damage threshold than the amorphous materials conventionally used for mirror fabrication, and hence the reflectors were expected to be of interest as high power laser mirrors as well as high temperature sensors. Structures of various geometries were fabricated using shutters programmed via *LabVIEW*, including 145 layer stacks exhibiting >99% reflection as well as π shifted designs. A crystalline apodised sample was grown by mixing plumes to obtain an approximately Gaussian grating-strength profile, the first known example of such sophisticated crystal engineering with PLD. As expected, this was shown to substantially reduce side lobe reflections. Peak reflection wavelength could be tuned by changing incident position on the sample, due to the surface curvature.

YAG and GGG were used as they had the largest index contrast of the garnets available; however, the compromised conditions required for automated growth resulted in layers that, while single-phase crystalline, had stoichiometry far from bulk. This is likely to have adversely influenced the structures' ability to withstand high temperature annealing.

An array of double-clad crystal rib waveguides was fabricated by a combined PLD-precision machining technique. The guides had thicknesses of ∼40 µm and widths of ∼40 and ∼60 µm, and hence have dimensions suitable for diode pumping. Fabrication of a 13-rib array took less than 10 hours in total (excluding polishing), a time which may reduced yet further in future with the use of a multi-beam geometry: the technique is hence potentially useful as a rapid prototyping method for thick crystalline channel waveguide fabrication. Losses in the ribs, however, are believed to be very high (exact values could not be measured), likely at least in part due to scattering from particulates in the film and side-wall chipping resulting from the micromachining process.

Horizontal confinement of garnet crystal by PLD was demonstrated in both single- and multi-plume geometries. In the former case, millimetre-sized crystal features were deposited by shadow masking, using laser-machined silicon wafers as masks. In the latter case, multi-plume cone growth resulted in a hybrid crystal of YAG and GGG, non-functional materials used to clearly demonstrate the hybrid nature of the film. The YAG plume was funnelled through a stainless steel cone, while GGG was deposited around the outside as the substrate rotated. As a consequence of plume mixing after the funnelled plume exited the cone, controlled horizontal grading between the central and outer sections of the hybrid crystal was achieved. The surface profile of the hybrid crystal was not flat but exhibited a raised central feature; this may be polished back in the case of a practical laser crystal.

9.2 Future directions

Although the results presented in this thesis represent significant contributions to crystal and structure engineering by PLD, only the first steps have been taken. In each case, future goals and improvements have been discussed at the end of the relevant chapter, with only a summary given in this section.

Although the shutter technique has been used successfully to grow a variety of prototype structures, many improvements are still required before shuttered PLD can be considered a realistic manufacturing technique. Issues with repeatability can be addressed by the introduction of in-situ thickness measurement, possibly using a HeNe laser. This will, however, require the use of different materials. Such materials may include YIG/GGG stacks, which are also of interest for their magneto-optic applications, and sesquioxides, which may present additional advantages in the form of higher power/temperature damage thresholds. Improvements to the *LabVIEW* control programs should be made to allow for automation of apodised structures, and *MATLAB* modelling should be extended to include apodised designs. Non-Gaussian apodisation profiles are also still to be attempted, as is chirped growth: highly-reflective chirped Bragg gratings should be composed of >250 layers and growth has hence not been attempted due to the time constraints.

Quantification of propagation loss of the double-clad channel waveguides described in chapter 7 may be possible by the Findlay-Clay technique if lasing could be achieved, for example by diode pumping. This may be possible with existing samples; however, losses and hence lasing thresholds are suspected to be prohibitively high. Potential avenues for reducing waveguide loss include improvements to the PLD growth to reduce particulates and increase side wall cladding thickness, use of alternative saw blades to reduce side wall chipping and precision dicing to ensure channel perpendicularity. PLD may also be combined with other methods of double-clad channel waveguide fabrication (replacing physical micromachining with ion beam etching for example), with practical limitations and device performance compared with the PLD-sawing technique.

The hybrid crystal described in chapter 8 was grown with one plume funnelled through a cone held in place with an arrangement of metal foils. A more rigid setup is required if repeatable hybrid growth is to be achieved. Further investigations into the effect of hybridisation on a crystal need to be undertaken with functional materials, and appropriate (possibly compromised) growth conditions determined. Yb:GGG is a candidate for a thin disc material due to the possibility of ablation with both excimer and quadrupled Nd:YAG radiation, a problem that prohibits the growth of Yb:YAG in this geometry with the equipment available. Any such new material might also be grown in planar form in order for losses to be quantified and to allow comparison with hybrid crystals. A third target of the same material as the outer part of the crystal (i.e GGG in the case exhibited in this thesis) may be introduced to increase the growth rate of the outer part and perhaps provide some control over the shape and size of any raised features in the centre of a crystal, which may prove of interest as crystalline microlenses.

Additional improvements may be possible in many cases by the use of sesquioxides in place of garnet. In the case of Bragg stacks, they may prove superior to garnets in terms of damage threshold and compromised-condition multilayer growth. Thick and/or multilayer channel waveguide laser fabrication could be attempted in doped sesquioxides (e.g. Yb:Lu_2O_3), although as with garnets specialist high-hardness blades may be required to obtain chip-minimised (i.e. low loss) waveguides. Doped sesquioxides are of great interest for thin disc laser applications due to their high thermal conductivities. As in the Bragg case they should have a wider window of optimal conditions, and hence may prove ideal candidates for further hybrid crystal cone growth experiments. Preliminary test growth of various sesquioxides has been attempted with very promising results, as described in appendix C.

Appendix A

Waveguide theory

This appendix outlines the theory describing planar and channel waveguide modes. A basic discussion of waveguiding principles has been presented in section 3.3.

A.1 Planar waveguide modes

A waveguide mode is a set of electromagnetic fields which maintain their spacial distribution at they propagate, varying only by a phase factor as described by the propagation constant β i.e.

$$E(x, y, z) = E(x, y)e^{i(\omega t - \beta z)} \tag{A.1a}$$

$$H(x, y, z) = H(x, y)e^{i(\omega t - \beta z)} \tag{A.1b}$$

where

$$\beta = \frac{2\pi}{\lambda} n_{eff} \tag{A.2}$$

The quantity n_{eff}, the effective refractive index, depends not just on the indices of the waveguide layers but also the waveguide design. As such is it usually computed using numerical methods.

The modes are solutions of the wave equation (Equation A.3) in each part of the guide. They can be separated into two waves: one that has only a transverse magnetic field i.e. $H_z = 0$ and one that has only a transverse electric field i.e. $E_z = 0$, which are known as transverse magnetic (TM) and transverse electric (TE) modes respectively.

$$\nabla^2 \mathbf{E} - \mu\epsilon \frac{\delta \mathbf{E}}{\delta t} = 0 \tag{A.3}$$

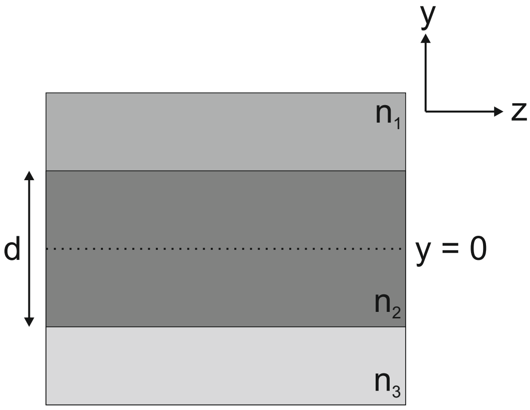

FIGURE A.1: Side-view schematic of an asymmetric slab waveguide, where light propagates in the z direction

A.1.1 Asymmetric slab waveguide

First we consider as slab waveguide as shown in figure A.1, consisting of three layers where $n_2 > n_1, n_3$. The derivations for TM and TE modes are similar; hence only the TE derivation will be shown in detail below. Both make use of Maxwell's equations:

$$\nabla \times \mathbf{E} = -\mu \frac{\delta \mathbf{H}}{\delta t} \tag{A.4a}$$

$$\nabla \times \mathbf{H} = \epsilon \frac{\delta \mathbf{E}}{\delta t} \tag{A.4b}$$

For an infinite slab the field does not vary in x and Equation A.3 reduces to:

$$\frac{\delta^2}{\delta y^2} E(x,y) + k_0^2 (n_{1,2,3}^2 - n_{eff}^2) E(x,y) = 0 \tag{A.5}$$

Solutions to this equation have the form:

$$E_x(y,z) = \begin{cases} A_1 e^{-\alpha_1 y} e^{-i\beta z} & \text{Cladding i.e.} y \geq d/2 \\ A_2 \cos(\alpha_2 y + \phi) e^{-i\beta z} & \text{Core i.e.} -d/2 < y < d/2 \\ A_3 e^{\alpha_3 y} e^{-i\beta z} & \text{Substrate i.e.} y \leq -d/2 \end{cases} \tag{A.6}$$

Inserting Equation A.6 into Equation A.5 gives the dispersion relations:

$$\alpha_1 = k_0 \sqrt{n_{eff}^2 - n_1^2} \tag{A.7a}$$

$$\alpha_2 = k_0 \sqrt{n_2^2 - n_{eff}^2} \tag{A.7b}$$

$$\alpha_3 = k_0\sqrt{n_{eff}^2 - n_3^2} \tag{A.7c}$$

The magnetic field is obtained using Maxwell's equation (Equation A.4a) to give solutions of the form:

$$H_z(y,z) = \begin{cases} \frac{-i}{\mu\omega} A_1 \alpha_1 e^{-\alpha_1 y} e^{-i\beta z} & \text{Cladding} \\ \frac{-i}{\mu\omega} A_2 \sin(\alpha_2 y + \phi) e^{-i\beta z} & \text{Core} \\ \frac{-i}{\mu\omega} A_3 \alpha_3 e^{\alpha_3 y} e^{-i\beta z} & \text{Substrate} \end{cases} \tag{A.8}$$

Solutions must be continuous across the boundaries (i.e. at $y = \pm d/2$) i.e.

$$A_1 e^{-\alpha_1 \frac{d}{2}} e^{-i\beta z} = A_2 \cos(\alpha_2 \frac{d}{2} + \phi) e^{-i\beta z} \tag{A.9a}$$

$$\frac{-i}{\mu\omega} A_1 \alpha_1 e^{-\alpha_1 y} e^{-i\beta z} = \frac{-i}{\mu\omega} A_2 \sin(\alpha_2 y + \phi) e^{-i\beta z} \tag{A.9b}$$

which as $\tan(x) = \tan(x \pm n\pi)$ can be rearranged to give the TE guidance condition:

$$\alpha_2 d - \tan^{-1}\left(\frac{\alpha_1}{\alpha_2}\right) - \tan^{-1}\left(\frac{\alpha_3}{\alpha_2}\right) = p\pi \tag{A.10}$$

where p is the mode number.

We can express A_1 and A_3 in terms of A_2 to give the solutions:

$$E_x(y,z) = \begin{cases} A_2 \cos(\frac{\alpha_2 d}{2} + \phi) e^{-\alpha_1 (y - \frac{d}{2})} e^{-i\beta z} & \text{Cladding} \\ A_2 \cos(\alpha_2 y + \phi) e^{-i\beta z} & \text{Core} \\ A_2 \cos(\frac{\alpha_2 d}{2} - \phi) e^{-\alpha_3 (y + \frac{d}{2})} e^{-i\beta z} & \text{Substrate} \end{cases} \tag{A.11}$$

TM modes can be derived similarly making use of Equation A.4b to obtain the solutions:

$$H_y(x,z) = \begin{cases} A_2 \cos(\frac{\alpha_2 d}{2} + \phi') e^{-\alpha_1 (x - \frac{d}{2})} e^{-i\beta z} & \text{Cladding} \\ A_2 \cos(\alpha_2 x + \phi') e^{-i\beta z} & \text{Core} \\ A_2 \cos(\frac{\alpha_2 d}{2} - \phi') e^{-\alpha_3 (x + \frac{d}{2})} e^{-i\beta z} & \text{Substrate} \end{cases} \tag{A.12}$$

A.1.2 Symmetric slab waveguide

For the special case where substrate and cladding have the same refractive index (a symmetric slab waveguide) $\alpha_1 = \alpha_3 = \alpha$ and Equation A.11 becomes:

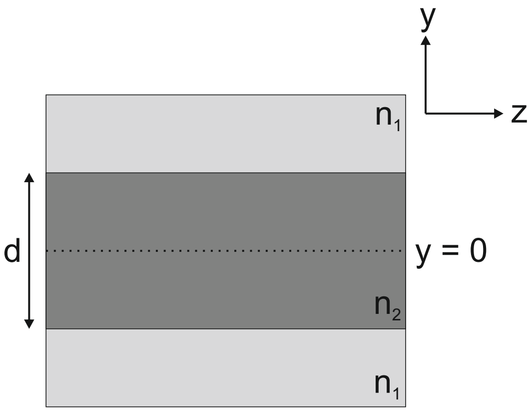

FIGURE A.2: Side-view schematic of a symmetric slab waveguide

$$E_x(y,z) = \begin{cases} A_2\cos(\frac{\alpha_2 d}{2})e^{-\alpha(y-\frac{d}{2})}e^{-i\beta z} & \text{Cladding} \\ A_2\cos(\alpha_2)e^{-i\beta z} \text{ or } A_2\sin(\alpha_2 y)e^{-i\beta z} & \text{Core} \\ A_2\cos(\frac{\alpha_2 d}{2})e^{-\alpha(y+\frac{d}{2})}e^{-i\beta z} & \text{Substrate} \end{cases} \tag{A.13}$$

Solutions of the form $\cos\alpha_2 y$ and $\sin\alpha_2 y$ are known as even and odd modes respectively. The guidance condition also reduces to:

$$\alpha_2 d - 2\tan^{-1}\left(\frac{\alpha_1}{\alpha_2}\right) = p\pi \tag{A.14}$$

For a guided mode, α should be real and positive. A cut-off exists, therefore, where $\alpha = 0$ and the guidance condition becomes:

$$\alpha_2 d = M\pi = \frac{2\pi}{\lambda}\text{NA} \tag{A.15a}$$

$$M = \frac{2d}{\lambda}\text{NA} \tag{A.15b}$$

where M is the maximum number of modes supported above the fundamental.

A.2 Channel waveguides

A rectangular channel waveguide guides light in two dimensions rather than one (i.e. $\delta/\delta x \neq 0$). It can be approximated by ignoring the blue areas in figure A.3(a) (where the field distribution will be low), and treating the guide as two separate three-layer planar waveguides (see figure A.3(b)). The resulting two guidance conditions in the x and y directions are given in Equation A.16 and the dispersion relations in Equation A.17.

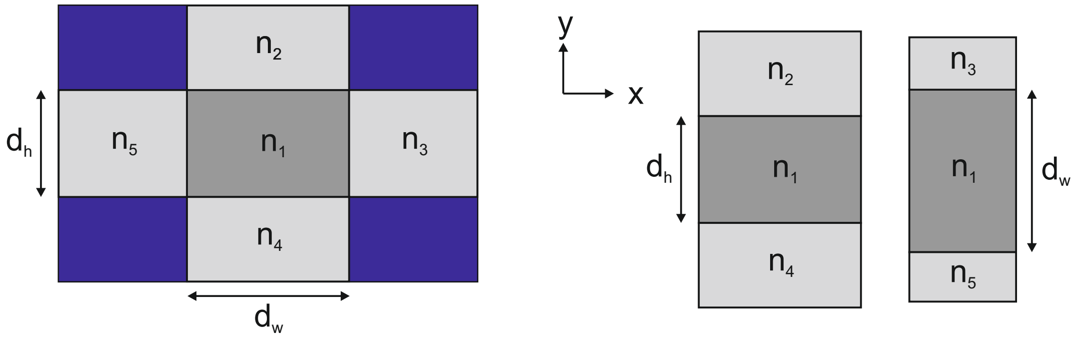

(a) (b)

Figure A.3: End-on channel waveguide schematic; blue areas can be ignored and the waveguide approximated as two planar waveguides

$$\alpha_{2(x,y)} d_{w,h} - \tan^{-1}\left(\frac{\alpha_1}{\alpha_2}\right) - \tan^{-1}\left(\frac{\alpha_3}{\alpha_2}\right) = p\pi \tag{A.16}$$

$$\alpha_{1(x,y)} = k_0\sqrt{n^2_{eff(x,y)} - n^2_{(5,2)}} \tag{A.17a}$$

$$\alpha_{2(x,y)} = k_0\sqrt{n^2_1 - n^2_{eff(x,y)}} \tag{A.17b}$$

$$\alpha_{3(x,y)} = k_0\sqrt{n^2_{eff(x,y)} - n^2_{(3,4)}} \tag{A.17c}$$

Appendix B

Bragg reflection theory

The response of a Bragg grating can be modelled by considering the characteristic matrix, which represents the sum of responses from each interface. This appendix details how the characteristic matrix of a stack can be defined in general, as well as the specific example of a quarter-wave stack, and how these matrices can be used to obtain design information for a stack.

These derivations have been taken primarily from chapters 2 and 6 of *Thin-Film Optical Filters* 4th edition by H. Angus Macleod pub. CRC Press 2010.

B.1 Characteristic matrix of a dielectric stack

B.1.1 Single layer

First we consider a single layer. The front interface is interface a and the back interface (interface with substrate) is interface b. The fields in the layer can be considered as a sum of the waves travelling in the +z and -z directions:

$$E = E^{+} + E^{-} \tag{B.1a}$$

$$H = H^{+} + H^{-} \tag{B.1b}$$

At interface b, these equations become:

$$E_b = {E_{1b}}^{+} + {E_{1b}}^{-} \tag{B.2a}$$

$$H_b = \eta {E_{1b}}^{+} + \eta {E_{1b}}^{-} \tag{B.2b}$$

where η is the admittance of the layer, defined as the ratio of the electric to magnetic fields H/E. Rearranging, we obtain:

$$E_{1b}{}^{+} = E_b - E_{1b}{}^{-} \tag{B.3a}$$

$$E_{1b}{}^{-} = E_{1b}{}^{+} - \frac{H_b}{\eta} \tag{B.3b}$$

$$E_{1b}{}^{+} = \frac{1}{2}\left[E_b + \frac{H_b}{\eta}\right] \tag{B.3c}$$

‘

$$E_{1b}{}^{-} = \frac{1}{2}\left[E_b - \frac{H_b}{\eta}\right] \tag{B.3d}$$

Fields at interface a can be found by multiplying the fields at interface b by a phase term δ:

$$\delta = \frac{2\pi}{\lambda} N_1 d \cos\theta \tag{B.4}$$

where d and $N = n + ik$ are the thickness and complex refractive index of the film d respectively, λ is the wavelength of interest and θ is the angle of incidence.

$$E_{1a}{}^{+} = E_{1b}{}^{+} e^{i\delta} \tag{B.5a}$$

$$E_{1a}{}^{-} = E_{1b}{}^{-} e^{-i\delta} \tag{B.5b}$$

$$H_{1a}{}^{+} = H_{1b}{}^{+} e^{i\delta} \tag{B.5c}$$

$$H_{1a}{}^{-} = H_{1b}{}^{-} e^{-i\delta} \tag{B.5d}$$

By inserting Equations B.3 into Equations B.5 and rearranging we obtain terms for E_a and H_a:

$$E_a = E_b \cos\delta + H_b \frac{i \sin\delta}{\eta} \tag{B.6a}$$

$$H_a = E_b i\eta \sin\delta + H_b \cos\delta \tag{B.6b}$$

These two equations can be written in matrix form as:

$$\begin{bmatrix} E_a \\ H_a \end{bmatrix} = \begin{bmatrix} \cos\delta & \frac{i\sin\delta}{\eta} \\ i\eta\sin\delta & \cos\delta \end{bmatrix} \begin{bmatrix} E_b \\ H_b \end{bmatrix} \tag{B.7}$$

Normalising relative to E_b we obtain:

$$\begin{bmatrix} B \\ C \end{bmatrix} = \begin{bmatrix} \cos\delta & \frac{i\sin\delta}{\eta} \\ i\eta\sin\delta & \cos\delta \end{bmatrix} \begin{bmatrix} 1 \\ \eta_{sub} \end{bmatrix} \tag{B.8}$$

Where η_{sub} is the substrate admittance and B and C are elements of the characteristic matrix of the layer.

B.1.2 Multiple layers

If a second layer is added, Equation B.7 becomes:

$$\begin{bmatrix} E_a \\ H_a \end{bmatrix} = \begin{bmatrix} \cos\delta_1 & \frac{i\sin\delta_1}{\eta_1} \\ i\eta_1\sin\delta_1 & \cos\delta_1 \end{bmatrix} \begin{bmatrix} \cos\delta_2 & \frac{i\sin\delta_2}{\eta_2} \\ i\eta_2\sin\delta_2 & \cos\delta_2 \end{bmatrix} \begin{bmatrix} E_c \\ H_c \end{bmatrix} \tag{B.9}$$

where $\delta_{1/2}$ and $\eta_{1/2}$ are the phase terms and admittances associated with the first and second layers respectively.

The characteristic matrix of a multilayer stack with q layers can therefore be generalised as:

$$\begin{bmatrix} B \\ C \end{bmatrix} = \left[\prod_{r=1}^{q} \begin{bmatrix} \cos\delta_r & \frac{i\sin\delta_r}{\eta_r} \\ i\eta\sin\delta_r & \cos\delta_r \end{bmatrix}\right] \begin{bmatrix} 1 \\ \eta_{sub} \end{bmatrix} \tag{B.10}$$

The overall optical admittance of the system $Y = C/B$. This value, obtained by dividing the calculated elements of the characteristic matrix, can be used to calculate the reflectivity of the system by the following relations:

$$r = \frac{\eta_0 - Y}{\eta_0 + Y} \tag{B.11a}$$

$$R = \left(\frac{\eta_0 - Y}{\eta_0 + Y}\right)\left(\frac{\eta_0 - Y}{\eta_0 + Y}\right)^* \tag{B.11b}$$

B.2 Quarter-wave peak reflection

In the case of a quarter-wave Bragg stack $\delta = m\frac{\pi}{2}$ where m is an odd number, $\sin\delta = \pm 1$ and $\cos\delta$=0. The characteristic matrix (based on Equation B.10) then becomes:

$$\begin{bmatrix} B \\ C \end{bmatrix} = \left[\prod_{r=1}^{q} \begin{bmatrix} 0 & \frac{i}{\eta_r} \\ i\eta_r & 0 \end{bmatrix}\right] \begin{bmatrix} 1 \\ \eta_{sub} \end{bmatrix} \tag{B.12}$$

Assuming a structure in air made up of $2p+1$ layers of two alternating materials with refractive indices n_H and n_L respectively, with no absorption and an incident angle of 0, admittance η becomes equivalent to refractive index n and the matrix elements simplify to:

$$B = n_L^{2p} n_{sub} \tag{B.13a}$$

$$C = n_H^{2p+2} \tag{B.13b}$$

The resulting optical admittance and reflectivity are hence:

$$Y = \frac{n_H^{2p+2}}{n_L^{2p} n_m} \tag{B.14a}$$

$$R = \left[\frac{1 - \frac{n_H^{2p+2}}{n_L^{2p} n_m}}{1 + \frac{n_H^{2p+2}}{n_L^{2p} n_m}} \right]^2 \tag{B.14b}$$

If Y is large i.e. $n_H > n_L$ and $2p+1$ is large, R can be approximated as:

$$R = 1 - \frac{4 n_L^{2p} n_{sub}}{n_H^{2p+1}} = 1 - 4\left(\frac{n_L}{n_H}\right)^{2p}\left(\frac{n_{sub}}{n_H^2}\right) \tag{B.15}$$

and transmission T as:

$$T = 4\left(\frac{n_L}{n_H}\right)^{2p}\left(\frac{n_{sub}}{n_H^2}\right) \tag{B.16}$$

As a result, if two more layers are added to the stack, the transmission will decrease by a factor of $\left(\frac{n_L}{n_H}^2\right)$. Increasing the index contrast will also result in an decrease in transmission for a given number of layers.

B.3 HR peak widths

Although the peak reflectivity of a quarter-wave reflector structure may approach 100%, there is a limit to the width of the central peak even when the number of layers becomes very high. This section describes how this maximum HR peak width can be quantified.

The matrix $\mathbf{M}$ of a structure made up of a repeated set of layers (e.g. alternating high- and low-index layers in the structure above) can be written as $\mathbf{M} = [M]^q$ where $[M]$ is the matrix of the fundamental structure with elements:

$$\begin{bmatrix} M_{11} & M_{12} \\ M_{21} & M_{22} \end{bmatrix} \tag{B.17}$$

Reflectivity increases with number of fundamental periods where:

$$\left| \frac{M_{11} + M_{22}}{2} \right| \geq 1 \tag{B.18}$$

with the edge of the HR zone at:

$$\left| \frac{M_{11} + M_{22}}{2} \right| = 1 \tag{B.19}$$

The fundamental matrix for a structure of alternating high and low index materials of equal optical thickness is (from Equation B.10):

$$M = \begin{bmatrix} \cos\delta & \frac{i\sin\delta}{n_L} \\ in_L \sin\delta & \cos\delta \end{bmatrix} \begin{bmatrix} \cos\delta & \frac{i\sin\delta}{n_H} \\ in_H \sin\delta & \cos\delta \end{bmatrix} \tag{B.20}$$

hence

$$\frac{M_{11} + M_{22}}{2} = \cos^2\delta - \frac{1}{2}\left[\frac{n_H}{n_L} + \frac{n_L}{n_H}\right]\sin^2\delta \tag{B.21}$$

The right side of Equation B.21 cannot be greater than one so to find the boundary we set $\frac{M_{11}+M_{22}}{2} = -1$, which can be rearranged to give:

$$\cos^2\delta_{edge} = \left(\frac{n_H - n_L}{n_H + n_L}\right)^2 \tag{B.22}$$

For a quarter wave structure $\delta = \frac{\pi}{2}\frac{\lambda_0}{\lambda}$, where λ_0 is the wavelength of peak reflection. We define a parameter $2\Delta g$, the width of the HR zone, so that:

$$\delta_{edge} = \frac{\pi}{2}(1 \pm \Delta g) \tag{B.23}$$

and:

$$\cos^2\delta_{edge} = \sin^2\left(\pm\frac{\pi\Delta g}{2}\right) = \left(\frac{n_H - n_L}{n_H + n_L}\right)^2 \tag{B.24}$$

hence:

$$\Delta g = \frac{2}{\pi} \sin^{-1}\left(\frac{n_H - n_L}{n_H + n_L}\right) \tag{B.25}$$

Equation B.25 shows clearly that the width of the HR zone depends solely on the refractive index contrast of the layers i.e. the greater the different in index the greater the width of the HR zone.

B.4 *MATLAB* model

Figure B.1 describes the operation of the *MATLAB* model used in chapter 6. The model was written by Michalis Zervas of the ORC, University of Southampton.

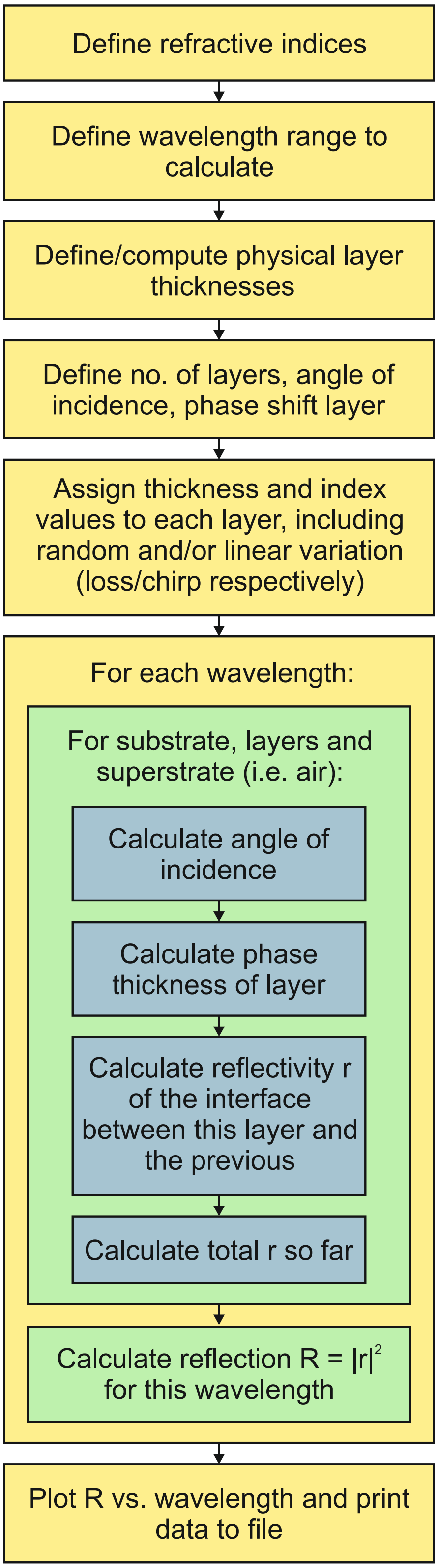

FIGURE B.1: Flowchart describing operation of Bragg structure modelling program created by Michalis Zervas (ORC)

Appendix C

Preliminary sesquioxide growth

This appendix describes promising preliminary growth of sesquioxides yttria, gallia and scandia (Y_2O_3, Ga_2O_3 and Y_2O_3 respectively). Some targets and substrates were provided by Sebastian Heinrich at the University of Hamburg.

C.1 Yb:yttria

C.1.1 Experimental setup

Growth of 5% at. Yb:Y_2O_3 test films was undertaken in Chamber 1 using sapphire and yttria substrates of size $10 \times 10 \times 0.5$ mm^3 and temperature ~1000°C. Fluence was ~3 J/cm^2 and laser repetition rate was 20 Hz, resulting in a growth rate of ~6.6 µm/hr (~0.9 nm/shot). The target-substrate distance was ~60 mm. Yttria substrates and targets were provided by the University of Hamburg. Target diameter was only ~20 mm and plume alignment was hence somewhat off-axis, as seen in figure C.1.

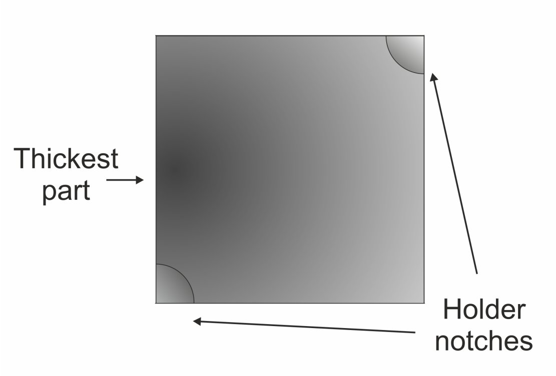

Figure C.1: Schematic of samples grown, showing film distribution (thickest on left side) and notches due to holder.

Relatively few reports exist of PLD growth of sesquioxides and there does not appear to be a consensus as to the best conditions. Three films approximately ∼3.3 µm thick were grown on sapphire at varying background O_2 pressures (1×10^{-2}, 2×10^{-2} and 4×10^{-2} mbar) to provide a rough indication of the optimum value. Slightly fewer particulates were observed in the 1×10^{-2} mbar, although accurate comparison was difficult due to the low number of particulates observed in each of the three measurements per sample (average of < 15 per measurement). 1×10^{-2} mbar was chosen as the pressure value for subsequent experiments; however, growth at higher pressures is likely to be achievable.

Four films have been analysed and discussed in detail: two on sapphire substrates (K208 and K214) and two on yttria substrates (K210 and K213). K208 and K210 are thin films (∼3.3 µm thick), while K214 and K213 are around 30 µm thick in the thickest part. XRD was carried out using a powder diffractometer, surface profiling using the Zescope optical profiler and particulate counting and roughness measurements using the SPIP software supplied with the profiler. Particulate and roughness values given are the average of three measurements ∼0.5 mm apart concentrated around the thickest part of each sample.

C.1.2 Analysis

Results of XRD analysis for films grown on sapphire and yttria substrates can be seen in figures C.2 and C.3 respectively. Films grown on c-cut sapphire exhibit strong peaks around 28.8°, suggesting that the films grew primarily in the (111) orientation (as observed in previous studies of yttria grown on sapphire [179, 37]). For the thin film on sapphire (K208), a strong peak at around 41.2° can be observed; this corresponds to the underlying substrate and is not observed for a much thicker film (X-rays do not penetrate to the substrate).

As expected, films grown on yttria (100) substrates grew in the (100) orientation. All peaks match those of the underlying substrate. In the case of the thinner film K210, it is difficult to differentiate X-ray scattering from the film from that from the substrate. However, the same peaks are observed for the thick film K213, where there should be no contribution from the substrate. There is some variation in peak position. This could be due to strain or slight differences in lattice constant, but is likely primarily due to slight differences in mounting the samples for XRD.

In the cases presented, growth on sapphire resulted in a larger number of particulates and lower average roughness compared with growth on yttria (see table C.1 and figure C.4). However, while growth on sapphire substrates results in crack-free films with many small particulates, films grown on yttria exhibit a smaller number of much larger particulates (see figures C.5 and C.6), along with some cracking. Sample Y213 (thick film on yttria) also exhibits surface ridges, unlike the thinner sample (see figure C.6(b)).

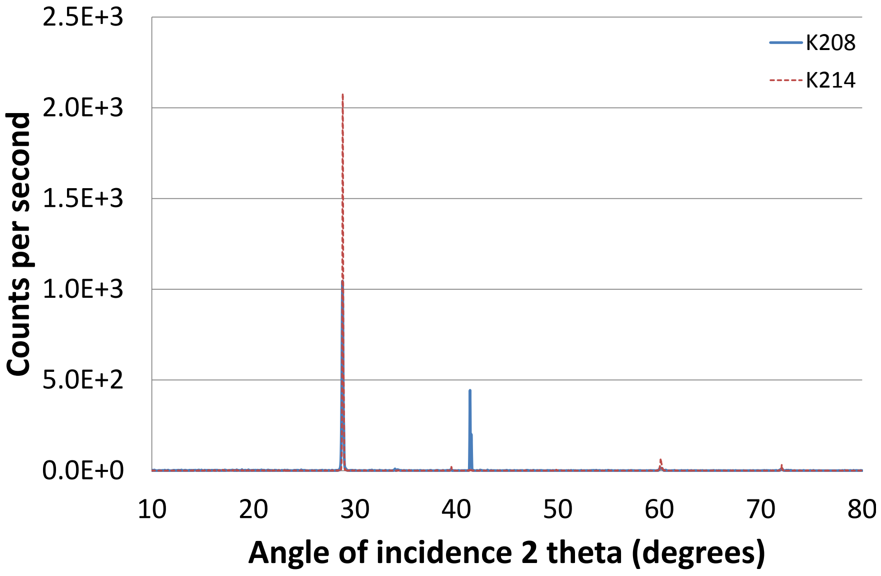

(a) Full XRD spectrum

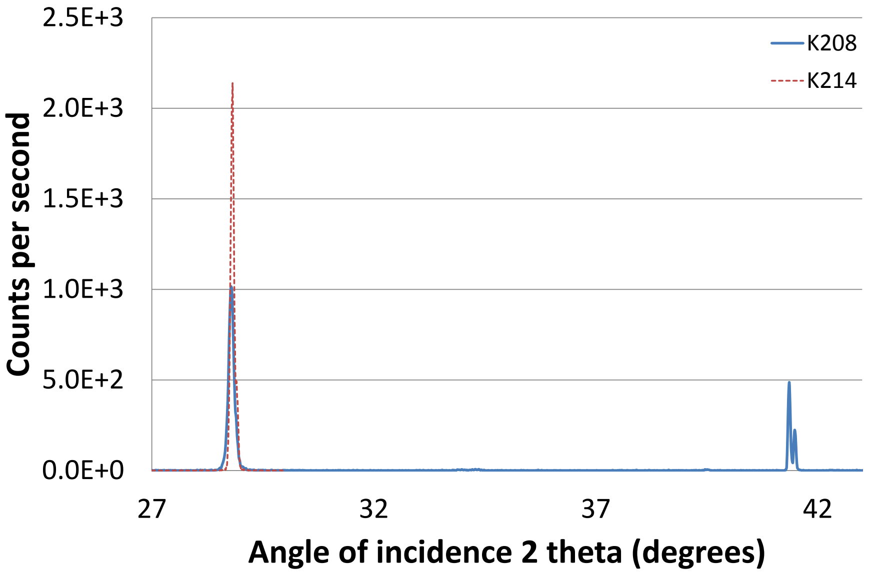

(b) Close up of XRD spectra showing (222) peaks of the yttria film and peak of the underlying sapphire substrate in the case of K208

FIGURE C.2: XRD spectra of thick and thin Yb:yttria films on sapphire substrates.

Sample	**Substrate**	**Thickness**	**Particulates /cm^2 (>50 nm)**	**Particulates /cm^2 (>100 nm)**	**Average roughness S$_a$ (nm)**
K208	Sapphire	~3.3 µm	4.6×10^5	2.3×10^5	9.2
K214	Sapphire	~30 µm	2.5×10^6	5.9×10^4	16.7
K210	Yttria	~3.3 µm	2.2×10^4	1.2×10^4	3.3
K213	Yttria	~30 µm	2.1×10^5	8.7×10^4	9.8

TABLE C.1: Summary of results for samples grown with final parameters

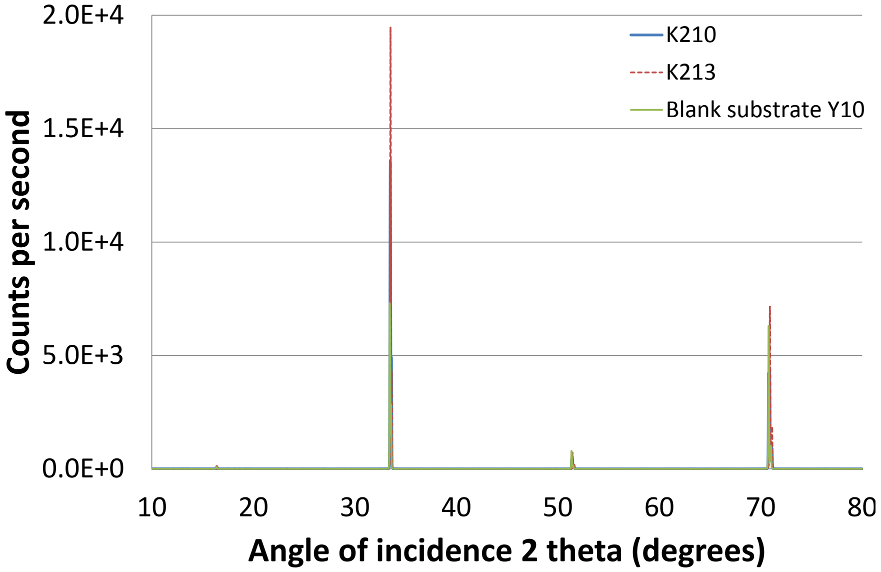

(a) Full XRD spectrum

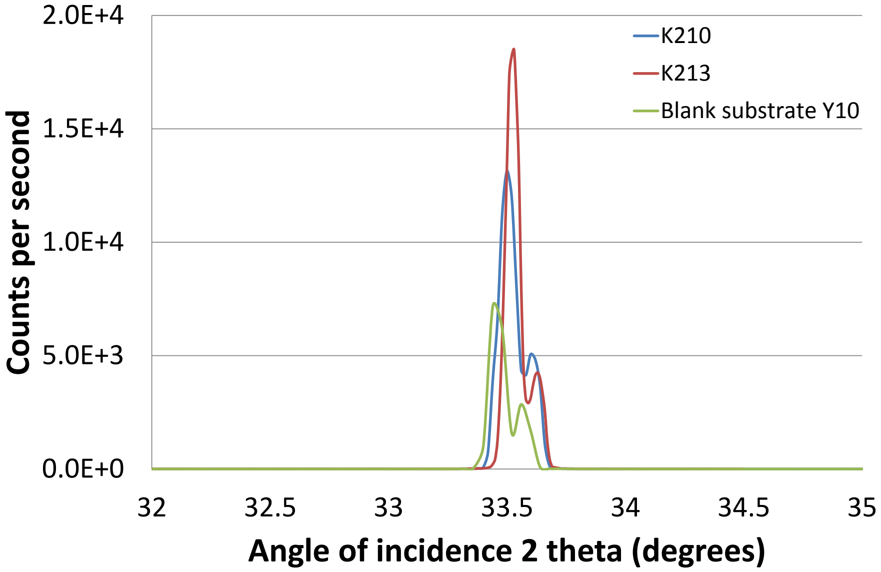

(b) Close up of XRD spectra showing (100 peaks of the yttria film

Figure C.3: XRD spectra of thick and thin Yb:yttria films on yttria substrates, as well as spectrum of a blank yttria substrate (Y10).

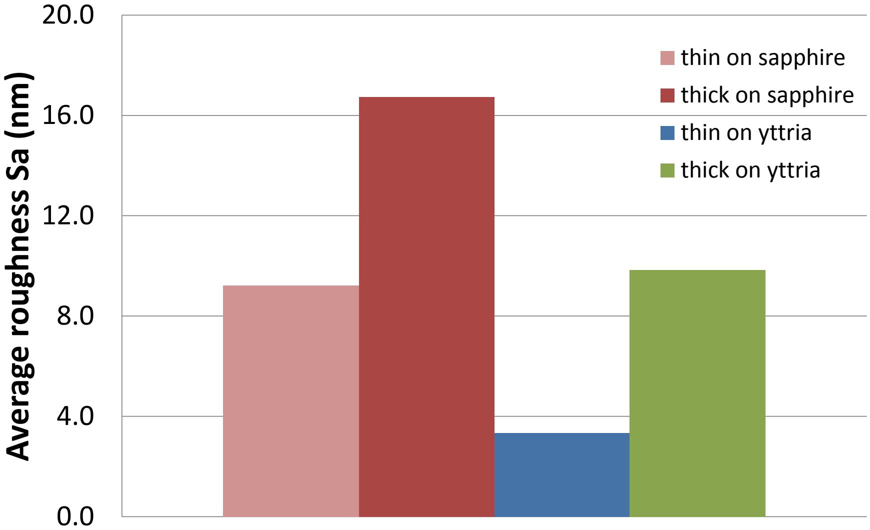

(a) Graph of average roughness values S_a.

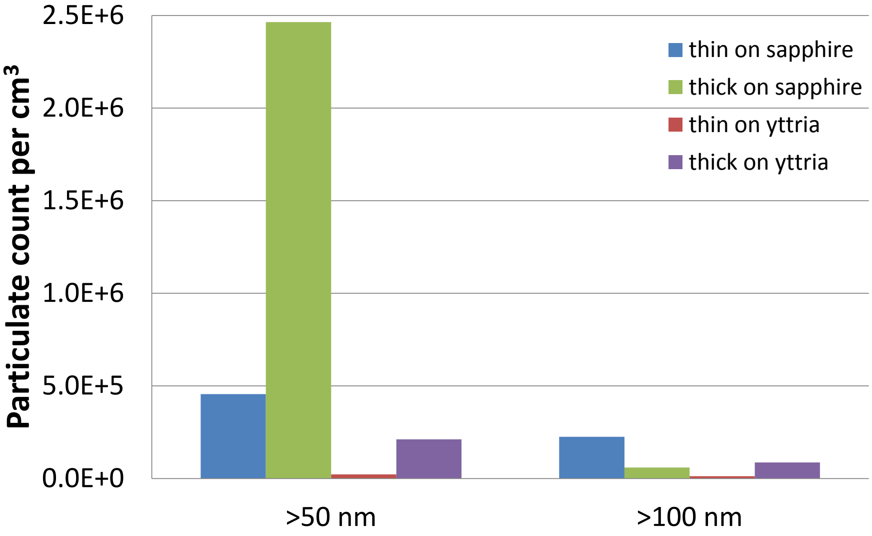

(b) Graph of average particulate count per cm^2.

FIGURE C.4: Graphs indicating surface quality of thin and thick samples grown on yttria and sapphire substrates.

Roughness of sample K208 (thin film on sapphire) is very similar to that obtained by Burmester et al [37], while roughness of the thin film on yttria is nearly three times lower.

In both cases, roughness was markedly greater for thicker films than thinner films. This is likely to be primarily a consequence of increased target surface damage over the 4.5 hours of deposition. It is expected that the surface quality could be improved by using larger targets: greater surface area results in longer ablation time before surface damage becomes prohibitive. Large features, possibly crystallite boundaries, can also be observed for sample K214, the thick film on sapphire (see figure C.7).

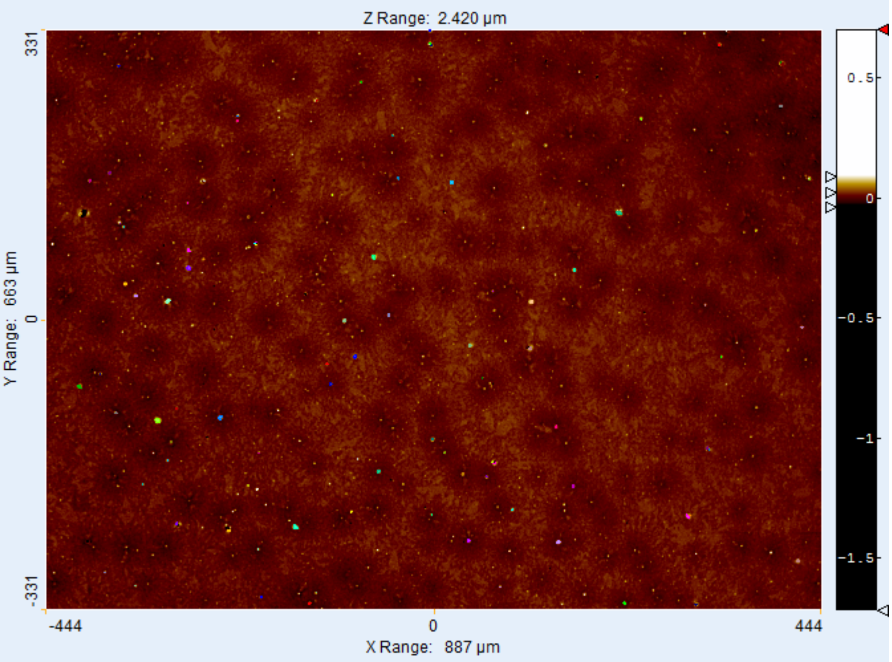

(a) Surface profile of sample K208 (sapphire substrate).

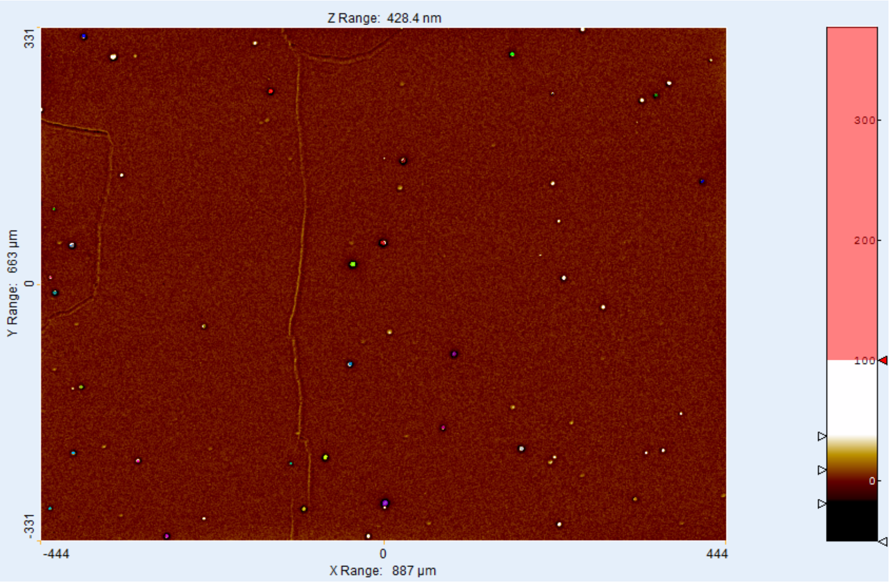

(b) Surface profile of sample K210 (yttria substrate).

FIGURE C.5: Optical profiler images of thin films on C.5(a)) sapphire substrate and C.5(b)) with particulates >100 nm in height highlighted (10x magnification).

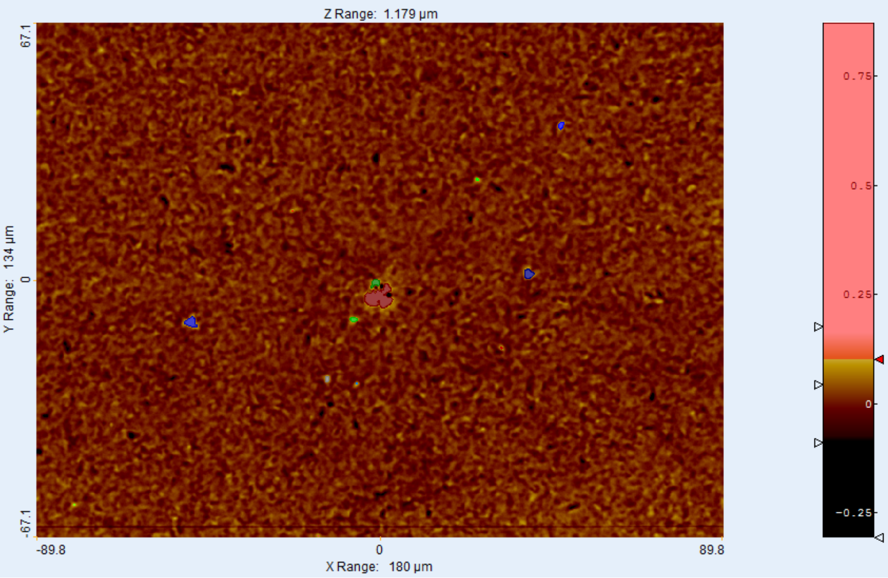

(a) Surface profiler of sample K214 (sapphire substrate) with particulates >100 nm in height highlighted.

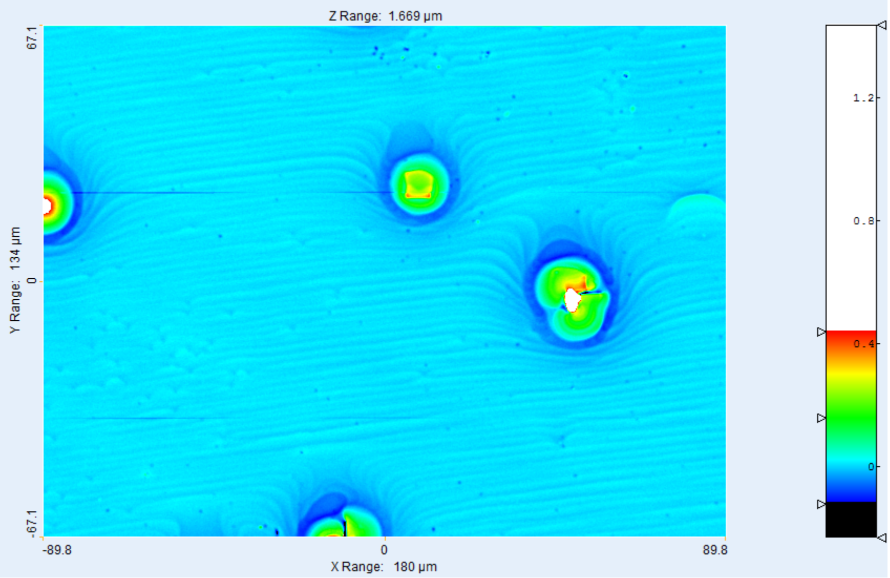

(b) Surface profiler of sample K213 (yttria substrate).

FIGURE C.6: Optical profiler images of thin films on C.6(a)) sapphire substrate and C.6(b)) yttria substrate (50x magnification).

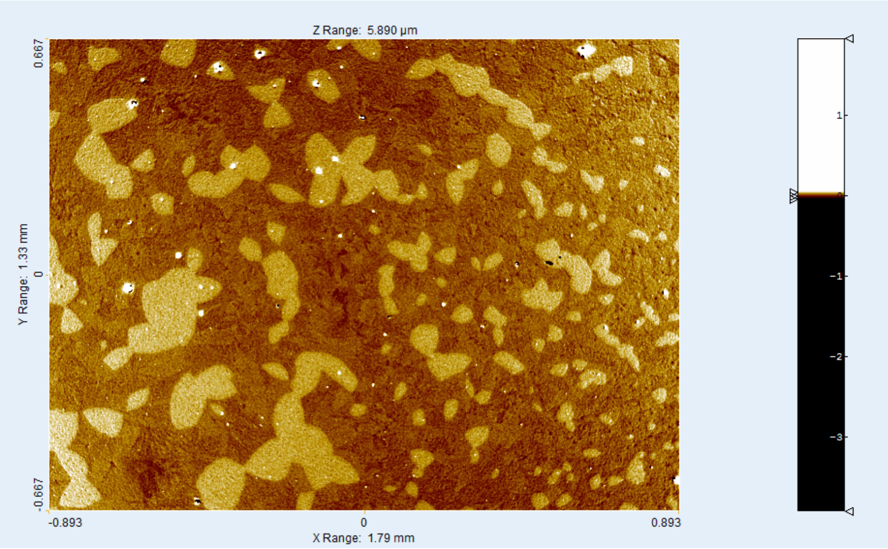

FIGURE C.7: Surface profiler image of thick Yb:yttria film on sapphire substrate (5x magnification).

It is interesting to note that earlier growth on sapphire (to roughly determine optimum deposition pressure) resulted in lower roughness and particulate count values. However, these were undertaken at a lower laser repetition rate: 10 Hz. It may be the case that particulate numbers for growth on sapphire could be reduced if a lower repetition rate was used; however, this could make thick film growth prohibitively slow if films >30 µm in thickness are required.

C.1.3 Conclusion

Thick and thin samples of Yb:yttria were grown successfully on yttria and sapphire substrates. Of the substrates described in detail, all exhibited strong XRD peaks. Growth on sapphire appeared to result in a higher number of particulates and greater surface roughness; however, films grown on yttria presented larger particulates and more cracking. In the latter case there should be no thermal expansion mismatch; cracking may instead be a result of stress induced in the films due to the high fluence and relatively low gas pressure. In both cases, thick film surface quality was markedly poorer than that of the thin films, likely the result of target modification.

Two steps immediately present themselves for immediate investigation. Firstly, further optimisation of growth parameters (particularly fluence and pressure) should be undertaken, something that has not yet been achieved due to time constraints and the limited number of substrates available. Secondly, larger targets should be acquired, allowing on-axis deposition of centro-symmetric films as well as growth of much thicker films.

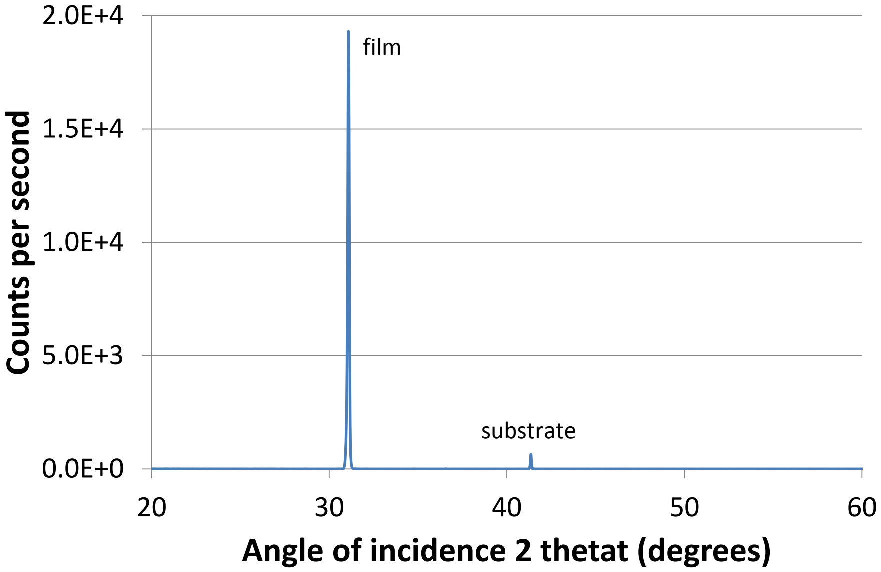

FIGURE C.8: XRD spectrum of a scandium film grown on sapphire, showing peaks from the film and substrate.

C.2 Other sesquioxides

Growth of scandia and gallia were also attempted on sapphire, although not analysed in detail. Depositions were carried out in Chamber 2, with a target-substrate distance of ∼45 mm and a substrate temperature of ∼ 750 °C. All other parameters matched those used for yttria growth in the previous section.

Gallia films could not be detected although the target ablated well. This is likely due to the lightness and volatility of gallium/gallium oxide plume and film components. Scandia, however, grew well. Film thickness was ∼3.6 µm (one hour deposition) and particulate counts were very low at 7.7×10^4 and 2.5×10^4 particulates per cm^2 for particulates of diameter >50 and >100 nm respectively. XRD (see figure C.8) shows that the film grew single-phase in the (111) orientation as expected.

References

[1] H. Kidoh, A. Morimoto, and T. Shimizu, "Synthesis of ferromagnetic Bi-substituted yttrium iron garnet films by laser ablation," *Applied Physics Letters*, vol. 59, no. 2, pp. 237–239, 1991.

[2] D. Gill, A. Anderson, R. Eason, T. Warburton, and D. Shepherd, "Laser operation of an Nd:$Gd_3Ga_5O_{12}$ thin-film optical waveguide fabricated by PLD," *Appl. Phys. Lett.*, vol. 69, p. 10, 1996.

[3] T. C. May-Smith, C. Grivas, D. P. Shepherd, R. W. Eason, and M. J. F. Healy, "Thick film growth of high optical quality low loss (0.1 dB cm^{-1}) $Nd : Gd_3Ga_5O_{12}$ on$Y_3Al_5O_{12}$ by pulsed laser deposition," *Appl. Surf. Sci.*, vol. 223, no. 4, pp. 361–371, 2004.

[4] T. C. May-Smith, D. P. Shepherd, and R. W. Eason, "Growth of a multilayer garnet crystal double-clad waveguide structure by pulsed laser deposition," *Thin Solid Films*, vol. 515, no. 20-21, pp. 7971–7975, 2007.

[5] M. Y. Chern, C. C. Fang, J. S. Liaw, J. G. Lin, and C. Y. Huang, "Study of ultrathin $Y_3Fe_5O_{12}/Gd_3Ga_5O_{12}$ superlattices," *Appl. Phys. Lett.*, vol. 69, pp. 854–856, 1996.

[6] R. Ramesh, T. Venkatesan, S. Lofland, M. Dominguez, S. Bhagat, B. Simion, and G. Thomas, "Magneto-optic and microwave properties of epitaxial garnet thin film heterostructures and superlattices," *Journal of Applied Physics*, vol. 79, no. 8, Part 2B, p. 5991, 1996.

[7] S. Kahl and A. M. Grishin, "Magneto-optical rotation of a one-dimensional all-garnet photonic crystal in transmission and reflection," *Phys. Rev. B*, vol. 71, p. 205110, May 2005.

[8] R. W. Eason, T. C. May-Smith, C. Grivas, M. S. B. Darby, D. P. Shepherd, and R. Gazia, "Current state-of-the-art of pulsed laser deposition of optical waveguide structures: Existing capabilities and future trends," *Appl. Surf. Sci.*, vol. 255, no. 10, pp. 5199–5205, 2009.

[9] M. S. B. Darby, T. C. May-Smith, and R. W. Eason, "Deposition and stoichiometry control of Nd-doped gadolinium gallium garnet thin films by combinatorial pulsed laser deposition using two targets of Nd:$Gd_3Ga_5O_{12}$ and Ga_2O_3," *Appl. Phys. A*, vol. 93, no. 2, pp. 477–481, 2008.

[10] R. Gazia, T. C. May-Smith, and R. W. Eason, "Growth of a hybrid garnet crystal multilayer structure by combinatorial pulsed laser deposition," *Journal of Crystal Growth*, vol. 310, no. 16, pp. 3848–3853, 2008.

[11] T. C. May-Smith, K. A. Sloyan, R. Gazia, and R. W. Eason, "Stress engineering and optimization of thick garnet crystal films grown by pulsed laser deposition," *Crystal Growth & Design*, vol. 11, no. 4, pp. 1098–1108, 2011.

[12] B. H. T. Chai, *Handbook of Optical Materials.* CRC Press, 2003.

[13] K. Develos-Bagarinao, H. Yamasaki, Y. Nakagawa, and K. Endo, "Relationship between composition and surface morphology in YBCO films deposited by large-area PLD," *Physica C: Superconductivity*, vol. 412-414, Part 2, no. 0, pp. 1286 – 1290, 2004.

[14] D. Gill, R. Eason, J. Mendiola, and P. Chandler, "Growth of crystalline $Gd_3Ga_5O_{12}$ thin-film optical waveguides by pulsed laser deposition," *Materials Letters*, vol. 25, no. 1-2, pp. 1–4, 1995.

[15] C. Grivas, T. C. May-Smith, D. P. Shepherd, and R. W. Eason, "Laser operation of a low loss (0.1 dB cm^{-1}) $Nd : Gd_3Ga_5O_{12}$ thick (40 µm) planar waveguide grown by pulsed laser deposition," *Opt. Commun.*, vol. 229, no. 1-6, pp. 355–361, 2004.

[16] S. Fukaya, T. Hasegawa, Y. Ishida, T. Shimoda, and M. Obara, "Fabrication of Nd^{3+}, Cr^{4+} co-doped $Gd_3Ga_5O_{12}$ thin film waveguide by two-target pulsed laser deposition," *Applied Surface Science*, vol. 177, no. 3, pp. 147 – 151, 2001.

[17] J. Lancok, C. Garapon, M. Jelinek, J. Mugnier, and R. Brenier, "Optical and structural properties of Pr:GGG crystalline thin film waveguides grown by pulsed-laser deposition," *Applied Physics A: Materials Science & Processing*, vol. 81, pp. 1477–1483, 2005. 10.1007/s00339-005-3255-8.

[18] T. Gün, Y. Kuzminykh, F. Tellkamp, K. Petermann, and G. Huber, "Epitaxial layer-by-layer growth of Yb:YAG and YbAG PLD-films," *Applied Physics A: Materials Science & Processing*, vol. 93, pp. 387–391, 2008. 10.1007/s00339-008-4844-0.

[19] N. Vainos, C. Grivas, C. Fotakis, R. Eason, A. Anderson, D. Gill, D. Shepherd, M. Jelinek, J. Lancok, and J. Sonsky, "Planar laser waveguides of Ti:sapphire, Nd:GGG and Nd:YAG grown by pulsed laser deposition," *Applied Surface Science*, vol. 127-129, no. 0, pp. 514–519, 1998.

[20] M. Ezaki, M. Obara, H. Kumagai, and K. Toyoda, "Characterization of Nd:$Y_3Al_5O_{12}$ thin films grown on various substrates by pulsed laser deposition," *Applied Physics Letters*, vol. 69, no. 20, pp. 2977–2979, 1996.

[21] H. Kumagai, K. Adachi, M. Ezaki, K. Toyoda, and M. Obara, "Epitaxial growth of Nd:YAG thin films by pulsed laser deposition," *Applied Surface Science*, vol. 109-110, no. 0, pp. 528–532, 1997.

[22] T. C. May-Smith and R. W. Eason, "Comparative growth study of garnet crystal films fabricated by pulsed laser deposition," *Journal of Crystal Growth*, vol. 308, no. 2, pp. 382–391, 2007.

[23] T. May-Smith, *Pulsed Laser Deposition of Thick Multilayer Garnet Crystal Films for Waveguide Laser Devices.* PhD thesis, University of Southampton, 2005.

[24] S. I. Khartsev and A. M. Grishin, "Heteroepitaxial $Bi_3Fe_5O_{12}/La_3Ga_5O_{12}$ films for magneto-optical photonic crystals," *Applied Physics Letters*, vol. 86, no. 14, p. 141108, 2005.

[25] P. C. Dorsey, S. E. Bushnell, R. G. Seed, and C. Vittoria, "Epitaxial yttrium iron garnet films grown by pulsed laser deposition," *Journal of Applied Physics*, vol. 74, no. 2, pp. 1242–1246, 1993.

[26] N. Ibrahim, C. Edwards, and S. Palmer, "Pulsed laser ablation deposition of yttrium iron garnet and cerium-substituted YIG films," *Journal of Magnetism and Magnetic Materials*, vol. 220, no. 2-3, pp. 183–194, 2000.

[27] S. Leitenmeier, A. Heinrich, J. K. N. Lindner, and B. Stritzker, "Growth of epitaxial bismuth and gallium substituted lutetium iron garnet films by pulsed laser deposition," *Journal of Applied Physics*, vol. 99, no. 8, p. 08M704, 2006.

[28] R. Lux, A. Heinrich, S. Leitenmeier, T. Korner, M. Herbort, and B. Stritzker, "Pulsed-laser deposition and growth studies of $Bi_3Fe_5O_{12}$ thin films," *Journal of Applied Physics*, vol. 100, no. 11, p. 113511, 2006.

[29] T. Tepper and C. Ross, "Pulsed laser deposition and refractive index measurement of fully substituted bismuth iron garnet films," *Journal of Crystal Growth*, vol. 255, no. 3-4, pp. 324–331, 2003.

[30] S. Kahl, V. Popov, and A. M. Grishin, "Optical transmission and faraday rotation spectra of a bismuth iron garnet film," *Journal of Applied Physics*, vol. 94, no. 9, pp. 5688–5694, 2003.

[31] H. Yamahara, M. Mikami, M. Seki, and H. Tabata, "Epitaxial strain-induced magnetic anisotropy in $Sm_3Fe_5O_{12}$ thin films grown by pulsed laser deposition," *Journal of Magnetism and Magnetic Materials*, vol. 323, no. 23, pp. 3143–3146, 2011.

[32] H. Kühn, S. Heinrich, A. Kahn, K. Petermann, J. D. B. Bradley, K. Wörhoff, M. Pollnau, and G. Huber, "Monocrystalline Yb3+:(Gd,Lu)$_2$O$_3$ channel waveguide laser at 976.8 nm," *Opt. Lett.*, vol. 34, pp. 2718–2720, Sep 2009.

[33] A. Kahn, S. Heinrich, H. Kühn, K. Petermann, J. D. Bradley, K. Wörhoff, M. Pollnau, and G. Huber, "Low threshold monocrystalline Nd:(Gd, Lu)$_2$O$_3$ channel waveguide laser," *Opt. Express*, vol. 17, pp. 4412–4418, Mar 2009.

[34] T. Gun, A. Kahn, B. Ileri, K. Petermann, and G. Huber, "Two-dimensional growth of lattice matched Nd-doped (Gd,Lu)$_2$O$_3$ films on Y$_2$O$_3$ by pulsed laser deposition," *Applied Physics Letters*, vol. 93, no. 5, p. 053108, 2008.

[35] T. Gun, Y. Kuzminykh, K. Petermann, H. Scheife, and G. Huber, "Epitaxial growth by pulsed laser deposition of Er-doped Sc$_2$O$_3$ films on sesquioxides monitored in situ by reflection high energy electron diffraction," *Applied Physics Letters*, vol. 91, no. 8, p. 083103, 2007.

[36] S. Bär, G. Huber, J. Gonzalo, A. Perea, A. Climent, and F. Paszti, "Europium-doped sesquioxide thin films grown on sapphire by PLD," *Materials Science and Engineering: B*, vol. 105, no. 1-3, pp. 30–33, 2003. EMRS 2003 Symposium J, Rare Earth Doped Materials for Photonics.

[37] P. Burmester, G. Huber, M. Kurfiss, and M. Schilling, "Crystalline growth of cubic (Eu, Nd):Y$_2$O$_3$ thin films on α-Al$_2$O$_3$ by pulsed laser deposition," *Appl Phys A*, vol. 80, pp. 627–360, 2005.

[38] E. R. Smith, J. B. Gruber, P. Wellenius, J. F. Muth, and H. O. Everitt, "Spectra and energy levels of Eu^{3+} in cubic phase Gd$_2$O$_3$," *Physica Status Solidi B*, vol. 247, pp. 1807–1813, JUL 2010.

[39] M. Pollnau, C. Grivas, L. Laversenne, J. Wilkinson, R. Eason, and D. Shepherd, "Ti:sapphire waveguide lasers," *Laser Physics Letters*, vol. 4, no. 8, pp. 560–571, 2007.

[40] R. Eason, *Pulsed Laser Deposition of Thin Films: Applications-Led Growth of Functional Materials.* Wiley, 2007.

[41] M. Jelinek, R. Eason, J. Lancok, A. Anderson, C. Grivas, C. Fotakis, L. Jastrabik, F. Flory, and H. Rigneault, "Waveguiding pulsed laser deposited Ti : sapphire layers on quartz," *Thin Solid Films*, vol. 322, no. 1-2, pp. 259–262, 1998.

[42] C. Grivas, D. Shepherd, T. May-Smith, R. Eason, and M. Pollnau, "Single-transverse-mode Ti : sapphire rib waveguide laser," *Opt. Express*, vol. 13, no. 1, pp. 210–215, 2005.

[43] H. Uetsuhara, S. Goto, Y. Nakata, N. Vasa, T. Okada, and M. Maeda, "Fabrication of a Ti:sapphire planar waveguide by pulsed laser deposition," *Applied Physics A: Materials Science & Processing*, vol. 69, pp. S719–S722, 1999. 10.1007/s003390051514.

[44] A. A. Anderson, R. W. Eason, L. M. B. Hickey, M. Jelinek, C. Grivas, D. S. Gill, and N. A. Vainos, "Ti:sapphire planar waveguide laser grown by pulsed laser deposition," *Opt. Lett.*, vol. 22, pp. 1556–1558, Oct 1997.

[45] G. Wang, O. Marty, C. Garapon, A. Pillonnet, and W. Zhang, "Rare earth doped a-alumina thin films prepared by pulsed laser deposition: structural and optical properties," *Applied Physics A: Materials Science & Processing*, vol. 79, pp. 1599–1602, 2004. 10.1007/s00339-004-2859-8.

[46] E. Loh, "Ultraviolet absorption and excitation spectrum of ruby and sapphire," *The Journal of Chemical Physics*, vol. 44, no. 5, pp. 1940–1945, 1966.

[47] B. Hirschauer, S. Söderholm, G. Chiaia, and U. Karlsson, "Highly oriented α-alumina films grown by pulsed laser deposition," *Thin Solid Films*, vol. 305, no. 1-2, pp. 243–247, 1997.

[48] G. C. Budakoti and R. S. Rawat, "Enhancement in crystalline quality of $LiNbO_3$ films by slow annealing at low temperatures," *Journal of Crystal Growth*, vol. 310, no. 18, pp. 4205–4208, 2008.

[49] S. S. N. Bharadwaja, T. Dechakupt, S. Trolier-McKinstry, and H. Beratan, "Excimer laser crystallized $(Pb,La)(Zr,Ti)O_3$ thin films," *Journal of the American Ceramic Society*, vol. 91, no. 5, pp. 1580–1585, 2008.

[50] F. Tang, Y. Cao, W. Guo, Y. Chen, J. Huang, Z. Deng, Z. Liu, and Z. Huang, "Fabrication and laser behavior of the Yb:YAG ceramic microchips," *Optical Materials*, vol. 33, no. 8, pp. 1278 – 1282, 2011.

[51] J. Shin, A. Goyal, K. More, and S.-H. Wee, "Fabrication of epitaxial γ-Al_2O_3 and spinel $NiAl_2O_4$ films on $SrTiO_3$ by pulsed laser ablation," *Journal of Crystal Growth*, vol. 311, no. 1, pp. 210–213, 2008.

[52] B. Berini, M. Evain, A. Fouchet, Y. Dumont, E. Popova, and N. Keller, "In situ optical characterization of metal-insulator transition in $LaNiO_3$ and $SrTiO_3$ perovskites in pulsed laser deposition chamber," *Phase Transitions*, vol. 84, no. 5-6, pp. 501–508, 2011.

[53] A. Ohkubo, A. Ohtomo, J. Nishimura, T. Makino, Y. Segawa, and M. Kawasaki, "Combinatorial synthesis and optical characterization of alloy and superlattice films based on $SrTiO_3$ and $LaAlO_3$," *Applied Surface Science*, vol. 252, no. 7, pp. 2488–2492, 2006. Proceedings of the Third Japan-US Workshop on Combinatorial Material Science and Technology.

[54] C. H. Hur and S. Y. Lee, “Fabrication of $YBa_2Cu_3O_{7-x}$ superconducting film with CeO_2/BaTiO double buffer layer,” *Thin Solid Films*, vol. 398-399, no. 0, pp. 444–447, 2001. Proceedings of the 28th International Conference on Metallurgic Coatings and Thin Films.

[55] J. Hu, J. Bultman, and J. Zabinski, “Microstructure and lubrication mechanism of multilayered MoS_2/Sb_2O_3 thin films,” *Tribology Letters*, vol. 21, pp. 169–174, 2006.

[56] B. M. Simion, G. Thomas, R. Ramesh, V. G. Keramidas, and R. L. Pfeffer, “Growth and characterization of ($Y_3Fe_5O_{12}$-$Bi_3Fe_5O_{12}$) heterostructures by pulsed laser deposition,” *Applied Physics Letters*, vol. 66, no. 7, pp. 830–832, 1995.

[57] J. Orlianges, C. Champeaux, P. Dutheil, A. Catherinot, and T. M. Mejean, “Structural, electrical and optical properties of carbon-doped CdS thin films prepared by pulsed-laser deposition,” *Thin Solid Films*, vol. 519, no. 21, pp. 7611–7614, 2011. Proceedings of the EMRS 2010 Spring Meeting Symposium M: Thin Film Chalcogenide Photovoltaic Materials.

[58] P. Schenck, J. Klamo, N. Bassim, P. Burke, Y. Gerbig, and M. Green, “Combinatorial study of the crystallinity boundary in the HfO_2-TiO_2-Y_2O_3 system using pulsed laser deposition library thin films,” *Thin Solid Films*, vol. 517, no. 2, pp. 691–694, 2008.

[59] T. Fukumura, M. Ohtani, M. Kawasaki, Y. Okimoto, T. Kageyama, T. Koida, T. Hasegawa, Y. Tokura, and H. Koinuma, “Rapid construction of a phase diagram of doped Mott insulators with a composition-spread approach,” *Applied Physics Letters*, vol. 77, no. 21, pp. 3426–3428, 2000.

[60] A. Gupta, “Novel pulsed laser deposition approaches,” in *Pulsed Laser Deposition of Thin Films* (D. Chrisey and G. Hubler, eds.), vol. 1, Wiley, 1993.

[61] A. Gorbunov, W. Pompe, A. Sewing, S. Gaponov, A. Akhsakhalyan, I. Zabrodin, I. Kaskov, E. Klyenkov, A. Morozov, N. Salaschenko, R. Dietsch, H. Mai, and S. Völlmar, “Ultrathin film deposition by pulsed laser ablation using crossed beams,” *Applied Surface Science*, vol. 96-98, no. 0, pp. 649–655, 1996. Proceedings of Symposium F: Third International Symposium on Laser Ablation of the 1995 E-MRS Spring Conference.

[62] A. Levin, D. Meyer, A. Gorbunov, A. Tselev, P. Gawlitza, H. Mai, W. Pompe, and P. Paufler, “Comparative study of interfaces of Fe-Al multilayers prepared by direct and crossed-beam pulsed laser deposition,” *Thin Solid Films*, vol. 391, no. 1, pp. 47–56, 2001.

[63] X. Liu, S. Chen, M. Li, and X. Wang, “Synthesis and characterization of ferromagnetic cobalt-doped tin dioxide thin films,” *Thin Solid Films*, vol. 515, no. 17, pp. 6744 – 6748, 2007.

[64] J. Li, Q. Huang, Z. W. Li, L. P. You, S. Y. Xu, and C. K. Ong, "Microstructure modification and magnetoresistance enhancement by Ag doping in $La_{2/3}Sr_{1/3}MnO_3$ thin films prepared by dual-beam pulsed laser ablation," *Journal of Physics: Condensed Matter*, vol. 13, no. 14, p. 3419, 2001.

[65] Y. Z. Peng, T. Liew, T. C. Chong, W. D. Song, H. L. Li, and W. Liu, "Growth and characterization of dual-beam pulsed-laser-deposited $Zn_{1-x}Co_xO$ thin films," *Journal of Applied Physics*, vol. 98, no. 11, p. 114909, 2005.

[66] L. Escobar-Alarcón, E. Camps, S. Romero, S. Muhl, I. Camps, and E. Haro-Poniatowski, "TiCN thin films grown by reactive crossed beam pulsed laser deposition," *Applied Physics A: Materials Science & Processing*, vol. 101, pp. 771–775, 2010. 10.1007/s00339-010-5935-2.

[67] A. Jesche, A. Gorbunoff, A. Mensch, H. Stocker, A. A. Levin, and D. C. Meyer, "Structure and giant magnetoresistance of granular Co-Cu nanolayers prepared by cross-beam pulsed laser deposition," *Journal of Applied Physics*, vol. 107, no. 2, p. 023904, 2010.

[68] E. György, J. Santiso, A. Giannoudakos, M. Kompitsas, I. Mihailescu, and D. Pantelica, "Growth of Al doped ZnO thin films by a synchronized two laser system," *Applied Surface Science*, vol. 248, no. 1-4, pp. 147–150, 2005. 4th International Conference on Photo-Excited Processes and Applications.

[69] E. Gyorgy, G. Sauthier, A. Figueras, A. Giannoudakos, M. Kompitsas, and I. N. Mihailescu, "Growth of Au-TiO_2 nanocomposite thin films by a dual-laser, dual-target system," *Journal of Applied Physics*, vol. 100, no. 11, p. 114302, 2006.

[70] C. K. Ong, S. Y. Xu, and W. Z. Zhou, "A novel approach for doping impurity in thin film in situ by dual-beam pulsed-laser deposition," *Review of Scientific Instruments*, vol. 69, no. 10, pp. 3659–3661, 1998.

[71] T. Bhutta, J. I. Mackenzie, D. P. Shepherd, and R. J. Beach, "Spatial dopant profiles for transverse-mode selection in multimode waveguides," *J. Opt. Soc. Am. B*, vol. 19, pp. 1539–1543, Jul 2002.

[72] J. Mackenzie, "Dielectric solid-state planar waveguide lasers: A review," *Selected Topics in Quantum Electronics, IEEE Journal of*, vol. 13, no. 3, pp. 626–637, 2007.

[73] L. M. B. Hickey, V. Apostolopoulos, R. W. Eason, J. S. Wilkinson, and A. A. Anderson, "Diffused Ti:sapphire channel-waveguide lasers," *J. Opt. Soc. Am. B*, vol. 21, pp. 1452–1462, Aug 2004.

[74] L.-L. Wang, K.-M. Wang, X.-Z. Liu, and Q.-M. Lu, "Monomode channel waveguide in $KTiOPO_4$ crystal produced by Rb^+ ion exchange combined with Si^+ ion implantation," *Applied Physics B: Lasers and Optics*, vol. 99, pp. 203–207, 2010.

[75] S. L. Rochelle, Y. Zhao, E. Knystautas, N. Bélanger, A. Villeneuve, and M. Saad, "Planar waveguides in ZBLAN fabricated by He ion implantation," in *Integrated Photonics Research*, p. IThI7, Optical Society of America, 2000.

[76] H. Li, X. Wu, R. Songa, J. Wang, and H. Zhang, "Growth of crystalline $\mathrm{YbVO_4}$ thin-film optical waveguides by pulsed laser deposition," *Vacuum*, vol. 82, pp. 463–467, 2008.

[77] J. Sonsky, J. Lancok, M. Jelinek, J. Oswald, and V. Studnicka, "Growth of active Nd-doped YAP thin-film waveguides by laser ablation," *Appl. Phys. A*, vol. 66, no. 5, pp. 583–586, 1998.

[78] K. M. Okoshi, M. and N. Inoue, "Optical waveguides fabricated by pulsed-laser deposition of $\mathrm{SiO_2}$ films with different refractive indices," *Appl. Phys. Lett.*, vol. 81, no. 5, pp. 789–791, 2002.

[79] E. Flores-Romero, G. V. Vázquez, H. Márquez, R. Rangel-Rojo, J. Rickards, and R. Trejo-Luna, "Laser emission in proton-implanted Nd:YAG channel waveguides," *Opt. Express*, vol. 15, pp. 17874–17880, Dec 2007.

[80] A. Benayas, D. Jaque, Y. Yao, F. Chen, A. A. Bettiol, A. Rodenas, and A. K. Kar, "Microstructuring of Nd:YAG crystals by proton-beam writing," *Opt. Lett.*, vol. 35, pp. 3898–3900, Dec 2010.

[81] M. Szachowicz, P. Moretti, M.-F. Joubert, M. Couchaud, and B. Ferrand, "Fabrication of $\mathrm{H^+}$ implanted channel waveguides in $\mathrm{Y_3Al_5O_{12}}$:Nd,Tm single crystal buried epitaxial layers for infrared to blue upconversion laser systems," *Applied Physics Letters*, vol. 90, no. 3, p. 031113, 2007.

[82] C. L. Sones, P. Ganguly, Y. J. Ying, F. Johann, E. Soergel, R. W. Eason, and S. Mailis, "Spectral and electro-optic response of UV-written waveguides in $\mathrm{LiNbO_3}$ single crystals," *Opt. Express*, vol. 17, pp. 23755–23764, Dec 2009.

[83] J. Siebenmorgen, T. Calmano, K. Petermann, and G. Huber, "Highly efficient Yb:YAG channel waveguide laser written with a femtosecond-laser," *Opt. Express*, vol. 18, pp. 16035–16041, Jul 2010.

[84] Y. Tan, F. Chen, J. R. V. de Aldana, G. A. Torchia, A. Benayas, and D. Jaque, "Continuous wave laser generation at 1064 nm in femtosecond laser inscribed Nd:$\mathrm{YVO_4}$ channel waveguides," *Applied Physics Letters*, vol. 97, no. 3, p. 031119, 2010.

[85] Y. Tan, A. Rodenas, F. Chen, R. R. Thomson, A. K. Kar, D. Jaque, and Q. Lu, "70% slope efficiency from an ultrafast laser-written Nd:$\mathrm{GdVO_4}$ channel waveguide laser," *Opt. Express*, vol. 18, pp. 24994–24999, Nov 2010.

[86] J. Bradley, F. Ay, K. Wörhoff, and M. Pollnau, "Fabrication of low-loss channel waveguides in Al_2O_3 and Y_2O_3 layers by inductively coupled plasma reactive ion etching," *Applied Physics B: Lasers and Optics*, vol. 89, pp. 311–318, 2007. 10.1007/s00340-007-2815-3.

[87] K. Worhoff, J. Bradley, F. Ay, D. Geskus, T. Blauwendraat, and M. Pollnau, "Reliable low-cost fabrication of low-loss Al_2O_3:Er^{3+} waveguides with 5.4-dB optical gain," *Quantum Electronics, IEEE Journal of*, vol. 45, pp. 454 –461, may 2009.

[88] L. Wilkens, D. Trager, H. Dotsch, A. F. Popkov, and A. M. Alekseev, "Nonreciprocal phase shift of TE modes induced by a compensation wall in a magneto–optic rib waveguide," *Applied Physics Letters*, vol. 79, no. 26, pp. 4292–4294, 2001.

[89] R. Gerhardt, J. Kleine-Borger, L. Beilschmidt, M. Frommeyer, H. Dotsch, and B. Gather, "Efficient channel-waveguide laser in Nd:GGG at 1.062 µm wavelength," *Applied Physics Letters*, vol. 75, no. 9, pp. 1210–1212, 1999.

[90] D. Wortmann and J. Gottmann, "Fs-laser structuring of ridge waveguides," *Appl. Phys. A*, vol. 93, pp. 197–201, 2008.

[91] J. Gottmann, D. Wortmann, I. Vasilief, L. Moiseev, and D. Ganser, "Manufacturing of Nd:$Gd_3Ga_5O_{12}$ ridge waveguide lasers by pulsed laser deposition and ultrafast laser micromachining," *Appl. Surf. Sci.*, vol. 254, pp. 1105–1110, 2007.

[92] D. Wang, K. Lor, K. Chung, H. Chan, K. Chiang, H. Chan, and C. Choy, "Optical rib waveguide based on epitaxial $Ba_{0.7}Sr_{0.3}TiO_3$ thin film grown on MgO," *Thin Solid Films*, vol. 510, no. 1-2, pp. 329 – 333, 2006.

[93] M. Gaidi, L. Stafford, J. Margot, M. Chaker, R. Morandotti, and M. Kulishov, "Microfabricated $SrTiO_3$ ridge waveguides," *Applied Physics Letters*, vol. 86, no. 22, p. 221106, 2005.

[94] M. Craven, P. Waltereit, F. Wu, J. Speck, and S. DenBaars, "Characterization of a-plane GaN/(Al,Ga)N multiple quantum wells grown via metalorganic chemical vapor deposition," *Jpn. J. Appl. Phys.*, vol. 42, pp. 235–238, 2003.

[95] A. Krost, F. Heinrichsdorff, D. Bimberg, A. Darhuber, and G. Bauer, "High-resolution x-ray diffraction of self-organized InGaAs/GaAs quantum dot structures," *Appl. Phys. Lett.*, vol. 68, no. 6, pp. 785–787, 1996.

[96] S. Senz, U. Egger, M. Schultz, U. Gosele, and H. Ito, "Interdiffusion in $GaAs_{(1-x)}Sb_x$/GaAs superlattices studied with high-resolution x-ray diffraction and secondary ion mass spectroscopy," *Journal of Applied Physics*, vol. 84, no. 5, pp. 2546–2550, 1998.

[97] S. Ishida, T. Miyamoto, and F. Koyama, "Short-period GaInAs/InP superlattice for distributed bragg reflector," *Japanese Journal of Applied Physics Part 2*, vol. 45, no. 24-28, pp. L723–L725, 2006.

[98] H.-H. Choy, *Quantum wells on indium gallium arsenic compositionally graded buffers realized by molecular beam epitaxy.* PhD thesis, Massachusetts Institute of Technology, 2005.

[99] Y. Ishibashi, N. Ohashi, and T. Tsurumi, "Structural refinement of x-ray diffraction profile for artificial superlattices," *Japanese Journal of Applied Physics Part 1*, vol. 39, no. 1, pp. 186–191, 2000.

[100] I. Schuller, "New class of layered materials," *Phys. Rev. Lett.*, vol. 44, no. 24, pp. 1597–1600, 1980.

[101] S.-J. Chiu, Y.-T. Liu, H.-Y. Lee, G.-P. Yu, and J.-H. Huang, "Growth of $BiFeO_3/SrTiO_3$ artificial superlattice structure by rf sputtering," *Journal of Crystal Growth*, vol. 334, no. 1, pp. 90 – 95, 2011.

[102] T. Kobata, G. Tsukahara, and Y. Uesu, "Fabrication of $LiNbO_3/LiTaO_3$ superlattice thin films and their second harmonic generation characteristics," *Ferroelectrics*, vol. 416, no. 1, pp. 125–132, 2011.

[103] F. Le Marrec, R. Farhi, D. Ariosa, M. El Marssi, J.-L. Dellis, and M. G. Karkut, "Mixed orientation $PbTiO_3/BaTiO_3$ superlattices: X-ray diffraction and raman spectroscopy," *Ferroelectrics*, vol. 241, pp. 125–131, 1999.

[104] M. Ziese, I. Vrejoiu, E. Pippel, E. Nikulina, and D. Hesse, "Magnetic properties of $Pr_{0.7}Ca_{0.3}MnO_3/SrRuO_3$ superlattices," *Applied Physics Letters*, vol. 98, no. 13, p. 132504, 2011.

[105] J. X. Zhang, J. Y. Dai, and H. L. W. Chan, "Interfacial engineering and coupling of electric and magnetic properties in $Pb(Zr_{0.53}Ti_{0.47})O_3/CoFe_2O_4$ multiferroic epitaxial multilayers," *Journal of Applied Physics*, vol. 107, no. 10, p. 104105, 2010.

[106] S. M. Hamidi, M. M. Tehranchi, and M. Shasti, "Engineered one-dimensional magneto-photonic crystals for wavelength division multiplexing systems," *Journal of Physics D: Applied Physics*, vol. 44, no. 20, p. 205107, 2011.

[107] S. I. Khartsev and A. M. Grishin, "$[Bi_3Fe_5O_{12}/Gd_3Ga_5O_{12}]^m$ magneto-optical photonic crystals," *Applied Physics Letters*, vol. 87, no. 12, p. 122504, 2005.

[108] M. Lorenz, H. Hochmuth, R. Schmidt-Grund, E. Kaidashev, and M. Grundmann, "Single-transverse-mode Ti : sapphire rib waveguide laser," *Opt. Express*, vol. 13, no. 1, pp. 210–215, 2005.

[109] J. Sellmann, C. Sturm, R. Schmidt-Grund, C. Czekalla, J. Lenzner, H. Hochmuth, B. Rheinländer, M. Lorenz, and M. Grundmann, "Structural and optical properties of ZrO_2 and Al_2O_3 thin films and bragg reflectors grown by pulsed laser deposition," *physica status solidi (c)*, vol. 5, no. 5, pp. 1240–1243, 2008.

[110] R. Schmidt-Grund, B. Rheinländer, C. Czekalla, G. Benndorf, H. Hochmut, A. Rahm, M. Lorenz, and M. Grundmann, "ZnO based planar and micropillar resonators," *Superlattices and Microstructures*, vol. 41, no. 5-6, pp. 360–363, 2007.

[111] C. Sturm, H. Hilmer, R. Schmidt-Grund, and M. Grundmann, "Observation of strong exciton-photon coupling at temperatures up to 410 K," *New Journal of Physics*, vol. 11, no. 7, p. 073044, 2009.

[112] J. Shen and Y. Shen, "Investigation on the structural and spectral characteristics of deposited FBG stacks at elevated temperature," *Sensors and Actuators A: Physical*, vol. 147, no. 1, pp. 99 – 103, 2008.

[113] J. Bailey and J. Sharp, "Thin film polymer photonics: Spin cast distributed bragg reflectors and chirped polymer structures," *The European Physical Journal E: Soft Matter and Biological Physics*, vol. 33, pp. 41–49, 2010. 10.1140/epje/i2010-10657-4.

[114] M. Kolle, B. Zheng, N. Gibbons, J. J. Baumberg, and U. Steiner, "Stretch-tuneable dielectric mirrors and optical microcavities," *Opt. Express*, vol. 18, pp. 4356–4364, Mar 2010.

[115] A. Mouldi and M. Kanzari, "Broad multilayer antireflection coating by apodized and chirped photonic crystal," *Optics Communications*, vol. 284, no. 18, pp. 4124 – 4128, 2011.

[116] W. P. Latham, A. Lobad, T. C. Newell, and D. Stalnaker, "6.5 kW, Yb:YAG ceramic thin disk laser," *AIP Conference Proceedings*, vol. 1278, no. 1, pp. 758–764, 2010.

[117] M. Tsunekane and T. Taira, "300 W continuous-wave operation of a diode edge-pumped, hybrid composite Yb : YAG microchip laser," *Opt. Lett.*, vol. 31, no. 13, pp. 2003–2005, 2006.

[118] A. Giesen and J. Speiser, "Fifteen years of work on thin-disk lasers: Results and scaling laws," *IEEE J. Sel. Top. Quant.*, vol. 13, no. 3, pp. 598–609, 2007.

[119] D. Kouznetsov and J.-F. Bisson, "Role of undoped cap in the scaling of thin-disk lasers," *Journal of the Optical Society of America B*, vol. 25, no. 3, pp. 338–345, 2008.

[120] M. Tsunekane and T. Taira, "Design and performance of compact heatsink for high-power diode edge-pumped, microchip lasers," *IEEE J. Sel. Top. Quant.*, vol. 13, no. 3, pp. 619–625, 2007.

[121] M. Tsunekane and T. Taira, "High-power operation of diode edge-pumped, composite all-ceramic Yb:$Y_3Al_5O_{12}$ microchip laser," *Appl. Phys. Lett.*, vol. 90, p. 121101, 2007.

[122] T. Dascalu, N. Pavel, and T. Taira, "90 W continuous-wave diode edge-pumped microchip composite Yb:$Y_3Al_5O_{12}$ laser," *Applied Physics Letters*, vol. 83, no. 20, pp. 4086–4088, 2003.

[123] J. Dong, A. Shirakawa, K.-i. Ueda, H. Yagi, T. Yanagitani, and A. Kaminskii, "Laser-diode pumped heavy-doped Yb:YAG ceramic lasers," *Opt. Lett.*, vol. 32, no. 13, pp. 1890–2, 2007.

[124] S. Chenais, F. Druon, F. Balembois, P. Georges, A. Brenier, and G. Boulon, "Diode-pumped Yb:GGG laser: comparison with Yb:YAG," *Optical Materials*, vol. 22, no. 2, pp. 99 – 106, 2003.

[125] J. Dong, K. Ueda, and A. Kaminskii, "Laser-diode pumped efficient Yb:LuAG microchip lasers oscillating at 1030 and 1047 nm," *Laser Physics Letters*, vol. 7, no. 10, pp. 726–733, 2010.

[126] R. Peters, C. Krankel, S. Fredrich-Thornton, K. Beil, K. Petermann, G. Huber, O. Heckl, C. Baer, C. Saraceno, T. Sudmeyer, and U. Keller, "Thermal analysis and efficient high power continuous-wave andmode-locked thin disk laser operation of Yb-doped sesquioxides," *Applied Physics B: Lasers and Optics*, vol. 102, pp. 509–514, 2011. 10.1007/s00340-011-4428-0.

[127] H. Yoshioka, S. Nakamura, T. Ogawa, and S. Wada, "Diode-pumped mode-locked Yb:YAG ceramic laser," *Opt. Express*, vol. 17, pp. 8919–8925, May 2009.

[128] S. Rivier, X. Mateos, Òscar Silvestre, V. Petrov, U. Griebner, M. C. Pujol, M. Aguiló, F. Díaz, S. Vernay, and D. Rytz, "Thin-disk Yb:KLu$(WO_4)_2$ laser with single-pass pumping," *Opt. Lett.*, vol. 33, pp. 735–737, Apr 2008.

[129] S. B. Ubizskii, A. O. Matkovskii, S. S. Melnyk, I. M. Syvorotka, V. Muller, V. Peters, K. Petermann, A. Beyertt, and A. Giesen, "Optical properties of epitaxial YAG:Yb films," *Physica Status Solidi (a)*, vol. 201, no. 4, pp. 791–797, 2004.

[130] C. Chaneliere, J. Autran, R. Devine, and B. Balland, "Tantalum pentoxide (Ta_2O_5) thin films for advanced dielectric applications," *Mat. Sci. Eng. R*, vol. 6, pp. 269–322, 1998.

[131] J. Cuomo, V. Sadagopan, J. DeLuca, P. Chaudhari, and R. Rosenberg, "Growth of uniaxial magnetic garnet films by rf sputtering," *Applied Physics Letters*, vol. 21, no. 12, pp. 581–584, 1972.

[132] Y. Deng, J. Fowlkes, J. Fitz-Gerald, and P. Rack, "Combinatorial thin film synthesis of Gd-doped $Y_3A_5O_{12}$ ultraviolet emitting materials," *Applied Physics A: Materials Science & Processing*, vol. 80, pp. 787–789, 2005. 10.1007/s00339-003-2385-0.

[133] W.-H. Chao, R.-J. Wu, and T.-B. Wu, "Structural and luminescent properties of YAG:Ce thin film phosphor," *Journal of Alloys and Compounds*, vol. 506, no. 1, pp. 98–102, 2010.

[134] C. Holmes, *Direct UV written planar devices for sensing and telecommunication applications.* PhD thesis, University of Southampton, 2009.

[135] G. R. Bai, H. L. M. Chang, and C. M. Foster, "Preparation of single-crystal $Y_3Al_5O_{12}$ thin film by metalorganic chemical vapor deposition," *Applied Physics Letters*, vol. 64, no. 14, pp. 1777–1779, 1994.

[136] D. M. Gualtieri, "Liquid phase epitaxy of yttrium aluminum garnet: Reduction of growth rate by germanium oxide," *Applied Physics Letters*, vol. 59, no. 6, pp. 650–652, 1991.

[137] R. Gupta and N. Chaudhury, "Entrapment of biomolecules in sol-gel matrix for applications in biosensors: Problems and future prospects," *Biosensors and Bioelectronics*, vol. 22, pp. 2387–2399, 2007.

[138] D. Shepherd, C. Bonner, C. Brown, W. Clarkson, A. Tropper, and D. Hanna, "High numerical-aperture, contact-bonded, planar waveguides for diode bar-pumped lasers," *Opt. Commun.*, vol. 160, no. 1-3, pp. 47–50, 1999.

[139] S. J. Hettrick, J. I. Mackenzie, R. D. Harris, J. S. Wilkinson, D. P. Shepherd, and A. C. Tropper, "Ion-exchanged tapered-waveguide laser in neodymium-doped BK7 glass," *Opt. Lett.*, vol. 25, pp. 1433–1435, Oct 2000.

[140] D. J. Moss, V. G. Ta'eed, B. J. Eggleton, D. Freeman, S. Madden, M. Samoc, B. Luther-Davies, S. Janz, and D.-X. Xu, "Bragg gratings in silicon-on-insulator waveguides by focused ion beam milling," *Applied Physics Letters*, vol. 85, no. 21, pp. 4860–4862, 2004.

[141] R. Kelly and A. Miotello, "Mechanisms of pulsed laser sputtering," in *Pulsed Laser Deposition of Thin Films* (D. Chrisey and G. Hubler, eds.), vol. 1, Wiley, 1993.

[142] J. Perriere, E. Millon, W. Seiler, C. Boulmer-Leborgne, V. Craciun, O. Albert, J. C. Loulergue, and J. Etchepare, "Comparison between ZnO films grown by femtosecond and nanosecond laser ablation," *Journal of Applied Physics*, vol. 91, no. 2, pp. 690–696, 2002.

[143] M. Darby, *Femtosecond pulsed laser deposition.* PhD thesis, University of Southampton, 2009.

[144] R. Stoian, A. Rosenfeld, D. Ashkenasi, I. V. Hertel, N. M. Bulgakova, and E. E. B. Campbell, "Surface charging and impulsive ion ejection during ultrashort pulsed laser ablation," *Phys. Rev. Lett.*, vol. 88, p. 097603, Feb 2002.

[145] M. N. R. Ashfold, F. Claeyssens, G. M. Fuge, and S. J. Henley, "Pulsed laser ablation and deposition of thin films," *Chem. Soc. Rev.*, vol. 33, pp. 23–31, 2004.

[146] S. Barrington, T. Bhutta, D. Shepherd, and R. Eason, "The effect of particulate density on performance of Nd:$Gd_3Ga_5O_12$ waveguide lasers grown by pulsed laser deposition," *Opt. Commun.*, vol. 185, pp. 145–152, 2000.

[147] D. Arnold and E. Cartier, "Theory of laser-induced free-electron heating and impact ionization in wide-band-gap solids," *Phys. Rev. B*, vol. 46, pp. 15102–15115, Dec 1992.

[148] P. R. Willmott and J. R. Huber, "Pulsed laser vaporization and deposition," *Rev. Mod. Phys.*, vol. 72, pp. 315–328, Jan 2000.

[149] D. Geohegan, "Diagnostics and characteristics of pulsed laser deposition laser plasmas," in *Pulsed Laser Deposition of Thin Films* (D. Chrisey and G. Hubler, eds.), vol. 1, Wiley, 1993.

[150] R. K. Singh and J. Viatella, "Estimation of plasma absorption effects during pulsed laser ablation of high-critical-temperature superconductors," *Journal of Applied Physics*, vol. 75, no. 2, pp. 1204–1206, 1994.

[151] A. V. Bulgakov and N. M. Bulgakova, "Gas-dynamic effects of the interaction between a pulsed laser-ablation plume and the ambient gas: analogy with an underexpanded jet," *Journal of Physics D: Applied Physics*, vol. 31, no. 6, p. 693, 1998.

[152] R. Wood, J. Leboeuf, D. Geohegan, A. Puretzky, and K. Chen, "Dynamics of plume propagation and splitting during pulsed-laser ablation of Si in He and Ar," *Phys. Rev. B*, vol. 58, pp. 1533–1543, 1998.

[153] D. Norton, "Synthesis and properties of epitaxial electronic oxide thin-film materials," *Mat. Sci. Eng. R*, vol. 43, pp. 139–247, 2004.

[154] J. S. Horwitz and J. A. Sprague, "Film nucleation and film growth in pulsed laser deposition of ceramics," in *Pulsed Laser Deposition of Thin Films* (D. Chrisey and G. Hubler, eds.), vol. 1, Wiley, 1993.

[155] L. V. Zhigilei, "Crystal defects." Lecture notes, Department of Materials Science and Engineering, University of Virginia, 2011.

[156] J. Kvapil, J. Kvapil, B. Perner, B. Mánek, K. Blažek, and Z. Hendrich, "Nonstoichiometric defects in YAG and YAP," *Crystal Research and Technology*, vol. 20, no. 4, pp. 473–478, 1985.

[157] L. Chen, "Particulates generated by pulsed laser ablation," in *Pulsed Laser Deposition of Thin Films* (D. Chrisey and G. Hubler, eds.), vol. 1, Wiley, 1993.

[158] P. E. Dyer, S. D. Jenkins, and J. Sidhu, "Development and origin of conical structures on XeCl laser ablated polyimide," *Applied Physics Letters*, vol. 49, no. 8, pp. 453–455, 1986.

[159] L. K. Ang, Y. Y. Lau, R. M. Gilgenbach, H. L. Spindler, J. S. Lash, and S. D. Kovaleski, "Surface instability of multipulse laser ablation on a metallic target," *Journal of Applied Physics*, vol. 83, no. 8, pp. 4466–4471, 1998.

[160] M. Bolle and S. Lazare, "Characterization of submicrometer periodic structures produced on polymer surfaces with low-fluence ultraviolet laser radiation," *Journal of Applied Physics*, vol. 73, no. 7, pp. 3516–3524, 1993.

[161] C. Grivas, "Optically pumped planar waveguide lasers, Part I: Fundamentals and fabrication techniques," *Progress in Quantum Electronics*, vol. 35, no. 6, pp. 159 – 239, 2011.

[162] D. P. Shepherd, S. J. Hettrick, C. Li, J. I. Mackenzie, R. J. Beach, S. C. Mitchell, and H. E. Meissner, "High-power planar dielectric waveguide lasers," *Journal of Physics D: Applied Physics*, vol. 34, no. 16, p. 2420, 2001.

[163] B. D. Snow, *Liquid Crystal Adaptive Planar Optical Devices.* PhD thesis, University of Southampton, 2010.

[164] S. Green, A. Pique, K. Harshavardhan, and J. Bernstein, "Equipment," in *Pulsed Laser Deposition of Thin Films* (D. Chrisey and G. Hubler, eds.), vol. 1, Wiley, 1993.

[165] T. C. May-Smith, A. C. Muir, M. S. B. Darby, and R. W. Eason, "Design and performance of a ZnSe tetra-prism for homogeneous substrate heating using a CO_2 laser for pulsed laser deposition experiments," *Appl. Optics*, vol. 47, no. 11, pp. 1767–1780, 2008.

[166] M. Enrech, *Pulsed laser deposition, characterisation and properties of metallic films and Co/Pd and Fe/Pd multilayers.* PhD thesis, University of Dublin, 1993.

[167] S. Stepanov, "GID_sl on the web."

[168] Department of Physics, University of Aachen, "X-ray-reflectometry (XRR)."

[169] L. Peter and R. Noll, "Material ablation and plasma state for single and collinear double pulses interacting with iron samples at ambient gas pressures below 1 bar," *Appl Phys B*, vol. 86, pp. 159–167, 2007.

[170] L. Freund and S. Suresh, *Thin Film Materials: Stress, Defect Formation and Surface Evolution.* Cambridge University Press, 2003.

[171] L. Azaroff, *Elements of X-ray crystallography.* McGraw-Hill, 1968.

[172] D. H. Blank, G. Koster, G. A. Rijnders, E. van Setten, P. Slycke, and H. Rogalla, "Epitaxial growth of oxides with pulsed laser interval deposition," *Journal of Crystal Growth*, vol. 211, no. 1-4, pp. 98 – 105, 2000.

[173] M. Bass, *Handbook of Optics*, vol. 4. McGraw-Hill, 2009.

[174] R. Swanepoel, "Determination of the thickness and optical constants of amorphous silicon," *J. Phys. E: Sci. Instrum.*, vol. 16, pp. 1214–1222, 1983.

[175] R. Serna and C. N. Afonso, "In situ growth of optically active erbium doped Al_2O_3 thin films by pulsed laser deposition," *Applied Physics Letters*, vol. 69, no. 11, pp. 1541–1543, 1996.

[176] E. Hecht, *Optics*. Pearson Education Inc., 4^{th} ed., 2002.

[177] C. Jerez-Hernandez, D. Qiao, and S. Lau, "A study of Si wafer bonding via methanol capillarity," *Materials Chemistry and Physics*, vol. 77, pp. 751–754, 2002.

[178] J. M. González-Leal and J. A. Angel, "Fabrication of axicons by CW laser effusion," *Opt. Lett.*, vol. 32, pp. 2384–2386, Aug 2007.

[179] A. K. Pradhan, K. Zhang, S. Mohanty, J. Dadson, D. Hunter, G. B. Loutts, U. N. Roy, Y. Cui, A. Burger, and A. L. Wilkerson, "Luminescence and spectroscopic behavior of Eu^{3+}-doped Y_2O_3 and Lu_2O_3 epitaxial films grown by pulsed-laser deposition," *Journal of Applied Physics*, vol. 97, p. 023513, 2005.